Université de Limoges

École Doctorale Sciences et Ingénierie des Matériaux, Mécanique, Énergétique – SIMME (ED 609)

Institut de Recherche sur les Céramiques (IRCER) – UMR CNRS 7315

Thèse pour obtenir le grade de
Docteur de l'Université de Limoges
Matériaux Céramiques et Traitements de Surface

Présentée et soutenue par
Mohammed Reda ZAKI

Le 14 mars 2018

Synthèse, structure et propriétés optiques de nouveaux verres à base d'oxyde de tellure dans les systèmes TeO_2-TiO_2-WO_3 et TeO_2-$NbO_{2,5}$-WO_3

Thèse dirigée par **David HAMANI**, **Olivier MASSON** et **Philippe THOMAS**

Jury :

Rapporteurs
Marc DUSSAUZE, Chargé de Recherche CNRS - HDR, ISM, Bordeaux
Mikhaïl SMIRNOV, Professeur, Université d'État de Saint-Pétersbourg (Russie)

Examinateurs
Thierry CARDINAL, Directeur de Recherche CNRS, ICMCB, Bordeaux
David HAMANI, Maître de Conférences, IRCER, Limoges
Olivier MASSON, Professeur, IRCER, Limoges
Philippe THOMAS, Directeur de Recherche CNRS, IRCER, Limoges

Membre invité
Maggy DUTREILH-COLAS, Chargée de Recherche CNRS - HDR, IRCER, Limoges

Université de Limoges

Université de Limoges

École Doctorale Sciences et Ingénierie des Matériaux, Mécanique, Énergétique – SIMME (ED 609)

Institute of Research on Ceramics (IRCER) – UMR CNRS 7315

Thesis submitted for the degree of

Doctor of philosophy of the University of Limoges

Ceramic Materials and Surface Treatments

Presented by
Mohammed Reda ZAKI

March 14, 2018

Synthesis, structure and optical properties of new tellurium oxide-based glasses within the TeO$_2$-TiO$_2$-WO$_3$ and TeO$_2$-NbO$_{2.5}$-WO$_3$ systems

Supervisors: **David HAMANI**, **Olivier MASSON** and **Philippe THOMAS**

Jury:

<u>Referees</u>
Marc DUSSAUZE, CNRS Researcher - HDR, ISM, Bordeaux
Mikhaïl SMIRNOV, Professor, Saint Petersburg State University (Russia)

<u>Inspectors</u>
Thierry CARDINAL, CNRS Research Director, ICMCB, Bordeaux
David HAMANI, Associate Professor, IRCER, Limoges
Olivier MASSON, Professor, IRCER, Limoges
Philippe THOMAS, CNRS Research Director, IRCER, Limoges

<u>Invited member</u>
Maggy DUTREILH-COLAS, CNRS Researcher - HDR, IRCER, Limoges

Dedicated to my beloved parents and family for their love, endless support, encouragement and sacrifices.

"What you are basically, deep deep down, far far in, is simply the fabric and structure of existence itself. Reality itself is gorgeous!"

Alan Watts

Acknowledgments

Table of contents

General introduction

One of the last major scientific and technological revolutions has been the spectacular development of the optical communication technology laying the foundations for the digital revolution and information age. Today, smartphones and massive access to and share of information via the Internet have deeply shifted and elevated the way we interact with the world. Among the foundations of this scientific, technological, and social shift are the nonlinear optical telecommunication systems which permit, at lower costs, the transmission of a much larger amount of information (~Gbit/s) than the classic transmission media, *e.g.,* radio waves (~kbit/s) and copper wires (~Mbit/s) [1].

The development of nonlinear optical communication systems, such as optical amplifiers, modulators, sensors and high-speed optical switches, has stimulated a plethora of scientific investigations in search of the optimal material exhibiting the desired physical properties and most importantly high linear and nonlinear optical indices which are altogether necessary to properly fulfill one or many functions within a given optical system. Among the promising materials for such applications, the heavy-metal oxide-based glasses doped with transition-metal oxides (*e.g.,* TiO_2, WO_3 and $NbO_{2.5}$) and rare-earth ions occupy a privileged position owing to their remarkable physical characteristics. For several decades, considerable efforts have been devoted to their fundamental research and development, and yet many of their aspects remain poorly uncovered to this date.

Tellurium oxide-, germanium oxide- and antimony oxide-based glasses are some of the most attractive heavy-metal oxide-based glasses due to their large optical transmittances, high nonlinear optical responses and acceptance of rare-earth ions in their glass-forming networks [2]. In particular, tellurium oxide or TeO_2-based glasses (commonly referred to as tellurite glasses) exhibit remarkable chemical and physical properties making them very promising materials for the development of more advanced nonlinear optical devices. Thanks to their ease of glass formation combined with good thermal and chemical properties, TeO_2-based glasses can be manufactured in a variety of forms such as bulk glasses, films, optical fibers, *etc.* These glasses exhibit good chemical stabilities, high mechanical resistance, large optical transmittance window (0.3–5 μm), high linear refractive indices of ~2 and particularly high third-order nonlinear susceptibilities $\chi^{(3)}$ which are 10 to 50 times higher than the conventional silica SiO_2-based glasses [3].

Specifically, the remarkably high linear and nonlinear optical performances of TeO_2-based glasses have aroused the curiosity of many researchers as to the nature of the structural origins leading to such exceptional properties. Investigations on this matter constituted a dynamic research area in the IRCER laboratory (formerly called SPCTS) and eventually revealed the active contributions of *(i)* the lone electron pair on the tellurium Te^{4+} cation [4–8] and *(ii)* the inherent …–Te–O–Te–… framework [9–11] to the high nonlinear performance in these glasses. In the same spirit, the present work is a continuation of those efforts with the ultimate aim of reaching a comprehensive understanding of the structural features of TeO_2-based glasses containing TiO_2, WO_3 and $NbO_{2.5}$ and how they affect their optical properties.

This work is organized as follows.

The first chapter is dedicated to *(i)* introducing the basic concepts in the field of glass science, *(ii)* highlighting the state-of-the-art on the structure of amorphous and crystalline TeO_2, and *(iii)* reviewing the previous studies on the structure and properties of specific binary glasses within TeO_2-TiO_2, TeO_2-WO_3 and TeO_2-$NbO_{2.5}$ systems and ternary TeO_2-TiO_2-WO_3 and TeO_2-$NbO_{2.5}$-WO_3 glasses that are investigated in this work.

In the second chapter, we first outline the essence of the cationic field strength theory by Dietzel and then report the uncovered correlations between the calculated cationic field strengths and the state-of-the-art phase relations in various crystalline and amorphous TeO_2-based systems. The goal of this approach is to enable a fast and reliable structural prediction in simple TeO_2-based glasses (*i.e.,* binary systems) by evaluating the field strength difference between the two constituent cations of the glass network.

The third chapter is devoted to the description of the experimental conditions under which the studied glasses in this work have been prepared, namely, the pure TeO_2 glass and glasses within the TeO_2-TiO_2, TeO_2-TiO_2-WO_3 and TeO_2-$NbO_{2.5}$-WO_3 systems. Moreover, the measurement conditions of their physical properties, namely the density, thermal, structural and optical properties are documented. A detailed description of the post-treatment of Raman spectra and particularly the spectral decomposition process is given. In addition, we bring to attention the necessity of controlling the light polarization when recording Raman spectra from TeO_2-based glasses and report our recorded polarized Raman spectra from pure TeO_2 glass and comment on the associated depolarization ratio.

In the fourth chapter, we report the obtained glass-forming domain within the TeO_2-TiO_2-WO_3 system, density, thermal, structural (by Raman spectroscopy) and optical (linear and

nonlinear) properties of the prepared glass samples. We mainly focus on *(i)* revealing the structural effects of adding TiO_2 and WO_3 on the glass structure based on a full-scale Raman spectral decomposition, and *(ii)* discussing their contributions to the linear (refractive index n) and nonlinear (third-order nonlinear susceptibility $\chi^{(3)}$) response in the studied glasses.

In the fifth chapter, and along the same lines, we report the identified glass-forming domain within the TeO_2-$NbO_{2.5}$-WO_3 system, density, thermal, structural and optical properties of the obtained glass samples. Again, we chiefly focus on *(i)* revealing the structural effects of adding $NbO_{2.5}$ and WO_3 on the structural network, and *(ii)* discussing their contributions to the linear and nonlinear response in the studied glasses. In addition, we compare the two ternary systems in terms of their structural networks and optical performances.

Chapter I.   State-of-the-art review: amorphous and crystalline TeO₂-based materials

I.1. Introduction

In this chapter, we first review some of the fundamental concepts related to the glassy state of matter (*section I.2.*) and then highlight several aspects of TeO₂-based glasses outlining their glass-forming ability, structural and physical properties and technological applications (*section I.3*). The most common approach to understand the origins of the glass structural and physical properties is based on the close examination of the structural aspects of the parent crystalline system. For this reason, we review in *section I.4.1* the structural and vibrational aspects of each of the tellurium oxide TeO₂ polymorphs. Furthermore, we summarize the previous studies on equilibrium and non-equilibrium phase diagrams of the three binary systems TeO₂-TiO₂, TeO₂-WO₃ and TeO₂-NbO₂.₅. This part serves as a descriptive support for *Chapters IV and V* dealing with the experimental results obtained from ternary TeO₂-TiO₂-WO₃ and TeO₂-NbO₂.₅-WO₃ systems respectively.

I.2. General introduction to oxide glasses

Vitreous materials in the form of glazed stones and faience were first produced from about the 4ᵗʰ millennium B.C. in the Near East and Egypt [12]. Small objects made of glass are found dating from the late 3ʳᵈ millennium B.C. onward. However, it was not until about 1500 B.C. that considerable amounts of glass (mostly silica-based), including glass vessels, began to be produced. The scientific study of glasses started with Faraday (1791-1867) and others at the beginning of the 19ᵗʰ century. Over two centuries later, today, glass science is a well matured subject and from the technological standpoint, many novel materials are produced in the amorphous form holding special properties destined for specific technological applications.

I.2.1. Glass nature

The "glassy" or "vitreous" state refers to the underlying structural arrangement of atoms within the network of these solids. Glasses in the wider sense of the word, can be defined as solid materials that are characterized by a random atomic arrangement with no specific long-range order, and thus resembling liquids to some extent more than crystals in terms of their atomic

structure. In essence, glasses are disordered materials that lack the periodicity of crystals but behave mechanically like solids. Recently, Zanotto and Mauro [13] proposed the following modern and improved definition for the glassy state of matter: ***"Glass is a nonequilibrium, noncrystalline condensed state of matter that exhibits a glass transition. The structure of glasses is similar to that of their parent supercooled liquids (SCL), and they spontaneously relax toward the SCL state. Their ultimate fate is to solidify, i.e., crystallize"***.

I.2.2. Glass structure

According to Zachariasen's random network theory [14], the atomic structural arrangement in crystals and glasses is built up from cations' coordination polyhedra. To illustrate the main structural difference, Fig. I.1 depicts the structural arrangement for a hypothetical compound A_2O_3 in the two forms. It should be noted that structural disorder in terms of A–O–A bond angles and A–O lengths between AO_3 triangles contributes to atomic disorder in the short- to medium-range structure of glasses.
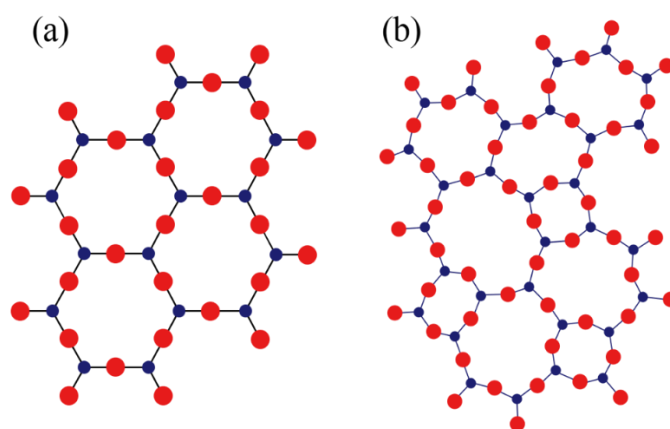
Fig. I.1. Comparison of the short- to long-range structure between A_2O_3 (a) crystal and (b) glass according to Zachariasen. Dark blue and red spheres represent A and O atoms respectively.

The atomic interactions (interatomic potentials, orbitals, *etc.*) in both crystals and glasses are of the same nature. Consequently, when interpreting the measured glass structural characteristics, it is often accepted, to some extent, that the structural details (especially at the short-range order) are close to those revealed from a related crystal structure [15]. However, although the atomic interactions are of the same nature, this does not necessarily imply that the structural details are exactly identical. Thus, it is more appropriate to assume that the interatomic bonding in glasses

obeys the same rules as in crystals, instead of assuming that the short-range order is "exactly" the same.

I.2.3. Glass formation

In spite of being an impressively active area of research and development, the complete understanding of glass nature and properties is still lacking several pieces of the puzzle. For instance, despite a myriad of theoretical and experimental efforts, the nature of glass transition and glassy state is still considered the deepest and most interesting unsolved issue in the condensed matter physics [16]. Glass formation is common in substances that remain liquid over a wide range of temperatures, *i.e.,* good glass-formers such as borates, silicates, phosphates, *etc*. Though, it can still be brought from most liquids if the cooling rate is fast enough to bypass crystallization.

The nature of the liquid-to-glass transition can be explained using the well-known volume (or enthalpy) *vs.* temperature diagram given below in Fig. I.2 (for more details, readers are referred to the *Chapter II* of Varshneya's book on the fundamentals of inorganic glasses [17]).
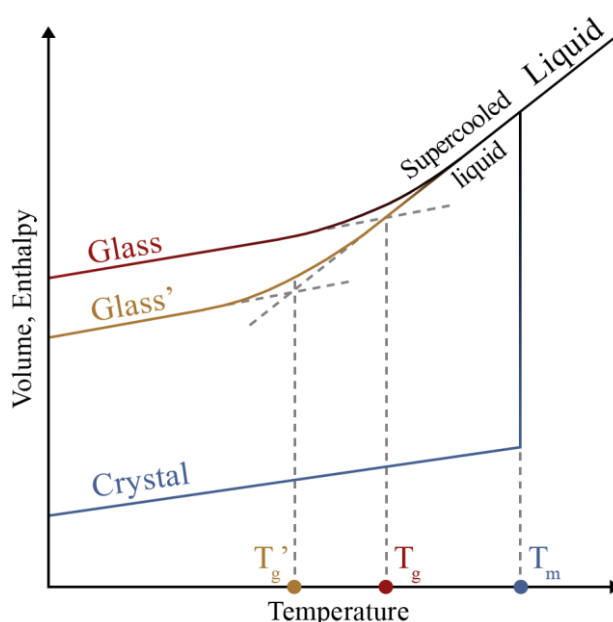
Fig. I.2. Temperature dependence of a liquid's volume or enthalpy at constant pressure. T_m is the melting temperature. A fast melt-cooling rate leads to a glass transition at T_g; a slower cooling rate produces a glass transition at T_g'.

In the course of cooling a liquid (in equilibrium-state), the crystallization phenomenon begins when the solidification (or melting) temperature T_m is approached. During this process, a significant decrease of the volume is recorded around T_m leading eventually to a crystalline solid material. However, when fast-cooling a glass-forming melt, this crystallization phenomenon does not take place and leads to the so-called supercooled liquid. The volume of the latter decreases following the liquid line simply because at this state, the system remains genuinely liquid. The liquid-to-glass transition occurs as the supercooled liquid gradually solidifies upon cooling into a glass. Subsequently, the continuous volume decrease is nearly parallel to that of the crystalline solid reflecting the solid character of the glass. The latter is thermodynamically in a non-equilibrium state.

The temperature at which the liquid-to-glass transition (T_g) occurs is a function of the liquid cooling rate (Glass *vs.* Glass' in Fig. I.2). The slower a liquid is cooled, the longer the time accessible for configurational sampling at each temperature, and therefore the colder will be before falling out of liquid-state equilibrium [18]. Consequently, the higher the cooling rate, the higher T_g will be. The glass properties are tied to the process by which it is formed. In practice, the dependence of T_g on the cooling rate is relatively weak (changing by 3 °C to 5 °C when the cooling rate changes by an order of magnitude [18]).

I.2.4. Glass formers, intermediates and formers

The glass former network can be structurally modified by the so-called "network modifiers" such as alkali and alkaline-earth-metal oxides. Adding such modifiers to the network former is often driven by the need to adjust the physical properties since several local structural configurations (atomic environments) are unlocked by the action of network modification and thus enabling the modification of properties.

To illustrate the close relationship between network modification and the resulting properties, let us consider a major thermal feature, the glass transition temperature. It is affected upon adding modifier cations as a result of at least three factors [3]:

- Reduction in the covalent crosslinking density from the forming network.

- Change in the number and strength of former cation-oxygen bonds.

- Change in the oxygen packing density of the glass network.

According to many classical structure theories [19], the large modifier cations fill any available vacancies created by the open network of the glass former (*e.g.,* inside rings built by the corner-sharing SiO_4 tetrahedra in SiO_2-based glasses) in a statistical and uniform way.

Among all the cations that participate in the oxide glass formation, Zachariasen [14] suggested to categorize them into the three following categories:

- The <u>glass formers</u>, such as Si^{4+}, P^{5+}, B^{3+}, Ge^{4+}, *etc.*, form the interconnected (or crosslinked) backbone glass network. They have coordination numbers of 3 to 4.

- The <u>glass network modifiers</u>, such as Li^+, Na^+, K^+, *etc.*, are very often present as ions to alter the glass network; and often reduce its connectivity. They have higher coordination numbers (more than 6) compared to the glass formers.

- The <u>intermediates</u>, such as Zn^{2+}, Nb^{5+}, Te^{4+}, *etc.*, can act as network formers or modifiers. Depending on the glass composition, they can either reinforce the glass network structure (*e.g.,* as tetrahedral units) or loosen it up as the basic network modifiers.

According to Dietzel's cationic field strength theory [20] (discussed in *Chapter II*) on the interaction of cationic forces during the melt cooling, the oxide glass formers have the highest field strengths with values ranging between ~1.3 and 2; the modifiers have the lowest with field strengths less than 0.4; and finally, the intermediates with values between ~0.5 and 1.2.

I.3. General introduction to tellurium oxide-based glasses

Oxide glasses make up the largest group of inorganic glasses. They have become widespread owing to their wide-ranging applications in our daily lives, but also in more advanced technological fields such as radiation protection, optical fibers and devices or lab glassware. They are quite often prepared by mixing network formers such as borates, silicates or phosphates, and network modifiers like alkali, alkaline-earth and transition metals. The compositional dependence of their structure and properties have been thoroughly examined in numerous reviews and textbooks [21–23], yet there is still no satisfactory universal theory relating their structure and properties.

I.3.1. Review of early research on TeO$_2$-based glasses

As stated by J. E. Stanworth [24], the original research on TeO$_2$-based glasses was reported in 1834 by J. J. Berzelius [25] who prepared the first synthetic tellurite glasses from molten tetratellurites of alkali metals and barium. Since the early work of Berzelius, very little has been contributed to the chemistry of TeO$_2$-based materials.

Nearly eighty years later, the first systematic study was published in 1913 by V. Lenher and E. Wolesensky [26], and has mainly focused on the oxidation behavior upon heating of a wide variety of metallic (potassium, sodium, silver, barium, magnesium, cadmium, nickel, cobalt, manganese and lead) tellurites. Moreover, the authors reported the tendency of sodium di- and tetratellurites melts to solidify into clear glasses upon cooling.

In 1952, J. E. Stanworth reported a pioneer description of the optical and dielectric properties of TeO$_2$-rich glasses within the TeO$_2$-BaO and TeO$_2$-PbO binary systems along with ternary glasses containing different amounts of Li$_2$O, Na$_2$O, BaO, B$_2$O$_3$, WO$_3$ and ZnF$_2$ compounds [24]. This prominent work was motivated by the expectedly promising physical properties of TeO$_2$-based glasses as ambitiously expressed by Stanworth:

> *An investigation of tellurite glasses was thought to be worthwhile, not only for its fundamental interest, but also because it could be expected that these glasses would have physical properties of value* (1952, p. 581 in [24]).

This investigation has concluded that TeO$_2$-based glasses possess higher refractive indices compared to the usual oxide glasses, larger optical transmission in the infrared region and exceptionally high dielectric constants in the range of 25 to 30. Stanworth's valuable work has drawn considerable attention to the family of TeO$_2$-based glasses for their potential use as optical components owing to their high refractive indices. In respect of the glass-forming ability, Stanworth speculated that tellurium oxide should behave analogously to phosphorous oxide as tellurium and phosphorous have very close electronegativities, namely 2.1 and 2.19 respectively.

Later in the same decade, a good deal of research has subsequently shed light on both the structural and optical properties of TeO$_2$ and TeO$_2$-based glasses [27–30]. Among these works is the first investigation of the structure of "TeO$_2$" glass (the glass was found to contain 7.5 mol.% of Li$_2$O after microanalysis) using the X-ray diffraction technique by G. W. Brady [29,30]. To describe the short-range order in the TeO$_2$-rich glass, Brady relied on the earlier structural description of the TeO$_2$ crystal by Ito and Sawada [31] where its crystal lattice has

been considered as isostructural with brookite (TiO_2) and Te atoms being surrounded by six O atoms at 2.05, 2.07, 2.12, 2.20, 2.68 and 2.79 Å. The reported X-ray analysis of the TeO_2-rich glass [29,30] suggested that Te atoms are more or less octahedrally coordinated to O atoms within the amorphous network structure. Although the latter description might appear to be in conflict with W. H. Zachariasen's theory [14] on the atomic arrangement in the glass network, Brady speculated the presence of unit-cell-sized crystallites of TeO_2 embedded within the amorphous network structure of the investigated TeO_2-rich glass [30]. Driven by the expected presence of corner-sharing TeO_6 octahedra in the matrix of TeO_2-based glasses and its fundamental conflict with the postulated rules for glass formation by Zachariasen, Brady's findings arouse the curiosity of many more researchers to investigate the local- and medium-range structure of TeO_2-based glasses.

In the early 1960's, Ya. S. Bobovich and A. K. Yakhkind (see [32–34]) have made major progress in the understanding of the structure of TeO_2-based glasses by recording the Raman spectra of a series of glasses belonging to the binary TeO_2-Na_2O, TeO_2-BaO, TeO_2-WO_3 and TeO_2-B_2O_3 systems. They concluded by comparing the spectral features in the recorded Raman spectra of TeO_2-based glasses to those previously measured from TiO_2-containing glasses [35], that considering the significant contrast between the two families, it is unlikely for Te atoms to be octahedrally coordinated to O atoms within the glass network of TeO_2-based glasses [33].

The next breakthrough was Yakhkind's research [34] on the glass-forming ability and compositional-dependence of the physical properties, especially the linear optical properties, of TeO_2-based glasses in various binary and ternary systems containing alkali, alkaline-earth and heavy metal oxides. Since then, many more researchers have been excited by the promising physical properties of TeO_2-based glasses and their potential technological use in optical systems. Thereupon, a large number of studies have been conducted over the following decades up to the present time.

A very important contribution was reported in 1984 by Lambson *et al.* [36] where the authors argued that many of the glasses reported in the literature up to then were contaminated from the crucible they had been melted in, usually silica or alumina. These impurities were found in concentrations as high as 7 mol.% which significantly influence the properties of the resulting glasses. It is now very common to use gold or platinum crucibles as these metals are much less soluble in the glass melts.

The most comprehensive state-of-the-art source of glass formation ranges in TeO_2-based glasses is the early systematic study reported by Imaoka and Yamazaki in 1968 [37]. In this

paper, the authors reported and commented glass-forming domains in 23 binary and over 100 ternary systems explored by cross-combining oxides of the following elements: K, Na, Li, Ba, Sr, Ca, Mg, Be, La, Al, Th, Zr, Ti, Ta, Nb, W, Tl, In, Cd, Zn, Pb, Sn and Bi. Gold alloy (containing 15% Pd) crucibles were used to melt the glass batches. With respect to borate and silicate glasses, TeO_2-based glass melts demonstrate a better glass-forming ability allowing them to be prepared across relatively broad compositional ranges [37]. Indeed, a very large number of studies have reported glass-forming domains in binary, ternary and quaternary systems. It is practically complex to provide a satisfying and global picture about the glass-forming ability due to changing experimental conditions (purity of powders, crucible's composition, temperature and time of melting, cooling rate/type, atmospheric conditions, *etc.*) among these studies.

By means of laser ultramicroscopy, Zorin *et al.* [38] reported data suggesting the presence of micro-inhomogeneities of 0.07–0.2 µm in size within 9 different binary and ternary glass compositions. The possible micro-inhomogeneities are air bubbles, pores, platinum particles, and oxide crystallites. Their size and concentration were found to vary as a function of the glass composition and experimental conditions.

To illustrate the growth rate in both fundamentally and technologically-oriented research on the family of TeO_2-based glasses, we performed a field search using primarily ScienceDirect database to estimate the decennial evolution of the number of papers, book chapters *etc.* discussing or reporting findings related to the physics and chemistry of TeO_2-based glasses. In the advanced field searching process, the two keywords "glass" and "tellurite" were submitted and restricted to Abstract and All Fields respectively. An exponential growth (Fig. I.3) of the scientific production has marked the 66 years following the first pioneer works on TeO_2-based glasses by Stanworth, Brady and researchers of their era.
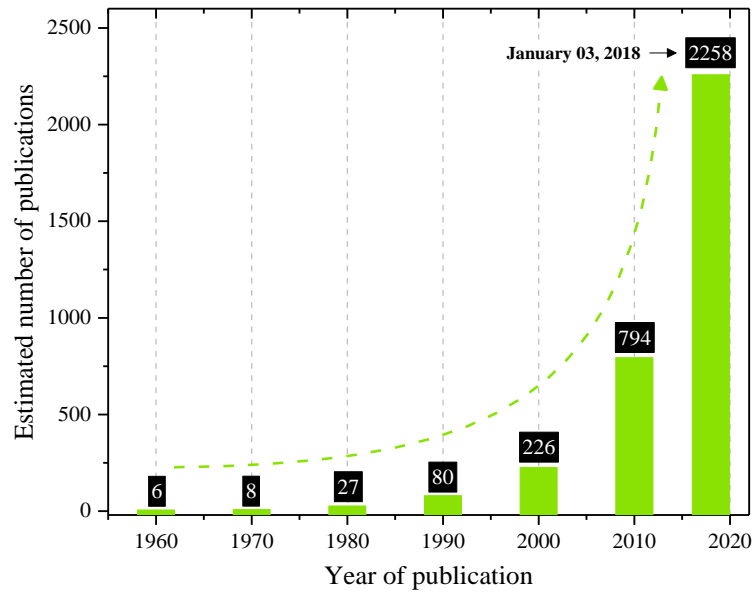
Fig. I.3. Graph showing an estimated decennial evolution of the scientific production in the arena of TeO$_2$-based glasses over the years. The data are mainly compiled from ScienceDirect database especially for the recent statistics.

Since the early 50's, only few studies were carried out over a long period of four decades. For the first time, consequential development of TeO$_2$-based glass fibers as optical amplifiers has been initiated in 1994 with the significant work of Wang *et al.* [39] involving fiber drawing and rare-earth doping of Na$_2$O–ZnO–TeO$_2$ glasses. Soon after, a great deal of studies aimed to understand their properties and develop more advanced TeO$_2$-based glasses for various applications, especially in the field of photonics.

I.3.2. Properties and applications of TeO$_2$-based glasses

There is a need in the field of high-speed optical communications for the development of new materials able to sustain increased information flow for a more adequate use of available communication channels and for accessing new spectral bandwidths. TeO$_2$-based glasses are excellent candidates for such applications owing to their broad optical transmission range (0.3–5 µm) and their high Raman cross-section as compared to existing commercial fibers materials. As predicted in the literature [4], the fraction of TeO$_4$ disphenoids increases with increasing TeO$_2$ content, and thus the higher the Raman cross-section and Raman gain coefficients for the 665 cm^{-1} Raman band in TeO$_2$-rich glasses. In fact, TeO$_2$-based glasses exhibit Raman gain coefficients up to 30 times greater than that of silica glass [40].

Physical properties and technological applications of TeO_2-based glasses have been reported by Rivera and Manzani in a very recent book entitled "Technological Advances in Tellurite Glasses" [2]. These glasses are believed to offer the best compromise for future applications in the mid-infrared region. They also exhibit low intrinsic losses (compared to chalcogenide glasses), little photosensitivity and high optical damage threshold [2]. Furthermore, thanks to their network flexibility in terms of broad chemical composition possibilities, TeO_2-based glasses can be easily modified (*e.g.,* by doping) to adjust their refractive index dispersion profiles, maximize their nonlinear optical coefficients and emission cross-sections.

Owing to their high nonlinear optical properties, TeO_2-based glasses are potential candidates for advanced optical device applications. Their third-order nonlinear optical susceptibility χ^3 values are 50 times greater than those of SiO_2-based glasses.

Up to now, the most comprehensive literature review on TeO_2-based glasses is the "Tellurite Glasses Handbook, Physical Properties and Data" by El-Mallawany [3] where glass-forming ranges, densities, elastic, thermal, electrical, structural and optical properties can be found. These glasses possess large glass-forming domains, good thermal and chemical stabilities, and low melting and glass transition temperatures. They are also commonly known for their excellent rare-earth ion solubility. The outcome of doping with rare-earth or metallic nanoparticles has attracted great interest owing to their consequential contributions in enhancing photoluminescence and nonlinear optical properties.

The two most interesting properties of these glasses are *(i)* the peculiar character of their atomic structure and *(ii)* their remarkable optical performance compared to other oxide glass formers. These characteristics have vividly attracted the curiosity of many researchers to explore and develop more advanced TeO_2-based glass compositions having the best compromise between several physical properties (*e.g.,* viscoelastic, thermo-mechanical, optical…).

Previous studies have shown that adding d^0 transition metal cations (W^{6+}, Nb^{5+}, Ta^{5+}, Ti^{4+}, *etc.*) or those with lone electron pairs such as Tl^+ or Pb^{2+} allows maintaining a high optical nonlinearity and Raman gain [41,42]. Adding oxides like TiO_2, WO_3 and Nb_2O_5 to TeO_2-based glass network to form binary systems increases both the linear refractive index and the third-order nonlinear susceptibility χ^3 [41]. This positive effect was explained in terms of the empty d-orbitals contribution, namely via virtual electronic transitions from anionic valence p-orbitals to empty cationic d-orbitals [43].

Metal oxides such as ZnO, alkali and/or alkaline-earth have been also reported to make glasses more suitable for optical fiber fabrication [44]. However, as highlighted in the next section on the structural properties, adding such oxides induces the **structural depolymerization** leading to quasi-isolated TeO_3 units (as opposed to polymerized Te–O–Te bridges mainly constituted of TeO_4 units). In this manuscript, we use the term of depolymerization (as opposed to crosslinking) to refer to the action of bond-breaking in Te–O–Te bridges and/or between Te–O chains. This transformation decreases the nonlinear electronic polarization within the glass network and therefore reducing its nonlinear optical response [45].

I.3.3. Structure of TeO_2-based glasses

It is of fundamental interest in glass science to identify the building blocks within the structure of intermediate network formers of which the cations have field strengths (FS) ranging between 0.5 and 1.2 (*cf. section I.2.4*). The FS of Te^{4+} is equal to 0.990 in oxide materials (*cf. section II.3*) and allows to classify it in the category of intermediates (closer to the formers than to the modifiers). As a consequence, pure TeO_2 is only a conditional glass former and thus requires a fast-quenching technique for cooling in order to solidify into a glass [46] (*cf. section III.2.1*).

The investigation on the structure of TeO_2-based glasses is still ongoing and can be explained by the richness of their crystal chemistry compared to other oxide formers like SiO_2 and P_2O_5. The local structural units constituting the building blocks within the structure feature two peculiarities: *(i)* the local environment of a Te^{4+} cation is asymmetric due to the steric effect of its lone electron pair and *(ii)* the units may strongly vary according to the quantity and the kind of an added modifier oxide M_xO_y.

As an illustration, let us consider the crystal structures of alkali tellurites. The wide variety of tellurium structural environments observed in these crystals is believed to play a major role in stabilizing alkali tellurite glasses [47]. The challenge in identifying these structural changes upon adding alkali oxide modifiers is tied to the variety of electronic charge compensating species due to the charge delocalization that commonly occurs in Te–O bonds. For instance, α-TeO_2 consists of $TeO_{4/2}$ disphenoids (so TeO_4 units where all of the 4 oxygen atoms are shared between 2 tellurium atoms) while M_2TeO_3 (M = Li, Na, K, Cs) features $TeO_{3/0}$ trigonal pyramids (so quasi-isolated TeO_3 units expressing $[TeO_3]^{2-}$ anions coordinated by alkali cations) [48]. These structural units along with intermediate ones are presented in Fig. I.4.
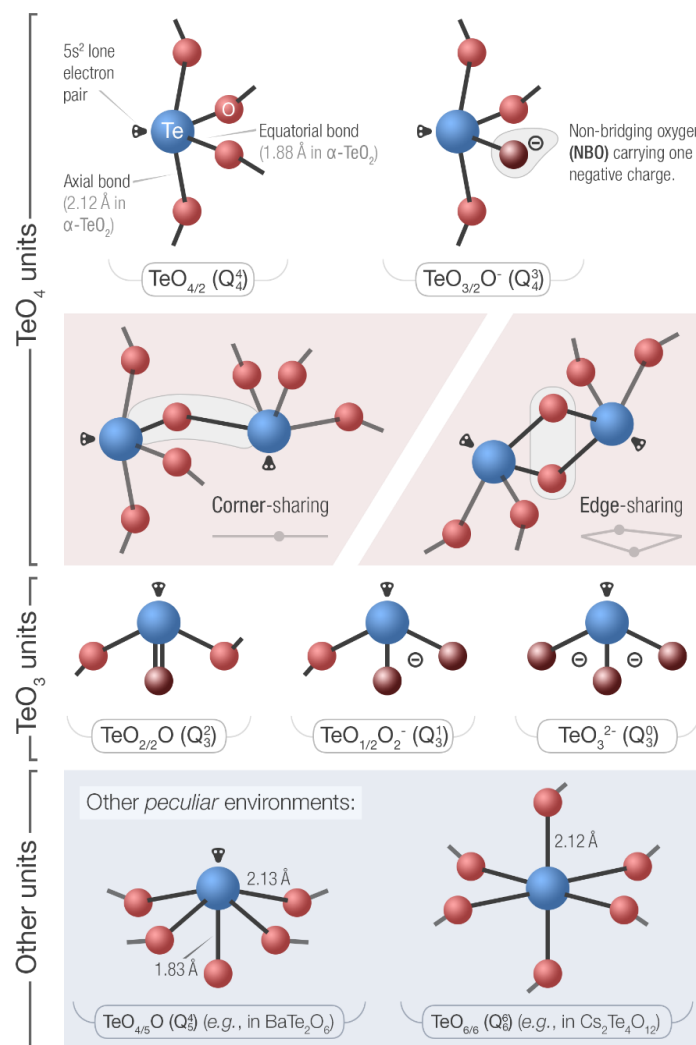
Fig. I.4. Basic structural units found in tellurite crystals. The units are labelled in both conventional and Q_m^n notations. In the latter, n is the coordination number of the central Te atom (number of nearest neighbor oxygen atoms) and m represents the number of bridging oxygens and hence, $m \leq n$. Both $TeO_{4/5}O$ [49] and $TeO_{6/6}$ [50] units are less common in TeO_2-based systems. Reproduced from [48].

As previously outlined, the TeO_4 disphenoid is commonly considered as the basic structural unit in TeO_2-based compounds. Several authors [47,48,51,52] have reported the changing coordination number of Te atoms in TeO_2-based glasses along the following pattern: TeO_4 disphenoids are gradually transformed into TeO_3 units through intermediate TeO_{3+1} distorted disphenoids (having three short bonds and one long bond) upon adding modifier oxides like alkali or alkaline-earth-metal oxides. The respective proportions among these units have been often estimated using the intensity ratios of Raman bands responsible for stretching Te–O vibrations (> 550 cm^{-1}) from the Raman spectra of TeO_2-based glasses.

The structural transformation of TeO_4 into TeO_3 units reduces the average coordination number, and thus promoting a weaker bonding network exhibiting a relatively low glass transition temperature. For this reason, this transformation is commonly referred to as structural depolymerization. In addition to alkali and alkaline-earth-metal oxides, other oxides inducing this structural depolymerization with variable extents have been reported in the literature; these include ZnO [53], La_2O_3 and Y_2O_3 [54], Ag_2O and Tl_2O [55], PbO [56] and Bi_2O_3 [57].

Evidence for the structural transformation of TeO_4 units into TeO_3 ones in a given TeO_2-based system is often based on the Raman spectra examination with addition of the modifier oxide. As an illustration, let us consider the case of binary $(1-x)TeO_2$-xTl_2O glasses [58] (*cf.* Raman spectra in Fig. I.5). Increasing the Tl_2O content from x = 0.07 to x = 0.5 results in *(i)* an intensity increase of the band at ~720 cm^{-1} (associated with Te–O vibrations in TeO_3 units), *(ii)* intensity decrease of the band at ~660 cm^{-1} (associated with Te–O vibrations in TeO_4 units) and *(iii)* vanishing of the band centered at ~450 cm^{-1} (associated with stretching vibrations of Te–O–Te bridges). These evolutions indicate a significant structural depolymerization of the Te–O–Te bond network upon substituting TeO_2 with Tl_2O.
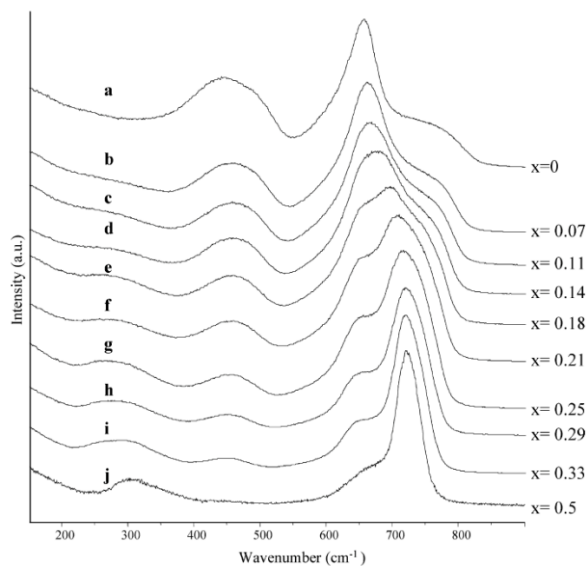
Fig. I.5. Composition dependence of the Raman spectra of $(1-x)TeO_2$-xTl_2O glasses. Taken from [58].

Most of the structural studies as a function of M_xO_y content have targeted their attention towards *(i)* the potentiality of the TeO_4 to TeO_3 depolymerization and *(ii)* the physico-chemical character of Te–O–M bridges. It appears though that the local environment around $M^{(2y/x)+}$ cations and its compositional dependence have been somewhat overlooked. Therefore, we aim

in this work to elucidate such structural features as well in order to generate a more comprehensive structural understanding of the studied glasses.

Let us now focus on the structural features of crystalline TeO_2 polymorphs and those of pure TeO_2 glass.

I.4. Description of crystalline and amorphous TeO_2

I.4.1. Structure of crystalline TeO_2

At ambient conditions, tellurium oxide (TeO_2) is commonly known to exist in the two polymorphs: paratellurite α-TeO_2 [59,60] and tellurite β-TeO_2 [61]. The former phase is stable at ambient temperature and pressure; the latter, which is metastable, is the natural form of the tellurium oxide mineral. Two more polymorphs of TeO_2, namely the γ- [62,63] and δ- [62,64] phases were discovered at the IRCER laboratory (formerly called SPCTS) via X-ray diffraction of recrystallized TeO_2-rich glasses in TeO_2-WO_3 and TeO_2-$NbO_{2.5}$ systems. In the following, we will focus on describing in a bit more detail, the structural and vibrational properties of TeO_2 polymorphs (primarily α-, β- and γ-TeO_2).

I.4.1.1. α-TeO_2 polymorph

The α-TeO_2 crystal or paratellurite, has a tetragonal symmetry and belongs to the $P4_12_12$ space group with the following lattice parameters: a = b = 4.8082 Å and c = 7.6212 Å [60]. As shown in Fig. I.6, each tellurium atom is coordinated with four oxygen atoms constituting two equatorial bonds (1.879 Å) and two longer axial bonds (2.121 Å) [60]. Detailed structural information in terms of Te–O bonds' lengths and angles is given in Table I.1.
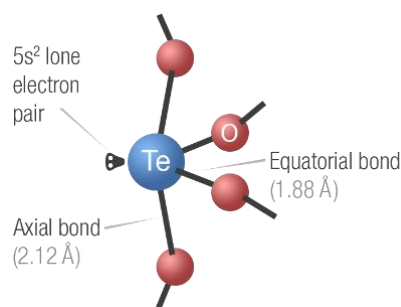
Fig. I.6. Structural representation of the TeO_4E trigonal bipyramid (tbp) unit in α-TeO_2 crystal. The dark grey shape accompanying the Te atom represents the lone electron pair $5s^2$ (E).

The crystal lattice of α-TeO$_2$ can be regarded as a three-dimensional network of corner-sharing TeO$_4$ disphenoids (*cf.* Fig. I.7). The interconnection style of these structural units gives rise to highly asymmetric Te–$_{eq}$O$_{ax}$–Te bridges. In other words, each oxygen atom is connected to two tellurium atoms by one axial bond from one side and one equatorial bond from the other.

Bond length (Å)		Bond angle (deg.)	
Te–$_{eq}$O	1.879	O$_{eq}$–Te–$_{eq}$O	103.37
Te–$_{eq}$O	1.879	O$_{eq}$–Te–$_{ax}$O	88.32
Te–$_{ax}$O	2.121	O$_{eq}$–Te–$_{ax}$O	84.22
Te–$_{ax}$O	2.121	O$_{ax}$–Te–$_{ax}$O	167.97
		Te–$_{eq}$O$_{ax}$–Te	138.61

Table I.1. Bond lengths and angles in the α-TeO$_2$ crystal [60].
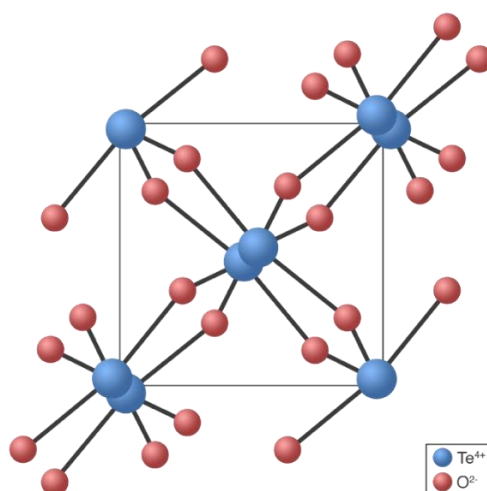
Fig. I.7. Projection of α-TeO$_2$ crystal lattice along the c axis.

The general aspects of the lattice dynamics of α-TeO$_2$ have been previously discussed in the literature [65–67]. Mirgorodsky *et al.* [64] studied the lattice-dynamical aspects of α-TeO$_2$ along with the other polymorphs using Raman spectroscopy (the theoretical background of this technique is given in *Chapter III*). They found by calculating the potential energy distribution of the stretching vibrational modes ($\nu > 550$ cm^{-1}) observed in the Raman spectrum of α-TeO$_2$ (*cf.* Fig. I.14) that these modes are largely dominated by the motions of equatorial Te–$_{eq}$O bonds while the contribution of axial Te–$_{ax}$O bonds is much smaller. Nevertheless, it was shown that in order to reproduce the large range of stretching vibrational modes ($\nu > 550$ cm^{-1}), it was necessary to take into account the relatively weak axial Te–$_{ax}$O bonds in the potential function.

This study has been conducted within the framework of the short-range interaction force approximation. The values of the force constants were empirically estimated given that the main attention was exclusively paid to α-TeO$_2$ since detailed and relevant information about Raman and IR active vibrational modes [68,69], and elastic constants [70] have been reported for this crystal. The interatomic Te–O distances corresponding to the coordination spheres around tellurium atoms covered the range 1.83–2.25 Å. Therefore, the dependence of the force constants K_{Te-O} on interatomic distances d_{Te-O} was plotted (Fig. I.8).
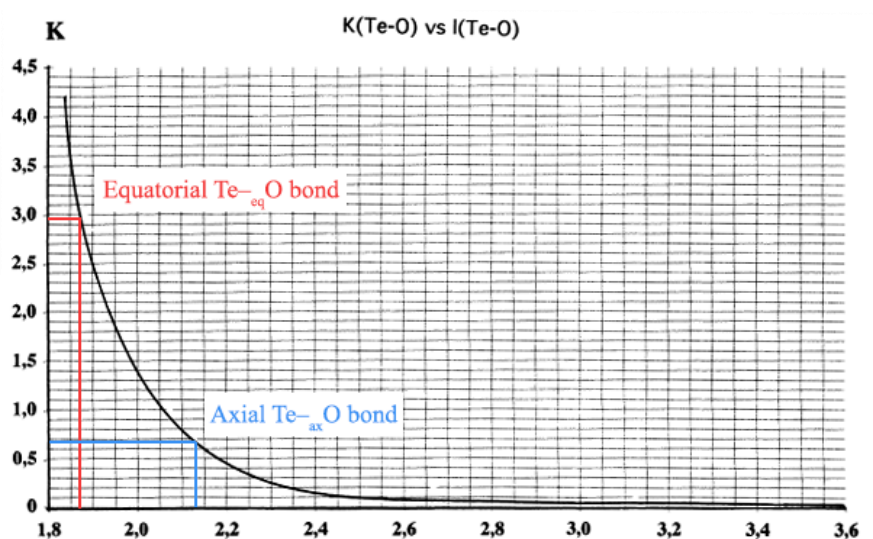
Fig. I.8. Force constants K_{Te-O} (in mdyn.Å^{-1}) as a function of Te–O bond lengths (Å). Reproduced from [64].

From the Te–O interatomic bond length dependence of the force constant K_{Te-O}, one could estimate the force constant of equatorial and axial bonds in α-TeO$_2$ crystal: ~3 mdyn.Å^{-1} and ~0.7 mdyn.Å^{-1} respectively. Therefore, from the crystal chemistry viewpoint, it seems unreasonable to assign a framework character to the crystal lattice of α-TeO$_2$ but instead, a quasimolecular network of TeO$_2$ units (more precisely Te–$_{eq}$O$_2$ units) connected together via relatively weak "axial" Te–$_{ax}$O bonds [64,71]. This perspective is rigidly supported by valence force field calculations [71] and a more recent *ab initio* investigation of the vibrational properties of α-TeO$_2$ crystal [72]. Furthermore, it is worth mentioning that, in the gaseous state, the TeO$_2$ molecule (O=Te=O) has a geometry ($d_{Te=O}$ = 1.84 Å, O-Te-O = 110° [73]) that is very close to that of quasimolecular TeO$_2$ units in α-TeO$_2$ structure. In this regard, the molecular-like character is again rigidly supported by the calculated bond orders of Te–O bonds in α-TeO$_2$: 1.7 and 0.3 for equatorial and axial bonds respectively [74]. The bond order represents

the number of chemical bonds between a pair of atoms and indicates the stability of the bond itself. Consequently, and as suggested by Rodriguez *et al.* [75], the vibrational modes of the α-TeO$_2$ crystal lattice should be classified into two categories: the *internal* modes of the TeO$_2$ quasimolecules, and their *external* rotational, translational and librational modes.

It is important to stress that there is a very good agreement among the findings of the previously cited works in that they all acknowledge the necessity to describe the lattice as built by TeO$_2$ quasimolecules. Though as will be discussed later, the axial bonds do influence by participating in the bending vibrational modes of TeO$_2$ quasimolecules in such a way that these modes can be equally regarded as the vibrations of asymmetric Te–$_{eq}$O$_{ax}$–Te bridges.

Now let us focus on the vibrational modes of the α-TeO$_2$ crystal lattice. The Raman active modes in this crystal are A$_1$, B$_1$, B$_2$ and E modes while A$_2$ and E modes are IR active [72]. In the following, we first start by describing the vibrational modes responsible for the *"internal"* features in high-wavenumber region ($\nu > 300$ cm^{-1}) and then the *"external"* features in low-wavenumber region ($\nu < 300$ cm^{-1}) will be highlighted.

a) Internal vibrational modes ($\nu > 300$ cm^{-1})

These modes correspond to the different vibrations occurring within the TeO$_2$ quasimolecule itself emerging from the vibrations of Te–O and O–Te–O linkages. In the region where these modes are expected, several lines can be distinguished over the Raman spectrum of α-TeO$_2$; these modes are experimentally observed at 393, 415, 590, 648 and 784 cm^{-1} and are assigned to A$_1$, B$_2$, B$_1$, A$_1$ and B$_2$ modes respectively (*cf.* Fig. I.9). Furthermore, relatively less intense E (TO+LO) modes are also observed at 336, 645, 718 and 766 cm^{-1}. The abbreviations TO and LO refer to the transverse and longitudinal optical phonon modes respectively.
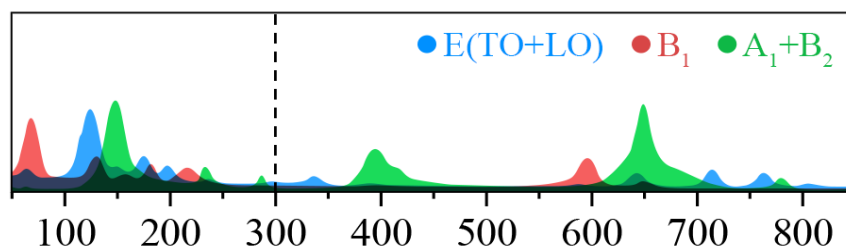
Fig. I.9. Representation of the different Raman vibrational modes in α-TeO$_2$ crystal generated from its polarized Raman spectra found in [75].

These internal vibrational modes are expected to consist of *(i)* symmetric and *(ii)* antisymmetric stretching vibrations of Te$_{-eq}$O bonds in the 500–800 cm^{-1} region, and finally *(iii)* the bending vibrations of O–Te–O bridges within TeO$_2$ quasimolecules in the 300–500 cm^{-1} range [75]:

(i) Symmetric stretching	*(ii)* Antisymmetric stretching	*(iii)* Bending
A1 + B2 + E	**A2 + B1 + E**	**A1 + B2 + E**

The displacement patterns of these modes in the wavenumber range $300 < \nu < 800$ cm^{-1} are schematically given in Fig. I.10.
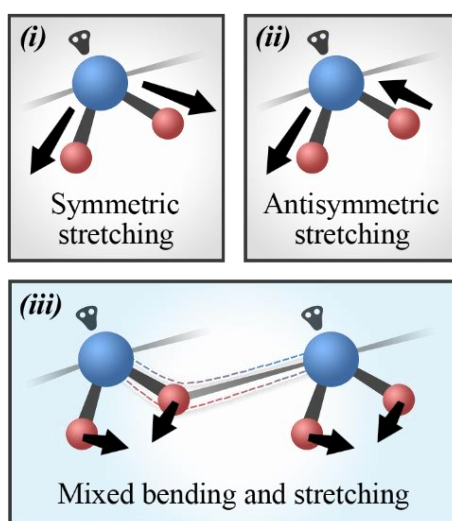
Fig. I.10. Displacement patterns of the internal vibrational modes in α-TeO$_2$ crystal. Tellurium and oxygen atoms are represented by blue and red spheres respectively.

Lattice-dynamical [64] and *ab initio* [72] calculations have shown that due to the non-negligible axial Te$_{-ax}$O interactions, no pure bending motions of TeO$_2$ quasimolecules take place within the crystal lattice of α-TeO$_2$; that is to say, the force constants of these relatively weak Te$_{-ax}$O bonds can still influence the bending motions of TeO$_2$ quasimolecules. Therefore, the involvement of axial Te$_{-ax}$O bonds in the bending modes (expected in 300–550 cm^{-1} region) results in vibrations that rather concern asymmetric Te$_{-eq}$O$_{ax}$–Te bridges [64]. In fact, this gives a reason for the significant wavenumber shift between the bending mode of these TeO$_2$ quasimolecules and ideally isolated TeO$_2$ molecules as the latter's bending mode is observed at much lower wavenumbers, namely 270 cm^{-1} [73]. Hence, within the mid-wavenumber region ($300 < \nu < 550$ cm^{-1}), the vibrational modes in the crystal lattice of α-TeO$_2$ can be regarded as a mixture of bending (of TeO$_2$ quasimolecules) and symmetric stretching (of asymmetric Te$_{-eq}$O$_{ax}$–Te bridges) modes [64].

b) External vibrational modes ($\nu < 300$ cm^{-1})

They include the optical modes associated with rotational, translational or librational (which is a type of reciprocating motion) vibrational modes which modulate the lengths of axial Te$-_{ax}$O bonds between TeO$_2$ quasimolecules.

The Raman spectrum of α-TeO$_2$ features in the low-wavenumber region three strong lines followed by a much less intense peak. These modes are experimentally observed at 62, 122, 150 and 173 cm^{-1} and are assigned to B$_1$, E (TO+LO), A$_1$+B$_2$ and E (TO) modes respectively (Fig. I.9).

I.4.1.2. β-TeO$_2$ polymorph

Tellurite β-TeO$_2$ is the natural form of tellurium dioxide. It transforms irreversibly to paratellurite α-TeO$_2$ at around 600 °C. This crystal has an orthorhombic symmetry and belongs to the *Pbca* space group with the following lattice parameters: a = 12.035 Å, b = 5.464 Å and c = 5.607 Å [61].

Each tellurium atom is coordinated with four oxygen atoms constituting two equatorial bonds (1.877 and 1.927 Å) and two longer axial bonds (2.070 and 2.196 Å). Hence, it is important to note that the bond lengths of Te–O equatorial and axial bonds in β-TeO$_2$ are not as homogeneous as in α-TeO$_2$ crystal. Detailed structural information (bond lengths and angles) on the β-TeO$_2$ crystal lattice is given in Table I.2.

Bond length (Å)		Bond angle (deg.)	
Te–$_{eq}$O(1)	1.877	O(1)$_{eq}$–Te–$_{eq}$O(2)	101.15
Te–$_{eq}$O(2)	1.927	O(1)$_{eq}$–Te–$_{ax}$O(1)	78.13
Te–$_{ax}$O(1)	2.196	O(1)$_{eq}$–Te–$_{ax}$O(2)	90.06
Te–$_{ax}$O(2)	2.070	O(2)$_{eq}$–Te–$_{ax}$O(1)	90.03
		O(2)$_{eq}$–Te–$_{ax}$O(2)	89.67
		O(1)$_{ax}$–Te–$_{ax}$O(2)	167.89
		Te–$_{eq}$O(1)$_{ax}$–Te	101.88
		Te–$_{eq}$O(2)$_{ax}$–Te	137.46

Table I.2. Bond lengths and angles in the β-TeO$_2$ crystal [61].

As opposed to paratellurite α-TeO$_2$, the crystal lattice of β-TeO$_2$ has a layered structure with weakly bonded layers where the TeO$_4$ disphenoids share alternately corners and (Te–$_{eq}$O$_{ax}$–Te) edges (Fig. I.11). The layers are situated along the b axis and separated by a distance of 3.07 Å [61]. The particularity of this crystalline polymorph of TeO$_2$ is that tellurium atoms are connected via double Te$\overset{_{eq}O_{ax}}{\underset{_{ax}O_{eq}}{\lessgtr}}$Te bridges.
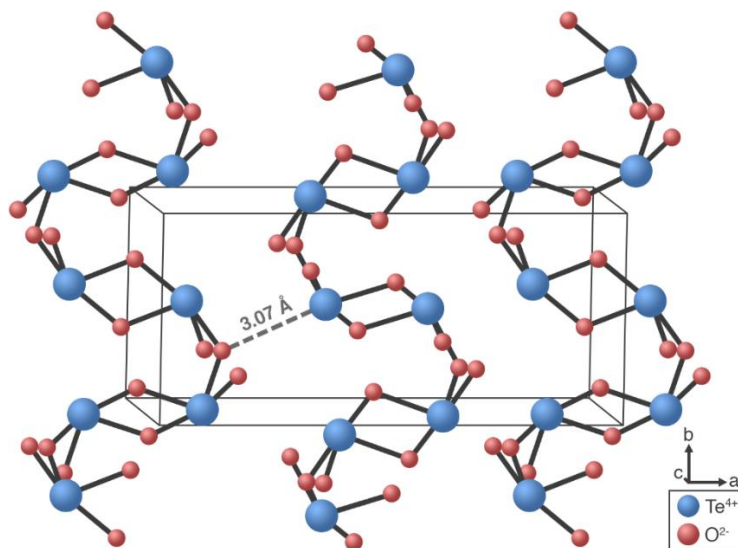
Fig. I.11. Projection of β-TeO$_2$ crystal lattice along the c axis.

To a lesser extent, the quasimolecular viewpoint (TeO$_2$ quasimolecules instead of TeO$_4$ disphenoids) for describing the crystal lattice can be applied as well for β-TeO$_2$: compared to α-TeO$_2$ crystal, it should be noted that the Te–$_{eq}$O$_{ax}$–Te bridges are less asymmetric and thus, from the crystal chemistry point of view, the concept of "framework-quasimolecule" duality seems more or less relevant to describe β-TeO$_2$ crystal lattice.

Over the Raman spectrum of β-TeO$_2$, one can notice two major lines in the low-wavenumber region that are both assigned to external vibrational modes. At higher wavenumbers (300–800 cm^{-1} range), four internal modes can be easily identified. These vibrational modes are observed at 450, 595, 661 and 673 cm^{-1} (*cf.* Fig. I.14(b)).

It is important to note that the wavenumbers of stretching vibrational modes between β- and α-TeO$_2$ polymorphs do not differ markedly. However, due to the exclusive presence of double Te–$_{eq}$O$_{ax}$–Te bridges in β-TeO$_2$, more internal vibrations (of weak intensities) are observed in the mid-wavenumber region 300–550 cm^{-1}: symmetric vibrations of Te–$_{eq}$O$_{ax}$–Te bridges are

observed 336 and 370 cm^{-1}, those of double Te–$_{eq}$O$_{ax}$–Te bridges at 450 and 490 cm^{-1} [64]. More than one symmetric stretching mode is observed beyond 600 cm^{-1}, and that is due to the inequivalent bond lengths of equatorial Te–$_{eq}$O bonds.

I.4.1.3. γ-TeO$_2$ polymorph

As stated earlier, the metastable γ-TeO$_2$ polymorph was discovered about 19 years ago at the IRCER (formerly called SPCTS laboratory) via X-ray diffraction of recrystallized TeO$_2$-rich glasses in TeO$_2$-WO$_3$ and TeO$_2$-NbO$_{2.5}$ systems [62,63]. Later, well crystallized γ-TeO$_2$ was prepared by slowly heating pure TeO$_2$ glass up to 390 °C followed by annealing the sample for 24 hours at this temperature [64]. Recently, single crystals of γ-TeO$_2$ in the form of colorless needles were obtained and thus allowing a more accurate structural determination of this compound [76].

This crystal has an orthorhombic symmetry and belongs to the P2$_1$2$_1$2$_1$ space group with the following lattice parameters: a = 4.8809 Å, b = 8.5668 Å and c = 4.3433 Å [63]. Again, this structure can be described as corner-sharing TeO$_4$ disphenoids (Fig. I.12(a)); however, compared to α- and β-TeO$_2$ polymorphs, the featured TeO$_4$ disphenoid has a much more distorted geometry (Fig. I.12(b)): one Te–O bond is essentially longer than the other three (thus the polyhedron is referred to as TeO$_{3+1}$) and when this bond is not considered, a chain-like network organization appears and can be described as an infinite zigzag chain of TeO$_3$ units along the c axis (cf. Fig. I.13).
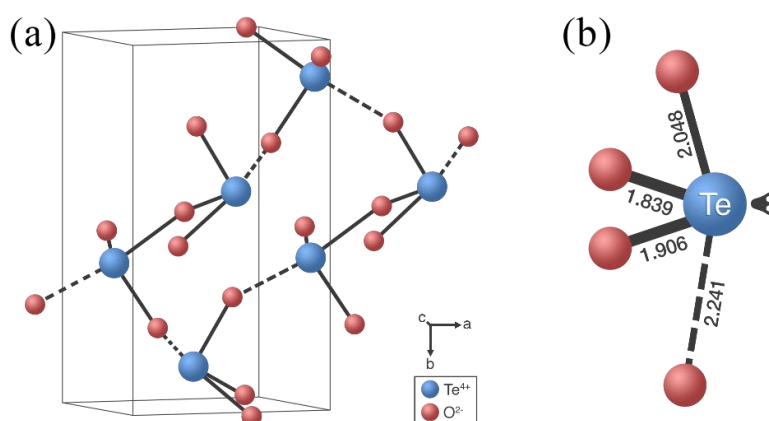
Fig. I.12. (a) Three-dimensional lattice of γ-TeO$_2$ and (b) representation of the basic TeO$_{3+1}$ structural unit. Bond lengths are given in Å.
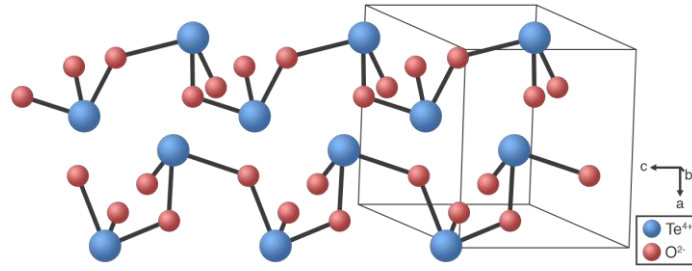
Fig. I.13. Chain-like organization of γ-TeO₂ obtained when the longest axial bonds are not considered.

Another peculiarity of this polymorph (compared to α and β) is the presence of two types of Te–O–Te bridges: highly asymmetric Te–$_{eq}$O(1)$_{ax}$–Te (1.839 – 2.241 Å) and nearly symmetric Te–$_{eq}$O(2)$_{ax}$–Te (1.906 – 2.048 Å) bridges (Table I.3).

Bond length (Å)		Bond angle (deg.)	
Te–$_{eq}$O(1)	1.839	O(1)$_{eq}$–Te–$_{eq}$O(2)	100.36
Te–$_{eq}$O(2)	1.906	O(1)$_{eq}$–Te–$_{ax}$O(1)	91.69
Te–$_{ax}$O(1)	2.241	O(1)$_{eq}$–Te–$_{ax}$O(2)	93.14
Te–$_{ax}$O(2)	2.048	O(2)$_{eq}$–Te–$_{ax}$O(1)	75.60
		O(2)$_{eq}$–Te–$_{ax}$O(2)	78.68
		O(1)$_{ax}$–Te–$_{ax}$O(2)	154.28
		Te–$_{eq}$O(1)$_{ax}$–Te	131.6
		Te–$_{eq}$O(2)$_{ax}$–Te	125.18

Table I.3. Bond lengths and angles in the γ-TeO₂ crystal [76].

In the following, we briefly recall the vibrational properties (revealed by Raman spectroscopy) of each TeO₂ polymorph along with those of pure TeO₂ glass.

I.4.2. Structure of pure TeO₂ glass

Mirgorodsky *et al.* [64] have reported a thorough study of the vibrational and structural properties of α- and β-TeO₂ polymorphic varieties. The Raman spectral features of these crystals along with those of the then newly discovered γ- [62,63] and δ- [62,64] TeO₂ polymorphs were closely examined to clarify the plausible relationships with the interatomic bonding and the general structural features of pure TeO₂ glass network.

Another significant step in revealing the characteristics of the structural organization, at both short- and medium-range order, in TeO₂-based amorphous and crystalline materials was

initiated by Champarnaud-Mesjard *et al.* [63] via a lattice-dynamics study of the γ-TeO$_2$ structure. This study has delivered a fresh viewpoint over the structural network of TeO$_2$ glass that was presumed to hold a chain character promoted by the potential presence of symmetric Te–O–Te bridges.

The Raman spectra of TeO$_2$ polymorphs and TeO$_2$ glass are jointly presented below in Fig. I.14. External vibrational modes are observed in the low-wavenumber region below 300 cm^{-1}.
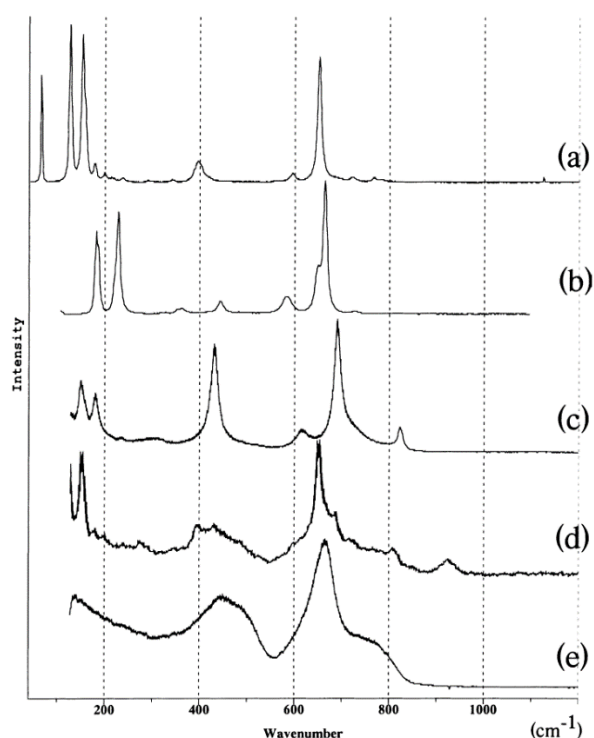
Fig. I.14. Raman spectra of (a) α-TeO$_2$, (b) β-TeO$_2$, (c) γ-TeO$_2$, (d) δ-TeO$_2$ and (e) pure TeO$_2$ glass. Taken from [64].

Unlike α-, β- and δ-TeO$_2$, the γ-TeO$_2$ crystal lattice features a remarkably intense peak in the mid-wavenumber region (300 < ν < 550 cm^{-1}) (Fig. I.14(c)) which represents the signature of a slightly different type of Te–O–Te bridges within the three-dimensional network of this polymorph, namely assigned to the symmetric stretching of nearly symmetric Te–O–Te bridges [63]. In the high-wavenumber region (ν > 550 cm^{-1}), the observed sharp and intense peaks are due to the stretching vibrational modes of equatorial Te–$_{eq}$O bonds.

By comparing the Raman spectra of the different TeO$_2$ polymorphs to that of pure TeO$_2$ glass (Fig. I.14(e)), it can be suggested that the structural features of γ-TeO$_2$ are the closest to those featured by the disordered network of TeO$_2$ glass. Thus, one can argue that the amorphous

network of TeO_2 features a more or less pronounced chain-like character as in γ-TeO_2. The structural similarities between these two phases were validated at short-range order but also revealed at medium-range order using X-ray total scattering [77].

In the following sections, we briefly review the previous works on the equilibrium and non-equilibrium diagrams of the three binary systems TeO_2-TiO_2, TeO_2-WO_3 and TeO_2-$NbO_{2.5}$.

I.5. Description of crystalline and amorphous compounds in binary TeO_2-TiO_2, TeO_2-WO_3, TeO_2-$NbO_{2.5}$ and ternary TeO_2-TiO_2-WO_3 and TeO_2-$NbO_{2.5}$-WO_3 systems

I.5.1. Equilibrium and non-equilibrium phases in binary TeO_2-TiO_2 system

I.5.1.1. System at equilibrium state

The equilibrium phase diagram of binary TeO_2-TiO_2 was determined by Yamanaka *et al.* [78]. They confirmed the existence of only one oxide in this system, namely $TiTe_3O_8$ phase corresponding to the composition $75TeO_2$-$25TiO_2$ as first reported by Meunier *et al.* [79]. Another more recent study by Udovic *et al.* [80] also reported that $TiTe_3O_8$ is the only compound from TeO_2-TiO_2 system which is stable in air.

In the following, we describe the crystal structures of TiO_2 (rutile and anatase) and $TiTe_3O_8$ phases. Identifying their characteristic structural features is a key step to reveal the glass structure in both TeO_2-TiO_2 and TeO_2-TiO_2-WO_3 systems discussed in *Chapter IV*.

a) Rutile and anatase TiO_2

The two most common polymorphs of titanium oxide are the stable rutile and metastable anatase. The latter transforms irreversibly to rutile upon heating above 600 °C [81]. Brookite is another metastable polymorph of which the preparation process is comparatively more complex [82]. In the following, we only focus on the structural characteristics of rutile and anatase forms.

Both rutile (space group $P4_2/mnm$ [83]) and anatase (space group $I4_1/amd$ [84]) are tetragonal in structure. Both crystal structures consist of TiO_6 octahedra, sharing two edges in rutile and four in anatase [82]. In both structures, each oxygen atom is tri-coordinated by titanium atoms making $Ti-O{<}^{Ti}_{Ti}$ the only existing type of bridges which we simply refer to as Ti–O–Ti bridges

in the rest of this manuscript. These structures are illustrated in Fig. I.15(a) and (b). More data regarding their physical properties are listed in Table I.4.
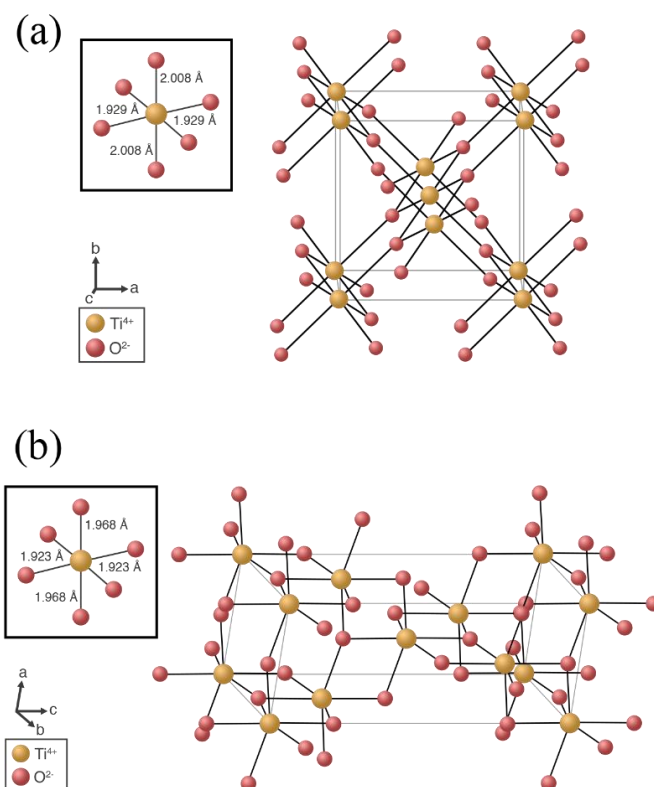
Fig. I.15. Crystal lattice of (a) TiO_2 rutile and (b) TiO_2 anatase. Insets (top left): bond lengths within the TiO_6 octahedron.

Property	Rutile	Anatase
Crystal system	Tetragonal	Tetragonal
Space group	P42/mnm	I41/amd
Formula units (Z)	2	4
Lattice parameters	a = 4.5922 Å	a = 3.7640 Å
	c = 2.9576 Å	c = 9.4610 Å
Unit cell volume	62.37 $Å^3$	134.04 $Å^3$
Calculated density (g.cm^{-3})	4.12	3.83
Measured density (g.cm^{-3})	4.250 *	3.894 *
Measured band gap (eV)	3.1 §	3.2 §
Refractive index (at λ = 550 nm)	2.75 °	2.54 °

Table I.4. Properties of rutile and anatase TiO_2 polymorphs. References: *, § and ° from [85], [86] and [87] respectively.

The anatase to rutile phase transformation is reconstructive in nature, *i.e.,* the transformation involves the breaking and reforming of Ti–O bonds [88]. This is in contrast to a displacive transformation, in which the original bonds are distorted but retained. The study of this transformation is usually performed using Raman spectroscopy [89]. The reason is that the Raman spectra of anatase and rutile TiO_2 polymorphs (*cf.* Fig. I.16(a) and (b)) exhibit distinct features which can therefore be used for qualitative and quantitative analysis.
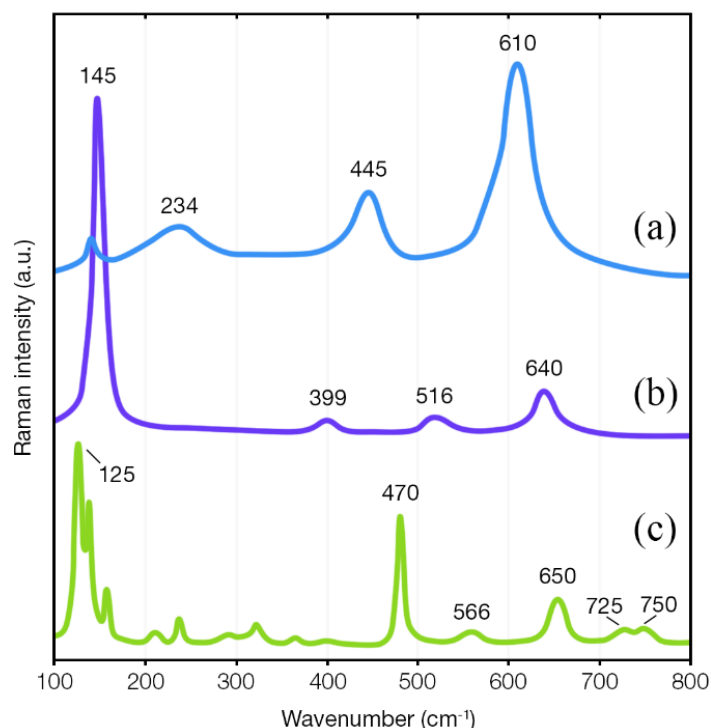
Fig. I.16. Superimposed Raman spectra of (a) TiO_2 rutile, (b) TiO_2 anatase and (c) $TiTe_3O_8$. The spectra of $TiTe_3O_8$ and TiO_2 were reproduced from [71] and [90] respectively.

The Raman spectrum of rutile features four Raman active modes ($A_{1g} + B_{1g} + B_{2g} + E_g$) and shows three major bands at 234, 445 and 610 cm^{-1} (Fig. I.16(a)). The Raman spectrum of anatase corresponds to six Raman active vibrational modes ($A_{1g} + 2B_{1g} + 3E_g$) [91] and features a very intense peak in the low-wavenumber region at ~145 cm^{-1} and weaker bands at ~399, ~516 and ~640 cm^{-1} (Fig. I.16(b)). In contrast to rutile where all four fundamental Raman modes are purely oxygen-atom vibrations (titanium atoms do not move), only the mode A_{1g} (at ~516 cm^{-1}) is predicted to be the pure oxygen vibration in anatase [91].

b) Crystalline TiTe₃O₈ phase

i) Description of the crystal structure

The winstanleyite $TiTe_3O_8$ crystal (space group $I2_1/a\overline{3}$) has a fluorite-type structure with a = 10.965 Å and Z = 8 [92]. More data on its crystallographic and physical properties are listed in Table I.5. The crystal lattice (Fig. I.17(a)) contains interconnected polyhedra of regular TiO_6 octahedra (Ti–O of 1.955 Å) and TeO_4 disphenoids (Te–$_{eq}$O and Te–$_{ax}$O of 1.867 Å and 2.113 Å respectively). The corner-shared TeO_4 disphenoids constitute a 3D network within which TiO_6 octahedra are embedded to support the cohesion of the crystal edifice by sharing their corners with TeO_4 disphenoids via nearly symmetric Te–O–Ti (1.867–1.955 Å) bridges.
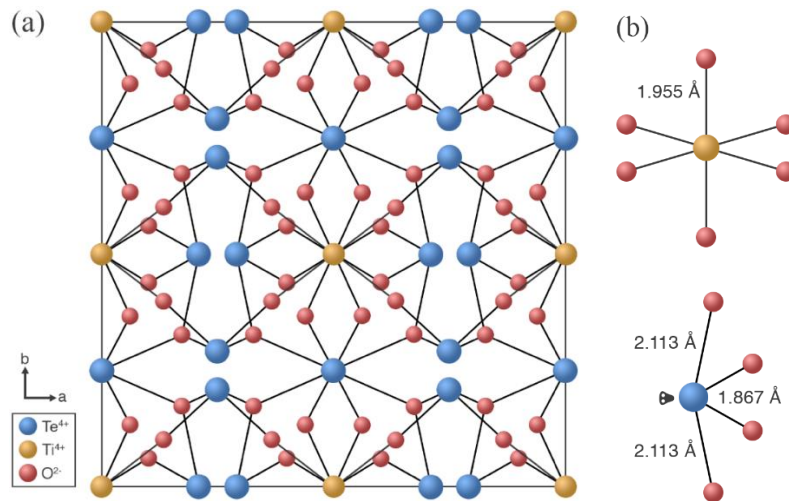
Fig. I.17. (a) Projection of the cubic cell of the $TiTe_3O_8$ crystal lattice along the c axis, and (b) environments of titanium (regular octahedron) and tellurium (disphenoid) cations.

Property	Winstanleyite
Crystal system	Cubic
Space group	$I2_1/a\overline{3}$
Formula units (Z)	8
Lattice parameters	a = 10.965 Å
Unit cell volume	1318.34 Å³
Calculated density (g.cm⁻³)	5.45
Measured density (g.cm⁻³)	5.57 *
Refractive index (λ is not available)	2.34 *

Table I.5. Properties of winstanleyite $TiTe_3O_8$ crystal. * From [93].

ii) Analysis of the Raman spectrum

The Raman spectrum of powdered $TiTe_3O_8$ sample is given in Fig. I.16(c) from [71]. Its mid- to high-wavenumber region is dominated by the band centered at around 470 cm^{-1} followed by a less intense one at 650 cm^{-1}. Weaker bands are observed at around 566, 725 and 750 cm^{-1}.

To assign the origin of the observed bands, Soulis *et al.* [94] have calculated the Raman spectrum of this compound and suggested that the dominant band at 470 cm^{-1} is likely to originate from symmetric vibrations of Te–O–Ti bridges. Given the high intensity of this band, these bridges are expected to be highly symmetric where the Te–O (1.867 Å) and Ti–O (1.955 Å) bonds are chemically indiscernible.

I.5.1.2. System at non-equilibrium state

In the next pages, we review, based on reported experimental data, the preparation conditions of binary TeO_2-TiO_2 glasses accompanied with some of their physical properties (thermal stability, density, optical indices, *etc.*). It is important to stress that despite our strict data selection, we only offer an overview and more details for both the preparation and properties' measurement conditions can be found in the cited works. For instance, we do not indicate the wavelength of light at which the refractive indices of glasses have been measured nor by which means (*e.g.*, by ellipsometry or from the transmission curves). Unfortunately, experimental details such as the wavelength of measurement are infrequently cited by the authors.

The binary $(100-x)TeO_2$-$xTiO_2$ system seems to support only a limited glass-forming domain with a TiO_2 molar content of not more than 20% as reported by several studies (*cf.* Table I.6). Moreover, involving fast-quenching methods (*e.g.,* ice or fast-roller-quenching) proved to be mandatory in order to obtain "TiO_2-rich" glass compositions with $15\% < x \leq 20\%$. We will reconsider this poor glass-forming ability within the frame of our structural investigation of binary TeO_2-TiO_2 and ternary TeO_2-TiO_2-WO_3 glasses (*Chapter IV*).

In general, the structure and properties of all glasses are firmly ruled by the thermal history (conditions of melting, quenching and relaxation processes) during which the glass is first solidified from the supercooled liquid and then eventually relaxed (and continues to relax) by releasing the internal stresses. In other words, for the same melt composition, operating under different experimental conditions results in structurally distinct glasses in which the main

structural configurations (*e.g.,* connection style between polyhedra, correlations at the medium-range structure, bond network density, *etc.*) could vary accordingly.

In Table I.6, one can notice that from one study to another, various quenching methods have been applied to prepare TeO_2-TiO_2 glasses, *i.e.,* these reported glasses have solidified from practically the "same" melt compositions but at different cooling rates: from roughly 10^1-10^2 °C/s by air quenching to over 10^6-10^9 °C/s using the fast-roller quenching method.

Apart from quenching, the other major factor is *melting* that is governed by three main parameters, namely, the temperature, time and mixing frequency, which jointly guarantee the desirable homogeneity of glass melts.

Regarding the melting conditions of TeO_2-TiO_2 melts, one can notice that their batches have been melted at different temperatures ranging from 720 to 950 °C (Table I.6). Generally, the commonly adopted melting temperature for TeO_2-based glass systems lies within the range of 800-900 °C. In fact, raising this temperature within the same chemical system by many authors can be explained by the necessity of dissolving any possible heterogeneous regions. Although the contribution of the other two parameters (melting time and mixing frequency) to the melt's overall homogeneity is as much important as that of the melting temperature, it can be seen from Table I.6 that in some studies, they were relatively underestimated by either melting during quite short time periods (*e.g.,* 10 min) or without mixing/stirring the melt (at least not explicitly mentioned in their reports). Moreover, the batch weights and the crucible's composition are two key parameters that are not always communicated by the authors.

Authors	Glass-forming domain (mol.% of TiO_2)	Melting temperature (°C)	Melting time (min)	Mixing (*during melting*)	Quenching/cooling method	Crucible's composition
Kim and Yoko [41]	5–15 (3 compositions)	800–900	10	N/A	Quenching onto a brass mold at room temperature	5% Au-doped Pt
Sabadel *et al.* [95,96]	7–20 (4 compositions)	900–950	120	Yes	Fast-roller-quenching	Au or Pt
Udovic *et al.* [57]	10–15 (2 compositions)	900	10	N/A	Air quenching	Pt
	5–18 (4 compositions)				Ice quenching[1]	
Villegas and Navarro [97]	10 (1 composition)	720–840	30	Yes	Casting onto a preheated brass plate at 400–440 °C and further cooled at 3 °C/min down to room temperature	
Soulis *et al.* [94]	5–18 (4 compositions)	800	30	N/A	Ice quenching	Au

Table I.6. Preparation conditions of binary (100-x)TeO$_2$-xTiO$_2$ glasses reflecting their thermal histories from different works found in the literature.

The given experimental data on Table I.7 suggest that adding TiO_2 from 5 mol.% to 15 mol.% results in the following trends:

- Increase of the glass transition temperature by approximately 15 % [53,57,98].

- Increase of the thermal stability by almost 50 % [53,57,98].

- Marginal density decrease by less than 3 % [41,94,99]. This trend can be explained by the lower molar mass of TiO_2 (79.9 g.mol^{-1}) compared to that of TeO_2 (159.6 g.mol^{-1}).

- Slight increase of the linear refractive index by 1.4 % from 2.147 to 2.176 [41].

- Increase of the third-order nonlinear optical susceptibility $\chi^{(3)}$ by 17 % [41]. Among other transition-metal oxides MO_x, TiO_2 contributes the most to $\chi^{(3)}$ response in binary TeO_2-MO_x (*cf.* Fig. 1 in [41]).

---

[1] We refer to this technique as melt-fast-quenching (MFQ) – *cf. Chapter III*.

Glass system	TiO$_2$ content x (mol.%)	Glass transition temperature T$_g$ (°C)	Thermal stability ΔT (°C)	Density ρ (g.cm^{-3})	Optical band gap energy E$_g$ (eV)	Linear optical refractive index n	Third-order nonlinear optical susceptibility χ$^{(3)}$ (esu)
Binary (100-x)TeO$_2$- **x**TiO$_2$	5	313 [57]	48 [57]	5.52 [99] 5.56 [41] 5.57 [94]	–	2.147 [41]	14.2*10^{-13} [41]
	10	335 [57]	62 [57]	5.43 [99] 5.50 [41] 5.46 [97] 5.47 [94]	2.88 [97]	2.164 [41]	15.8*10^{-13} [41]
	15	356 [57]	71 [57]	5.36 [99] 5.47 [41] 5.36 [97] 5.39 [94]	–	2.176 [41]	16.6*10^{-13} [41]
	18	372 [57]	74 [57]	5.31 [99] 5.33 [94]	–	–	–
(95-x)TeO$_2$- 5ZnO- **x**TiO$_2$ [53]	5	321	53	5.54	–	–	–
	10	347	73	5.43	2.75	2.082	8.8*10^{-13}
	15	368	83	5.44	–	–	–

Table I.7. Physical properties of binary (100-x)TeO$_2$-xTiO$_2$ glasses and TeO$_2$-rich ternary (95-x)TeO$_2$-5ZnO- xTiO$_2$ glasses.

I.5.2. Equilibrium and non-equilibrium phases in binary TeO$_2$-WO$_3$ system

The phase diagram of binary TeO$_2$-WO$_3$ system was determined by Blanchandin *et al.* [62] using differential scanning calorimetry and high-temperature X-ray diffraction, and an eutectic was detected at 622 ± 5 °C at 22 mol.% of WO$_3$. The results of this study indicate that there exist no crystalline phase within the equilibrium TeO$_2$-WO$_3$ system; and such a compound has never been identified in the preceding works.

In the following, we briefly describe the crystal structure and the features derived from the Raman spectrum of the monoclinic γ-WO$_3$ phase.

I.5.2.1. System at equilibrium state

a) γ–WO₃ phase

i) Description of the crystal structure

The γ-WO₃ phase crystallizes in the P121/n1 space group with the following lattice parameters: a = 7.30 Å, b = 7.53 Å, c = 7.68 Å and β = 90.90° [100]. More crystallographic data are jointly listed in Table I.8. The structure contains two crystallographically distinct W atoms; each is surrounded by six O atoms to form slightly distorted WO₆ octahedra (*cf.* Fig. I.18). There are 12 different W–O bond lengths: 4 short (1.84-1.86 Å) and 8 longer (1.90-2.01 Å) bonds (*cf.* Table I.9).

Property	γ-WO₃
Crystal system	Monoclinic
Space group	P121/n1
Atoms per unit cell (Z)	8
Lattice parameters	a = 7.30 Å
	b = 7.53 Å
	c = 7.68 Å
Unit cell volume	422.11 Å^3
Measured density (g.cm^{-3})	7.16 g.cm^{-3}

Table I.8. Properties of the γ-WO₃ phase.
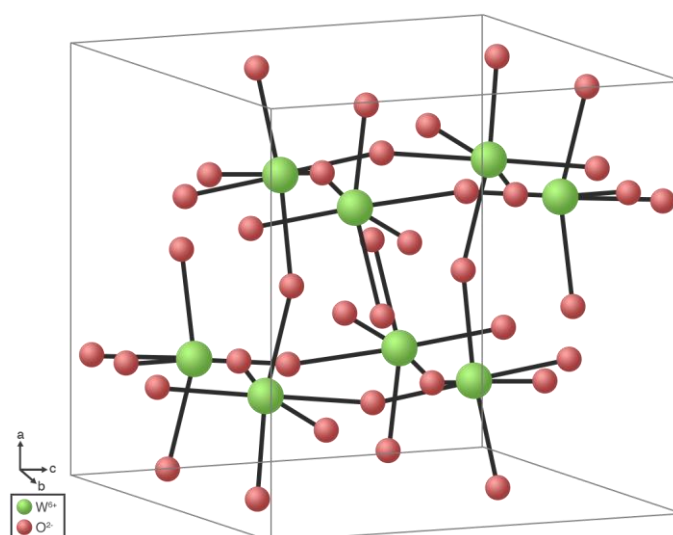
Fig. I.18. Representation of the crystal lattice of γ-WO₃.

Bond length (Å)	
W1–O1	1.899
W1–O2	1.852
W1–O3	1.843
W1–O4	2.013
W1–O5	1.975
W1–O6	1.919
W2–O1	1.855
W2–O2	1.913
W2–O3	1.861
W2–O4	1.985
W2–O5	1.924
W2–O6	1.962

Table I.9. Bond lengths in the γ-WO$_3$ phase.

ii) Analysis of the Raman spectrum

The Raman spectrum of γ-WO$_3$ crystal is presented in Fig. I.19. The low-wavenumber region features a band at approximately 275 cm^{-1} which corresponds to the bending vibrational mode of WO$_6$ octahedra [101]. At higher wavenumbers, two relatively broad bands at 719 and 808 cm^{-1} are observed; they correspond to symmetric and asymmetric stretching vibrations in W–O–W bridges respectively [101].
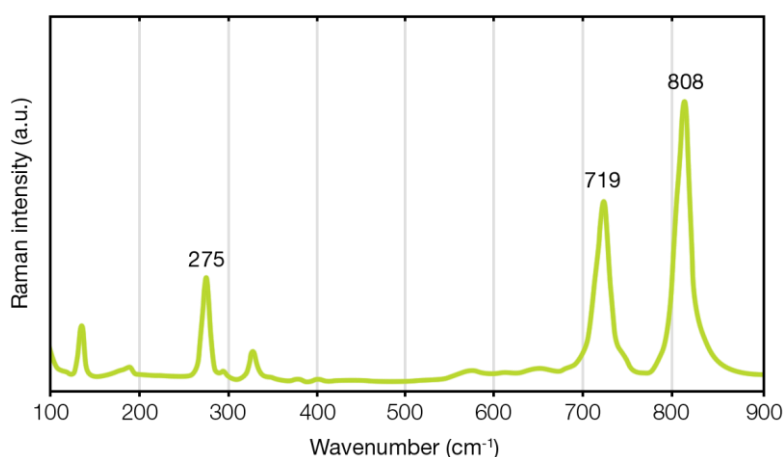
Fig. I.19. Raman spectrum of γ-WO$_3$ crystal reproduced from [102].

I.5.2.2. System at non-equilibrium state

The binary (100-x)TeO_2-xWO_3 glass system seems to support a relatively large glass-forming domain in which increasing WO_3 content results in an overall improvement of the thermal and optical properties [41,62]. Glasses were successfully prepared with WO_3 content ranging from 5 to 30 mol.% as highlighted by most of the conducted studies (Table I.10). Moreover, TeO_2-rich glass compositions containing less than 5 mol.% in WO_3 have been achieved by means of fast quenching techniques [62].

Authors	Glass-forming domain (mol.% of WO_3)	Melting temperature (°C)	Melting time (min)	Mixing (*during melting*)	Quenching/cooling method	Crucible's composition
Sekiya *et al.* [103]	5–30 (6 compositions)	850–950	15–30	N/A	Ice quenching	Pt
Shaltout *et al.* [104]	5–31.5 (7 compositions)	800	30		Casting onto a stainless steel plate at room temperature	
Kim and Yoko [41]	10–30 (3 compositions)	800–900	10		Quenching onto a brass mold at room temperature	5% Au-doped Pt
Blanchandin *et al.* [62]	2.5–30 (7 compositions)	850	30		Rapid casting onto a preheated brass mold at 60 °C and quickly quenched by pressing into thin sheets of ~1.5 mm thick.	Pt
Charton *et al.* [105,106]	5–32.5 (7 compositions)	900	15		Ice quenching	
Upender *et al.* [107]	10–40 (4 compositions)	800–950	30	Yes	Casting onto a stainless steel plate	
Kaur *et al.* [108]	10–25 (4 compositions)	800–850	30	N/A	Casting onto a brass block	

Table I.10. Preparation conditions of binary TeO_2-WO_3 glasses reflecting their thermal histories from different works found in the literature.

The experimental data given in Table I.11 suggest that adding WO_3 from 5 mol.% to 30 mol.% results in the following trends:

- Increase of the glass transition temperature by approximately 11 % [104].

- Sharp increase of the thermal stability from only 18 °C to 80 °C [104].

- Slight density increase by over 4 % [41]. This trend can be explained by the higher molar mass of WO_3 (231.8 $g.mol^{-1}$) compared to that of TeO_2 (159.6 $g.mol^{-1}$).

- Fairly constant behavior of the linear refractive index with a value of 2.12 [41,109].

- Increase of the third-order nonlinear optical susceptibility $\chi^{(3)}$ by approximately 12 % from $14.2*10^{-13}$ (10 mol.%) to $15.9*10^{-13}$ (30 mol.%) [41]. Muñoz-Martín $et\ al.$ [109] investigated the effect of various oxides on the nonlinear optical performance of $80TeO_2$-$15WO_3$-$5MO_x$ glasses (Table I.11). Their results confirm the expected increase of $\chi^{(3)}$ when other lone electron pair holders such as Bi and Pb atoms are incorporated within the glass network.

Glass system	WO$_3$ content x (mol.%)	Glass transition temperature T$_g$ (°C)	Thermal stability ΔT (°C)	Density ρ (g.cm^{-3})	Optical band gap energy E$_g$ (eV)	Linear optical refractive index n	Third-order nonlinear optical susceptibility χ$^{(3)}$ (esu)
Binary (100-x)TeO$_2$-**x**WO$_3$	5	333 [104]	18 [104]	–	3.49 [110]	–	–
	10	323 [107]	37 [107]	5.82 [108] 5.73 [41]	3.43 [110]	2.122 [41]	14.2*10^{-13} [41]
	15	347 [104]	43 [104]	5.90 [108]	3.40 [110] 3.30 [109]	2.120 [109]	12±4*10^{-13} [109]
	20	359 [104] 343 [107]	72 [104] 67 [107]	5.99 [108] 5.89 [41]	3.38 [110]	2.124 [41] 2.120 [109]	14.8*10^{-13} [41]
	25	370 [104]	76 [104]	6.05 [108]	3.38 [110]	–	–
	30	369 [104] 367 [107]	80 [104] 89 [107]	5.98 [41]	3.32 [110]	2.126 [41]	15.9*10^{-13} [41]
(95-x)TeO$_2$-**x**WO$_3$-5TiO$_2$	15	–	–	–	3.32 [109]	2.120 [109]	9±3*10^{-13} [109]
(95-x)TeO$_2$-**x**WO$_3$-5Nb$_2$O$_5$		–	–	–	3.41 [109]	2.125 [109]	7±3*10^{-13} [109]
(95-x)TeO$_2$-**x**WO$_3$-5Ta$_2$O$_5$		–	–	–	3.44 [109]	2.110 [109]	11±4*10^{-13} [109]
(95-x)TeO$_2$-**x**WO$_3$-5La$_2$O$_3$		–	–	–	3.45 [109]	2.090 [109]	6±2*10^{-13} [109]
(95-x)TeO$_2$-**x**WO$_3$-5Bi$_2$O$_3$		–	–	–	3.42 [109]	2.140 [109]	13±4*10^{-13} [109]
(95-x)TeO$_2$-**x**WO$_3$-5PbO		–	–	–	3.34 [109]	2.120 [109]	13±4*10^{-13} [109]

Table I.11. Physical properties of binary (100-x)TeO$_2$-xWO$_3$ glasses and TeO$_2$-rich ternary (95-x)TeO$_2$- xWO$_3$- 5MO$_x$ (M = Ti, Nb, Ta, La, Bi and Pb) glasses.

I.5.3. Equilibrium and non-equilibrium phases in binary TeO₂-NbO₂.₅ system

I.5.3.1. System at equilibrium state

Over the last 40 years, several studies have been conducted on this binary system; they collectively revealed the existence of the three following crystalline phases $Nb_2Te_4O_{13}$ ($2NbO_{2.5}$:$4TeO_2$), $Nb_2Te_3O_{11}$ ($2NbO_{2.5}$:$3TeO_2$) and Nb_6TeO_{17} ($6NbO_{2.5}$:TeO_2) [111–113]. Among these studies, one significant contribution was achieved by Blanchandin *et al.* [114] who determined the phase diagram under equilibrium and non-equilibrium conditions for the TeO₂-rich part of the binary TeO_2-Nb_2O_5 system.

In the following, we describe the crystal structures of each of the above-mentioned compounds along with that of H-Nb_2O_5 phase, and recall their vibrational properties as revealed by Raman spectroscopy.

a) H-Nb₂O₅ phase

i) *Description of the crystal structure*

The niobium pentoxide H-Nb_2O_5 phase (H for high temperature or *Hohen temperaturen* in German) named by Schäfer *et al.* [115] crystallizes in the P12/m1 space group with the following cell parameters: a = 21.153 Å, b = 3.823 Å, c = 19.356 Å and β = 119.80° [116]. Its crystallographic data and other few physical properties are listed in Table I.12. This crystal structure is characterized by the large Nb–O bond length distribution making the coordination sphere of Nb atoms considerably asymmetric (Fig. I.20 and Fig. I.21).

Property	H-Nb₂O₅
Crystal system	Monoclinic
Space group	P12/m1
Formula units (Z)	14
Lattice parameters	a = 21.153 Å
	b = 3.823 Å
	c = 19.356 Å
Unit cell volume	1358.40 Å^3
Calculated density (g.cm^{-3})	4.40
Measured band gap (eV)	3.85 *

Table I.12. Properties of H-Nb₂O₅ crystal. * From [117].
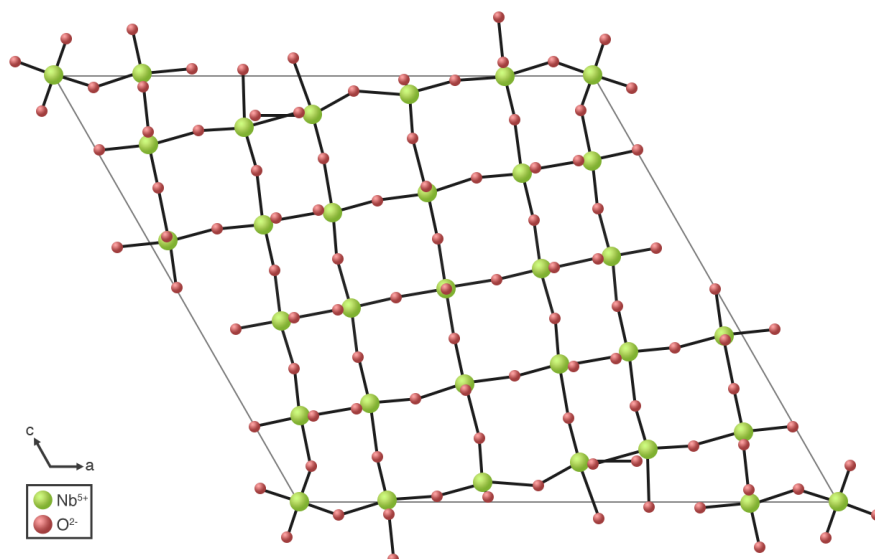
Fig. I.20. Projection of the structure of H-Nb$_2$O$_5$ along the b axis.
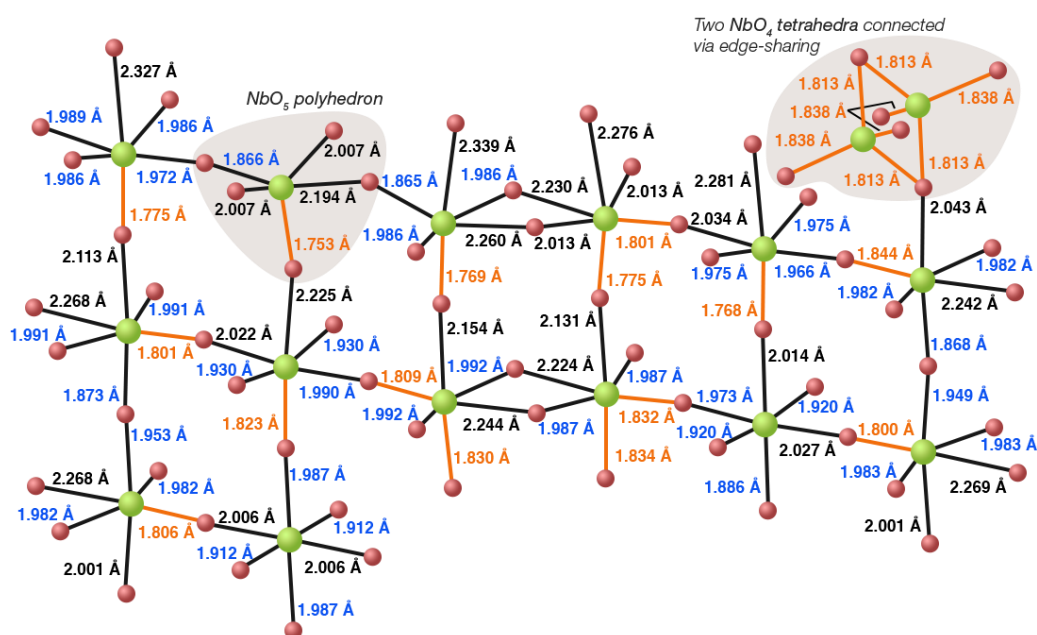
Fig. I.21. Representation of the 15 distinct NbO$_x$ polyhedra in H-Nb$_2$O$_5$ crystal. For a faster reading, bond lengths shorter than 1.85 Å are given in orange; those ranging between 1.85 and 2 Å in blue and the ones longer than 2 Å in black. Top-right: two NbO$_4$ tetrahedra sharing one edge though the structure contains only one crystallographically distinct NbO$_4$ tetrahedron.

ii) Analysis of the Raman spectrum

The Raman spectrum of crystalline H-Nb$_2$O$_5$ is given in Fig. I.22(a). In the low-wavenumber region, a broad band centered at 260 cm^{-1} due to the vibrations of Nb atoms within NbO$_x$ polyhedra. The high-wavenumber region features a broader band over the 500-800 cm^{-1} range

with three main contributions at ~545, ~620 and ~670 cm^{-1} along with an intense peak at 990 cm^{-1}. The latter is due to the stretching vibrations of the shortest Nb–O bonds (shorter than 1.85 Å, given in orange in Fig. I.21). The three bands at 545, 620 and 670 cm^{-1} correspond to stretching vibrations of relatively longer Nb–O bonds (between 1.85 and 2.1 Å) [94].
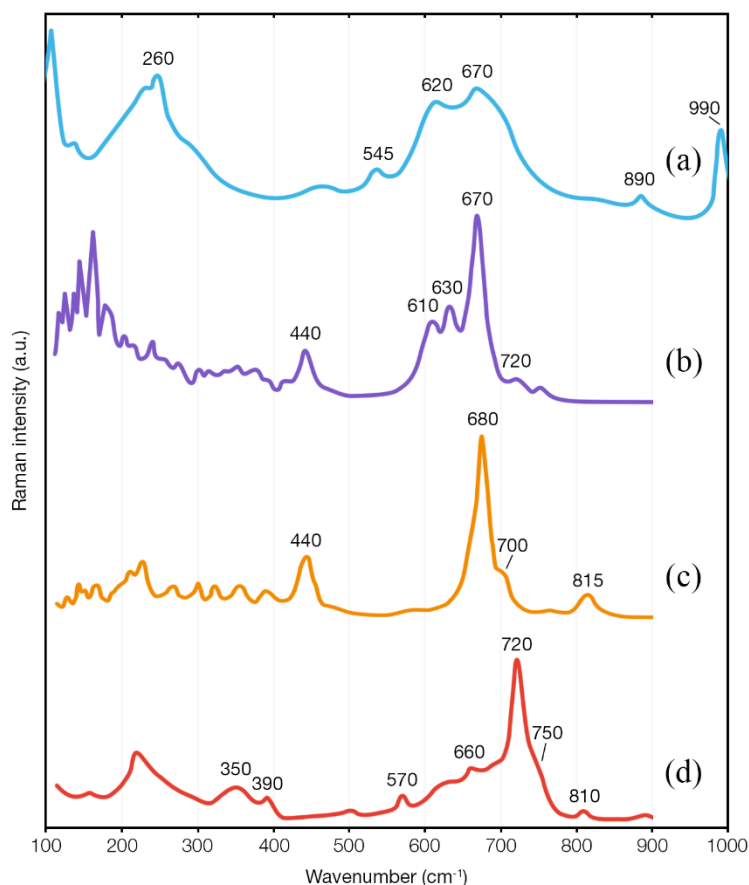
Fig. I.22. Superimposed Raman spectra of (a) H-Nb$_2$O$_5$, (b) Nb$_2$Te$_4$O$_{13}$, (c) Nb$_2$Te$_3$O$_{11}$ and (d) Nb$_6$TeO$_{17}$ recorded at room temperature. Reproduced from [94].

b) Nb$_2$Te$_4$O$_{13}$ (2NbO$_{2.5}$: 4TeO$_2$)

i) Description of the crystal structure

This compound crystallizes in the P-1 space group with the following cell parameters: a = 7.561 Å, b = 12.697 Å, c = 12.736 Å, α = 116.050°, β = 90.192° and γ = 90.031° (*cf.* Table I.13 for more details) [118]. It contains eight (four) crystallographically distinct Te (Nb) atoms. As shown in Fig. I.23, 6 out of 8 Te environments are TeO$_3$ trigonal pyramids; the remaining two are slightly closer to the intermediate TeO$_{3+1}$ configuration. Since the extended bonds in the latter units are considerably long, *viz.* 2.200 and 2.245 Å, they can practically be ignored from

the chemical viewpoint and thus transforming the four-membered chain in Fig. I.23(b) into two Te_2O_5 units. This means that despite the considerable amount of O atoms brought by adding Nb_2O_5, not all TeO_4 units are being transformed into TeO_3 ones. Hence, the Nb^{5+} cation should be considered as an intermediate cation.

Property	$Nb_2Te_4O_{13}$
Crystal system	Triclinic
Space group	P-1
Formula units (Z)	4
Lattice parameters	a = 7.5609 Å
	b = 12.697 Å
	c = 12.736 Å
Unit cell volume	1098.44 Å^3
Calculated density (g.cm^{-3})	5.29
Measured density (g.cm^{-3})	5.50 *

Table I.13. Properties of $Nb_2Te_4O_{13}$ crystal. * From [118].

This crystal structure can be alternatively described as being composed of two types of layers: the first contains interconnected NbO_6 octahedra via corner-sharing which are also connected to TeO_3 units via Te–O–Nb bridges; where the second type consists of the previously mentioned Te_2O_5 units.
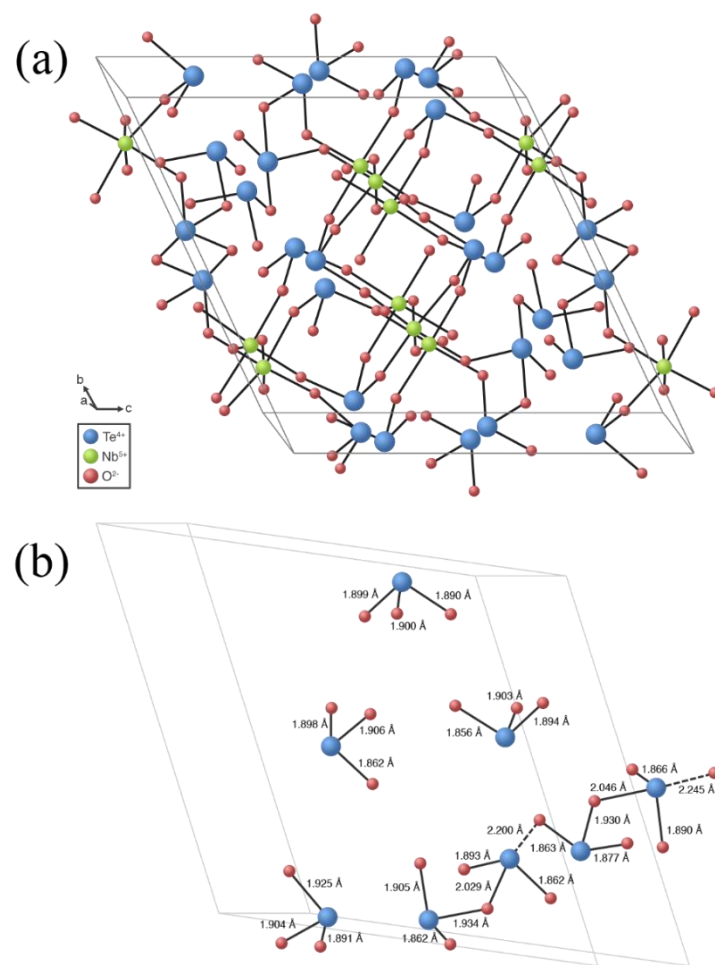
Fig. I.23. (a) Projection of the crystal structure of $Nb_2Te_4O_{13}$ and (b) the atomic environments of the 8 crystallographically distinct Te atoms (for the purpose of clarity, neighboring Nb atoms are not presented within the crystal lattice).

ii) Analysis of the Raman spectrum

The Raman spectrum of $Nb_2Te_4O_{13}$ crystal (Fig. I.22(b)) is dominated by the high-wavenumber intense band centered at ~670 cm^{-1} and emerging among the several relatively weak bands over the 580-750 cm^{-1} range. The mid-wavenumber range features a weaker band positioned at 440 cm^{-1}.

As briefly stated earlier, Soulis *et al.* [94] have calculated the Raman spectrum of this compound indirectly, *i.e.,* via the consideration of the two structural layers (NbO_6+TeO_3 and Te_2O_5). Their results suggest that the 400-450 cm^{-1} range which is dominated by the band at 440 cm^{-1} is due to the symmetric stretching of Te–O–Te bridges (1.934-2.029 Å) and highly symmetric Te–O–Nb (1.890-1.916 Å) bridges. At higher wavenumbers, the more intense bands in the 600-700 cm^{-1} range are attributed to stretching vibrations of highly asymmetric and almost terminal Te–O– – –Nb (1.890-2.078 Å) linkages. The weaker bands observed above 700

cm^{-1} are assigned to stretching vibrations of the highly asymmetric Nb–O– – –Nb (1.797-2.128 Å) linkages.

c) Nb$_2$Te$_3$O$_{11}$ (2NbO$_{2.5}$: 3TeO$_2$)

i) Description of the crystal structure

This compound crystallizes in the P2$_1$2$_1$2 space group with the following lattice parameters: a = 7.700 Å, b = 15.700 Å, c = 3.979 Å (*cf.* Table I.14 for more details) [111]. Its crystal structure hosts two (one) crystallographically distinct Te (Nb) atoms (Fig. I.24). Besides, not all TeO$_4$ disphenoids are converted into TeO$_3$ trigonal pyramids as a result of adding Nb$_2$O$_5$ oxide, and instead of Te$_2$O$_5$ units in Nb$_2$Te$_4$O$_{13}$, this structure accommodates Te$_3$O$_8$ units (*cf.* Fig. I.25).

Property	Nb$_2$Te$_3$O$_{11}$
Crystal system	Orthorhombic
Space group	P2$_1$2$_1$2
Formula units (Z)	2
	a = 7.700 Å
Lattice parameters	b = 15.700 Å
	c = 3.979 Å
Unit cell volume	481.02 Å^3
Calculated density (g.cm^{-3})	4.98

Table I.14. Crystallographic data of Nb$_2$Te$_3$O$_{11}$ crystal.
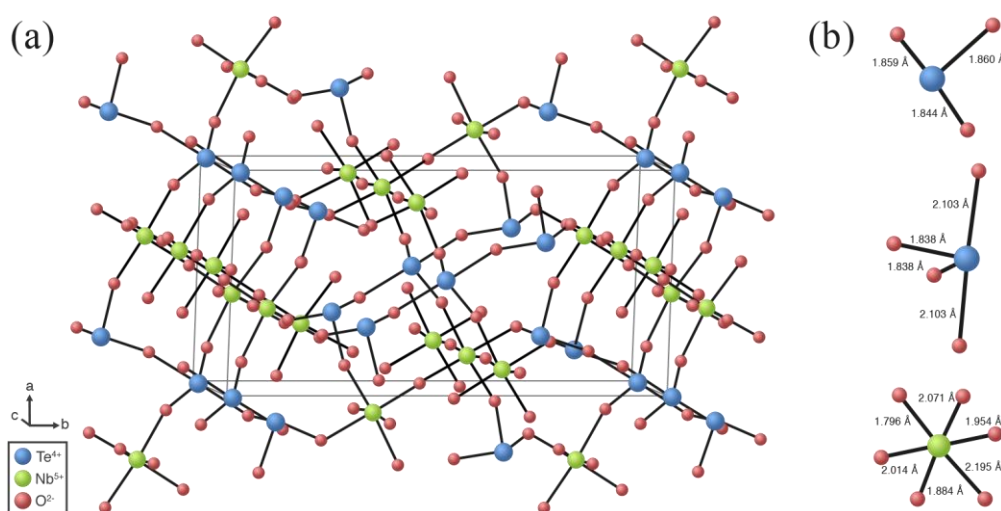
Fig. I.24. (a) Projection of the crystal structure of Nb$_2$Te$_3$O$_{11}$ and (b) the existing structural units of TeO$_3$, TeO$_4$ and NbO$_6$.
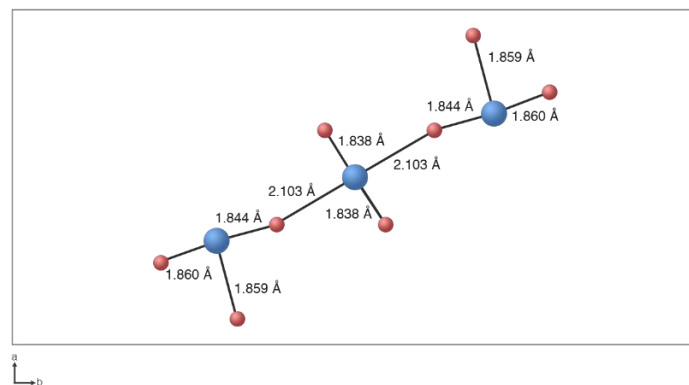
Fig. I.25. Representation of the Te_3O_8 unit in the $Nb_2Te_3O_{11}$ cell.

ii) Analysis of the Raman spectrum

The Raman spectrum of $Nb_2Te_3O_{11}$ crystal (Fig. I.22(c)) is dominated by a sharp and intense band centered at approximately 680 cm^{-1} and accompanied with a shoulder at 700 cm^{-1}. A much weaker band at 815 cm^{-1} is also observed in the high-wavenumber region. The mid-wavenumber range features a relatively intense band positioned at ~440 cm^{-1}.

Results of Raman spectrum calculation [94] suggest that the band at 440 cm^{-1} is due to symmetric stretching vibrations of Te–O–Te (1.844-2.103 Å) bridges from Te_3O_8 units, along with those from the nearly symmetric Te–O–Nb (1.859-1.954 Å) bridges. Stretching vibrational modes of the shortest Te–O bonds (1.838 Å) result in the intense band at 680 cm^{-1}. And finally, the high-wavenumber band at 815 cm^{-1} is attributed to stretching vibrations of the shortest Nb–O bonds (1.796 Å).

d) Nb_6TeO_{17} ($6NbO_{2.5}$: TeO_2)

The accurate crystal structure of this oxide has not been solved yet. However, using X-ray powder diffraction, Khodyakova *et al.* [119] suggested the following lattice parameters: a = 17.57 Å, b = 17.36 Å and c = 3.97 Å in the orthorhombic crystal system.

The Raman spectrum presented in (Fig. I.22(d)) was also obtained from a powdered sample of Nb_6TeO_{17} [94] and is dominated by an intense band centered at ~720 cm^{-1} and emerging among the several relatively weak bands over the 550-780 cm^{-1} range. It is also characterized by the absence of the mid-wavenumber band (at 440 cm^{-1} in the Raman spectra of both $Nb_2Te_4O_{13}$ and $Nb_2Te_3O_{11}$ compounds) which might indicate that symmetric (or nearly symmetric) Te–O–Te

and Te–O–Nb bridges are unlikely to exist [94]. Moreover, the intense band at ~720 cm^{-1} suggests the presence of terminal Te–O (<1.84 Å) and Nb–O (<1.80 Å) bonds.

I.5.3.2. System at non-equilibrium state

Several studies have been conducted on the binary (100-x)TeO$_2$-xNbO$_{2.5}$ system uncovering its glass-forming domain with a NbO$_{2.5}$ molar content of not more than 33.4-40% (*cf.* Table I.15). In addition to their physical properties, the structural features of TeO$_2$-NbO$_{2.5}$ glasses have been extensively investigated by various techniques: X-ray and neutron diffraction (see *e.g.,* [120]), X-ray absorption spectroscopy [121] and IR [122] and Raman [94,108] spectroscopies.

The experimental data given in Table I.16 suggest that a continuous increase of the NbO$_{2.5}$ molar content from 5 to 33.4 % results in the following trends:

- Continuous increase of the glass transition temperature by more than 26 % [108,123].

- Sharp increase of the thermal stability ΔT to over 140 °C at 18.2 mol.% of NbO$_{2.5}$; however, a reduction of ΔT is observed upon continuous adding [108,123]. In contrast, Hayakawa *et al.* [124] report a thermal stability of only 57 °C at 18.2 mol.% of NbO$_{2.5}$.

- Slight density decrease by approximately 5.6 % [41,108]. This evolution can be explained by the relatively low molar mass of NbO$_{2.5}$ (132.9 g.mol^{-1}) compared to that of TeO$_2$ (159.6 g.mol^{-1}).

- Marginal increase of the linear refractive index from 2.23 to 2.26 suggesting a rather steady evolution [123].

- Two studies reported contradicting evolutions of the third-order nonlinear optical susceptibility $\chi^{(3)}$: according to one, $\chi^{(3)}$ slightly decreases by 11 % from 13.2*10^{-13} (9.5 mol.%) to 11.7*10^{-13} (33.4 mol.%) [123], while the other suggests an increase of 12 % from 14.3*10^{-13} (18.2 mol.%) to 16.1*10^{-13} (33.4 mol.%) [124].

Authors	Glass-forming domain (mol.% of NbO$_{2.5}$)	Melting temperature (°C)	Melting time (min)	Mixing *(during melting)*	Quenching/cooling method	Crucible's composition
Kim and Yoko [41]	10–30 (3 compositions)	800–900	10	N/A	Quenching onto a brass mold at room temperature	5% Au-doped Pt
Berthereau et al. [123]	9.5–33.4 * (5 compositions)	850–1000	30–40		Quenching between two preheated graphite plates and annealed at T$_g$-30 °C	Pt
Blanchandin et al. [114]	5–25 (7 compositions)	800	30		Quenching by flattening between two brass blocks separated by a brass ring	
	2.5 (1 composition)				Ice quenching	
Soulis et al. [94]	9.5–40 * (4 compositions)					
Villegas and Navarro [97]	9.5–26.1 * (3 compositions)	720–840	30	Yes	Casting onto a preheated brass plate at 400–440 °C and further cooled at 3 °C/min down to 20 °C	
Lin et al. [125]	5.8–33.4 * (5 compositions)	750–850	15–20		Casting onto a cold stainless steel plate	Au
Hayakawa et al. [124]	18.2–33.4 * (2 compositions)	900	60	N/A	Casting onto a carbon mold, annealed at 400 °C for 4 h, and then cooled down to 20°C	Al$_2$O$_3$
Kaur et al. [108]	9.5–33.4 * (4 compositions)	800–850	30		Casting onto a brass block	Pt

Table I.15. Preparation conditions of binary TeO$_2$-NbO$_{2.5}$ glasses reflecting their thermal histories from different works found in the literature. * To compare the available data, we have converted the mol.% in Nb$_2$O$_5$ reported by the authors into mol.% NbO$_{2.5}$ for the purpose of clarity.

Glass system	NbO$_{2.5}$ content x (mol.%)	Glass transition temperature T$_g$ (°C)	Thermal stability ΔT (°C)	Density ρ (g.cm^{-3})	Optical band gap energy E$_g$ (eV)	Linear optical refractive index n	Third-order nonlinear optical susceptibility χ$^{(3)}$ (esu)
Binary (100-x)TeO$_2$-**x**NbO$_{2.5}$	2.5	~313 [114]	~47 [114]	5.70 [114]	–	–	–
	5	~327 [114]	~43 [114]	–	–	–	–
	10	~335 [114]	~71 [114]	–	–	2.126 [41]	14.1*10^{-13} [41]
	15	~349 [114]	~81 [114]	–	–	–	–
	20	~365 [114]	~95 [114]	–	–	2.182 [41]	16.1*10^{-13} [41]
	25	~383 [114]	~98 [114]	5.30 [114]	–	–	–
	30	–	–	–	–	2.192 [41]	16.9*10^{-13} [41]
	9.5 *	330 [108] 326 [123]	97 [108] 56 [123]	5.52 [97] 5.53 [108] 5.52 [123]	–	2.23 [123]	13.2*10^{-13} [123]
	18.2 *	357 [108] 357 [123] 442 [124]	143 [108] 164 [123] 57 [124]	5.41 [97] 5.43 [108] 5.40 [123]	3.14 [123]	2.24 [123] 2.04 [124]	11.8*10^{-13} [123] 14.3*10^{-13} [124]
	26.1 *	387 [108] 392 [123]	135 [108] 108 [123]	5.33 [97] 5.33 [108] 5.34 [123]	3.09 [123]	2.22 [123]	11.3*10^{-13} [123]
	33.4 *	416 [108] 426 [123] 497 [124]	125 [108] 92 [123] 77 [124]	5.23 [108] 5.20 [123]	3.06 [123]	2.26 [123] 2.06 [124]	11.7*10^{-13} [123] 16.1*10^{-13} [124]

Table I.16. Physical properties of binary (100-x)TeO$_2$-xNbO$_{2.5}$ glasses. * To compare the available data, we have converted the mol.% in Nb$_2$O$_5$ reported by the authors into mol.% NbO$_{2.5}$ for the purpose of clarity.

I.5.4. Previous works on TeO₂-TiO₂-WO₃ and TeO₂-NbO₂.₅-WO₃ glassy systems

In this section, we review the reported works on ternary TeO$_2$-TiO$_2$-WO$_3$ and TeO$_2$-NbO$_{2.5}$-WO$_3$ systems which represent the experimentally investigated materials in this work (*cf. Chapters IV and V)*. It is important to note that no crystal compound has ever been reported in any of these two ternary systems.

I.5.4.1. On the ternary TeO₂-TiO₂-WO₃ glassy system

Safonov [126] investigated the phase equilibria in the TeO$_2$-rich part of this ternary system within the range of 55-100 mol.% in TeO$_2$ by means of differential thermal analysis, visual polythermal analysis and X-ray powder diffraction techniques. Furthermore, TeO$_2$-TiO$_2$-WO$_3$ glasses were prepared by casting the melts into metal molds in order to determine the stable glass formation boundaries. It is important to mention that this paper does not report any properties of those glasses. The established equilibrium and non-equilibrium phase diagram is given below in Fig. I.26.
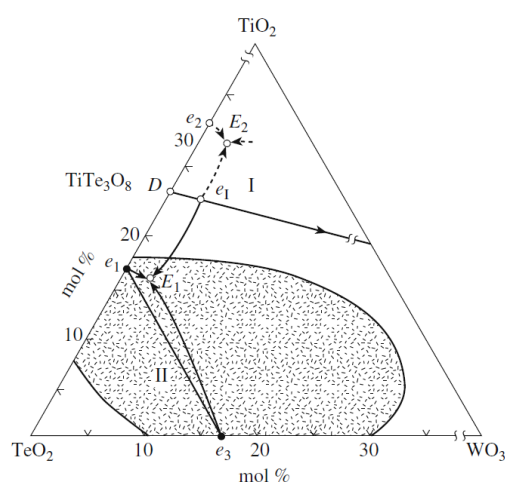
Fig. I.26. Ternary phase diagram in the TeO$_2$-TiO$_2$-WO$_3$ system with detected features such as the eutectic E$_1$ and E$_2$ points. Taken from [126].

Another systematic study by Imaoka and Yamazaki [37] on the glass formation ability of over 100 TeO$_2$-based systems reported the glass-forming domain in the TeO$_2$-TiO$_2$-WO$_3$ system as shown in Fig. I.27. Again, this work does not report any properties of those prepared glasses.
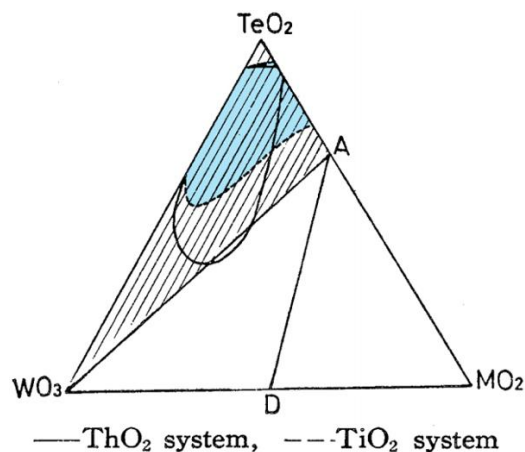
Fig. I.27. Glass-forming domain in the TeO_2-TiO_2-WO_3 system (*cf.* shaded area in blue).
Reproduced from [37].

To the best of our knowledge, the only glass composition in the ternary TeO_2-TiO_2-WO_3 system of which physical properties were measured, is $80TeO_2$-$5TiO_2$-$15WO_3$ by Muñoz-Martín *et al.* [109]. They investigated the structure by Raman spectroscopy and both linear and nonlinear optical properties by spectroscopic ellipsometry and degenerate four-wave mixing technique respectively. These properties were compared with those from other compositions belonging to the $80TeO_2$-$5R_xO_y$-$15WO_3$ system with R = Nb, Ta, La, Bi and Pb. For instance, by comparing their Raman spectral features (Fig. 3.11 in [109]), Muñoz-Martín *et al.* addressed the similarity between the Raman spectra of $80TeO_2$-$5R_xO_y$-$15WO_3$ glasses (R = Ti, Nb and Ta) and that of the binary $85TeO_2$-$15WO_3$ glass. The linear and nonlinear optical properties reported for this set of glasses are given in Table I.11 in *section I.5.2.2*.

Another investigation of close glass compositions was reported by Fares *et al.* [127] who studied the effect of adding WO_3 on the structural, thermal and optical properties of the Nd-doped quaternary $(89-x)TeO_2$-$10TiO_2$-xWO_3-$1Nd_2O_3$ system with x = 0, 10 and 20 mol.%. The authors argue that adding WO_3 results in *(i)* breaking the Te–O–Te bridges and *(ii)* improving the optical properties by increasing the linear refractive index.

I.5.4.2. On the ternary TeO_2-$NbO_{2.5}$-WO_3 glassy system

So far, there have been only a few studies devoted to revealing the physical properties of these glasses. In fact, aside from few investigations on the specific compositions described below, there is no reported systematic study within this ternary glass system. Carreaud *et al.* [128] and Dai *et al.* [129] recorded the Raman spectra of $75TeO_2$-$20NbO_{2.5}$-$5WO_3$ and $72TeO_2$-$18NbO_{2.5}$-

10WO$_3$ glass compositions along with their thermal and linear optical properties (*cf.* Table I.17). In addition, Muñoz-Martín [109] measured the linear and nonlinear optical properties of the 80TeO$_2$-5Nb$_2$O$_5$-15WO$_3$ composition (converted to 76.3TeO$_2$-9.4NbO$_{2.5}$-14.3WO$_3$ to enable comparison with the other compositions – *cf.* Table I.17).

Composition	T$_g$ (°C)	ΔT (°C)	Refractive index
75TeO$_2$-20NbO$_{2.5}$-5WO$_3$ [128]	375	153	2.211 *
72TeO$_2$-18NbO$_{2.5}$-10WO$_3$ [129]	380	175	2.2116 §
76.3TeO$_2$-9.4NbO$_{2.5}$-14.3WO$_3$ [109]	–	–	2.125 #

Table I.17. Glass transition temperature T$_g$, thermal stability ΔT and linear refractive index for glass compositions in the ternary TeO$_2$-NbO$_{2.5}$-WO$_3$ system. The labels *, § and # correspond to the following wavelengths of measurement: 1900 nm, 532 nm and 1500 nm respectively.

I.6. Conclusion

In this first chapter, we recalled some fundamental concepts in the field of glass science and reviewed, in a general fashion, the literature on early research relative to the family of TeO$_2$-based glasses, *i.e.*, their glass-forming ability, structural, physical properties and technological applications. We have also described the crystal structures of TeO$_2$ polymorphs (α, β and γ) along with the structural features of the pure TeO$_2$ glass.

In addition, we summarized the reported literature on both crystals and glasses from the binary TeO$_2$-TiO$_2$, TeO$_2$-WO$_3$ and TeO$_2$-NbO$_{2.5}$ systems by describing *(i)* the crystal structures of compounds isolated from each binary systems, and *(ii)* the preparation conditions, thermal, structural and optical properties of the binary glasses.

According to the literature, adding TiO$_2$ in binary TeO$_2$-TiO$_2$ glasses allows to enhance the glass-forming ability and maintain the original structural organization of pure TeO$_2$ glass. Hence, TiO$_2$-containing TeO$_2$-based glasses are of special interest since conserving the glass network of pure TeO$_2$ would probably ensure the high linear and nonlinear optical performances [41]. Moreover, it has been reported that adding WO$_3$ in binary TeO$_2$-WO$_3$ glasses improves the thermal and optical (linear and nonlinear) properties [41,62]. Besides, adding NbO$_{2.5}$ in binary TeO$_2$-NbO$_{2.5}$ glasses enhances both the linear and nonlinear optical properties [41] and increases the thermal stability [108,123] which is a crucial requirement in some optical glass manufacturing processes, *e.g.,* optical fiber drawing. An improvement of the network

reinforcement and mechanical strength was also reported as a result of incorporating $NbO_{2.5}$ within the TeO_2-rich network [130]. Keeping all these facts in focus, we have embarked upon investigating the two ternary TeO_2-TiO_2-WO_3 and TeO_2-$NbO_{2.5}$-WO_3 systems (*cf. Chapters IV and V* respectively).

In the next chapter, we introduce the cationic field strength theory and systematically apply it to TeO_2-based materials with the aim of predicting structural tendencies and behaviors in binary TeO_2-based glass systems.

Chapter II.   Application of the cationic field strength theory to TeO₂-based materials

II.1. Introduction

At the beginning of the 20th century, Tammann [131], as one of the first scientists to show curiosity about the structural organization in glasses, argued that glasses show substantial similarities with strongly supercooled liquids. In 1926, Goldschmidt [132] derived empirical rules for glass formation based on the criterion of cation-to-anion-radius ratio. Less than a decade later, more investigators attempted to predict the glass structure. For example, the significant work of Zachariasen-Warren [14,133] on the glass network represented a leap forward in unlocking the short- to medium-range structure of the glass network.

In parallel to these universal theories of which the ultimate aim was to predict the glass formation in all possible systems and explain its origins, more theories/models tried to establish the existing relationships between the glass formation and composition by focusing on how the melt's composition affects the outcome of cooling. Two of these theories, developed by Dietzel [20] and Sun [134] proved to be valid for a satisfying prediction of glass formation and network structure especially in oxide systems. Using close concepts, namely, the cationic field strengths and interatomic bond energies respectively, they often lead to very close conclusions.

First, we would like to make reference to Sun's theory on bond energies and their contribution to glass formation. Based on this concept, an analogy example for the two possible scenarios (crystallization vs. glass formation) expected upon the melt cooling was delivered by Sun (*cf.* page 278 in [134]). Inspired by that example, we provide in Fig. II.1 a pictorial version to emphasize the crucial role of strong bonds (simulated by the hands of soldiers) in the glass formation. The presence of these strong bonds, unlike in the first case of handless soldiers, makes the orderly arrangement (*i.e.,* crystallization) more difficult by resisting the breaking of linkages and therefore promoting the glass formation.
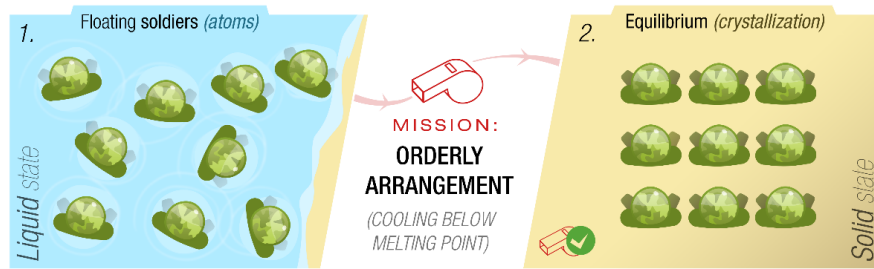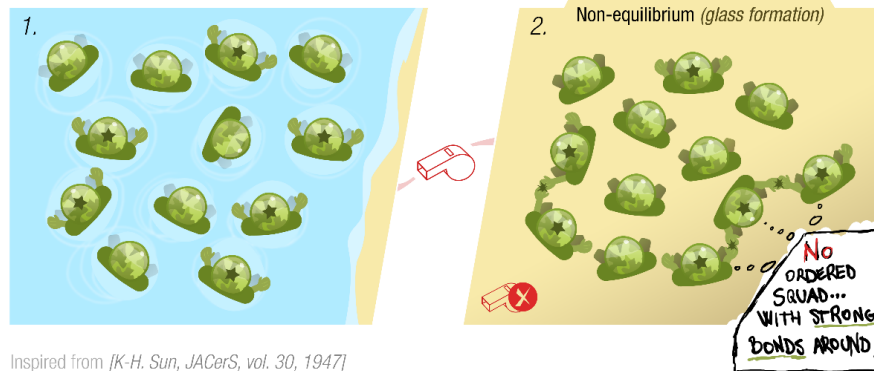
Fig. II.1. Illustration depicting the two scenarios of crystallization and glass formation based on Sun's bond energy theory (see text).

We dedicate this chapter to Dietzel's cationic field strength theory by applying it to TeO$_2$-based materials. In the following sections, we start by giving an overview of the theoretical background of the field strength concept. Then, we check its validity when applied to various binary TeO$_2$-based crystals and glasses with the ultimate aim of using this concept as a complementary tool for the structural prediction of TeO$_2$-based glasses.

II.2. On the concept of the cationic field strength

II.2.1. Background

While Goldschmidt considered only the ionic-size-ratio to predict properties such as the glass formation, Dietzel [20] suggested a more advanced concept, the field strength (FS) of ions, which enabled him to explain phenomena that could not be justified by Zachariasen-Warren's hypothesis alone.

Among all the other theories, the one suggested by Dietzel was the first to acknowledge the *ionic interaction* in terms of interionic forces and the resulting effects (glass *vs.* crystalline

compound formation, solid solution or immiscibility, *etc.*) during the solidification of the melt. He concluded that the electrostatic field q/a^2 (with q being the charge), due to the modifier cation (in SiO_2-based systems) at a distance a close to the sum of the ionic radii of the cation and anion (oxygen), correlates well with liquid immiscibility.

The energy of attraction U between a cation and an anion with ionic radii R_c and R_a and charge numbers Z_c and Z_a can be expressed as follows (with k being the Coulomb's constant and *e* the elementary charge):

$$U = k \, (Z_c \, Z_a \, e^2) \, / \, (R_c + R_a)$$

Using this quantity, the evolution of some properties as a function of the kind of cation within a particular group (*e.g.,* alkali or alkaline-earth cations) may be relatively well represented. This is not the case when comparing cations from different groups. For this reason, Dietzel suggested, on the basis of Coulomb's law, the FS concept to establish general dependencies across the periodic table by using the quantity of field strength FS:

$$FS = Z_c \, Z_a \, e^2 \, / \, (R_c + R_a)^2$$

When considering only one system in which the anion is always the same (*e.g.,* oxide systems) then in addition to the charge *e*, the charge number Z_a is also constant in the above equation, and therefore, the FS of the cation can be calculated using the following formula:

$$FS = Z_c \, / \, (R_c + R_a)^2$$

The FS magnitude increases with the charge number and decreases with the ionic radii. For instance, the P–O bond is extremely stable due to both the high charge number of P ($Z_c = 5$) and the small bond distance (~1.57 Å [135]). At the other extreme, the Cs–O bond is much weaker because of the small charge number of Cs ($Z_c = 1$) and the large bond distance (~3.1 Å to ~3.7 Å [136]). In the same spirit, cations with high strengths are referred to as strong cations; those with low strengths as weak cations [17]. The original strengths estimated by Dietzel can be found in [20,137].

It is important to recall that there is an inner connection between the cationic field strengths and the electronegativities. Since the latter do not always permit differentiating cations—especially transition metal cations of which the electronegativities are almost equivalent, the field strengths prove to be more useful as they show stronger differences between distinct cations but also for the same cation as a function of its coordination number.

The underlying idea is that, in a given system (*e.g.,* binary oxide), each cation seeks to 'shield' itself from other cations. The FS is the measure of the strength of this shielding which is achieved by surrounding the cation with anions. Dietzel correlated the field strength difference between two cations (labeled ΔFS) with the phase relations in a number of binary and ternary systems.

II.2.2. Application at equilibrium state

Based on the results of ΔFS obtained from several systems at equilibrium state, Dietzel postulated three empirical rules which were validated later by several works. For instance, Berkes and Roy [138] have established a correlation between ΔFS and the phase relations in 160 binary oxide systems with the aim of predicting features like the number of crystalline compounds in a given system, the presence and extent of solid solutions and phase separations, *etc*. The main results obtained from this study agree with Dietzel's rules and can be summarized as follows:

- The solid solution extent is at maximum when ΔFS $\approx$ 0 and rapidly decreases with increasing ΔFS (*e.g.,* TeO_2-TiO_2 system with the $TiTe_3O_8$ compound [79]);

- Phase separation, as a result of liquid immiscibility, tends to occur when $0.5 \leq \Delta$FS ≤ 1;

- The number of crystalline compounds increases with ΔFS (*e.g.,* ΔFS is equal to 0.867 in the TeO_2-$TlO_{0.5}$ [139] system where four compounds have been isolated).

II.2.3. Application at non-equilibrium state

The FS approach allows to predict the glass-forming ability of a given substance and the phase relations within a given system by predicting behaviors such as compound formation, solid solutions, immiscibility, *etc*. According to Dietzel, the network forming cations have high FS values of ~1.3 to 2, the network modifying cations show lower values (0.1 to 0.4), and the intermediates have in-between strengths comprised between ~0.5 and 1.2.

On the basis of these considerations, Dietzel formulated few basic rules with respect to the behavior of melts during the cooling process, and thus unlocking explanations for some phenomena that could not be interpreted on the basis of Zachariasen-Warren hypothesis. Those rules can be expressed as follows:

- For $\Delta FS \approx 0$, *i.e.,* both cations have very close strengths, the competition for the anions ends in segregation or dissociation into two separate pure phases. For instance, this is the case for binary SiO_2-B_2O_3 melts where $\Delta FS = 0.06$ [19].

- For $\Delta FS \geq 0.3$, there is a trend towards compound crystallization during the melt cooling. Moreover, at relatively higher ΔFS values, the tendency to form glasses becomes more likely along with an increase of the number of the crystallizing compounds.

- For $\Delta FS > 1.3$, glasses are readily obtained after melt cooling. For oxides, this is particularly the case in several binary melts containing one of the best-known glass formers, namely, B_2O_3, SiO_2 and P_2O_5 oxides.

II.3. Application to TeO$_2$-based materials

To the best of our knowledge, there is no previously reported work dedicated to the applicability of this concept in TeO_2-based systems. Nonetheless, a close concept on the strength of cations (weak *vs.* strong) has been commonly used in our laboratory for the last decade to classify cations as to their structural roles within the Te–O–Te bond network [94,140]: for a modifier oxide M_xO_y added to TeO_2, the $M^{(2y/x)+}$ cation can be characterized as:

- A **weak** cation, expressing a strong modifier oxide affecting the TeO_2-rich network. The Te^{4+} cation tends to attract the O^{2-} anions to the detriment of the weak cation, leading to a structural depolymerization (occurrence of quasi-isolated TeO_3 units). This case corresponds to an added cation with a FS weaker than that of Te^{4+}.

- A **strong** cation, expressing a weak modifier oxide affecting the TeO_2-rich network. The added cation does not easily 'give up' its O^{2-} anions to the Te^{4+} cation. In consequence, the structural units around Te^{4+} remain more or less distorted TeO_4 units (with only a weak depolymerization where only a small quantity of TeO_4 units being transformed into quasi-isolated TeO_3 units) or even tend to some peculiar environments such as TeO_5 or TeO_6 units (*cf.* Fig. I.4). This case corresponds to an added cation with a FS close to or superior to that of Te^{4+}, respectively.

In addition, the FS concept has been occasionally considered in some works on the structure of TeO_2-based glasses. For instance, McLaughlin *et al.* [47] supported their results obtained by

neutron and X-ray diffraction techniques with a discussion on the decreasing FS of Li^+, Na^+ and K^+ cations respectively. Our goal is to first check the practicability of this concept in binary TeO_2-based crystals with the ultimate aim of using it as a complementary tool in the structural investigation of TeO_2-based glasses.

We calculated, using the equation in *section II.2.1*, the FS of most of the cations participating along with Te^{4+} in the network of crystalline and amorphous binary TeO_2-based materials. The calculated FS of 61 cations are given in a periodic order in Fig. II.2 with a value of 0.990 for the FS of Te^{4+} cation. In general, our results agree with those originally reported by Dietzel in [137] (*cf.* tables in pp. 52–53 therein).

As an approach for appropriate data analysis and interpretation, we only consider charge numbers and coordination numbers (for ionic radii) that are the most common among amorphous and crystalline TeO_2-based materials. For instance, the O^{2-}, Te^{4+} and Ti^{4+} ions were considered to be two-fold, four-fold and six-fold coordinated respectively and having the following ionic radii: 1.35 Å, 0.66 Å and 0.605 Å according to Shannon [141]. We intentionally considered, for the Te^{4+} cation, the ionic radius associated with the four-fold coordination which is widely regarded as the basic structural unit in these materials.
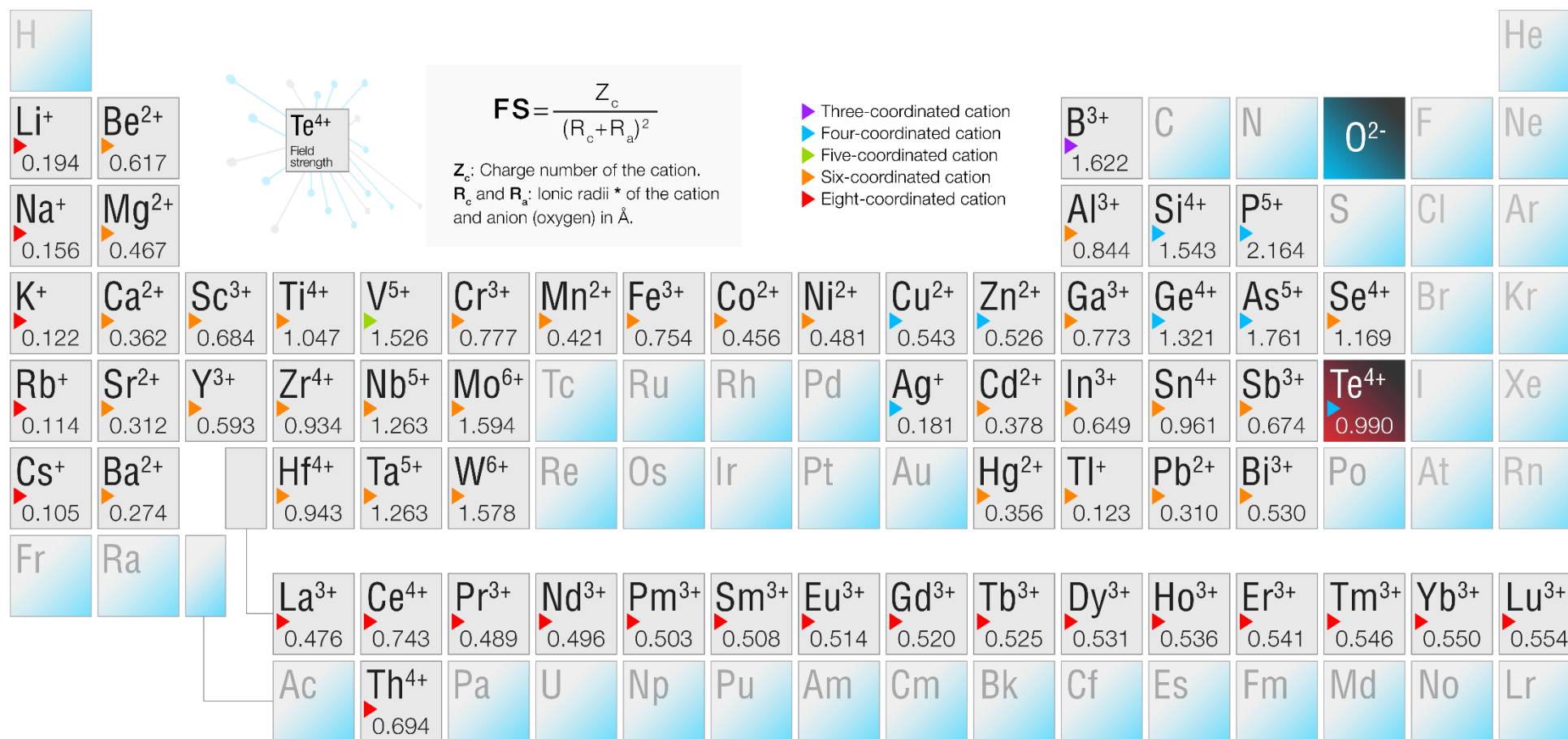
Fig. II.2. Field strengths of most of the cations known to form binary oxides when mixed with TeO₂. The chosen cationic radii for the calculation of strengths correspond to those associated with the most common coordination numbers of those cations as encountered in both amorphous and crystalline TeO₂-based materials.

II.3.1. Application to binary TeO₂-based crystals

To verify whether the FS theory applies to TeO₂-based compounds at the equilibrium conditions, we checked the *rule* on the correlation between the number of crystalline compounds and ΔFS (*cf. section II.2.2*). To do so, we conducted a systematic search using the inorganic crystal structure database ICSD (version 1.9.9 released in May 2017) to identify all the crystal structures reported so far in binary TeO₂-M$_x$O$_y$ systems. The gathered results are given below in Fig. II.3. ΔFS are used to evaluate the relative strength of Te^{4+} cation with respect to M$^{(2y/x)+}$ cations in each M$_x$O$_y$ oxide; they were calculated using individual cationic FS as follows: ΔFS = FS(Te^{4+}) − FS(M$^{(2y/x)+}$).
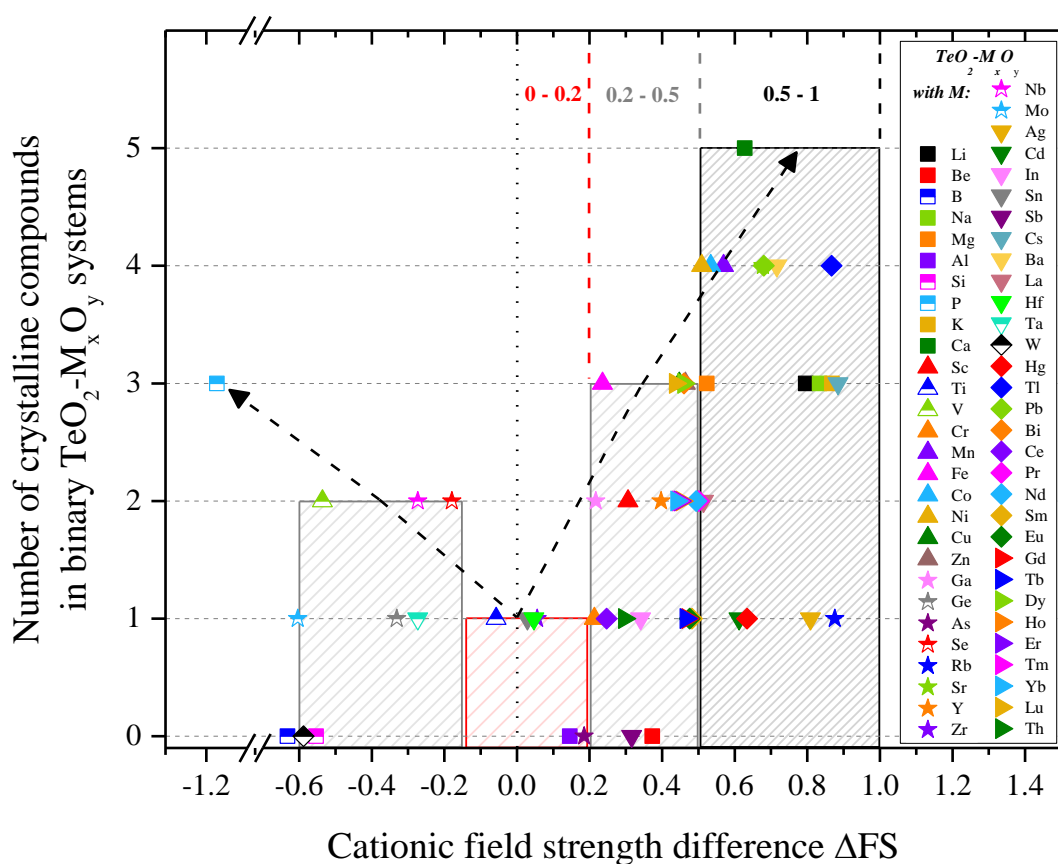
Fig. II.3. Correlation between the number of crystalline compounds and ΔFS in 111 binary TeO₂-based crystal compounds.

In agreement with the previously outlined findings of Berkes and Roy [138], we found that the number of crystalline compounds in 111 binary TeO₂-M$_x$O$_y$ systems increases with ΔFS (*cf.*

Fig. II.3). For positive ΔFS values, *i.e.,* $M^{(2y/x)+}$ cations having weaker strengths than that of Te^{4+}, the following three ranges can be distinguished:

- $0 \leq \Delta FS < 0.2$ where a maximum of only one crystal compound is reported to exist in each TeO_2-M_xO_y system;

- $0.2 \leq \Delta FS < 0.5$ where a maximum of three crystal compounds were identified in each TeO_2-M_xO_y system;

- $0.5 \leq \Delta FS \leq 1$ with a maximum of five compounds.

As shown in Fig. II.3, there are only 4 cations (Ti^{4+}, Zr^{4+}, Hf^{4+} and Sn^{4+}) with FS close to that of Te^{4+} cation (*i.e.,* $\Delta FS \approx 0$). In this range of ΔFS, the only 4 identified crystals belong to the family of isomorphous MTe_3O_8 (M = Ti, Zr, Hf and Sn) structures [79]. From a chemical viewpoint, these structures can be regarded as solid solutions of MO_2 in TeO_2 with a ratio of 1:3 respectively [94], and thus agreeing with the first rule of the FS theory (*section II.2.2*).

Finally, the rule on the tendency of melts to demix or phase separate at higher ΔFS ($0.5 \leq \Delta FS \leq 1$) also seems to be controlling the TeO_2-based melts containing weak modifier oxides such as Tl_2O where phase separation has been detected [58,139].

Furthermore, we have attempted to identify if there is any general correlation between the Te–O coordination spheres in binary TeO_2-based crystals and ΔFS. For this matter, we extracted the sets of Te–O bond lengths for each binary crystal and then classified them in two simple categories: relatively short and more covalent Te–O bonds of less than 1.94 Å, and longer ones exceeding 1.94 Å with less covalent character. For each crystal, the average short and long Te–O bonds are plotted against ΔFS in Fig. II.4. Depending on the extent of ΔFS, at least two tendencies can be distinguished; these are the following:

- For negative and close-to-zero ΔFS values ($\Delta FS \leq 0.2$), the two categories of Te–O bond lengths show a rather steady evolution with a possible increase of the short (< 1.94 Å) bond lengths as ΔFS becomes more negative. This trend is reasonable since cations of strengths higher than Te^{4+} (*e.g.,* P^{5+}, Mo^{6+} and Nb^{5+}) are expected to win over the competition on attracting O^{2-} anions (against Te^{4+} cations) which results in the extension of the average Te–O bond.

- For $0.4 \leq \Delta FS \leq 0.9$, a general decrease of short Te–O bond distances is observed with increasing ΔFS values. This downward trend is accompanied with an increase of longer Te–O bond distances, and thus depicting the effect of weak cations (*e.g.,* Li^+, K^+ and Tl^+) in reducing the coordination number of Te^{4+} cation by readily giving away O^{2-} anions due to their weak strengths.
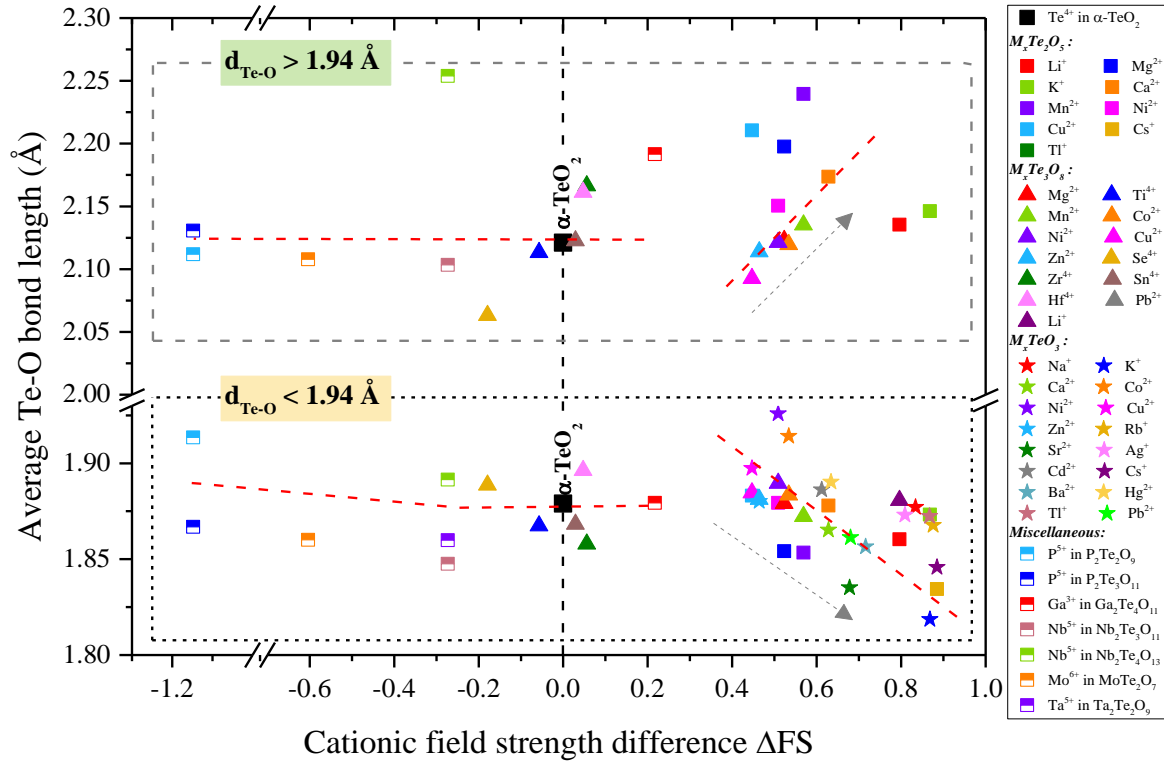
Fig. II.4. Evolution of the average Te–O bond length as a function of ΔFS in various binary TeO_2-based crystals belonging to families like $M_xTe_2O_5$, $M_xTe_3O_8$ and M_xTeO_3 compounds and others.

To gain more insight on the previously highlighted correlation, we focused our attention on two families of binary TeO_2-based crystals, namely $M_xTe_3O_8$ and M_xTeO_3. Regarding the former, among the 23 crystallographically distinct Te atoms gathered from the crystal data of this family, 14 exist as TeO_4 disphenoids, 5 as TeO_{3+1}, 3 as TeO_3 and only one as a TeO_5 unit. For each of the 14 disphenoids, we calculated the two average $Te-_{eq}O$ and $Te-_{ax}O$ bond lengths. Their evolution as a function of ΔFS is presented in Fig. II.5(a). For ΔFS values higher than 0.4, the average $Te-_{eq}O$ bonds become progressively shorter with increasing ΔFS as we go from $Cu_2Te_3O_8$ to $Pb_2Te_3O_8$. In parallel to this, the average $Te-_{ax}O$ bond lengths increase with ΔFS.

The observed dispersion of Te–O bond lengths in the vicinity of ΔFS = 0 can be explained by the fundamental differences among Ti, Sn, Hf and Zr atoms—especially their electronegativities, *viz.* 1.54, 1.96, 1.3 and 1.33 respectively (Pauling scale). With such a high electronegativity, Sn is the closest to Te (2.1) which might explain the very close Te–O bond lengths between α-TeO$_2$ and SnTe$_3$O$_8$ structures. The evolution of the average Te–O (d$_{Te-O}$ < 1.94 Å) bond lengths from TeO$_3$ units in M$_x$TeO$_3$ crystals (Fig. II.5(b)) shows the same downward trend with increasing ΔFS.
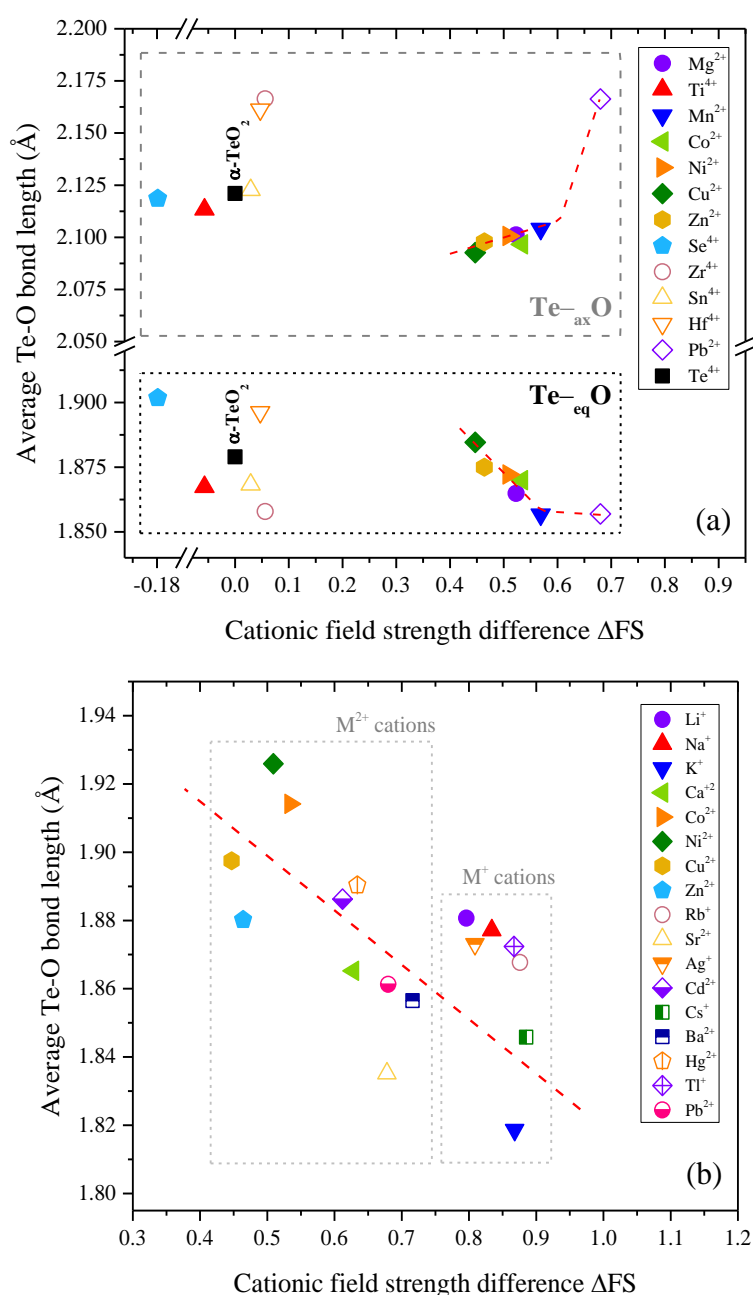
Fig. II.5. Evolution of the average Te–O bond length as a function of ΔFS in (a) M$_x$Te$_3$O$_8$ and (b) M$_x$TeO$_3$ crystals.

Finally, it appears that the cationic FS theory applies appreciably well to TeO$_2$-based compounds at equilibrium conditions. This is quite promising to further investigate the possible correlations between this concept and fundamental properties of TeO$_2$-based glasses such as their glass-forming ability and structure.

II.3.2. Application to binary TeO$_2$-based glasses

It is widely accepted that TeO$_2$ is only a conditional glass former requiring unconventional processing (high quenching rates and very limited batch weights) in order to solidify into small fragments of pure TeO$_2$ glass [46]. This difficulty in glass preparation is portrayed in Fig. II.2 by the relatively low FS of Te^{4+} cation (0.990) compared to those of good glass-forming cations such as B^{3+} (1.622), Si^{4+} (1.543) and P^{5+} (2.164). Therefore, Te^{4+} is considered as a member of the category of intermediate cations between the glass formers and the modifiers (*cf. section I.2.4*).

The good glass modifying cations are the ones having the lowest FS such as Cs$^+$ (0.105), Rb$^+$ (0.114) and Tl$^+$ (0.123) guaranteeing a ΔFS difference (with Te^{4+}) of at least 0.83 which, according to the theory (*cf. section II.2.3*), in the form of oxides are expected to increase the glass-forming ability when they are introduced to TeO$_2$-based melts.

In the following, we present and discuss our results regarding the evolution of the glass-forming ability in binary TeO$_2$-based glasses as a function of ΔFS. The glass-forming domains, in terms of the extent of molar content of the second oxide M$_x$O$_y$, are depicted in Fig. II.6 for 31 binary TeO$_2$-based systems [37,41,54,142–147]. Some of the preparation conditions (melting time and/or temperature) are mentioned whenever these pieces of information are found in the references. However, we do not specify the used quenching technique since this information was unfortunately either poorly described or unstated by most of the authors.

The extent of M$_x$O$_y$ content from one binary system to another is clearly dissimilar illustrating the variable glass-forming ability of binary TeO$_2$-based melts. While adding M$_x$O$_y$ (M = Sn, Zr, Cr and Bi) oxides yields no glass at all, the incorporation of some of the weakest cations (in form of oxides) such as Na$^+$ and Tl$^+$ significantly extends the glass-forming domain with extents of M$_x$O$_y$ content ranging from 15 to over 50 mol.% as can be seen in the range of high ΔFS values (Fig. II.6). Intermediate-to-relatively-large glass-forming domains with M$_x$O$_y$ extents ranging between 5 and 30 mol.% are observed in the range of 0.1-0.7 in ΔFS.

Fig. II.6. Representation of the glass-forming domains of 31 binary TeO_2-based systems as a function of the ΔFS difference (between Te^{4+} and each $M^{(2y/x)+}$ cation). The inset shows the evolution of the glass-forming ability in three sections (I, II and III) of ΔFS, with N representing the sum of the number of glass samples (at intervals of 5 mol.%) divided by the number of binary systems in each section. These data were curated from [37,41,54,142–147].

Based on these results, it is still difficult to argue with certainty on the existence of a correlation between the glass-forming ability of TeO_2-based melts and ΔFS. This is mainly due to the recurrent fluctuations among several glass-forming domains, *e.g.,* in the ΔFS range of 0.45-0.75. Nonetheless, it seems that there is a general trend towards larger domains at higher ΔFS values as shown by the evolution of the index N in the inset of Fig. II.6. In such a case, this would suggest that the FS theory applies to TeO_2-based glasses. In other words, the structural evolution of TeO_2-based melts upon cooling is governed by the contrast between the present cations in terms of their FS.

Let us now discuss the expected structural evolutions in binary TeO_2-based glasses based on the FS theory. We can organize these predictions in the three following distinct categories:

- *Network modification by weak cations ($\Delta FS > 0.75$)*

The cations having the lowest FS are the ones expected to engender the largest cleavage of the Te–O–Te bond network by transforming TeO_4 units into TeO_3 ones with non-bridging oxygen atoms. Typical modifying cations such as K^+, Tl^+, Rb^+ and Cs^+ have the lowest FS with an average of ~0.116. It is expected that these cations cause stronger impacts on the network of Te–O–Te when compared to others like Li^+ and Na^+ of which the FS (0.194 and 0.156) are 67% and 34% larger respectively. In this context, using neutron and X-ray diffraction techniques, McLaughlin *et al.* [47] argued that, compared to Li^+ and Na^+ cations, adding K^+ results in a stronger disruption of the network of binary TeO_2-based glasses.

- *Immiscibility in binary TeO_2-based glasses ($\Delta FS \approx 0$)*

According to the FS theory, segregation or phase separation tend to occur when ΔFS is close to zero. As previously outlined, this is the case in binary SiO_2-B_2O_3 glasses [19], but also in the ternary SiO_2-B_2O_3-MO_x ($MO_x = MoO_3$ and WO_3) systems [148,149]. It is important to stress that in these systems, all possible ΔFS values are close to zero, namely ranging between 0.035 and 0.079.

Based on our results (Fig. II.2), the cations with the closest FS to that of Te^{4+} (0.990) are all tetravalent M^{4+} and are the following: Sn^{4+} (0.961), Hf^{4+} (0.943), Zr^{4+} (0.934) and Ti^{4+} (1.047) where the maximum absolute[1] $|\Delta FS|$ ($|FS(Te^{4+}) - FS(M^{4+})|$) is less than 0.057. This means that there is potential for phase separation to take place in binary TeO_2-MO_2 (M = Sn, Hf, Zr and Ti) systems. It is worthwhile to recall here that the FS theory predicts well their equilibrium

---

[1] To include Ti^{4+} cation as it has a stronger FS than Te^{4+}.

binary phase diagrams, where only one phase (per each) is detected, namely isomorphous MTe_3O_8 that can be regarded as a solid solution. Therefore, according to the FS theory, a phase separation is likely to take place in these glasses since the coordination requirements of both Te^{4+} and M^{4+} cations can be much better satisfied if two phases existed in the glass network: TeO_2- and MO_2-rich phases.

- *Effect of transition-metal cations with higher strengths than Te^{4+} ($\Delta FS < 0$)*

The cations falling into this category are the following: Nb^{5+} (FS = 1.263), Ta^{5+} (1.263), V^{5+} (1.526), W^{6+} (1.578) and Mo^{6+} (1.594). The higher their FS, the larger is the $|\Delta FS|$ difference between each of them and Te^{4+} (0.990) cation: it evolves from ~0.3 (in the presence of pentavalent Nb^{5+} or Ta^{5+}) to ~0.6 (for hexavalent W^{6+} or Mo^{6+}). Based on the theory, larger glass-forming domains can be available for large $|\Delta FS|$ differences. This is in agreement with the reported literature on the glass-forming ability of TeO_2-based glasses containing such transition-metal oxides (TMO): glasses are obtained after substituting TeO_2 (5 to 25 mol.%) with $NbO_{2.5}$ [114], 5 to 15 mol.% with $TaO_{2.5}$ [150], 5 to 30 mol.% with WO_3 [103], and 5 to 40 mol.% with MoO_3 [151].

Several structural studies on binary and ternary TMO-containing TeO_2-based glasses unanimously agreed that short, and thus strong, M–O bonds (M = W and Mo) exist in the glass network along with TeO_4 and TeO_{3+1} units [103,151,152]. The vibrational signature of these bonds is manifested in the high-wavenumber region from the Raman spectra of TeO_2-MO_3 glasses (MO_3 = WO_3 and MoO_3) with a sharp peak centered at around 925 cm^{-1} that slightly shifts to higher wavenumbers with increasing MO_3 content as shown in Fig. II.7 (*cf.* red and blue vertical lines). This shift might indicate a decrease of the average M–O bond length.
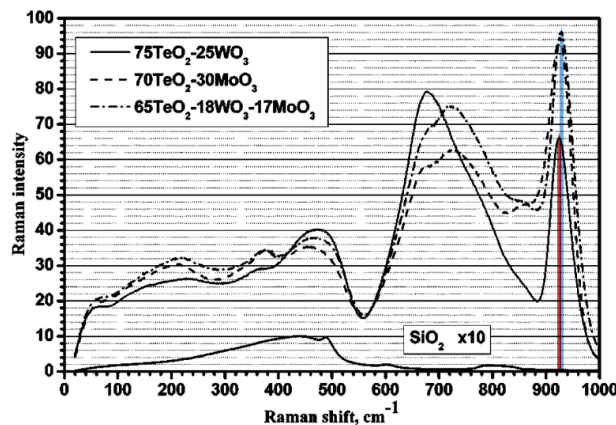
Fig. II.7. Reduced VV-polarized Raman spectra of TeO_2-based glasses containing WO_3 and MoO_3. Reproduced from [152].

On the basis of the FS theory, one would expect relatively few changes in the overall glass structure upon adding these transition-metal cations since, like Te^{4+}, they are also considered as intermediates from the glass formation viewpoint. However, having higher FS than that of Te^{4+} is likely to result in the association of the MO_x polyhedra to form their own domains which could extend from medium- to long-range structure.

Finally, it is worthwhile to make reference to another strong cation, namely Te^{6+} cation of which the FS (1.645)[1] is 66% stronger than Te^{4+} (0.990). Both of these two cations coexist in crystal structures like Te_4O_9 [153], Te_2O_5 [154], $BaTe_2O_6$ [49,155] or $Cs_2Te_4O_{12}$ [50,156]. These structures are very interesting from the crystal chemistry viewpoint as they host unusual environments of Te^{4+} cations (*cf. 'other units'* in Fig. I.4). To the best of our knowledge, TeO_3-containing TeO_2-based glasses (containing both Te^{6+} and Te^{4+} cations) have never been experimentally obtained or reported in the literature so far. According to the FS theory, it is expected that the structure of such glasses would feature $Te^{VI}O_3$ forming networks where Te^{4+} cations would rather play the role of modifiers, and thus surround themselves with a larger number of O^{2-} anions such as 5 or more (as opposed to the usual 4 in TeO_4, 3+1 in TeO_{3+1} and 3 in TeO_3 units).

II.4. Conclusion

In this chapter, we introduced the theoretical background of the field strength concept and attempted to apply this theory to the crystalline and amorphous TeO_2-based materials. At both equilibrium and non-equilibrium states, the predicted behaviors (upon cooling) of a large number of binary systems based on the cationic field strength difference ΔFS are found to be in very good agreement with the experimental works reported in the literature.

One of the most significant results obtained by this theoretical approach is the predicted phase separation in the glass structures of binary TeO_2-MO_2 (M = Sn, Hf, Zr and Ti) systems into two pure phases: TeO_2-rich and MO_2-rich networks. This idea will be discussed in *Chapter IV* on the study of binary TeO_2-TiO_2 and ternary TeO_2-TiO_2-WO_3 glasses.

In the next chapter, we summarize the experimental approaches to the study of pure TeO_2, binary TeO_2-TiO_2 and ternary TeO_2-TiO_2-WO_3 and TeO_2-$NbO_{2.5}$-WO_3 glasses from the sample preparation to the characterization and analysis processes.

---

[1] While considering Te^{6+} to be six-fold coordinated with an ionic radius of 0.56 Å [141].

Chapter III. Glass preparation, characterization methods and structural data analysis

III.1. Introduction

In this chapter, we review the experimental methods used to prepare and characterize the properties of the different glass samples investigated in this work which include pure TeO_2, binary TeO_2-TiO_2 and ternary TeO_2-TiO_2-WO_3 and TeO_2-$NbO_{2.5}$-WO_3 glasses. The two preparation techniques used to obtain either glass pellets or fragments from these systems are the conventional melting-casting (MC) and melting-fast-quenching (MFQ) respectively. We also describe the different experimental techniques used to characterize the glass samples.

- Density measured by helium pycnometry and characteristic thermal properties (*i.e.*, the glass transition and crystallization temperatures leading to the thermal stability) using differential scanning calorimetry.

- Structural properties including the glass-forming domain determination using X-ray powder diffraction, short- to medium-range structure probing by Raman spectroscopy, numerical analysis of the Raman spectra by a full-scale spectral decomposition, and finally the crystallization behavior by high-temperature X-ray diffraction.

- Linear and nonlinear optical properties measured from the glass pellets to determine specific characteristics such as the optical transmission window, linear refractive index, third-order nonlinear susceptibility $\chi^{(3)}$, *etc.*

III.2. Glass preparation

The characteristics of raw commercial powders used to prepare the investigated materials are gathered in Table III.1. Before using these substances, we first checked their chemical purities by means of X-ray powder diffraction.

Composition	Supplier	Purity (%)	Melting temperature (°C)
α-TeO_2	Alfa Aesar	99.99	733
TiO_2	Sigma-Aldrich	99+	1843
WO_3	Alfa Aesar	99.8	1473
Nb_2O_5	Alfa Aesar	99.999	1520

Table III.1. Characteristics of the used raw commercial powders.

The melting-fast-quenching (MFQ) technique can be useful to explore the glass-forming domains owing to the higher cooling rate experienced by the glass melts and thus allowing to check the "ultimate" extent of these domains. Moreover, batch mixtures of only few hundreds of milligrams can be processed as opposed to the conventional melting-casting (MC) technique which is based on casting of more important masses.

III.2.1. Pure TeO$_2$ glass

As opposed to the good glass-formers (*e.g.*, SiO$_2$ and P$_2$O$_5$), TeO$_2$ is only a conditional glass former that can only be prepared from small batch weights [46]. Moreover, a fast-quenching rate is required to obtain a totally amorphous and homogeneous glass from pure TeO$_2$ melt.

Pure TeO$_2$ glass samples were prepared via the MFQ technique and using α-TeO$_2$ powder (*cf.* Table III.1). A small pinch (60 mg) of α-TeO$_2$ is mixed using a mortar and pestle, then melted in brand-new Pt crucibles at 850 °C for 1 h in air atmosphere (using Nabertherm N7 furnace). To obtain homogeneous and totally amorphous TeO$_2$ glass, the crucible was stirred three times (once every 15 minutes) inside the furnace chamber and a severe quenching technique was performed using an integral ice bath (also containing NaCl and ethanol) of which the temperature is as low as -11 °C. This method was originally suggested by Kim *et al.* in [157]. A transparent pale-yellow glass fragment is obtained after dipping the bottom of crucible onto a pre-made hollow at the ice bath's surface. The thermal characteristics of prepared TeO$_2$ glass sample were measured by means of differential scanning calorimetry (DSC, *cf. section III.3.2*). The curve (Fig. III.1) was recorded from a small glass fragment (one from the batch shown in the inset). It is found that pure TeO$_2$ glass exhibits a relatively moderate thermal stability of ~64 °C.
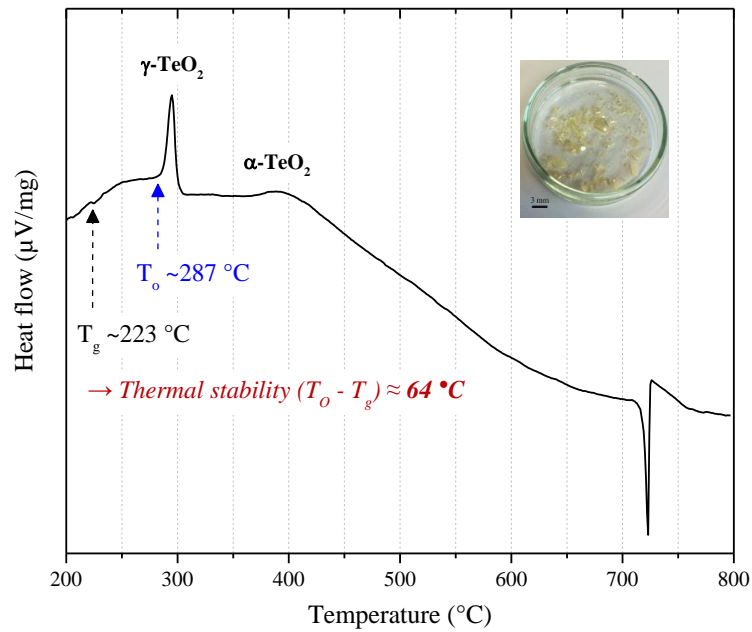
Fig. III.1. DSC curve measured from pure TeO$_2$ glass fragment. The inset shows the entire set of prepared TeO$_2$ samples.

III.2.2. Binary TeO$_2$-TiO$_2$ glasses

Binary (100-x)TeO$_2$-xTiO$_2$ (labeled TTx) glasses were systematically prepared from batch mixtures of 400 mg under the same conditions described above for pure TeO$_2$ glass samples using α-TeO$_2$ and anatase TiO$_2$ (*cf.* Table III.1).

Using the MFQ method, the glass-forming domain of binary TTx glasses has been extended to x = 15 mol.% whereas using the conventional melting-casting (MC) method resulted in an extensive crystallization of TiTe$_3$O$_8$ abolishing thus the glass-forming ability.

III.2.3. Ternary TeO$_2$-TiO$_2$-WO$_3$ and TeO$_2$-NbO$_{2.5}$-WO$_3$ glasses

New (100-x-y)TeO$_2$-xTiO$_2$-yWO$_3$ (labeled TTxWy) and (100-x-y)TeO$_2$-xNbO$_{2.5}$-yWO$_3$ (labeled TNxWy) glasses (samples of ~0.4 g and pellets of ~2 g) were prepared using α-TeO$_2$, anatase TiO$_2$, WO$_3$ and Nb$_2$O$_5$ powders (*cf.* Table III.1). In appropriate proportions, the raw powders (dried separately by preheating at 90 °C) have been ground for 40 minutes using agate mortar and pestle, put in Pt crucibles and finally melted at 850 °C for 1 h in air atmosphere.

In a first approach, the samples weighing ~0.4 g have been synthesized via the MFQ technique in order to determine the glass-forming domain. The percent change in mass was checked

before and after melting: a weight loss that is mainly due to the vaporization of TeO_2 reached a maximum of 6.71 wt.% in TeO_2-rich compositions (Table III.2 and Table III.3).

Sample	Mass (g)		Weight loss (%)
	Before melting	After melting	
TT5W5	0.3716	0.3493	6.00
TT5W10	0.3777	0.3584	5.11
TT5W15	0.3865	0.3700	4.27
TT5W20	0.3785	0.3653	3.49
TT5W25	0.3937	0.3821	2.95
TT10W5	0.3860	0.3695	4.27
TT10W10	0.3837	0.3668	4.40
TT10W15	0.3836	0.3649	4.87
TT10W20	0.3839	0.3741	2.55
TT10W25	0.3846	0.3765	2.11
TT15W5	0.3772	0.3601	4.53
TT15W10	0.3719	0.3612	2.88
TT15W15	0.3774	0.3667	2.84
TT15W20	0.3824	0.3707	3.06
TT15W25	0.3657	0.3509	4.05

Table III.2. Recorded compositional-dependence weight losses in TTxWy glasses.

Sample	Mass (g)		Weight loss (%)
	Before melting	After melting	
TN5W5	0.3879	0.3641	6.14
TN5W10	0.3858	0.3599	6.71
TN5W15	0.3849	0.3674	4.55
TN5W20	0.3820	0.3698	3.19
TN5W25	0.3860	0.3682	4.61
TN10W5	0.3877	0.3683	5.00
TN10W10	0.3887	0.3681	5.30
TN10W15	0.3871	0.3724	3.80
TN10W20	0.3886	0.3737	3.83
TN10W25	0.3871	0.3661	5.42
TN15W5	0.3918	0.3712	5.26
TN15W10	0.3894	0.3748	3.75
TN15W15	0.3918	0.3757	4.11
TN15W20	0.3886	0.3762	3.19
TN20W5	0.3925	0.3777	3.77
TN20W10	0.3906	0.3793	2.89
TN25W5	0.3841	0.3691	3.91

Table III.3. Recorded compositional-dependence weight losses in TNxWy glasses.

The glass pellets were prepared from batches weighing ~2 g. The particle-size distribution of the batch mixture has been measured using Horiba Partica LA-950V2 analyzer, indicating a volume mean diameter of ~3 µm (cf. example for a TTxWy sample in Fig. III.2).
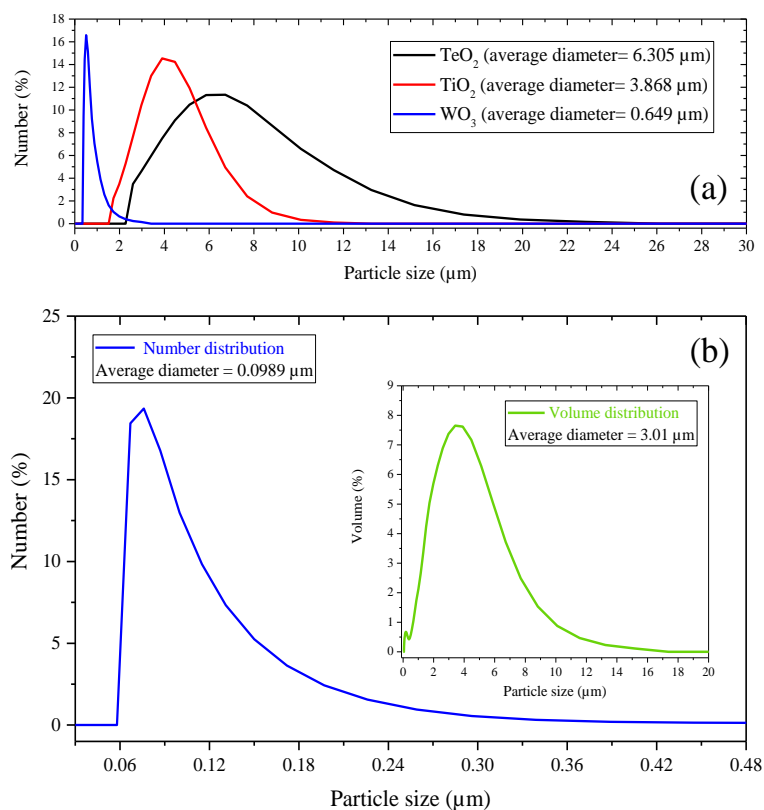
Fig. III.2. (a) Particle size distribution of raw oxide powders before grinding, and (b) example of TT15W15 powder mixture after 40 minutes of grinding and before melting.

The batches were stirred three times during melting (once every 15 minutes spent inside the furnace chamber) and, using the MC technique, quenched into a brass ring put over a preheated brass block (at 150 °C). After cooling down from 150 °C, glass pellets were systematically annealed at 15 °C below the glass transition temperature (T_g) for 12 h at a rate of 2 °C/min (during both heating and cooling) using Ceradel Socor furnace. This step is crucial in order to release the mechanical stresses resulting from thermal quenching. For the sake of consistency, all heat treatments (melting and annealing) have been performed using the same two furnaces.

Finally, the prepared TTxWy (15 samples) and TNxWy (17 samples) glass pellets with an average diameter of 8 mm were polished by PO.DE.O (French precision optics manufacturer). Surface polishing is essential to acquire the desired optical quality at both facets for the linear

and nonlinear optical measurements. The thickness of the double-side polished pellets is comprised within the range of 1.44–1.47 mm.

III.3. Characterization methods

III.3.1. Density and molar volume by helium pycnometry

Gas pycnometry is a very accurate method for measuring the density, or more accurately the volume of solids. The volume measured is the amount of three-dimensional space which is inaccessible to the used gas (*e.g.,* helium), and thus density can be calculated as the ratio of mass to volume. Densities of glass powder samples of 150 ± 20 mg were measured by helium pycnometry using Accupyc II 1340 pycnometer from Micromeritics. A set of 10 measurements were performed for each sample producing an average error less than 0.3%. All measurements were carried out at room temperature (between 20 and 30 °C). By definition, the molar volume is the volume occupied by one mole of a substance. Therefore, it can be calculated from the molar mass and the volume of that substance which can in turn be obtained from the density.

III.3.2. Thermal properties by differential scanning calorimetry

The characteristic temperatures of glasses, namely the glass transition (T_g) and onset crystallization (T_O) temperatures were measured with the aim to estimate the thermal range of stability ΔT which is defined as: $\Delta T = T_O - T_g$. The higher the thermal stability, the more stable the glass is with respect to devitrification.

We measured these thermal characteristics by heat flux differential scanning calorimetry (DSC) using NETZSCH STA 449 F3 Jupiter. About 25 ± 5 mg of glass fragments were put into Pt pans, and the measurements were performed under N_2 atmosphere between room temperature and 720 °C at a heating rate of 10 °C/min.

The T_g temperature is considered as the inflection point of the step change of the calorimetric signal associated with this transition; and the T_O temperature as the intersection of the extrapolated baseline and the extrapolation of the linear part of the first exothermic peak (*cf.* Fig. III.3). Both T_g and T_O temperatures were extracted using the equipment's data analysis software.
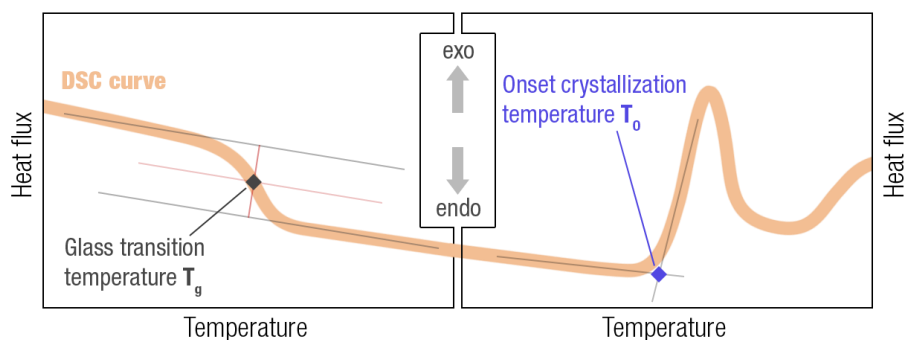
Fig. III.3. Illustration showing how the glass transition and onset crystallization temperatures are determined from DSC curves in this work.

III.3.3. Measurement of structural properties

III.3.3.1. Room-temperature X-ray diffraction

By means of X-ray powder diffraction (XRD), we performed both the amorphous state analysis (for the glass-forming domain determination) and crystal phase identification. The theoretical background of this technique can be found elsewhere (*e.g.,* in [158]). It is worthwhile though to recall its principle based on irradiating a sample with a monochromatic X-ray beam and measuring the scattered intensities on a large (2θ) angular domain.

The XRD patterns were recorded from powder samples using Bruker D8 Advance diffractometer with Bragg-Brentano geometry (copper $K_{\alpha 1}$ wavelength of 1.5406 Å, angular 2θ range of 20-50° with a step of 0.02° and 1s per step).

III.3.3.2. High-temperature X-ray diffraction

The same setup described above (Bruker D8 Advance) equipped with the furnace HTK 1200N from Anton Paar was used to record the XRD patterns upon heating. This furnace allows performing measurements at high temperatures up to 1200 °C. The XRD patterns were recorded at 30 °C and then from 430 °C to 580 °C with steps of 30 °C and a heating rate of 10 °C/min. The final XRD pattern was eventually recorded at 30 °C after cooling.

III.3.3.3. Raman spectroscopy

III.3.3.3.1. Principle of Raman scattering

When light travels through any type of medium except the vacuum, there is always a fraction of the energy of incident light beam that gives rise to scattered light propagating along all other directions through the medium. This scattered light is the result of an induced dipole moment in the molecules by the oscillating electric field of the incident light.

The Raman scattering or Raman effect is one type of light scattering among others, like Tyndall, Rayleigh, Mie and Brillouin effects. It corresponds to the inelastic scattering of a photon by molecules which are excited to higher vibrational or rotational energy levels. The theory behind this effect was originally predicted by A. Smekal in 1923 [159]. Only five years later, C. V. Raman and his student K. S. Krishnan [160] discovered and showed that if light of a specific frequency is travelling through any substance in gaseous, liquid or solid state, then the scattered light not only contains radiations of the original frequency (elastic Rayleigh effect) but also of some other frequencies which are generally lower but occasionally higher than the frequency of the incident light. By the late 1930's, Raman scattering had already become one of the leading methods of nondestructive chemical analysis for both organic and inorganic materials as each Raman spectrum serves as a fingerprint to be used for chemical analysis.

The inelastic Raman scattering effect can be either explained by the classical theory where the light-matter interaction is viewed as a perturbation of the molecule's electric field, or the quantum mechanical theory based on the consideration of energy level diagrams. According to the latter, an incident photon excites a vibrational mode towards a higher virtual energy state. This state then decays into a real vibrational state. The energy difference between the initial and final state represents a change of energy, or Raman shift, of the scattered photon (*cf.* Fig. III.4). If the final state is at a higher energy compared to the initial state, then the scattered photon will have a lower frequency than the incident photon; this is called the Stokes shift. Otherwise, the scattered photon will have gained energy and therefore an increase in frequency will be recorded; and this shift to higher frequency is called the Anti-Stokes shift. Since the intensity of the Stokes shifted light is much higher than the Anti-Stokes shifted light, most commercial Raman spectrophotometers are configured to detect the Stokes shifted photons.
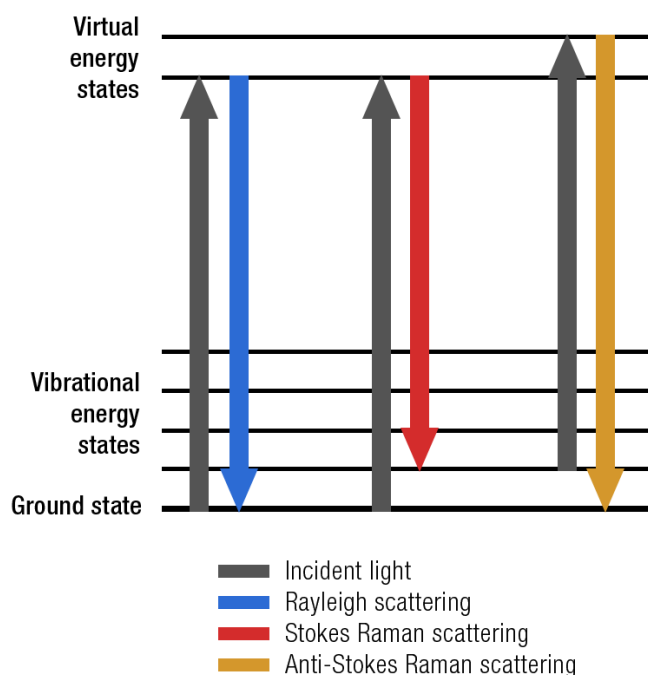
Fig. III.4. Energy-level diagram showing the energy states involved in the Raman scattering effect.

It is quite common to plot the Raman intensity with respect to the wavenumber $\tilde{v}$ (cm^{-1}) and not the frequency v (s^{-1}). Accordingly, we adopted this convention to be consistent with the literature. In fact, the wavenumber and frequency are proportional to each other, and are both proportional to energy E (eV) via the following expression: $v = E/h = 100\ \tilde{v}\ c$, where h is the Planck's constant.

The vibrational frequency v is related to the force constant k and the reduced mass μ of the atoms involved in the motion by: $v = (1/2\pi)\ (k/\mu)^{1/2}$ [161]. The force constant can be considered as the strength of the spring in the ball-and-spring model for molecular vibration. This bond strength is physically affected by a subtle balance of nuclear and electron repulsions and electron-nuclear attractions. None of these is affected by nuclear mass and, therefore, the force constant k is unaffected by isotopic substitution. From the previous expression, it can be noted that larger force constants k are associated with higher wavenumber interatomic vibrations.

Let us now briefly recall some basics of the classical approach to the theory of Raman scattering (more details can be found in [162]). According to this approach, the Raman effect is manifested in a polarizability change of the molecule as a result of its interaction with the incident light. This interaction leads to the *inelastic light scattering*, *i.e.,* exchange of energy between the light and the vibrations of the molecule. When a molecule is in an electric field E, the electron cloud and nuclei become polarized resulting in an induced dipole moment P of which the size is

controlled by the molecule's polarizability α (having a unit of volume): $P = \alpha\, E$, with P and E being vector quantities. The polarizability α determines the degree of scattering from the sample when subjected to the incident radiation. It is a measure of the degree to which the electrons in the molecule can be displaced relative to the nuclei. In general, the polarizability of a molecule is an anisotropic property, *i.e.,* at equal distances from the center of the molecule, it may have different magnitudes when measured from different directions.

The application of an electric field in one direction induces a dipole moment in the other direction, thus the polarizability α is a tensor (matrix) and can be written as:

$$\alpha = \begin{pmatrix} \alpha_{xx} & \alpha_{yx} & \alpha_{zx} \\ \alpha_{xy} & \alpha_{yy} & \alpha_{zy} \\ \alpha_{xz} & \alpha_{yz} & \alpha_{zz} \end{pmatrix} \qquad \text{And,} \begin{pmatrix} P_x \\ P_y \\ P_z \end{pmatrix} = \begin{pmatrix} \alpha_{xx} & \alpha_{yx} & \alpha_{zx} \\ \alpha_{xy} & \alpha_{yy} & \alpha_{zy} \\ \alpha_{xz} & \alpha_{yz} & \alpha_{zz} \end{pmatrix} \begin{pmatrix} E_x \\ E_y \\ E_z \end{pmatrix}$$

For instance, α_{xy} is the dipole moment along the x-direction due to a unit electric field polarized along the y-direction. The tensor for a totally symmetric vibrational mode can be expressed as follows:

$$\alpha = \begin{pmatrix} \alpha_{xx} & 0 & 0 \\ 0 & \alpha_{yy} & 0 \\ 0 & 0 & \alpha_{zz} \end{pmatrix}$$

III.3.3.3.2. Measurement conditions of Raman spectra

The Raman spectra of the obtained glass samples were recorded at 532 nm (laser's wavelength) using inVia Reflex Renishaw spectrophotometer, and at 514 nm using T64000 Horiba Jobin–Yvon spectrophotometer operating in triple subtractive configuration (1800 grooves/mm) associated to a liquid nitrogen-cooled CCD detector. They were recorded using x50LWD lens objectives with a spectral resolution of 2.5 cm^{-1} along the 15–1100 cm^{-1} wavenumber range while focusing the laser beam (exposure time of 10 seconds) at a depth of approximately 2 µm from the top surface of the glass samples. Laser powers of 30 mW and 3 mW were considered for bulk glass pellets and glass powders respectively. Half-wave plates and polarization analyzers have been used to monitor the polarization (parallel or perpendicular) of incident light and detect specific polarization components of the scattered light respectively. Under these conditions, we have recorded parallel (VV)[1] and perpendicular (VH) polarized Raman spectra

---

[1] V and H refer to vertically and horizontally polarized light respectively. The first letter of each configuration refers to the polarization state of the incident light; the second letter to that of the scattered or collected light.

from pure TeO_2 and binary TTx glass samples, and VH polarized spectra from ternary TTxWy and TNxWy glass pellets.

For each sample, three Raman spectra have been measured from three different spots; and a very good agreement among the set of spectra was obtained which demonstrates a high degree of topological homogeneity. As a reliable approach to study the compositional dependence of the spectra, no baseline correction treatment was carried out on any of the measured Raman spectra and the as-recorded intensities of each spectrum were divided by its total area.

III.3.4. Raman spectroscopic approach for the structural study of TeO_2-based glasses

III.3.4.1. Background on the approach (for oxide materials)

The following factors affect the Raman spectra envelopes of compounds (in terms of intensity and position of dominating bands): force constants accounting for the band positions, bond polarizability variation and number of vibrating entities governing the band intensities. It can be argued that the electronic polarizability variation induced by atomic vibrations correspond to the resulting bond length changes. Therefore, the totally symmetric combination of synchronous vibrations would generate the most intense band(s) in the Raman spectrum, whereas the non-symmetric ones have to be comparatively weak. Depending on the bond network nature of oxide compounds, three typical 'structure-Raman spectrum' relationships can be distinguished:

- **Island-type M_nXO_k structures** featuring quasi-isolated XO_k groups where all X–O bonds are terminal ones. In this case, the dominant Raman band(s) would be associated with synchronous stretching vibrations X–O bonds and present in high-wavenumber region (above 600 cm^{-1}). Among the good examples illustrating this case are the spectra from crystalline and amorphous TeO_2-Tl_2O system: namely, the Tl_2TeO_3 compound (*cf.* Fig. 1 in [140]) and (1-x)TeO_2-xTl_2O glasses (*cf.* Fig. I.5 for x = 0.5) respectively.

- **Three-dimensional XO_2 frameworks** featuring polymerized X–O–X networks with practically identical bridging X–O bonds. Therefore, the dominant bands would be related to totally symmetric stretching vibrations of X–O–X bridges via the motions of oxygen atoms along their bisectors. These bands would dominate the mid-wavenumber region 350–500 cm^{-1} as in the case of the Raman spectrum of α-quartz SiO_2 for example (*cf.* Fig. 3 in [163]).

- Oxides of which the bond networks combine **both X–O–X bridges and terminal X–O bonds**. This is typically observed in XO_2 structures with a chain-like character such as γ-TeO_2 polymorph [63]. In this case, the characteristic Raman bands are both present in mid- and high-wavenumber regions.

III.3.4.2. Polarized Raman spectroscopy: *promising approach for a cooperative and consistent structural description of TeO₂-based glasses*

III.3.4.2.1. Introduction

Inspecting the literature on the structure of TeO_2-based glasses revealed an extensive divergence of the measurement conditions of Raman spectra. In most studies, these "technical" aspects were ignored when comparing Raman spectra recorded under different conditions. We believe that such a variety of ways at probing the glass structure can be detrimental to the understanding of these glasses' structural features. Moreover, this could lead to disparities between structural studies on the same glass compositions investigated under dissimilar measurement conditions. As an illustration, we would like to consider the case of binary TeO_2-WO_3 glasses. As previously stated in *section I.5.4*, there is a lot of controversy in the literature regarding their network structures. We provide in Table III.4 the experimental conditions under which the Raman spectra were recorded from these glasses according to several authors.

Authors	Laser's wavelength (nm)	Scattering configuration (or geometry)	Controlled polarization	Sample's form
Sekiya *et al.* [103]	514.5	At 90°	Yes	Powder
Shaltout *et al.* [104]	514.5	Backscattering (at 180°)	N/A	Bulk
Plotnichenko *et al.* [152]	514.5	At 90°	Yes	Bulk
Sokolov *et al.* [164]	514.5	Backscattering	Yes	Bulk
Upender *et al.* [107]	488.0	Backscattering	N/A	N/A
Mirgorodsky *et al.* [165]	514.5	Backscattering	No	Bulk
Kaur *et al.* [108]	488.0	Backscattering	No	Powder

Table III.4. Measurement conditions of the Raman spectra of glasses in binary TeO_2-WO_3 system.

While some authors probed the "bulk" glass (often in the form of pellets), others analyzed the powdered samples instead (after grinding the bulk using a mortar and a pestle). In addition, the polarization state/direction of incident and scattered lights was not always controlled. In our opinion, these technical differences might have contributed to the above-mentioned controversy. Though, it is important to stress that other consequential factors have seemingly contributed as well. Some of those factors are the following:

- Glass preparation: the melting conditions in terms of temperature and time could alter the "targeted" or theoretical composition due to the rapid volatilization of TeO_2 at high temperatures [166] (above 850 °C). The quenching and annealing conditions are also important factors to be taken into consideration.

- Post-treatment of the recorded Raman spectra: baseline correction parameters as well as the normalization and decomposition processes adopted for the structural investigation.

One should be aware that even if the composition is the same, the Raman spectrum recorded from a glass pellet may show differences with that of the powdered form as a result of the following factors: *(i)* uncontrolled polarization direction along the optical path of the scattered light from the sample; and *(ii)* depending on several components of the spectrometer and their relative orientation, such as the optical elements (mirrors, lenses, *etc.*) and the diffraction grating system. Disregarding those factors leads to differences between the recorded Raman spectra from the pellet and its powdered form since the latter is expected to scatter light in all directions (*i.e.,* diffuse reflection) and alter the polarization direction of the incident laser beam as a result of multiple-scattering-induced change in polarization [167]. Therefore, it is essential to control the polarization of both incident and scattered lights. This can be achieved, for instance, by using *(i)* a polarized laser source (linearly polarized in our case) and *(ii)* polarization analyzers, put in front of the entrance slit of the spectrograph, to allow only one particular polarization component from the scattered light (*e.g.,* either parallel or perpendicular to that of the incident light) to be collected (*cf.* Fig. III.5).
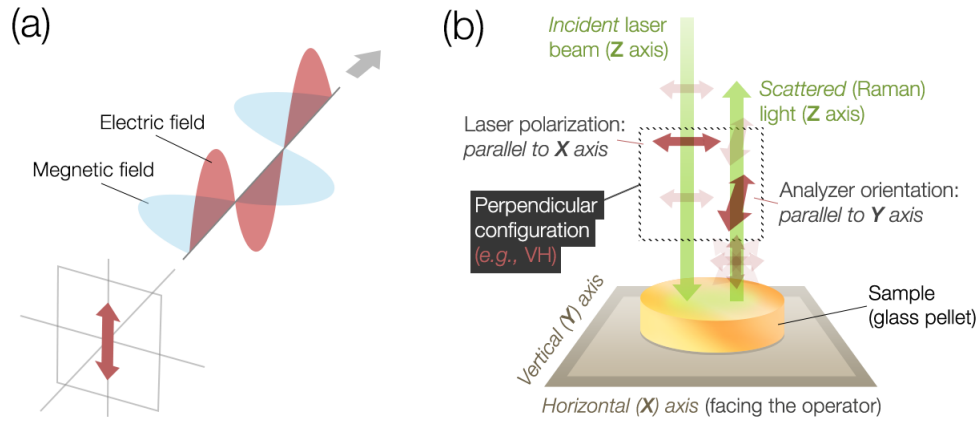
Fig. III.5. (a) Illustration depicting the linear polarization of a plane electromagnetic wave vertically polarized as defined by the electric field vector. (b) Example of the measurement, in the backscattering configuration, of the perpendicularly polarized (as to the incident beam) light scattered from a sample.

III.3.4.2.2. Polarized Raman spectra of pure TeO₂ glass

Since this section is largely devoted to the polarization effects on the Raman response, we suggest to report and discuss here the polarized Raman spectra recorded from pure TeO_2 glass (*cf. section III.2.1* for glass preparation conditions) which is the simplest model for the family of TeO_2-based glasses.

Let us now reconsider light polarization in the experimental context. When the incident light is polarized, then the scattered light from the sample may retain the initial polarization (parallel configuration), but it may also become depolarized (perpendicular configuration). The depolarization ratio ρ is an important experimental observable which gives important information for relevant vibrational mode assignment [162]. It is expressed as:

$$\rho = \frac{I_\perp}{I_{//}} = \frac{I_{VH}}{I_{VV}}$$

Where $I_{//}$ and $I_\perp$ are the intensities of the scattered light polarized parallel and perpendicular to the exciting light respectively. In the case of totally symmetric modes, ρ is equal to 0, and it takes on values between 0 and 0.75 for non-symmetric vibrations. In short, the more highly symmetric a vibrational mode is, the closer to zero ρ will be for the simple reason: since the vibration is symmetric, the scattering tends to be also symmetric and the possibility for the incident light to be depolarized is unimportant.

The recorded parallel and perpendicular (VV and VH) polarized spectra from TeO$_2$ glass are averaged to their total-area and given in Fig. III.6 along with the identified featured bands (A–I). The vibrational assignments of these bands is listed in Table III.5.
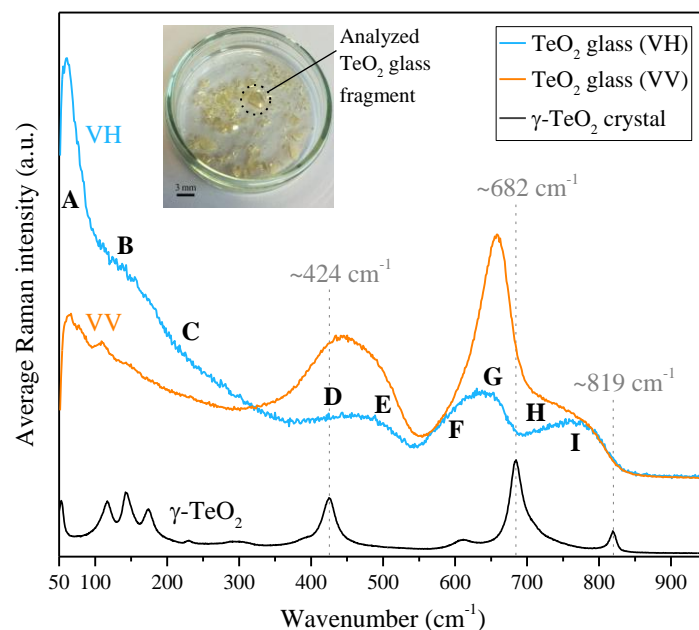
Fig. III.6. Total-area averaged polarized (VV and VH) Raman spectra recorded from pure TeO$_2$ glass fragment presented along with the Raman spectrum of γ-TeO$_2$ crystal for comparison.

Band	Wavenumber (cm^{-1})	Raman band assignments
A	~60	• The boson peak, due to an excess density of vibrational states [168].
B	~140	• Intra-chain vibrations of Te–Te bonds *(as in amorphous metallic t-Te)* [169].
C	~230	—
D	~425	• Symmetric stretching vibrations in nearly symmetric Te–O–Te bridges *(as in γ-TeO$_2$)* [63,64].
E	~500	• Symmetric stretching vibrations in Te–O–Te bridges [63,64].
F	~605	• Asymmetric stretching vibrations in nearly symmetric Te–O–Te bridges *(as in γ-TeO$_2$)* [63,64].
G	~660	• Asymmetric stretching vibrations in asymmetric Te–O–Te bridges, and synchronous pulsations of TeO$_2$ quasi-molecules [63,64].
H	~710	• Asymmetric stretching vibrations in asymmetric Te–O–Te bridges [63,64].
I	~770	• Asymmetric stretching of essentially covalent Te–$_{eq}$O bonds [63,64].

Table III.5. Bands' wavenumbers and vibrational assignments (according to the literature) of the Raman spectra (VV and VH) of TeO$_2$ glass.

To calculate the depolarization ratio ρ, we used the 'raw' intensities of as-recorded polarized Raman spectra shown below in Fig. III.7(a). As expected, the parallel polarized spectrum VV is more intense than the perpendicular polarized VH spectrum. The former spectrum is dominated by the two highly polarized bands in the mid- to high-wavenumber region, namely centered at ~450 cm^{-1} and ~660 cm^{-1}.
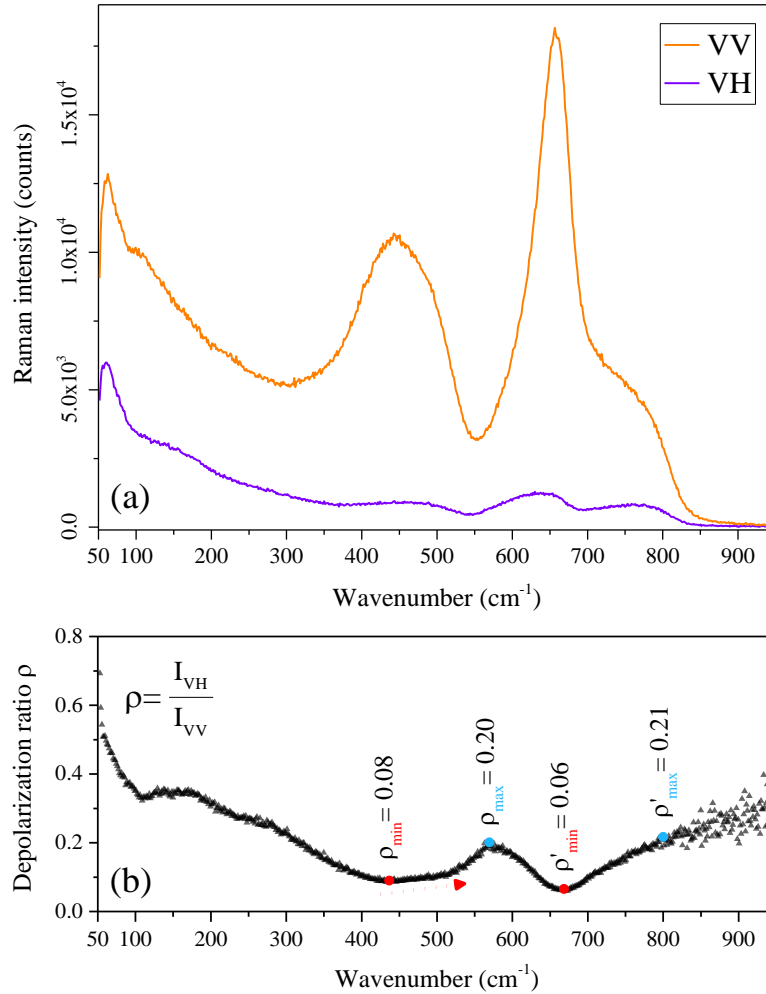
Fig. III.7. (a) Parallel VV and perpendicular VH polarized Raman spectra of TeO$_2$ glass fragment. (b) Wavenumber-dependence of the depolarization ratio ρ with the values of minima and maxima in the mid- to high-wavenumber region (300-850 cm^{-1}).

The wavenumber-dependence of the ratio ρ presented in Fig. III.7(b) is in good agreement with the literature on pure TeO$_2$ glass [170] and TeO$_2$-based glasses [144,171]. As previously outlined, the more symmetric a vibration is, the closer to zero ρ will be. Two minima (close to zero) and two maxima can be distinguished in the mid- to high-wavenumber region, which is in harmony with the vibrational assignment in crystalline TeO$_2$:

- Minima at ρ' = 0.06 and ρ = 0.08, corresponding to synchronous symmetric pulsation of Te$-_{eq}$O bonds from TeO$_2$ quasi-molecules (band G in Table III.5) and symmetric stretching vibrations of Te–O–Te bridges (bands D and E) respectively.

- Maxima at ρ = 0.20 and ρ' = 0.21, corresponding to asymmetric stretching vibrations of Te–O–Te bridges (band F) and asymmetric stretching of Te$-_{eq}$O bonds (bands H and I) respectively.

Therefore, the calculated depolymerization ratio ρ approves the vibrational modes (symmetric *vs.* asymmetric) of the featured bands in the Raman spectrum of TeO$_2$ glass given in Table III.5. This result is very meaningful as it paves the way for consistent structural descriptions of Te–O–Te bond network within the investigated TeO$_2$-based glasses in this work, namely binary TTx and ternary TTxWy and TNxWy glasses. It is worth noting that only VH polarized spectra were recorded from TTxWy and TNxWy glasses while both VH and VV were recorded from TTx glasses for the following reason: the Raman response of symmetric stretching vibrations of Te–O–Te and Te–O linkages (at ~450 and ~660 cm^{-1}) is highly polarized and thus much emphasized under the VV configuration. Therefore, it is more beneficial to use the perpendicular VH configuration to effectively elucidate the signatures associated with vibrating Ti–O, W–O and Nb–O bonds in both ternary systems.

III.3.4.3. Raman spectral decomposition

By means of the spectral decomposition technique, we have studied the structural features and compositional dependence of Raman spectra in pure TeO$_2$, binary TTx and ternary TTxWy and TNxWy glasses. This technique consists in fitting experimental Raman spectra by the addition of bands (*e.g.,* Gaussian functions) of which the position, width (FWHM: full width at half maximum) and intensity can be either assigned fixed values or left free (unconstrained). At the end of the fitting process, a Raman spectrum is generated from the sum of all the inserted bands.

As briefly stated earlier, prior to the decomposition process, in order to compare the as-recorded spectra and meticulously track the compositional dependence of the structure, the Raman spectra were systematically averaged to the total area, *i.e.,* by dividing the intensity at each wavenumber by the total area of the spectrum.

Using Focus 1.0 program [172], the total-area averaged Raman spectra were decomposed in the entire wavenumber range (15–1100 cm^{-1}) using a log-normal distribution for the boson peak

and Gaussian functions for the rest of the wavenumber range. The generated spectra are considered as matching the experimental ones with χ^2 values less than 0.05. The closer this value to zero, the better the generated spectrum fits the experimental one.

A total of 9 bands were inserted in the spectrum of pure TeO_2 glass (Fig. III.8), whereas 4 additional Gaussian functions were necessary to fit the larger envelopes featured by the Raman spectra of TTxWy and TNxWy glasses (*cf.* given examples in Fig. III.9 from TT5W15 and TN5W15 samples).
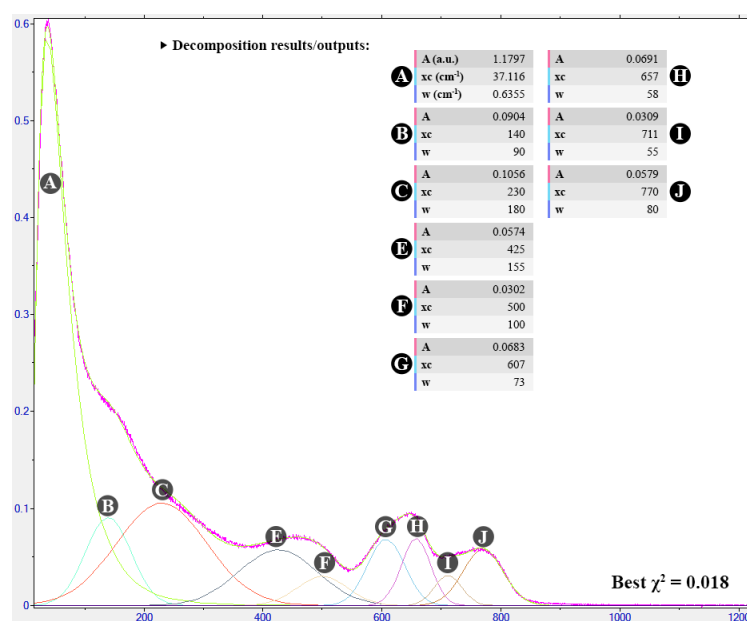
Fig. III.8. Snapshot from Focus program showing both experimental (pink line) and generated (smooth green line) Raman spectra of pure TeO_2 glass along with the inserted functions below the spectra. The inset gives the resulting set of data obtained at the end of the fitting procedure. Parameters A, xc and w correspond to the intensity, wavenumber and FWHM values respectively of the inserted functions.

Let us now focus on the content of the few suggested examples illustrating the spectral decomposition process from pure TeO_2 glass (Fig. III.8) and ternary TT5W15 and TN5W15 (Fig. III.9) glass samples. With respect to the high-wavenumber bands (E–J), the origin of the two bands B and C is less obvious though it is largely attributed to Te–Te interactions and vibrational modes of heavy atoms (*e.g.,* W and Nb) respectively. Therefore, the use of these two bands is mostly technical but at the same time substantial to achieve good fitting quality at their ends (or edges). For instance, let us consider the band B positioned at 140 cm^{-1} in TeO_2 glass and at 146.91 cm^{-1} in ternary TT5W15 and TN5W15 glasses. Besides its justified presence to account for the fairly weak shoulder laying in the 100-190 cm^{-1} range, its position and

relatively large width of 90 cm^{-1} in TeO$_2$ glass (Fig. III.8) and 100 cm^{-1} in TT5W15 and TN5W15 glasses (Fig. III.9) contribute to a better fit of the band A (boson peak) by allowing the log-normal function to correctly simulate its high-intensity profile. Likewise, the band C extensively supports the low-wavenumber region (bands A and B) but also contributes to a better fit of the band E which, along with band F, are two key bands as they collectively hold structural information about Te–O–Te bridges.

In the perspective of elucidating the compositional dependence of Raman spectra, several decisions regarding the state (fixed *vs.* unconstrained) of inserted bands' parameters had to be made. First and foremost, the intensities of inserted bands are never introduced as fixed values but instead left free to be adjusted by the fitting procedure. Moreover, in wavenumber regions where band shift and/or broadening can be visually detected with increasing transition-metal oxide (TiO$_2$, WO$_3$ or NbO$_{2.5}$) content, the inserted bands' wavenumbers and/or widths were respectively left unconstrained. This is the case for the bands A (boson peak), H and M (*cf.* inset in Fig. III.9). On the other hand, the bands C, E, G, I and K were assigned fixed wavenumber and width values for the following reasons: first, their profiles do not suggest any broadening or shifting behavior with composition (see *e.g.,* Fig. IV.10); and second, if left unconstrained, these bands often lead to uncontrolled outcomes, *e.g.,* unwanted drastic change of their wavenumber or width in order to simulate other areas of the spectrum.

Among the glass compositions of each ternary system (TTxWy and TNxWy), we chose to keep certain bands' parameters fixed in order to appropriately fit the overall spectrum. For instance, the bands F and L were introduced with unconstrained wavenumbers and fixed width values; the bands D and J with fixed wavenumbers and unconstrained width values. These decisions are in harmony with the ones discussed in the previous paragraph: let us consider the band F for example. Along with band E, they collectively simulate the broad band recorded in the ~360–550 cm^{-1} range, and since we decided to insert the band E with fixed wavenumber and width values, it is crucial to allow the neighboring band (F) to rectify and appropriately fit the higher wavenumber of this region. For this purpose, we chose to introduce the band F with unconstrained wavenumber value. Another example is the band J of which the two neighboring bands (I and K) are both fully constrained. We chose to insert this band with fixed wavenumber and unconstrained width values in order to account for the broad increase of intensity in the ~650–900 cm^{-1} range upon increasing WO$_3$ content.
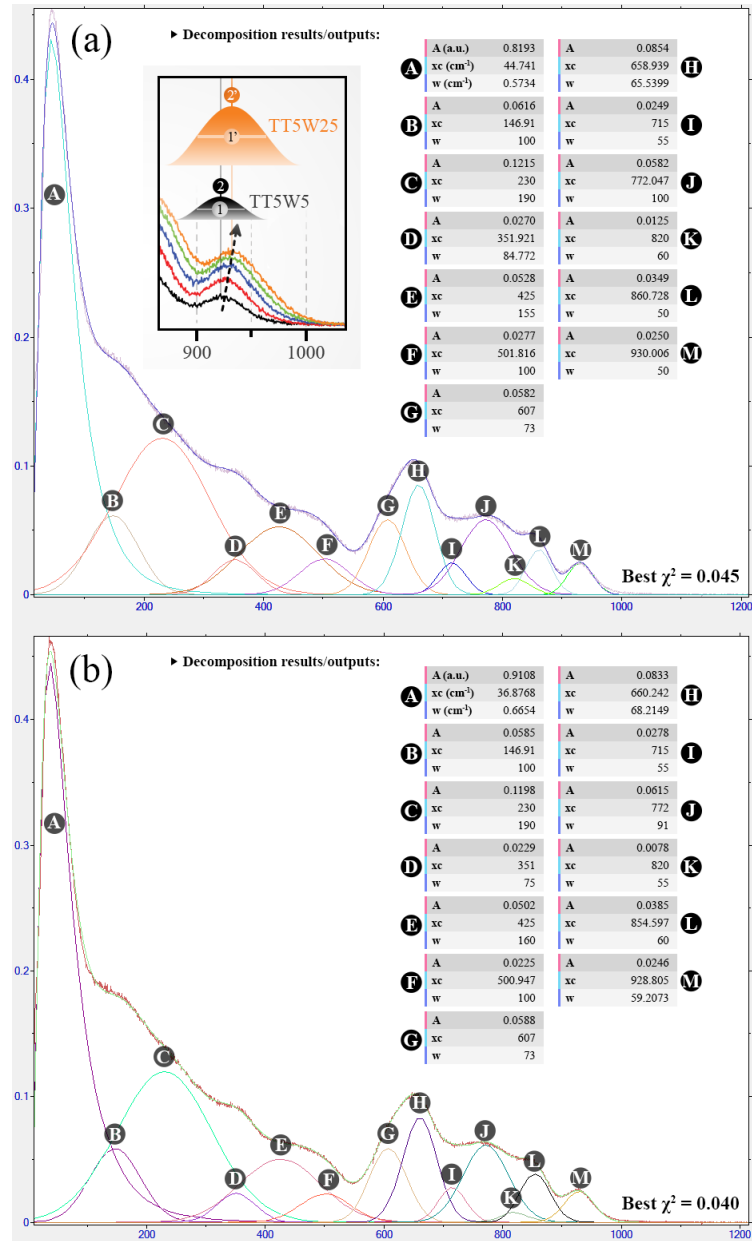
Fig. III.9. Snapshots showing the experimental and generated Raman spectra of (a) TT5W15 and (b) TN5W15 glasses. The inset (top left) gives the evolution of the band M upon adding WO$_3$ from 5 mol.% (TT5W5) to 25 mol.% (TT5W25). Given the increase of FWHM ((1)→(1')) and shift to higher wavenumbers ((2)→(2')), both the position and FWHM should be unconstrained for this band.

In regard to our decomposition approach, it is important to stress that if only a marginal shift of one band or shoulder is visually observed (from the experimental spectrum) as a function of the composition, then the wavenumber of that Gaussian function will be intentionally constrained. This is crucial for an appropriate comparison between the bands' relative evolutions (or ratios) of different glass compositions.

As outlined earlier, the fitting quality of spectra is judged by how close to zero the χ^2 value is. It can be noticed that unlike in pure TeO_2 glass, where this value is as small as 0.018, in ternary TTxWy and TNxWy glasses, it can be twice as high with values in the 0.030–0.048 range. This can be briefly explained as follows: *(i)* more bands emerge upon adding transition-metal oxides, and *(ii)* bands in the high-wavenumber region become broader and thus complicate the process of bands' parameters assignment that is crucial for an accurate fitting. Nevertheless, χ^2 values of around 0.05 are still considered fairly satisfying to study the compositional dependence of Raman spectra.

III.3.5. Measurement of linear and nonlinear optical properties

III.3.5.1. Background and state-of-the-art

III.3.5.1.1. UV-Vis-NIR optical transmission spectra

Several optical properties can be determined from a material's absorption spectrum ranging from the ultra-violet (UV) to the near-infrared (NIR) region. The most fundamental property is the spectral range over which the material is optically transparent. Besides, two main characteristics can be deduced from the transmission spectra: *(i)* the UV optical absorption edge featuring the short-wavelength end of the transmission window, and *(ii)* the refractive index n which represents one of the fundamental properties because of its close relationship with the polarizability of the constituent ions.

In principle, the refractive index increases with increasing electronic polarizability of ions and with the presence of lone electron pairs. It can be obtained from the optical transmission data in the transparent region using the following expression: $T = 2n/(n^2+1)$. It should be stressed that this equation slightly underestimates the refractive index value since the multiple reflections of light are neglected and most of the reflection is considered to occur at the two air/glass interfaces (Fresnel reflection).

The optical absorption edge of a given material is associated with the optical transitions and band gap which are governed by the chemical composition and structure (local order) within this material. Therefore, the compositional dependence of the position of the absorption edge can be used to study the structural evolution of the glass network. In this optical absorption process, one photon of a particular energy excites an electron from an energy state to a higher one. This phenomenon is described using the absorption coefficient α (in cm^{-1}) which represents

the ability of the material to absorb light at a given wavelength. It can be estimated using the following expression: $\alpha(\lambda) = (1/d) \ln(T_{max}/T(\lambda))$, where d is the sample thickness.

III.3.5.1.2. Optical absorption in amorphous materials

Fundamental (or band-to-band) optical absorption takes place as a result of the photo-excitation of an electron between the two extended bands, *i.e.,* from the valence to the conduction band across the electronic band gap, given that $E_g = E_c - E_v$ (Fig. III.10). Thus, the outcome of this optical transition is a created electron in the conduction band and a hole in the valence band. Two types of the fundamental optical transitions can be distinguished: direct and indirect transitions. Both involve the interaction of an electromagnetic wave with an electron in the valence band. In direct transitions, the momentum of electrons and holes is the same in conduction and valence bands which is not the case for indirect transitions. The latter involve simultaneous interactions with lattice vibrations (phonon-assisted transitions). A great deal of book chapters and reviews have addressed the fundamental optical absorption behavior of amorphous and crystalline solids (*e.g., Chapter II* in [173] and *Chapter VI* in [174]).
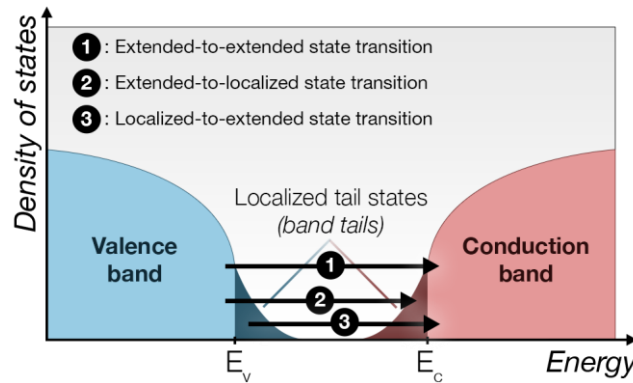
Fig. III.10. Schematic energy band diagram of disordered materials showing localized tail states extending into the band gap; their density of states decreases exponentially into the band gap.

Aside from the typical scenario of fundamental absorption, the concept of band-tailing arises to explain the involvement of localized states in the optical absorption of disordered materials. Band-tailing refers to the condition where E_v (valence band edge) and E_c (conduction band edge) are no longer well-defined cut-off energies, and extra electronic states (localized states)

exist above E_v and below E_c of which the density of states falls exponentially with energy away from the band edges towards the fundamental band gap (*cf.* Fig. III.10).

In principle, the deviations from perfectly ordered systems include narrowing of the band gap and formation of localized states within band tails as schematically illustrated above. The edges of the band gap clearly demonstrate the effects of the structural disorder on the electronic structure of amorphous solids. These effects on the electronic structure are manifested in the optical absorption edge, which can be interpreted in terms of two distinct regions: *(i)* Urbach and *(ii)* Tauc regions.

(i)   Sub-gap optical absorption–Urbach rule

The absorption of photons of energy less than the band gap energy (hν < E_g) in amorphous solids involves the localized tail states. The absorption coefficient α depends on incident photon energy exponentially giving rise to the so-called Urbach tail (an illustration is given in Fig. III.11 showing the absorption edges of TT5W15 glass – *cf. Chapter IV*).

The exponential dependence of the absorption edge on incident photon energy (hν) is referred to as Urbach rule. Urbach tails [175] were originally observed in a number of ionic crystals satisfying the dependence: $d\ln(\alpha)/d(h\nu) = -1/k\mathrm{T}$ (where k is a constant) due to thermally induced disorder. These band tails were also detected in substitutionally disordered materials and radiation-damaged materials. Regardless of the nature of atomic disorder, *i.e.,* structural (static), vibrational (thermally induced) or due to the presence of chemical impurities, several studies have suggested the additive character of disorder on the density of localized states and therefore the magnitude of Urbach tails (*cf.* [176] for example).

In principle, Urbach energy E_U corresponds to the width of these band tails, thus estimating their density. If we consider a set of glasses having close E_U values, then a close density of states in their electronic structure is expected. As a rule, a highly disordered glass network features a higher density of localized states in its electronic band structure, and thus having a high E_U value.

In the Urbach region, the absorption coefficient α can be expressed by the following form: $\ln(\alpha) = (h\nu/E_U) - C$, where C is a constant. Therefore, E_U can be obtained from the slope of the straight line of plotting $\ln(\alpha)$ as a function of the incident photon energy (hν).
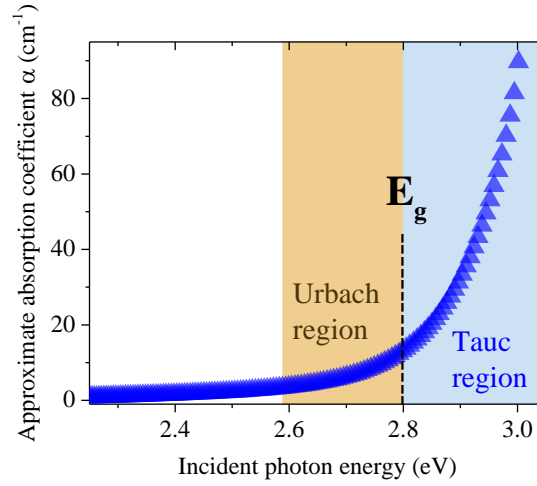
Fig. III.11. Example of the optical absorption edge from TT5W15 glass showing the two characteristic regions of optical transitions between localized and extended states (Urbach edge) and from extended to extended states (Tauc absorption).

(ii) *Optical band gap energy estimation–Tauc model*

The second region of the absorption edge is referred to as Tauc region [177], and is assigned to the electronic transitions between extended valence and conduction bands. In this region, the absorption coefficient α can be expressed by the following form: $(\alpha h\nu)^r = A\,(h\nu - E_g)$.

The value of the exponent r denotes the nature of the transition: $r = \frac{1}{2}$ and $r = 2$ for direct and indirect transitions respectively. The optical energy gap E_g is obtained by extrapolating the linear part of Tauc plots $(\alpha h\nu)^r$ as a function of the incident photon energy $h\nu$.

III.3.5.1.3. Wemple and DiDomenico single-effective-oscillator model

Wemple and DiDomenico analyzed the refractive index dispersion data below the interband absorption edge in more than 100 widely different solids (crystals) and liquids [178]. According to this model, the refractive index dispersion can be interpreted using the following equation:

$$\frac{1}{n^2 - 1} = \frac{E_0}{E_d} - \frac{(h\nu)^2}{E_0\,E_d}$$

Where $h\nu$ is the photon energy, E_0 is the single oscillator energy and E_d the dispersion energy. By plotting $1/(n^2-1)$ as a function of $(h\nu)^2$ and fitting a straight line, oscillator parameters E_d (dispersion energy) and E_0 (single oscillator energy) can be determined.

The dispersion energy E_d was first introduced by the same authors [179] in 1969. This energy parameter can be used to describe the dispersion of the refractive index. Its usefulness in measuring the average strength of interband optical transitions is essentially empirical. It was found to obey the following simple empirical relationship in more than 100 ionic and covalent crystals: $E_d = \beta\, N_c\, Z_a\, N_e$, where β approaches 0.26 ± 0.04 eV and 0.37 ± 0.05 eV in ionic and covalent crystals respectively. N_c is the coordination number of the cation, Z_a the absolute charge number of the anion and N_e the total number of valence electrons per anion. It can be established from the previous expression that, in mixed oxide glass systems, variations of E_d result primarily from changes in ionicity (evolution of the parameter β) and/or average local structure (evolution of the coordination number N_c).

According to Wemple and DiDomenico model, for incident photon energies E (E = hν) lower than the optical band gap energy E_g, the refractive index dispersion can be interpreted using the following equation:

$$\frac{1}{n^2 - 1} = \frac{E_0}{E_d} - \frac{E^2}{E_0\, E_d}$$

By plotting $1/(n^2-1)$ as a function of E^2 and fitting a straight line, the oscillator parameters (E_0 and E_d) can be determined.

III.3.5.1.4. Electronic polarizability of ions

The electronic polarizability of ions demonstrates the ease of deformation of their electronic clouds by applying an electromagnetic field. In other words, it represents the displacement magnitude of electrons to the electromagnetic field. It is closely connected to several physical properties such as refraction, conductivity, ferroelectricity, electro-optical effect, optical basicity and nonlinearity.

The electronic polarizability of ions can be modeled based on Hooke's law potential energy: $\alpha = e^2 \sum (n_i/k_i)$, where e is the elementary charge and n_i the number of electrons with binding force constant k_i. From the previous expression, one can notice that smaller force constants contribute more to the electronic polarizability of ions than the tightly bound inner-shell electrons.

In early 1939, Kordes [180] was the first scientist to apply the polarizability approach based on the Lorentz-Lorenz equation [181,182] to conventional oxide glasses using measured values of

the refractive index and density. In this equation, the molar refraction R_M has the dimension of molar volume (cm^3.mol^{-1}); when Avogadro's number N_A is introduced, the molar refraction R_M can be expressed as a function of molar polarizability α_M (in Å^3): $R_M = [(n^2-1)/(n^2+2)]\ V_M = (4/3)\ \pi\ N_A\ \alpha_M = 2.52\ \alpha_M$.

In principle, the electronic polarizability of an ion varies from one compound to another (*e.g.,* from the crystalline to the amorphous state) due to changing electronic structure and structural environments. In this connection, the electronic polarizability of one free ion is different from that of the same ion when coordinated to other ions in the condensed state.

Cations like B^{3+}, Si^{4+} and P^{5+} possess extremely low polarizabilities, namely, 0.002, 0.033 and 0.021 Å^3 respectively [183], and most of them have large positive charges. Their cationic field strength values [20] are very large (*cf.* Fig. II.2) and thus strongly affect the electron charge density of their surrounding oxide ions. In this connection, glasses containing high concentrations of classical glass-formers such as B_2O_3, SiO_2 and P_2O_5 show low oxide ion polarizabilities (α_{O2-}) and refractive indices. Among the conventional glasses, germanate glasses have the highest refractive indices. In fact, Ge^{4+} cation has a large polarizability of 0.137 Å^3 [184] (higher than B^{3+}, Si^{4+} and P^{5+} cations), and therefore, it affects less the electron charge density of the oxide ions, which explains the relatively higher electronic polarizability of oxide ion in GeO_2 oxide. In contrast, the cationic field strengths of Te^{4+}, Sb^{3+} and Bi^{3+} are much smaller. These cations possess very high polarizabilities (1.595, 1.111 and 1.508 Å^3 respectively [183]) and have strongly polarizable lone electron pairs in their valence shells [184].

Following the polarizability approach developed by Dimitrov and Komatsu [183] which is based on the Lorentz-Lorenz equation, the E_g-based electronic polarizability of the oxide ion can be calculated using the following equation:

$$\alpha_{O2-}\ (E_g\text{-based}):\ \alpha_{O2-} = \{(V_m/2.52)\ [1 - (E_g^{1/2} - 0.98)/1.23] - \textstyle\sum p\alpha_i\}\ q^{-1}$$

Where p and q are the numbers of cations and oxide ions in the chemical formula of the oxide A_pO_q. The free-cation polarizability α_i values of Te^{4+} (1.595 Å^3), Ti^{4+} (0.184 Å^3), Nb^{5+} (0.242 Å^3) and W^{6+} (0.147 Å^3) ions were collected from [183].

III.3.5.2. Linear optical properties

III.3.5.2.1. UV-Vis-NIR optical transmission

To evaluate the optical transmission of TTxWy and TNxWy glasses, we measured the UV-Vis-NIR spectra at room temperature from double side polished pellets of 1.44–1.47 mm in thickness over a wide wavelength range from 300 to 3300 nm with a spectral resolution of 2 nm using the Varian Cary 5000 spectrophotometer. As outlined in *section III.3.5.1*, several optical constants can be estimated from the recorded spectra, such as the refractive index, absorption coefficient, optical band gap and Urbach energies.

III.3.5.2.2. Spectroscopic ellipsometry

Ellipsometry is an optical characterization technique for determining, among others, the thickness and optical properties of materials [185]. In principle, an ellipsometric measurement consists of the following five steps:

1. A light beam is generated in a predetermined polarization state.

2. The beam is reflected from or transmitted through a sample having reflecting plane-parallel surfaces, leading to an interaction that changes the polarization state of incident light.

3. The polarization state of the reflected or transmitted beam is measured.

4. Parameters are determined that characterize the interaction in terms of the change in polarization state.

5. From these parameters, information about the sample can be obtained.

Using the same samples (polished pellets), the refractive index dispersion was recorded by means of spectroscopic ellipsometry using a phase-modulated ellipsometer (Horiba Jobin–Yvon UVISEL) with a fixed 60° incidence angle. The state of the samples implies the existence of "parasite" effects due to the back-surface reflection during the measurements (Fig. III.12). To bypass this reflected light, only areas close to the edge of the pellets were probed and the reflected light was partly collected using a diaphragm.
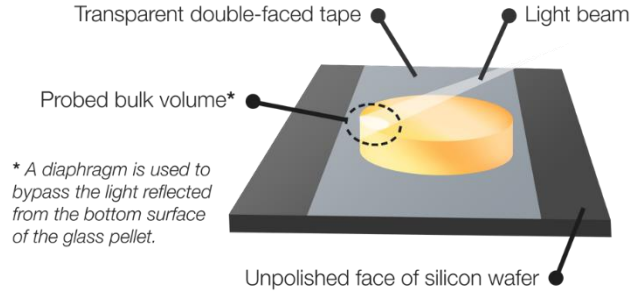
Fig. III.12. Illustration showing the experimental condition to bypass back-reflected light.

From the measured dispersion curves of TTxWy and TNxWy glasses (*cf. Chapter IV and V respectively*), we derived the refractive indices n_∞ extrapolated to infinite wavelength using Sellmeier's dispersion formula [186,187]: $n = (A + B/(1-C/\lambda^2) + D/(1-E/\lambda^2))^{1/2}$ where A–E are fitting constants specific to each sample, allowing to determine $n_\infty = (A + B + D)^{1/2}$. An excellent fitting quality was achieved as demonstrated by the R^2 coefficients ranging between 0.9970 and 0.9999.

III.3.5.3. Nonlinear optical properties by Z-scan technique

The nonlinear optical measurements were conducted in collaboration with Professor Tomokatsu Hayakawa from the Nagoya Institute of Technology (NiTech) laboratory in Nagoya, Japan. The Z-scan technique was used to measure the third-order nonlinear susceptibility $\chi^{(3)}$ of ternary TTxWy and TNxWy glasses.

This technique is based on measuring the transmitted light from the sample in order to extract both the nonlinear refractive index and absorption coefficient. Further experimental details and a comprehensive theoretical background are given by Sheik-Bahae *et al.* in [188].

The third-order nonlinear susceptibilities $\chi^{(3)}$ were measured from double-side polished glasses employing the Z-scan technique, and using a comparative route in respect with the data collected for a reference fused silica plate [189]. Pulses from regenerative Ti:sapphire laser (Spectra Physics, Hurricane) at 800 nm were used at a repetition rate of 1 kHz and with ~90 fs pulse duration. A lens ($f = 200$ mm) was positioned along the optical path (Z axis), and the glass samples were moved forward and backward from the focal point (Z = 0 mm), namely along the Z range between -25 mm and +25 mm at intervals of 0.5 mm (*cf.* Fig. III.13). At each step, the optical transmittance was measured with the optical power meter system (Newport 2930-C/818-SL silicon photodiodes in the close and open configurations [188]). The Z-scan measurement

is completed as the sample is moved away from the focal point (around which nonlinear phenomena occur) such that the transmittance becomes linear since the irradiance on the sample is low again.
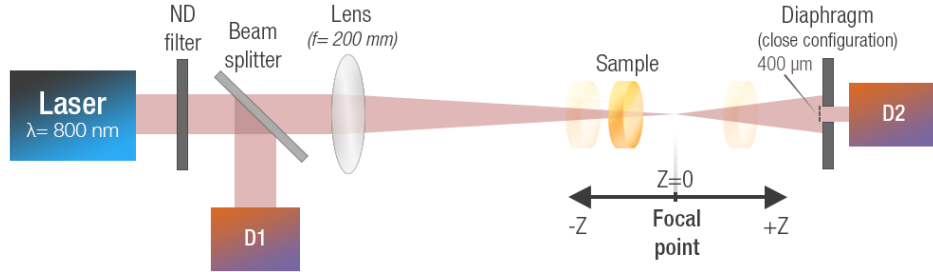
Fig. III.13. Femtosecond Z-scan setup used to measure the third-order nonlinear susceptibility $\chi^{(3)}$.

The optical measurement on each glass sample was repeated three times. Each consists in four measurements: two at a power of 250 nW and two at 2 nW. The difference between the two (at 250 nW *vs.* at 2 nW) is whether a diaphragm (pinhole size of 400 µm) is put before D2 detector (close configuration) or not (open configuration). The **close** configuration can be used to extract the nonlinear refraction from the nonlinear coefficient γ of the transmitted light; whereas the **open** configuration allows to evaluate the nonlinear absorption coefficient β since the detected transmittance is insensitive to beam distortion and is only a function of the nonlinear absorption [188]. In order to extract the nonlinear coefficient γ, we corrected the baseline of the measured raw Z-scans and removed the absorptive contributions using the following formula (with C being a calibration factor):

$$\gamma = \frac{\text{Close}_{250\text{nW}}}{\text{Open}_{250\text{nW}}} * \frac{\text{Open}_{2\text{nW}}}{\text{Close}_{2\text{nW}}} * C$$

Let us now focus on how we obtain the real part of the third-order nonlinear susceptibility $\text{Re}(\chi^{(3)})_{\text{glass}}$ for TTxWy and TNxWy glasses. The same previously described procedure to obtain the coefficient γ has been applied on pure SiO_2 glass which is therefore our reference material. More details on how we obtained the real part of the third-order nonlinear susceptibility $\chi^{(3)}_{(glass)}$ can be found in the literature (*e.g.,* [190]) leading to the following expression:

$$\text{Re}(\chi^{(3)})_{glass} = \text{Re}(\chi^{(3)})_{SiO2} * \left(\frac{\Delta\phi_{(glass)}}{\Delta\phi_{(SiO2)}} \cdot \frac{I_{0\,(SiO2)}}{I_{0\,(glass)}} \cdot \frac{L_{eff\,(SiO2)}}{L_{eff\,(glass)}} \cdot \frac{n^2_{0\,(glass)}}{n^2_{0\,(SiO2)}} \right)$$

With $\Delta\phi$ corresponds to self-phase modulation which is proportional to the difference ΔT_{p-v} ($\Delta T_{p-v} = 0.406\ \Delta\phi$ [188]) between maximum transmittance T_p (p for peak) and minimum T_v (v for valley). I_0 represents the intensity of the incident laser beam, L_{eff} the thickness of the sample and n_0 the linear refractive index measured by spectroscopic ellipsometry. For the third-order nonlinear susceptibility of silica glass $Re(\chi^{(3)})_{SiO2}$, we extracted its value from the dispersion curve (Fig. III.14) established by Milam [191] who reviewed over 30 reported nonlinear refractive indices of silica glass at different wavelengths. Since we use a laser wavelength of 800 nm in our Z-scan measurements, we extracted the nonlinear refractive index of silica glass at the same wavelength; as shown in Fig. III.14, the obtained value is ~2.8 $*10^{-16}$ cm^2/W or 1.5 $*10^{-14}$ esu. However, in order to compare our normalized experimental $\chi^{(3)}$ values to other TeO$_2$-based glasses, we had to readjust the state-of-the-art values (often obtained by considering a $\chi^{(3)}{}_{SiO2}$ of 2.8 $*10^{-14}$ esu reported by Kim *et al.* [157]) by dividing them by 1.87 which is the factor between $\chi^{(3)}{}_{SiO2}$ obtained by Milam and Kim *et al.*. Such argumentation is developed in detail in [189].
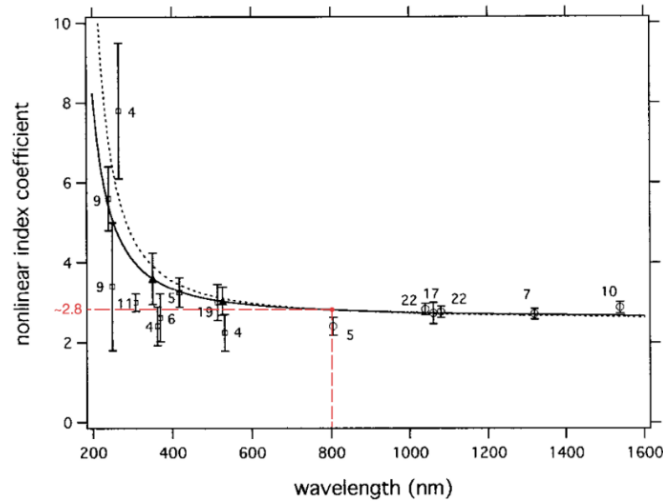
Fig. III.14. Nonlinear refractive index coefficient γ dispersion of silica glass. Coefficients are plotted in multiples of 10^{-16} cm^2/W. Adapted from [191].

From the measured Z-scan transmittance curves, the extracted peak-valley transmittance change ΔT_{p-v} (*cf.* example of TN15W20 in Fig. III.15) was used to derive the $\chi^{(3)}$ values for all of the prepared glass samples.
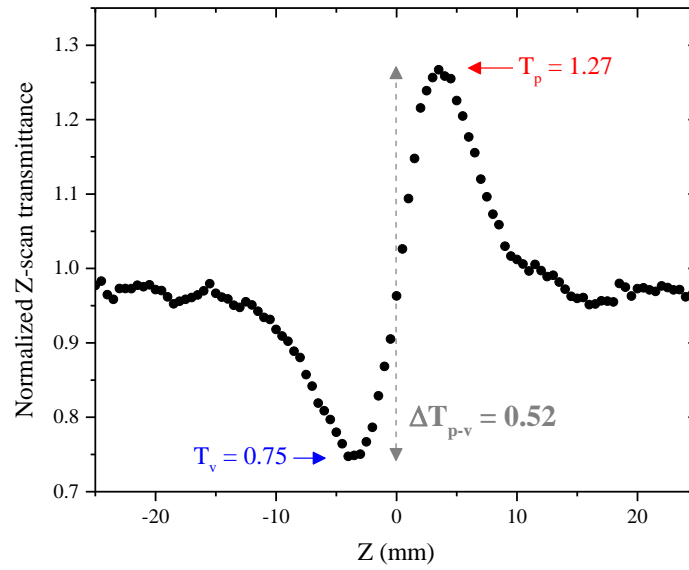
Fig. III.15. Example of a measured Z-scan curve from the TN15W20 glass sample.

Finally, the estimated error of $\chi^{(3)}$ values take into account the standard deviation of the set of the three extracted γ coefficient values as well as the errors associated with the linear refractive indices (measured by spectroscopic ellipsometry).

III.4. Conclusion

In this chapter, we summarized the experimental approaches to the study of pure TeO_2, binary TeO_2-TiO_2 and ternary TeO_2-TiO_2-WO_3 and TeO_2-$NbO_{2.5}$-WO_3 glasses. First, we described the experimental conditions under which these glass samples were prepared via the two different preparation methods of melting-casting (MC) and melting-fast-quenching (MFQ). The characterization techniques used for the glass-forming domain determination and measurement of density, thermal, structural and optical properties were described together with the experimental conditions. As the structural understanding of the bond networks in these glasses represents a very important part of this work, a detailed description of the Raman spectral decomposition process was given and highlighted with a few examples. Moreover, the fundamental background of the measured optical properties was outlined along with the measurement conditions.

Chapter IV.   Synthesis, thermal, structural and optical properties of new glasses within the TeO₂-TiO₂-WO₃ system

IV.1. Introduction

From the optical properties viewpoint, the high linear and nonlinear optical properties of TeO_2-based glasses have been associated with the presence of the Te^{4+} lone electron pair [4–8] and characteristic Te–O–Te bridges [3,9–11]. It was shown that adding transition-metal oxides of empty d-orbital cations (*e.g.*, TiO_2, WO_3 and Nb_2O_5) enhances the optical performance of TeO_2-based glasses, *i.e.*, their nonlinear optical response reaching values of third-order nonlinear susceptibility $\chi^{(3)}$ 10 to 50 times greater than those of silica-based glasses [3].

We have embarked upon studying dual-transition-metal oxide-containing TeO_2-based glasses within the ternary TeO_2-TiO_2-WO_3 system. To the best of our knowledge, only a handful studies have investigated very close compositions to the TeO_2-TiO_2-WO_3 system: Safonov [126] attempted to determine its equilibrium and non-equilibrium phase diagram; Muñoz-Martín *et al.* [109] prepared and measured the structural and optical properties of the glass composition $80TeO_2$-$5TiO_2$-$15WO_3$; and finally, an investigation of the same nature was performed on the quaternary $(89-x)TeO_2$-$10TiO_2$-xWO_3-$1Nd_2O_3$ system by Fares *et al.* [127]. Our aim is to elucidate the structural effects of TiO_2 and WO_3 on the TeO_2-rich network in these glasses and to establish relationships with their linear and nonlinear optical performances.

In this chapter, we report the glass-forming domain within the TeO_2-TiO_2-WO_3 system and the measured properties from the obtained glasses, namely, their densities, thermal characteristics, structural and optical (linear and nonlinear) properties. These findings have been published in the Journal of Non-Crystalline Solids [192].

IV.2. Glass-forming domain determination

Under the experimental conditions described in *section III.2.3*, we have explored the glass-forming domain within the $(100-x-y)TeO_2$-$xTiO_2$-yWO_3 system (TTxWy). The amorphous state of TTxWy samples was checked by X-ray powder diffraction in order to determine the glass-forming domain shown in Fig. IV.1(a). It extends from x = 5 to 15 mol.% in TiO_2 and from y = 5 to 25 mol.% in WO_3. In total, fifteen melt compositions have yielded transparent

yellowish glasses. Upon increasing WO_3 content, the color shifted to honey-brown, and remained practically unchanged upon adding TiO_2 (*cf.* Fig. IV.1(b)).
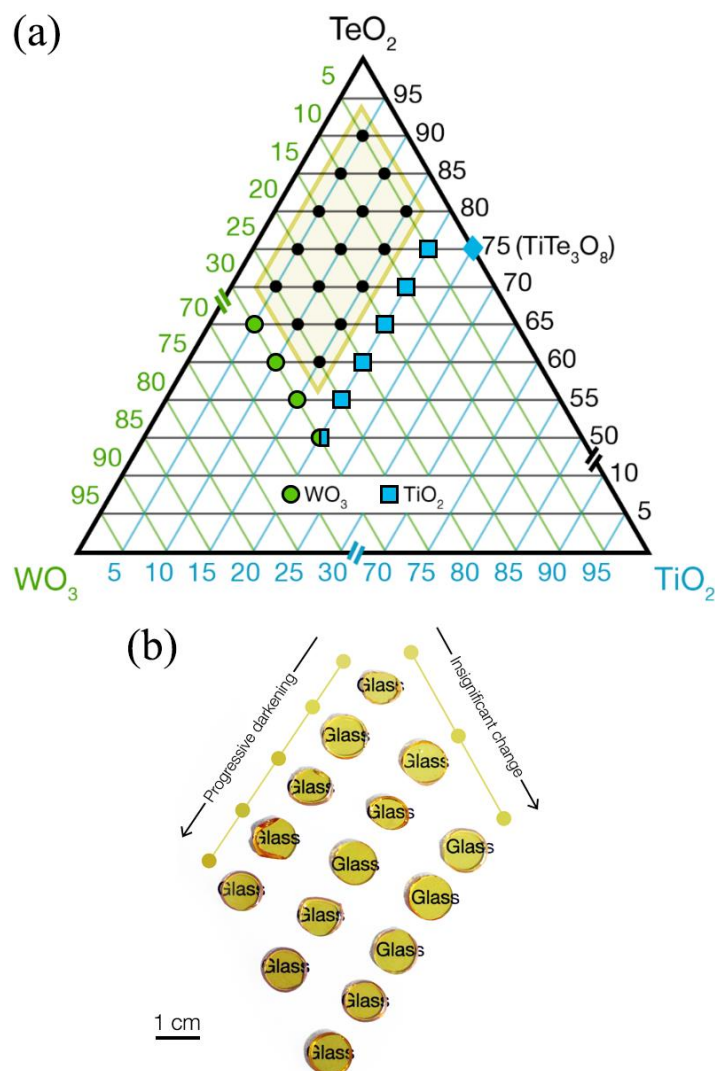
Fig. IV.1. (a) Glass-forming domain obtained within the $(100-x-y)TeO_2-xTiO_2-yWO_3$ system (labeled TTxWy) surrounded by the yellow frame. Blue and green colored squares and spots correspond to partially crystallized samples in TiO_2 and WO_3 respectively. (b) Photograph of the obtained glass pellets in their final polished state. The relative positions of pellets are in accord with the black spots in the glass-forming domain.

Crystals of γ-WO_3 [100,193] are detected in TTxW30 samples (Fig. IV.2). The corresponding peaks become sharper and more intense upon adding TiO_2 suggesting an increase of the number and/or average size of WO_3-rich regions. At 20 mol.% of TiO_2, crystals of rutile TiO_2 phase [83] are detected in TT20Wy samples without any trace of $TiTe_3O_8$ or anatase TiO_2 phases.
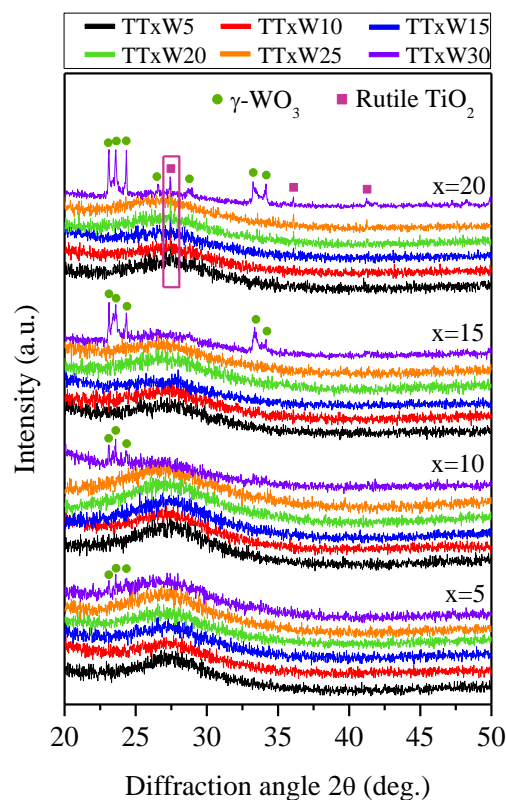
Fig. IV.2. X-ray diffraction patterns of the prepared TTxWy samples. Note that crystals of rutile TiO_2 were detected in all samples containing 20 mol.% of TiO_2 (x = 20).

To evaluate the glass compositions in terms of molar ratios, the glass samples were analyzed by energy dispersive X-ray microanalysis (EDS) using the Quanta FEG-450 scanning electron microscope which provides only approximate quantitative analysis. The elemental analysis results (Table IV.1) indicate that most of the obtained glass samples have close compositions to the theoretical (or targeted) ones with the exception of TT10W25 sample where a relatively strong difference is recorded.

Sample	Theoretical composition (mol.%)			Measured composition (mol.%) ± 2 mol.%		
	TeO_2	TiO_2	WO_3	TeO_2	TiO_2	WO_3
TT5W5	90	5	5	89	5	6
TT5W10	85	5	10	83	4	13
TT5W15	80	5	15	81	3	16
TT5W20	75	5	20	76	4	20
TT5W25	70	5	25	67	5	28
TT10W5	85	10	5	85	8	7
TT10W10	80	10	10	80	10	10
TT10W15	75	10	15	75	9	16
TT10W20	70	10	20	70	9	21
TT10W25	65	10	25	60	7	33
TT15W5	80	15	5	81	12	7
TT15W10	75	15	10	80	10	10
TT15W15	70	15	15	68	13	19
TT15W20	65	15	20	63	13	24
TT15W25	60	15	25	61	12	27

Table IV.1. Comparison between the expected and measured TTxWy glass compositions.

IV.3. Physical properties of TeO₂-TiO₂-WO₃ glasses

IV.3.1. Density and molar volume

Using helium pycnometry, we have measured the densities of TTxWy glass samples (in powdered form) and extracted molar volumes for each composition taking into account their theoretical molar masses (*cf*. Table IV.2). Since very close trends of these properties are observed upon adding TiO_2 (or WO_3) at different WO_3 (or TiO_2) contents, we suggest to consider TTxW5 and TT5Wy sets of samples for the sake of simplicity. The density increases with addition of WO_3 by approximately 6% from TT5W5 (5.59 g.cm^{-3}) to TT5W25 (5.93 g.cm^{-3}). On the other hand, a density decrease by approximately 2% is recorded upon adding TiO_2 from TT5W5 (5.59 g.cm^{-3}) to TT15W5 (5.45 g.cm^{-3}). Therefore, the compositional dependence of the density seems to follow the *additive density rule*: densities of raw oxides TiO_2, TeO_2 and WO_3 are respectively 3.90, 6.13 and 7.16 g.cm^{-3}. The density evolutions in TTxWy glasses are logically assigned to the higher molar mass of WO_3 (231.8 g.mol^{-1}) and lower molar mass of TiO_2 (79.9 g.mol^{-1}) than that of TeO_2 (159.6 g.mol^{-1}).

Sample	Density (g.cm^{-3})	Molar volume (cm^3.mol^{-1})
TT5W5	5.586 ± 0.003	28.50 ± 0.06
TT5W10	5.677 ± 0.008	28.68 ± 0.06
TT5W15	5.777 ± 0.007	28.81 ± 0.06
TT5W20	5.764 ± 0.006	29.50 ± 0.06
TT5W25	5.925 ± 0.008	29.31 ± 0.06
TT10W5	5.529 ± 0.009	28.08 ± 0.06
TT10W10	5.643 ± 0.010	28.15 ± 0.06
TT10W15	5.748 ± 0.008	28.26 ± 0.06
TT10W20	5.799 ± 0.006	28.64 ± 0.06
TT10W25	5.860 ± 0.004	28.96 ± 0.06
TT15W5	5.454 ± 0.004	27.73 ± 0.06
TT15W10	5.535 ± 0.004	27.98 ± 0.06
TT15W15	5.623 ± 0.008	28.18 ± 0.06
TT15W20	5.682 ± 0.007	28.53 ± 0.06
TT15W25	5.757 ± 0.005	28.79 ± 0.06

Table IV.2. Measured densities and molar volumes of TTxWy glasses.

IV.3.2. Thermal characteristics

The thermal properties of TTxWy glasses were measured by means of differential scanning calorimetry (DSC) to evaluate the compositional dependence of specific characteristics such as the glass transition temperature T_g and thermal stability ΔT. The analyzed glass samples were in powdered form and weighing ~20 mg.

The glass transition temperature T_g in TTxWy glasses increases linearly upon adding either TiO$_2$ or WO$_3$ ($T_{g(min)}$ = 328 °C and $T_{g(max)}$ = 426 °C). It increases by ~16% from TT5W5 (328 °C) to TT15W5 (380 °C) and by ~15% from TT5W5 (328 °C) to TT5W25 (376 °C) (*cf.* Fig. IV.3 and Table IV.3). A step increase by 10 mol.% in TiO$_2$ induced an overall rise of T_g that is twice more consequential (increase by ~50 °C) than in the case of WO$_3$ (increase by ~25 °C). We assign the T_g increase to the fact that Ti–O and W–O bonds have higher dissociation energies compared to Te–O bonds, namely, 666.5 kJ.mol^{-1}, 720 kJ.mol^{-1} and 377 kJ.mol^{-1} respectively [194].

Sample	T_g (°C) ± 1	T_O (°C) ± 1	ΔT (°C) ± 1
TT5W5	328	359	31
TT5W10	341	377	36
TT5W15	355	393	38
TT5W20	365	403	38
TT5W25	376	417	41
TT10W5	353	398	45
TT10W10	364	410	46
TT10W15	376	428	52
TT10W20	389	443	54
TT10W25	399	456	57
TT15W5	380	418	38
TT15W10	391	430	39
TT15W15	405	445	40
TT15W20	414	466	52
TT15W25	426	474	48

Table IV.3. Thermal characteristics of TTxWy glasses measured by DSC.

It is worth pointing out that the thermal stabilities ($\Delta T = T_O - T_g$), which reflect the ability of the glass network to resist against devitrification upon heating above T_g, are fairly moderate among TTxWy glasses ($\Delta T_{min} = 31$ °C and $\Delta T_{max} = 57$ °C) with an average of 44 °C (versus 64 °C in pure TeO$_2$ glass, *cf.* Fig. III.1). These thermal stabilities might represent a limiting factor for the use of these glasses in the optical fiber technology, for which as an "experimental standard", a minimum value of 100 °C is needed. Adding TiO$_2$ induces an increase of ΔT from TT5Wy to TT10Wy glasses before a decrease in TT15Wy glass samples. It seems though that ΔT is marginally improved with continuous increase in WO$_3$ content.
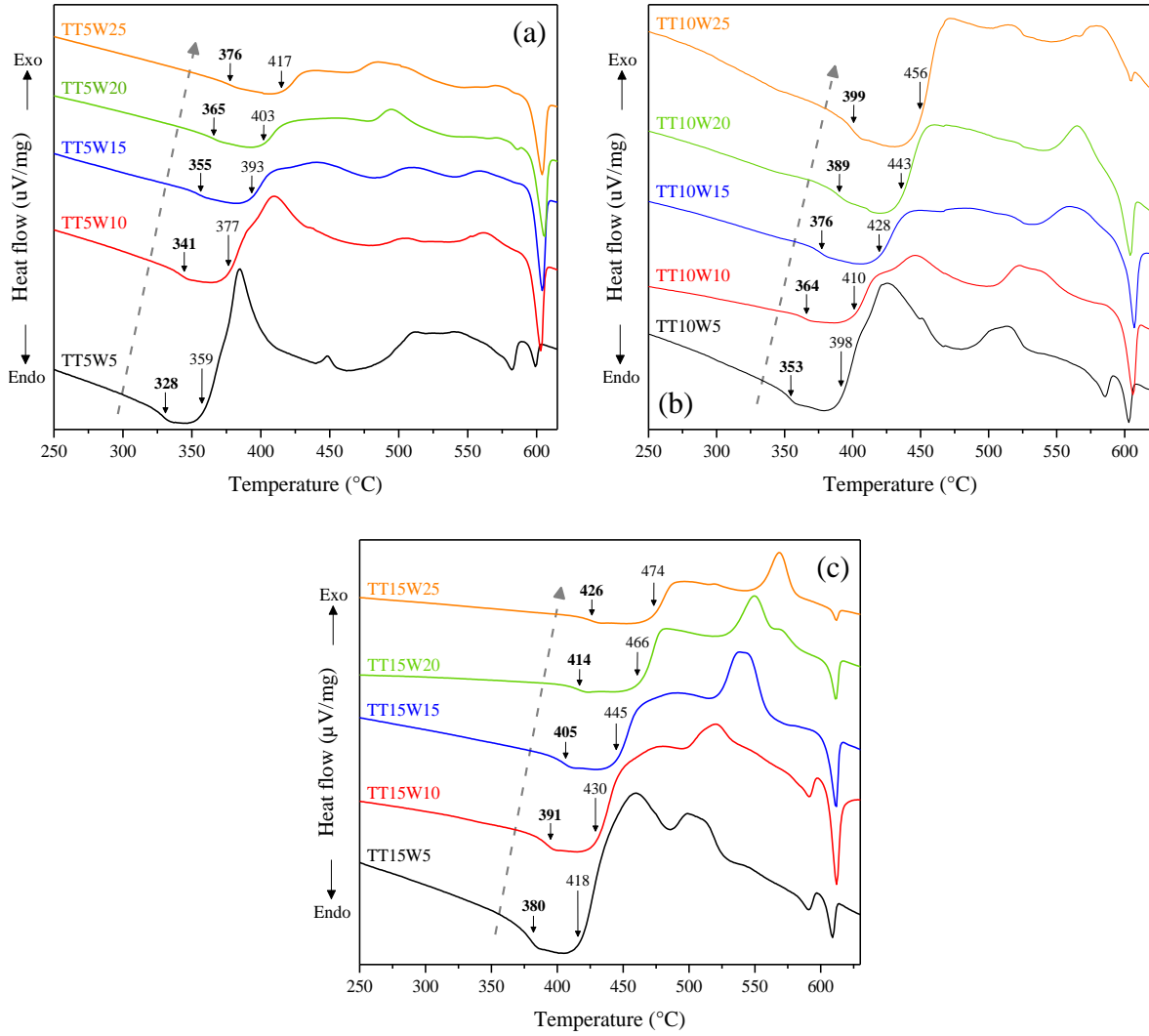
Fig. IV.3. DSC curves of TTxWy glasses with glass transition T_g and onset crystallization T_O temperatures given in bold and non-bold typefaces respectively.

To identify the compounds crystallizing upon heating, we have performed high-temperature X-ray powder diffraction (*cf. section III.3.3.2* for more details) on the $70TeO_2\text{-}15TiO_2\text{-}15WO_3$ glass composition (TT15W15). The recorded XRD patterns are superimposed in Fig. IV.4. The first crystals start to appear at a temperature of 460 °C, *i.e.,* 55 °C higher than the T_g. The identified crystallizing compounds are α-TeO_2 and $TiTe_3O_8$. Upon heating, the peaks corresponding to these compounds become more intense, and thus suggesting their increasing crystallization extents. Moreover, $WO_{2.83}$ phase appears at 490 °C and persists up to 550 °C before transforming into γ-WO_3 phase at 580 °C. These crystallization events and phase transformations coincide with the exothermic events recorded on the DSC curve (Fig. IV.5).
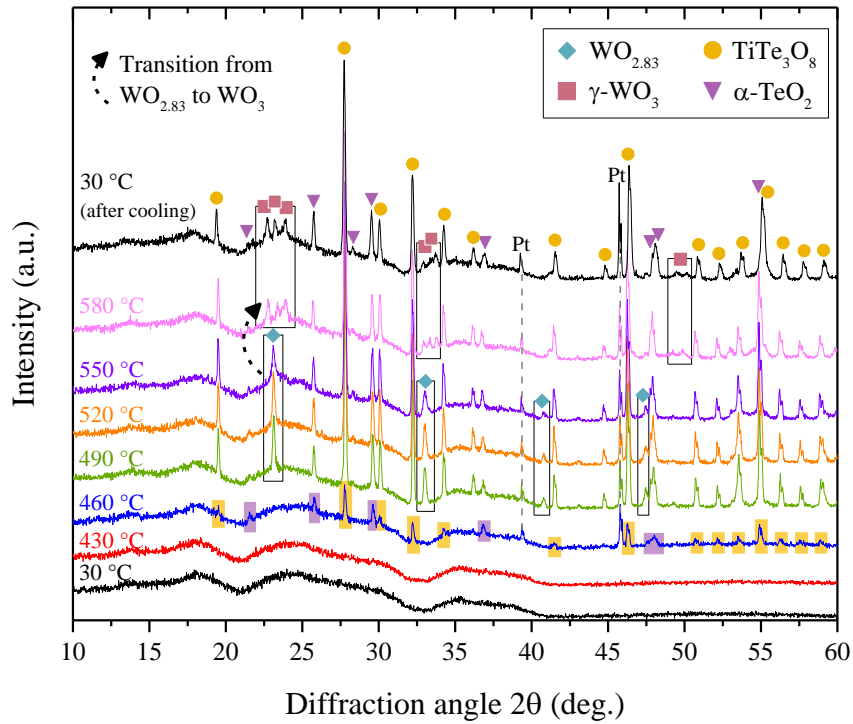
Fig. IV.4. High-temperature XRD patterns recorded from TT15W15 glass sample.
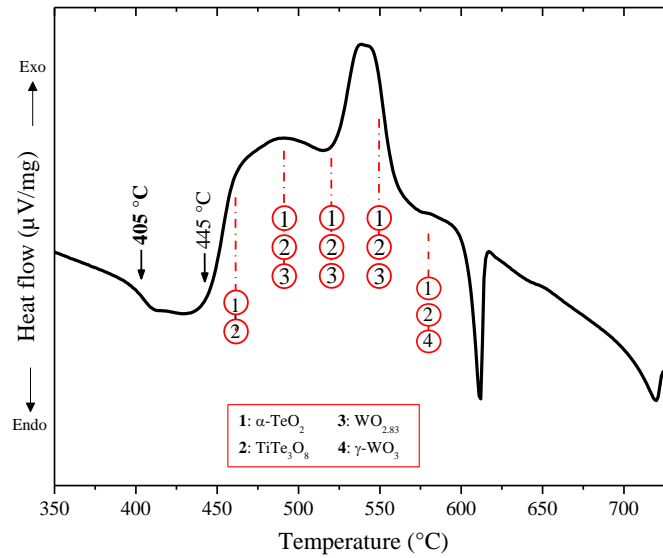
Fig. IV.5. DSC curve of TT15W15 with the identified crystal compounds.

IV.4. Structural properties of TeO₂-TiO₂-WO₃ glasses

IV.4.1. Background and state-of-the-art

It is well established that adding modifier oxides to TeO_2 glass induces the structural transformation of TeO_4 disphenoids into TeO_3 trigonal pyramids, and therefore contributes to

the short-range modification of the glass network [3,47,144]. This transformation is regarded as a "structural depolymerization" since it reduces the network crosslinking density by breaking Te–O–Te bridges. Moreover, it has been demonstrated that this transformation is accompanied with a decrease of the nonlinear optical properties [3,45]. By means of Raman spectroscopy, some authors claimed that adding WO_3 induces this structural transformation in TeO_2-based glasses [127,195], which is not the case upon adding TiO_2 [96,99,140].

Adding TiO_2 to TeO_2 allows to *(i)* enhance the glass-forming ability and obtain homogeneous glasses in the $(100-x)TeO_2$-$xTiO_2$ binary system with a glass-forming domain up to x = 18 mol.%, and *(ii)* maintain the original structural organization of pure TeO_2 glass [57,140]. Hence, TiO_2-containing TeO_2-based glasses are of special interest thanks to the positive role of TiO_2 in conserving the glass network of pure TeO_2 which contributes to the high linear and nonlinear optical properties [41,45,53,99]. Most of the preceding studies [53,57,96] dealing with the structure of TeO_2-TiO_2 glasses supported the existence of Te–O–Ti bridges replacing the Te–O–Te ones in the glass network upon increasing TiO_2 content. This idea is based on the unique phase from the TeO_2-TiO_2 system, $TiTe_3O_8$ [79,92], which features interconnected TeO_4 and TiO_6 polyhedra via nearly symmetric Te–O–Ti bridges with the following bond lengths: 1.867 Å and 1.955 Å respectively (*cf. section I.5.1.1*).

With increasing WO_3 content in binary TeO_2-WO_3 glasses, the thermal and optical properties are progressively improved [41,62]. These glasses have been extensively studied and the fact that no crystalline phase, *i.e.* no "parent crystalline model", has ever been identified in the binary TeO_2-WO_3 system led to considerable efforts for the understanding of their structural features. Most of these studies focused on the tungsten local environment (to demonstrate whether WO_4 or WO_6 polyhedra exist in the glass network) using IR and/or Raman spectroscopy techniques [103,104,196,197]; yet, despite many efforts, this basic information is still obscure and controversial [107,108,164,165,195].

IV.4.2. Structural effect of adding TiO_2

According to Dietzel's field strength theory (*cf. Chapter II*), in binary oxide melts where the two constituent cations have very close field strength (FS) values, a slow cooling rate (towards crystallization) is expected to lead to a **solid solution** type of organization in the crystal; whereas faster cooling/quenching rates (towards glass formation) would result in a **phase separation** between the two pure oxide phases. It is very important to highlight that *(i)* the FS

values for Te^{4+} (0.990) and Ti^{4+} (1.047) cations are very close, and that *(ii)* the only reported crystal compound from binary TeO_2-TiO_2 system, namely $TiTe_3O_8$, is in fact a solid solution of TiO_2 in TeO_2 with a ratio of 1:3 respectively. Therefore, since the FS theory proves to be valid for the equilibrium TeO_2-TiO_2 system, one would expect that it would successfully predict the structure of binary TTx glasses as well. In other words, a phase separation within the glass network could be predicted and thus resulting in TeO_2-rich and TiO_2-rich regions. The limited experimentally-detected glass forming ability upon adding TiO_2 (maximum of x = 15 mol.% in both TTx and TTxWy glasses) supports this predicted heterogeneous nature of the glass networks.

To elucidate the structural effect of adding TiO_2, we first examine the TTx system before rushing into the more complicated TTxWy system given that: *(i)* identical glass forming ability upon adding TiO_2 (limited to 15 mol.%) is found in TTx and TTxWy systems; *(ii)* the close force constants of Te–O and Ti–O bonds (*cf.* Fig. 5 in [140]) would likely cause strong overlapping of their corresponding bands in the Raman spectra of TiO_2-containing TeO_2-based glasses.

- ***Binary (100-x)TeO₂-xTiO₂ glasses (TTx glasses)***

As detailed in *section III.2.2*, binary TTx glasses were prepared using the melting-fast-quenching (MFQ) technique. The recorded perpendicular (VH) and parallel (VV) polarized Raman spectra are given Fig. IV.6 and Fig. IV.7. Both sets of spectra show a Raman intensity increase at ~445, ~615 and ~850 cm^{-1} upon adding TiO_2 from 2.5 to 15 mol.%. Moreover, an intensity decrease of bands at ~660 and ~730 cm^{-1} is observed from the VV-polarized spectra. The vibrational assignment of these bands is given in Table IV.4 (*cf. section IV.4.3*); particularly, that of Ti–O vibrations is based on the refs [198–200].

Fig. IV.6. Total-area averaged VH-polarized Raman spectra of TTx glasses (x = 0, 2.5, 5, 10 and 15). The Raman spectra of nano-rutile TiO₂ is reproduced from [198].

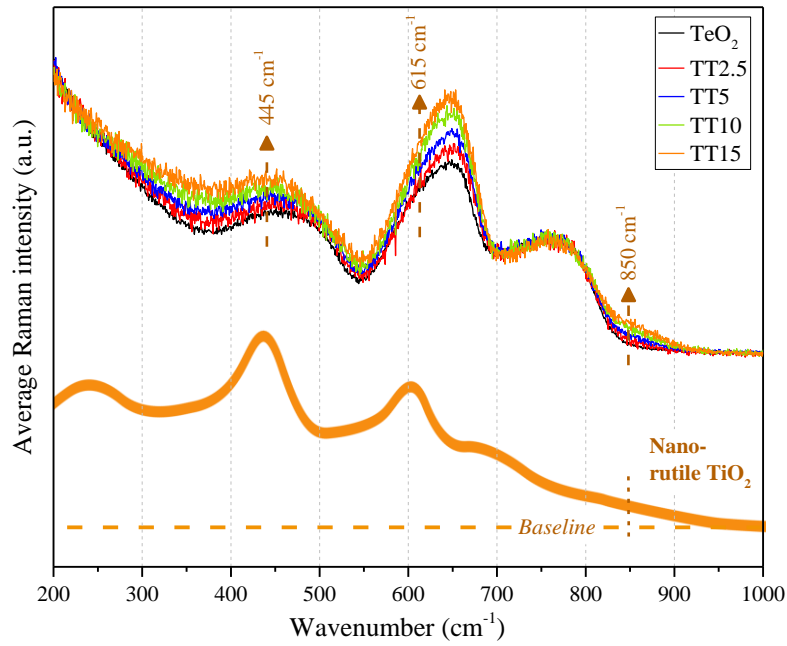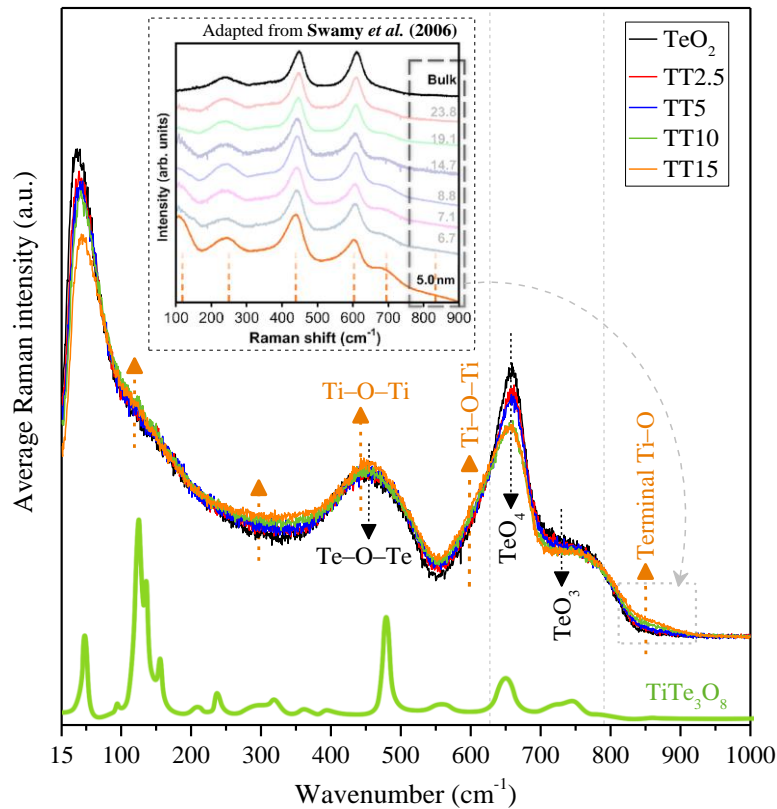Fig. IV.7. Total-area averaged VV-polarized Raman spectra of TTx glasses (x = 0, 2.5, 5, 10 and 15) along with the Raman spectrum of TiTe₃O₈ compound (from [140]). The inset is adapted from Fig. 2 in [198] and shows Raman spectra recorded from rutile TiO₂ samples with different average crystallite sizes ranging from 5 nm up to the bulk.

Since the bands at ~660 and ~730 cm^{-1} are associated with Te–O vibrations in TeO$_4$ and TeO$_3$ units respectively, their decreasing number and/or polarizability change with addition of TiO$_2$ suggests that no structural depolymerization takes place in TTx glasses (as opposed to a striking depolymerization observed for example in TeO$_2$-Tl$_2$O glassy system [58] where a decreasing Raman intensity associated with TeO$_4$ units and increasing intensity relative to TeO$_3$ takes place, *cf.* Fig. I.5).

It appears that this decreasing number of TeO$_4$ and TeO$_3$ units is compensated by an increasing number of Ti–O–Ti bridges (at ~445 cm^{-1} and ~615 cm^{-1}) and terminal Ti–O bonds (at ~850 cm^{-1}). The presence of Ti–O–Ti and Ti–O linkages in the glass network is supported by the features of the Raman spectrum of nano-rutile TiO$_2$ (*cf.* inset in Fig. IV.7). As highlighted in the inset, the shoulder at ~850 cm^{-1} is only detected from the few-nanometer-sized rutile TiO$_2$ samples (*cf.* spectrum in orange) and absent in the bulk sample (spectrum in black). It is associated with the antisymmetric stretching vibrations of Ti–O bonds from distorted TiO$_{6-x}$ polyhedra at the surface of TiO$_2$ nanoparticles [198,199]. Therefore, it seems that amorphous "rutile-like" TiO$_2$-rich regions (of few nanometers) exist separately from the TeO$_2$-rich network and their number increases with increasing TiO$_2$ content from 2.5 to 15 mol.% in TTx glasses before an extensive growth takes place via the crystallization of rutile TiO$_2$ at 20 mol.% detected by X-ray powder diffraction.

A thorough search of the relevant literature yielded only a single and unanimously accepted structural description of the TiO$_2$-containing TeO$_2$-based glasses [53,57,96,140,201,202] (and above all, the binary TeO$_2$-TiO$_2$ glasses [57,96,140]). This description is based on the participation of symmetric Te–O–Ti bridges in the glass network by replacing the original Te–O–Te ones. It was largely supported by the fact that these two bridges are chemically indiscernible, thus explaining the insignificant changes in the Raman spectra upon adding TiO$_2$. However, as expressed in the following, we provide here a new viewpoint regarding this description.

Let us consider the symmetric Te–O–Ti bridges. The latter exist in the TiTe$_3$O$_8$ compound, and their symmetric stretching vibrational mode gives rise to the most intense band at ~477 cm^{-1} (*cf.* Fig. IV.6 and Fig. IV.7). If those symmetric Te–O–Ti bridges truly constituted the backbone of the structural network in TTx glasses, then we would have recorded a significant intensity increase at ~477 cm^{-1} upon adding TiO$_2$, which is clearly not the case when analyzing the spectra of TTx glasses. Therefore, since the number of Te–O–Ti bridges does not increase with addition of TiO$_2$ and since the vibrational signature of nano-rutile TiO$_2$ is observed, we propose

that the structure of the glass network is made of "rutile-like" TiO_2-rich regions in a TeO_2-rich network implying a phase separation as initially predicted using the field strength theory.

- ***Ternary $(100-x-y)TeO_2-xTiO_2-yWO_3$ glasses (TTxWy glasses)***

The Raman spectra of TTxWy glasses upon adding TiO_2 are given in Fig. IV.8. A similar spectral evolution, *i.e.* intensity increase at ~445, ~615 and ~850 cm^{-1} is observed from TTxWy glasses. Because of two overlapping bands at ~860 and ~925 cm^{-1} due to vibrating W–O bonds, the intensity increase at ~850 cm^{-1} is less noticeable than from TTx glasses. It is important to recall here that, same as in binary TTx, the glass-forming domain in TTxWy is limited to only 15 mol.% of TiO_2. Hence, it seems that the influence of TiO_2 on a network of either pure TeO_2 (TTx system) or WO_3-containing TeO_2 (TTxWy system) is indifferent.

Fig. IV.8. Evolution of total-area averaged VH-polarized Raman spectra of TTxWy glasses as a function of TiO_2 content. The low-wavenumber (boson peak) and mid- to high-wavenumber regions are supplied apart for more clarity.

From the above discussion, we argue that a phase separation between amorphous TeO_2-rich and amorphous "rutile-like" TiO_2-rich regions occurs in TTxWy glasses and very likely in TiO_2-

containing TeO$_2$-based glasses. This interpretation is shared with a previous study [71] that predicted phase separation in the 75TeO$_2$-25TiO$_2$ glass composition.

IV.4.3. Structural effect of adding WO$_3$

The evolving features of the Raman spectra of TTxWy glasses with increasing WO$_3$ content (Fig. IV.9) are in agreement with the reported studies on WO$_3$-containing TeO$_2$-based glasses by Raman spectroscopy [103,108,195]. These studies have shown that three additional bands (at ~360, ~860 and ~925 cm^{-1}) emerge at the spectra and increase in intensity upon adding WO$_3$.

Since the same structural evolutions are observed from TT5Wy, TT10Wy and TT15Wy samples, we suggest to focus on the set of TT5Wy for the sake of simplicity (Fig. IV.10). One can assume that substituting TeO$_2$ with WO$_3$ does not result in any significant change of the glass network structure. This is particularly true for the Raman response within the ~400-800 cm^{-1} which is typically characteristic of the network of Te–O–Te bridges.
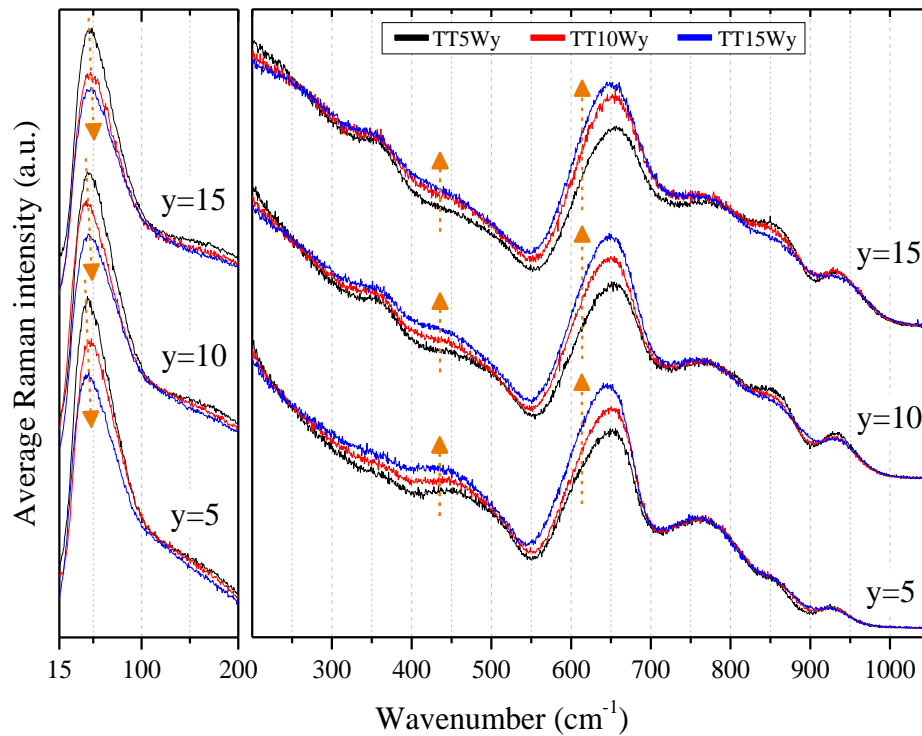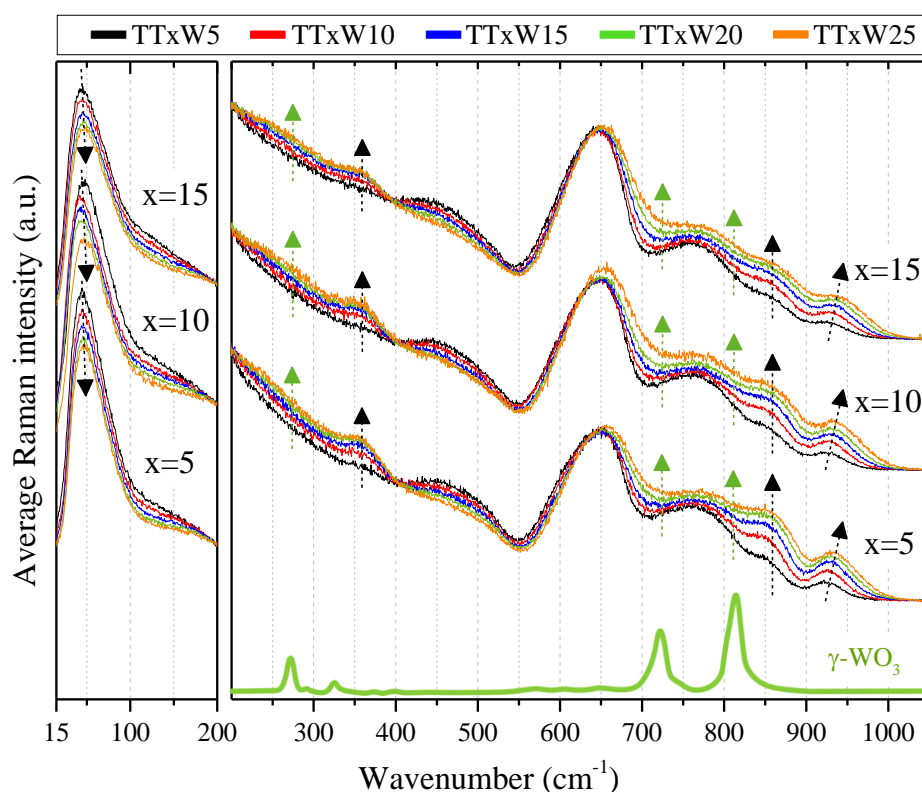

Fig. IV.9. Evolution of total-area averaged VH-polarized Raman spectra of TTxWy glasses as a function of WO$_3$ content. The low-wavenumber (boson peak) and mid- to high-wavenumber regions are supplied apart for more clarity. The Raman spectrum of γ-WO$_3$ is reproduced from [101].
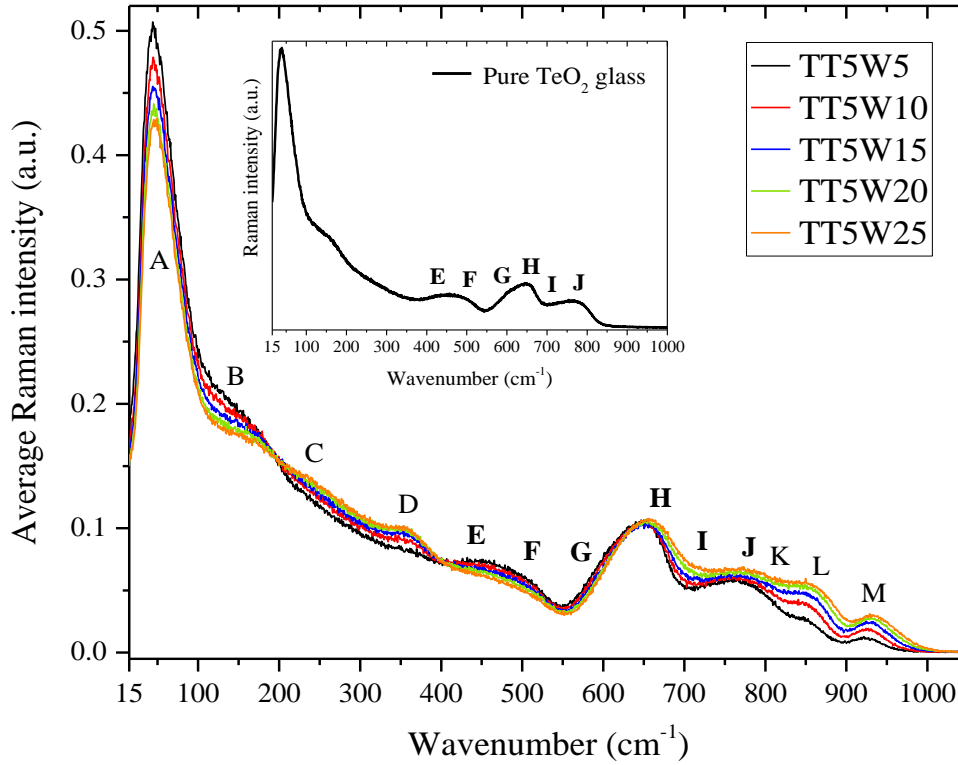
Fig. IV.10. Total-area averaged VH-polarized Raman spectra of TT5Wy glasses. The labels A–M correspond to the inserted bands for spectral decomposition. Inset: measured Raman spectrum of pure TeO_2 glass featuring the three major broad bands (E+F, G+H and I+J).

The assignment of the Raman bands is given in Table IV.4. The origin of bands E-J (425-772 cm^{-1}) is supported by previous pioneer works on the vibrational and structural properties of the three TeO_2 polymorphs (α [64], β [64] and γ [63]). The other identified Raman bands (C-D extending from 230 to 351 cm^{-1} and K-M from 820 to ~934 cm^{-1}) are associated with the vibrational response of distorted WO_6 octahedra. The basis of the previous assignment is a analysis of the vibrational (Raman spectra) *vs.* structural features that we conducted on a large number of tungsten-containing oxides (metal tungstates for the most part, *e.g.*, K_2WO_4 [203], $K_2W_3O_{10}$ [204], $K_2W_4O_{13}$ [205], $Rb_{22}W_{32}O_{107}$ [206], $ZnWO_4$ [207], Sr_2NiWO_6 [208]). A similar approach has been previously undertaken on few tungstates by Sekiya *et al.* [103]. In the low-wavenumber region, the band B is attributed to intra-chain vibrations of Te–Te bonds (as in the amorphous metallic trigonal Te [169]) and the band A (boson peak) is linked to the glass network at medium-range scale [168,209,210].

Inserted band	Wavenumber (cm^{-1})	Raman band assignments
A	44.0 – 45.6	• The boson peak, ascribed to an excess density of vibrational states [168].
B	146.9 (*fixed*)	• Intra-chain vibrations of Te–Te bonds (as in amorphous metallic t-Te) [169].
C	230 (*fixed*)	• Bending vibrations of WO$_6$ octahedra (as in γ-WO$_3$) [101].
D	351 (*fixed*)	• Bending vibrations of distorted WO$_6$ octahedra [101].
E	**425 (*fixed*)**	• **Symmetric stretching vibrations in nearly symmetric Te–O–Te bridges (as in γ-TeO$_2$)** [63,64]. • Motions of oxygen atoms in O–Ti–O bridges along the *c* axis (E$_g$ mode of rutile TiO$_2$) [200].
F	**501.8 – 505.8**	• **Symmetric stretching vibrations in Te–O–Te bridges** [63,64].
G	**607 (*fixed*)**	• **Asymmetric stretching vibrations in nearly symmetric Te–O–Te bridges (as in γ-TeO$_2$)** [63,64]. • Motions of O atoms in O–Ti–O bridges perpendicular to the *c* axis (A$_{1g}$ mode of rutile TiO$_2$) [200].
H	**657.9 – 660.4**	• **Asymmetric stretching vibrations in asymmetric Te–O–Te bridges** [63,64].
I	**715 (*fixed*)**	• **Asymmetric stretching vibrations in asymmetric Te–O–Te bridges** [63,64]. • Symmetric stretching vibrations in W–O–W bridges (as in γ-WO$_3$) [101].
J	**772 (*fixed*)**	• **Asymmetric stretching of essentially covalent Te–$_{eq}$O bonds** [63,64].
K	820 (*fixed*)	• Asymmetric stretching vibrations in W–O–W bridges (as in γ-WO$_3$) [101].
L	852.3 – 863.1	• Stretching vibrations of W–O bonds in W–O–W bridges [103]. • Antisymmetric stretching vibrations of Ti–O bonds (B$_{2g}$ mode of rutile TiO$_2$) [198,199].
M	925 – 934	• Asymmetric stretching vibrations of W–O bonds [101].

Table IV.4. Wavenumbers and vibrational assignments of the inserted bands. Raman bands arising from TeO$_2$ network and their assignments are highlighted in bold typeface. In the spectral decomposition process, the wavenumbers of A, F, H, L and M bands were unconstrained and are given herein as ranges from the set of TT5Wy glasses with increasing y.

In the following, we mainly concentrate on the structural evolutions with increasing WO$_3$ content (at constant TiO$_2$ content) based on the Raman spectral decomposition results (*cf. section III.3.4.3* for more details on the decomposition process).

As can be seen in Fig. IV.10, the features shown by the set of vibrational modes of Te–O bonds in asymmetric and nearly symmetric Te–O–Te bridges (bands E-J), compared to those of pure TeO$_2$ glass, have only been slightly modified in terms of their bands' profiles, positions and intensity ratios upon increasing WO$_3$ content. The key information with respect to the

crosslinking of Te–O–Te bridges within the glass network is contained within the 400-550 cm^{-1} range (bands E and F). In this region, the intensity barely decreases suggesting that the network of Te–O–Te bridges has been only slightly modified. Thus, it seems that adding WO$_3$ does not considerably alter the original structural features within the network of Te–O–Te bridges.

In order to exclude the compositional effect, we have calculated the normalized intensities of the decomposed bands E–H by dividing their areas by the TeO$_2$ molar content (attributed to vibrations of Te–O bonds) and those of the bands D and K–M by the WO$_3$ molar content (attributed to vibrations of W–O bonds). The compositional-dependence of the normalized intensities of these bands in TT5Wy glasses is plotted in Fig. IV.11. As mentioned earlier, almost the same revealed trends for TT5Wy are observed in TT10Wy and TT15Wy glasses as well (*cf.* Table IV.5 for bands E-H). A more extended analysis of the effect of WO$_3$ on the structure of TT5Wy, TT10Wy and TT15Wy sets of glasses is highlighted in the *section V.4.3* in comparison with (100-x-y)TeO$_2$-xNbO$_{2.5}$-yWO$_3$ glasses (TNxWy glasses).
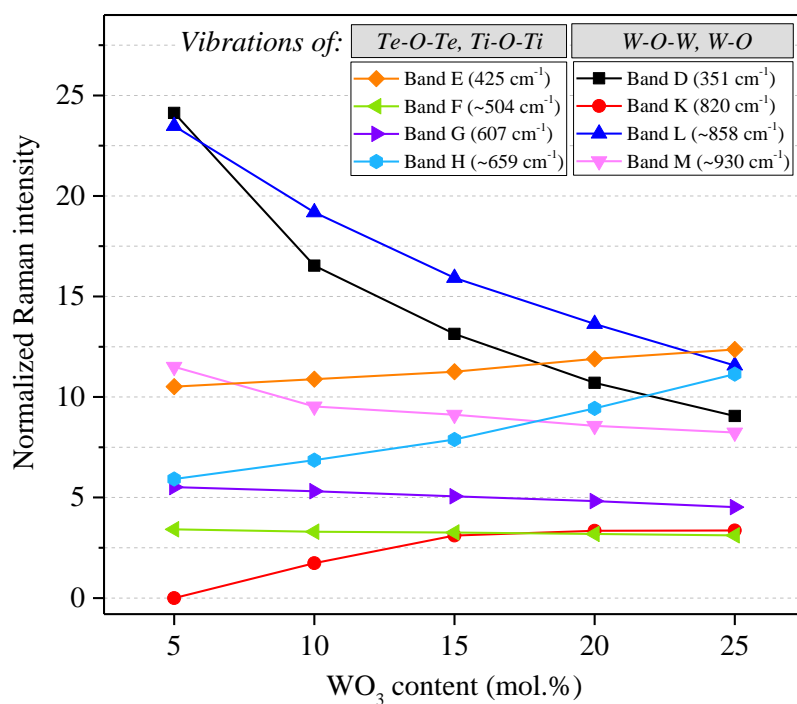
Fig. IV.11. Compositional dependence of the normalized intensities of inserted bands for the Raman spectral decomposition of TT5Wy glasses.

Set of samples	Samples	Raman band normalized intensity			
		Band E	Band F	Band G	Band H
TT5Wy	TT5W5	10.519	3.418	5.514	5.920
	TT5W10	10.883	3.296	5.314	6.858
	TT5W15	11.262	3.256	5.057	7.888
	TT5W20	11.901	3.188	4.822	9.435
	TT5W25	12.360	3.113	4.519	11.140
Intensity evolution (%)		+17.50	-8.95	-18.04	+88.18
TT10Wy	TT10W5	12.045	3.410	6.257	7.121
	TT10W10	12.508	3.307	6.430	7.909
	TT10W15	12.836	3.232	6.223	9.294
	TT10W20	13.429	3.233	6.172	10.783
	TT10W25	14.531	3.528	5.690	13.591
Intensity evolution (%)		+20.64	+3.44	-9.05	+90.86
TT15Wy	TT15W5	14.215	3.290	7.362	8.149
	TT15W10	14.592	3.243	7.172	9.337
	TT15W15	15.209	3.357	7.134	11.011
	TT15W20	15.887	3.427	6.978	12.923
	TT15W25	16.578	3.610	6.928	15.102
Intensity evolution (%)		+16.62	+9.72	-5.90	+85.32

Table IV.5. Decomposition results of bands E-H at the Raman spectra of TTxWy glasses.

Regarding the TeO_2-rich network, the evolution of the normalized intensities of bands E-G suggests a minor structural modification of the glass network since the bands F and G seem to be unaffected upon adding WO_3. The band E shows a moderate increase of its normalized intensity that might be due to a slightly increasing number of nearly symmetric Te–O–Te bridges. Given the relatively insignificant modification of the crosslinked network of Te–O–Te bridges, and in agreement with the forthcoming discussion on WO_3 effect, we assign the increasing intensity of bands I and J (attributed to vibrations of Te–O and W–O bonds) to an increase of W–O–W bridges as in γ-WO_3. Since these two bands are highly interactive via overlapping, we intentionally omitted their compositional evolutions from Table IV.5 and Fig. IV.11. Increasing W–O–W bridges in the glass network upon adding WO_3 is also responsible for the broadening of the band H (assigned to asymmetric stretching vibrations in asymmetric Te–O–Te bridges) observed in Fig. IV.10, and which results in the increase of its normalized intensity (Fig. IV.11). It is important to recall that the band H is inserted as a fully unconstrained band, and therefore, increasing its width to correctly fit the observed broadening is expected to result in a normalized intensity increase. The involvement of W–O–W bridges in the band H makes it complicated to interpret the evolution of its normalized intensity upon adding WO_3, which is, therefore, disregarded in this work.

Let us now consider the Raman bands D, K, L and M associated with distorted WO_6 octahedra. The normalized intensity decrease of the bands D, L and M upon increasing WO_3 content implies that less and less short W–O bonds (shorter than ~1.80 Å) exist in the network. In other words, less and less uniformly dispersed WO_6 octahedra are directly connected to the glass network. In fact, the normalized intensity increase of the band K suggests an increase of the number of corner-sharing WO_6 octahedra as in γ-WO_3 (also supported by Sekiya et al. [103] in TeO_2-WO_3 glasses). Therefore, it seems that the intensity increase of the large shoulder within the ~660-820 cm^{-1} range (cf. Fig. IV.10) arises from vibrating W–O–W bridges in the continuously growing WO_3-like regions upon increasing WO_3 content. It is important to recall that within this wavenumber range, symmetric and asymmetric stretching vibrational modes of W–O–W bridges are expected in the γ-WO_3 phase at around 715 and 820 cm^{-1} respectively (cf. Raman spectrum in Fig. IV.9). Moreover, the weak intensity increase in the 200-300 cm^{-1} range is probably due to bending vibrational modes of WO_6 octahedra as observed in γ-WO_3 [101]. These findings are in agreement with the X-ray photoelectron spectroscopy (XPS) results [105] that show a decrease of O1s binding energy in (100-x)TeO_2-xWO_3 glasses from x = 5 to 30 mol.%, indicating that oxide ions are more likely to participate within the glass network as bridging ones.

Concerning the evolution of the band A (boson peak), the position of its maximum intensity insignificantly red-shifts accompanied with an intensity decrease with addition of TiO_2 or WO_3 contents (cf. Fig. IV.8 and Fig. IV.9). According to previous works [168,171], this evolution of boson peak's position and intensity could suggest a crosslinking density increase in the glass network at the medium-range scale. This behavior is in agreement with the continuous increase of the glass transition temperature upon adding TiO_2 or WO_3.

Since the same compositional evolutions of structural features as revealed by Raman spectroscopy are observed upon increasing WO_3 content at different TiO_2 contents with no further emerging bands (Fig. IV.9), it seems unlikely that Ti–O–W bridges participate in the crosslinking within the glass network.

From the above discussion, we argue that unlike the peculiar structural effect of TiO_2 promoting a phase separation within the amorphous glass network, the incorporation of WO_3 results in uniformly dispersed (throughout the glass network) WO_6 octahedra which tend to form amorphous WO_3-like regions before ending with crystallized γ-WO_3 at 30 mol.%. This might explain why the addition of TiO_2 and WO_3 results in relatively moderate thermal stabilities of TTxWy glasses and relatively limited glass-forming domain.

IV.4.3.1. The W^{6+} local environment peculiarity

To the best of our knowledge, the fact that has never been brought to light in the literature is the identical structural behavior of tungsten polyhedra in various glass-forming systems. The supporting evidence for this statement is based on the comparison of reported experimental results obtained by Raman and X-ray absorption spectroscopies on WO_3-containing glasses in the following glass-forming systems: B_2O_3-, P_2O_5- and TeO_2-based systems. Upon adding WO_3, all of these systems tend to share common vibrational properties as revealed by Raman spectroscopy: the same vibrational modes specific to tungsten polyhedra are recorded at around 360, 860 and 930 cm^{-1} in B_2O_3- (Fig. 2 in [211]), P_2O_5- (Fig. 4 in [212]) and TeO_2- (Fig. 1 in [103]) based systems. Using the X-ray absorption near edge structure (XANES), W^{6+} cations are found in distorted octahedral coordination environments in both P_2O_5- (Fig. 1 in [212]) and TeO_2- (Fig. 5 in [105]) based systems.

It is important to note that, given the fundamental difference among the cations (B^{3+}, P^{5+} and Te^{4+}), one would rather expect a set of variable coordination environments around W^{6+} cations within the glass networks of each of these systems. According to Dietzel's field strength theory [20,213] (*cf. Chapter II*), P^{5+} cations have the highest field strength (FS) among all of the glass-forming cations with a value of 2.164; those specific to B^{3+} and Te^{4+} cations are 1.622 and 0.990 respectively. As for the "modifier" W^{6+} cation, its field strength (1.578) leaves the door open for a wide range of possible structural configurations within the respective glass networks of each of those systems. However, despite the significant difference of the field strengths among B^{3+}, P^{5+} and Te^{4+} glass-forming cations, W^{6+} cations seem to exhibit identical structural features in each of the B_2O_3-, P_2O_5- and TeO_2-based glasses. This suggests that the responsible factor behind this particular behavior might be related to the intrinsic properties of W^{6+} cations, and particularly their high out-of-center distortion tendency that leads to the observed (by XANES) distorted coordination environments. In fact, the bond network of nearest neighbors to octahedrally-coordinaetd d^0 transition-metal cations is tightly correlated with the degree of such distortions [214].

Taking all the above into consideration, we suggest the following hypothesis regarding the common structural properties of W^{6+} cations in the various glass-forming systems. In the same manner as in TTxWy glasses, the networks of B_2O_3-, P_2O_5- and TeO_2-based glasses feature uniformly distributed WO_6 octahedra which tend to interconnect via corner-sharing and thereby forming WO_3-like regions especially at high WO_3 contents.

IV.5. Linear and nonlinear optical properties of TeO$_2$-TiO$_2$-WO$_3$ glasses

In the following, we report the linear and nonlinear optical properties measured from double side polished glass pellets in the TeO$_2$-TiO$_2$-WO$_3$ system. The set of optical parameters and characterization techniques used here are introduced in *section III.3.5*.

IV.5.1. Linear optical properties of TeO$_2$-TiO$_2$-WO$_3$ glasses

IV.5.1.1. Refractive index, optical band gap and Urbach energies by UV-Vis-NIR optical transmission

IV.5.1.1.1. Refractive index from the optical transmission spectra

By means of UV-Vis-NIR spectroscopy, we have recorded the optical transmission spectra of TTxWy glass pellets (1.44-1.47 mm in thickness) over a wide wavelength range extending from 300 to 3300 nm (*cf.* Fig. IV.12). The optical transmission spectra of 14 out of 15 glass samples show a transparency over 75% in the 800-2600 nm range. Only the sample TT15W25 showed a markedly lower transparency of ~68% in this region. This can be related to its peculiar composition (richest in both TiO$_2$ and WO$_3$ oxides) at the boundary of the glass-forming domain. The large absorption band onsetting at ~2800 nm is recorded in all of the samples. It corresponds to the stretching mode of bound hydroxyl groups (R-OH), and both symmetric and asymmetric stretching modes of H$_2$O molecules [215].

As shown in the plots of the three sets of glasses (Fig. IV.12), there is no clear transmission evolution (in the 800-2600 nm range) as a function of the glass composition. In fact, the transmission percentage is neither enhanced nor reduced upon adding WO$_3$ but it rather slightly fluctuates within a relatively narrow range of less than 1.5%. This is also the case with increasing TiO$_2$ content (see *e.g.*, TTxW5 glasses in Fig. IV.13).

The refractive indices were extracted from the optical transmission data at $\lambda = 1.5$ µm using the following equation: $T = 2n/(n^2+1)$. The refractive indices ($n_{1.5}$) are listed in Table IV.6. In general, the results suggest a practically constant behavior of the refractive index upon adding either TiO$_2$ or WO$_3$ with high values ranging approximately from ~2.10 to ~2.15. This is in agreement with literature as the refractive indices of bulk glasses belonging to three ternary WO$_3$-containing TeO$_2$-based systems (containing each TiO$_2$, Nb$_2$O$_5$ and Ta$_2$O$_5$) [109] also lie within the previous range. It should be stressed that this equation slightly underestimates the refractive index value since the multiple reflections of light are neglected and most of the reflection is considered to occur at the two air/glass interfaces (Fresnel reflection).
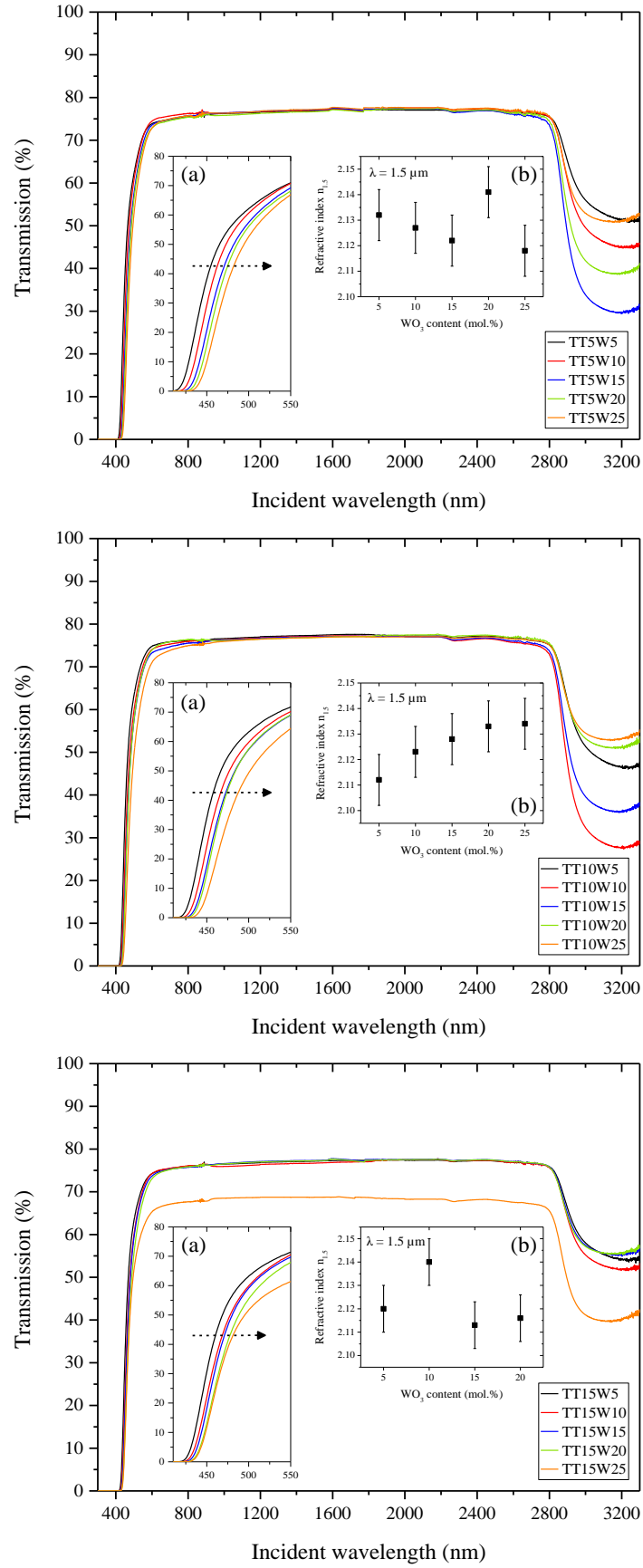
Fig. IV.12. UV-Vis-NIR optical transmission spectra of TTxWy glasses. Insets: (a) zoom-in plots of the UV absorption edge; (b) compositional dependence of the refractive index $n_{1.5}$ extracted at 1.5 µm.
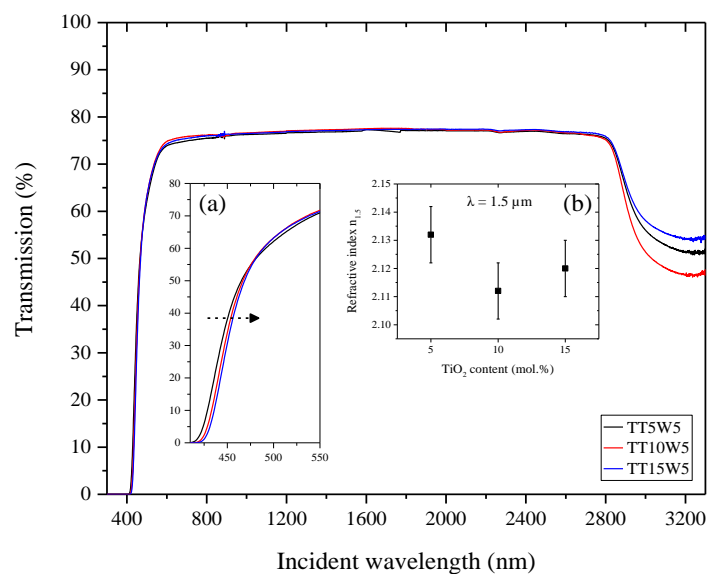
Fig. IV.13. UV-Vis-NIR optical transmission spectra of TTxW5 glasses. Insets for TTxW5: (a) zoom-in plot of the UV absorption edge; (b) compositional dependence of $n_{1.5}$ index extracted at 1.5 µm.

Sample	$n_{1.5}$ ± 0.010	n_∞	E_g (eV) ± 0.020	E_U (eV) ± 0.002
TT5W5	2.132	2.195 ± 0.015	2.880	0.105
TT5W10	2.127	2.188 ± 0.011	2.842	0.105
TT5W15	2.122	2.186 ± 0.027	2.789	0.106
TT5W20	2.141	2.173 ± 0.019	2.764	0.105
TT5W25	2.118	2.191 ± 0.020	2.744	0.107
TT10W5	2.112	2.185 ± 0.030	2.843	0.100
TT10W10	2.123	2.197 ± 0.014	2.812	0.103
TT10W15	2.128	2.182 ± 0.024	2.776	0.103
TT10W20	2.133	2.191 ± 0.013	2.758	0.103
TT10W25	2.134	2.190 ± 0.018	2.736	0.108
TT15W5	2.120	2.198 ± 0.024	2.826	0.096
TT15W10	2.140	2.198 ± 0.012	2.800	0.102
TT15W15	2.113	2.206 ± 0.015	2.782	0.100
TT15W20	2.116	2.196 ± 0.023	2.761	0.103
TT15W25	—	2.199 ± 0.011	2.758	0.100

Table IV.6. Refractive indices $n_{1.5}$ and n_∞, optical band gap E_g and Urbach E_U energies of TTxWy glasses.

The UV absorption edge red-shifts from 410-420 nm and across approximately 15-25 nm with increasing WO_3 content (in TT5Wy, TT10Wy and TT15Wy glasses, *cf.* Fig. IV.12(a)) implying

a gradual decrease of the optical band gap energy E_g. Likewise, a minor red-shift is observed from 410 to 420 nm upon adding TiO_2 in TTxW5 glasses (Fig. IV.13(a)). The color evolution of glass samples (described in *section IV.2*) is in agreement with the detected red-shifts of the absorption edge.

IV.5.1.1.2. Optical band gap energy E_g

We have extracted the optical band gap energy E_g for all TTxWy glasses from their respective UV absorption edges. Based on the wavelength-dependence of the approximate absorption coefficient (*cf.* Fig. IV.14(a)), we plotted $(\alpha h\nu)^{\frac{1}{2}}$ versus the incident photon energy $h\nu$, which is commonly known as Tauc plot, to estimate E_g (Fig. IV.14(b)). The E_g values lie in the range of 2.73–2.88 eV (*cf.* Table IV.6).

Decreasing E_g upon adding WO_3 in different TeO_2-based systems has been previously reported [216,217]. In agreement with literature, a slight decrease of E_g in TTxWy glasses is recorded upon increasing WO_3 content, namely from 5 mol.% (2.88 eV in TT5W5) to 25 mol.% (2.74 eV in TT5W25). Upon adding TiO_2, E_g tends towards a marginal decrease in WO_3-poor compositions (TTxW5) and seems to remain constant in WO_3-rich ones (TTxW25).
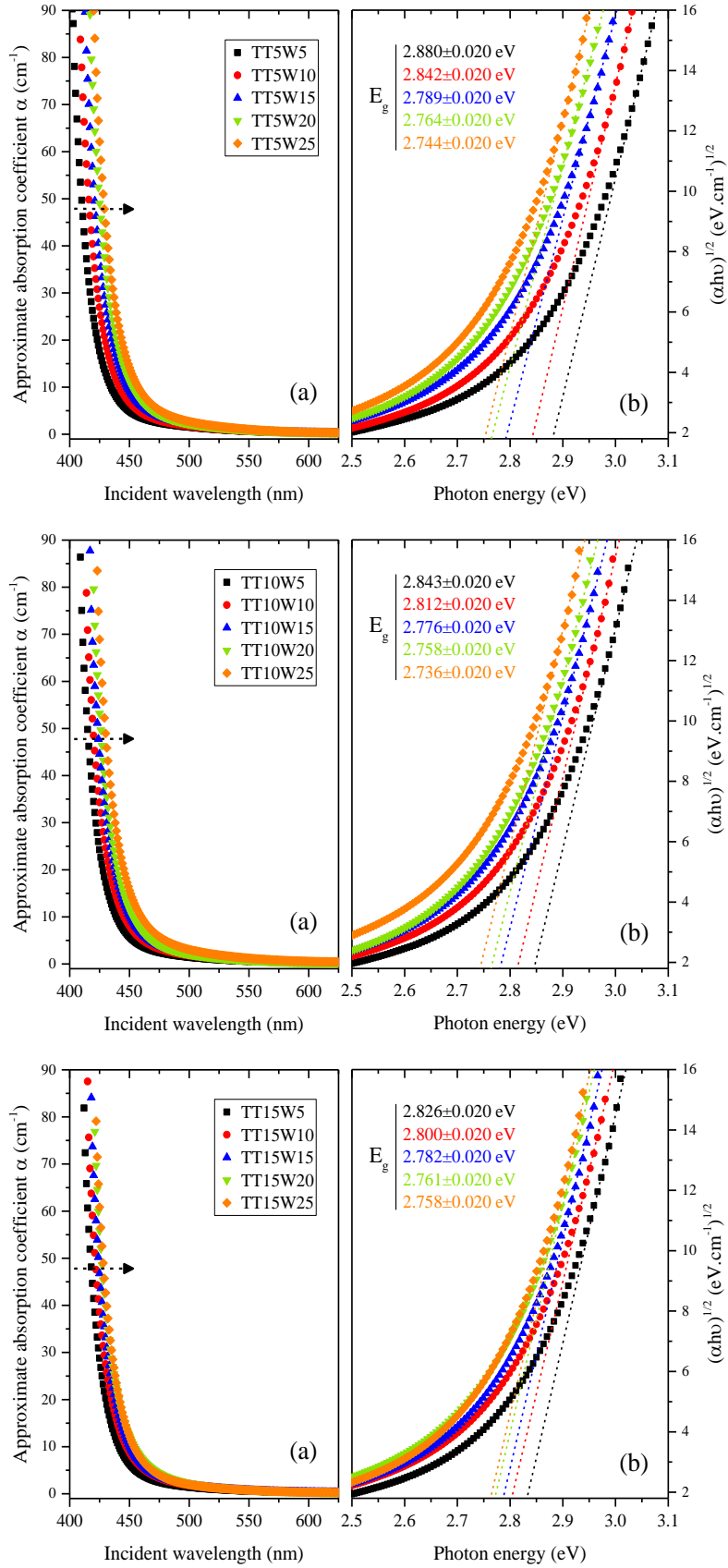
Fig. IV.14. (a) Evolution of the approximate absorption coefficient as a function of the incident wavelength in TTxWy glasses; (b) Tauc plot for the optical band gap energy E_g derived from the absorption coefficient.

IV.5.1.1.3. Urbach energy E_U

We also have extracted the Urbach energy E_U values. As explained in more details in *section III.3.5.1.2*, E_U is characteristic of the width of the band-tails at the top of the valence band and the bottom of the conduction band, thus estimating the density of localized states. A highly disordered glass network features a higher density of localized states in the band gap and thus having a high E_U value. The E_U value is obtained from the inverse of the slope of the straight line by plotting $\ln(\alpha)$ against hv (*cf.* Fig. IV.15).
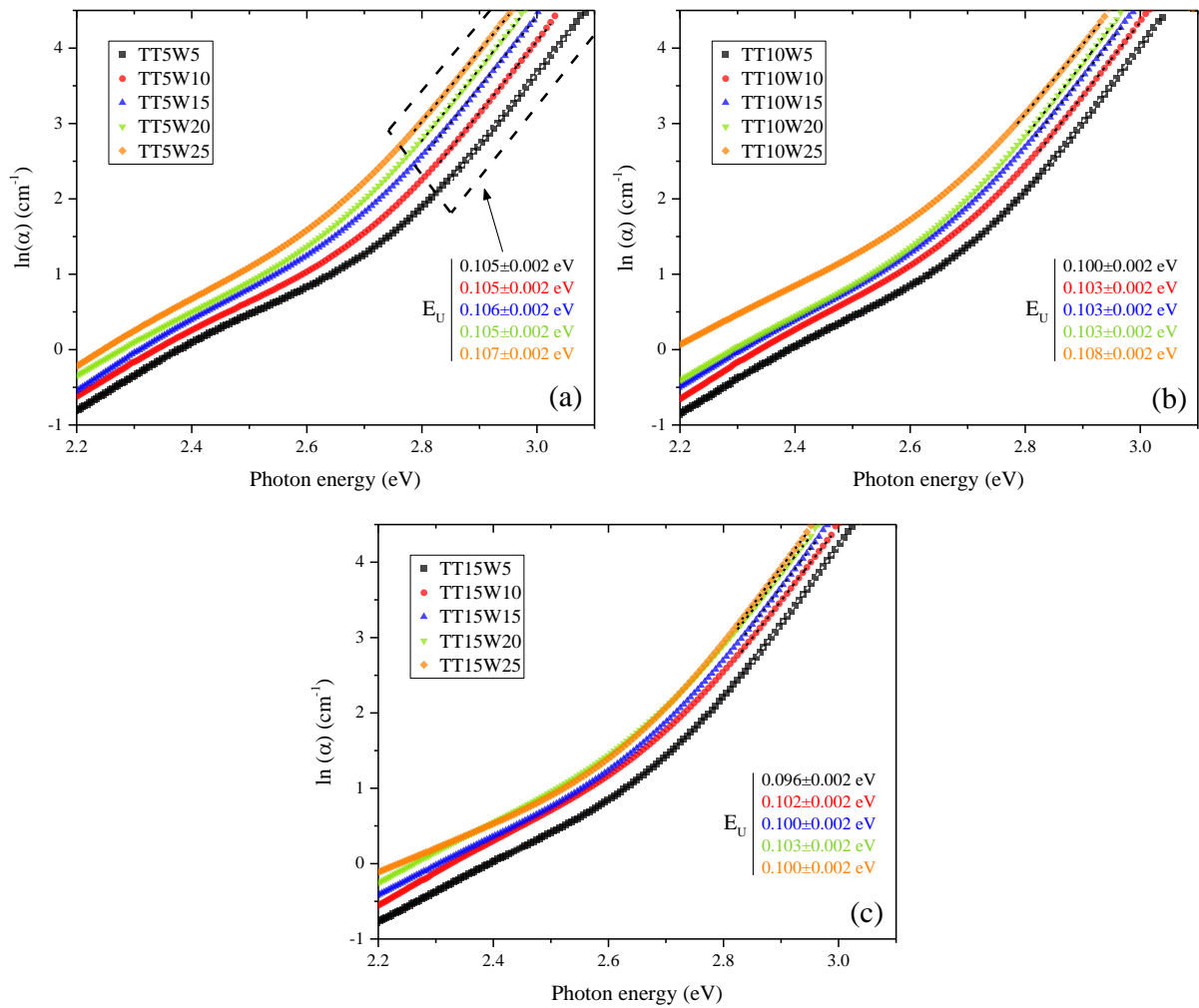
Fig. IV.15. Plots of $\ln(\alpha)$ versus hv for Urbach energy E_U determination of TTxWy glasses.

For TTxWy glasses, the E_U values are gathered in Table IV.6 and lie in the range 0.096–0.108 eV. E_U is found to remain globally stable with increasing WO_3 content (~0.106 eV in TT5Wy glasses). However, a slight decrease is observed upon adding TiO_2 at constant WO_3 content (for instance from 0.105 to 0.096 eV in TTxW5 glasses). Ghribi *et al.* [98] recently

reported the same behavior in $(100-x-y)TeO_2-xTiO_2-yZnO$ glasses, namely decreasing E_U from 0.105 eV (at x = 5 and y = 15) to 0.097 eV (at x = 10 and y = 15). It is also worth mentioning that our estimated E_U values are very close to those reported in literature for WO_3-containing TeO_2-based glasses [109] of approximately 0.100 eV. Therefore, it can be argued that adding TiO_2 to the TeO_2-rich network does not induce any significant structural modification of the glass network but instead, considering the compositional dependence of E_U, its incorporation might slightly "lessen" the average structural disorder. In this connection, it is important to recall that upon adding TiO_2, we found the glass-forming ability to be substantially reduced due to the crystallization of rutile TiO_2 in TT20Wy samples.

IV.5.1.2. Refractive index dispersion by spectroscopic ellipsometry

From the refractive index dispersion curves of TTxWy glasses (Fig. IV.16) measured by spectroscopic ellipsometry, we derived the refractive indices n_∞ (*cf.* Table IV.6) extrapolated to infinite wavelength using Sellmeier's dispersion formula as described in *section III.3.5.2.2*.

The dependence of n_∞ on TiO_2 content suggests a steady evolution from an average value of ~2.19 in TT5Wy to 2.20 in TT15Wy glasses with the highest value ($n_\infty \approx 2.21$) recorded from the TT15W15 composition. Adding WO_3 results in a steady behavior with an average value of ~2.19 in TTxW5 and TTxW25. A similar steady evolution of refractive indices is observed in binary TeO_2-TiO_2 and TeO_2-WO_3 glasses [129] with n = 2.211–2.226 from 5 to 15 mol.% upon adding TiO_2 and n = 2.211–2.219 from 10 to 30 mol.% upon adding WO_3 respectively.
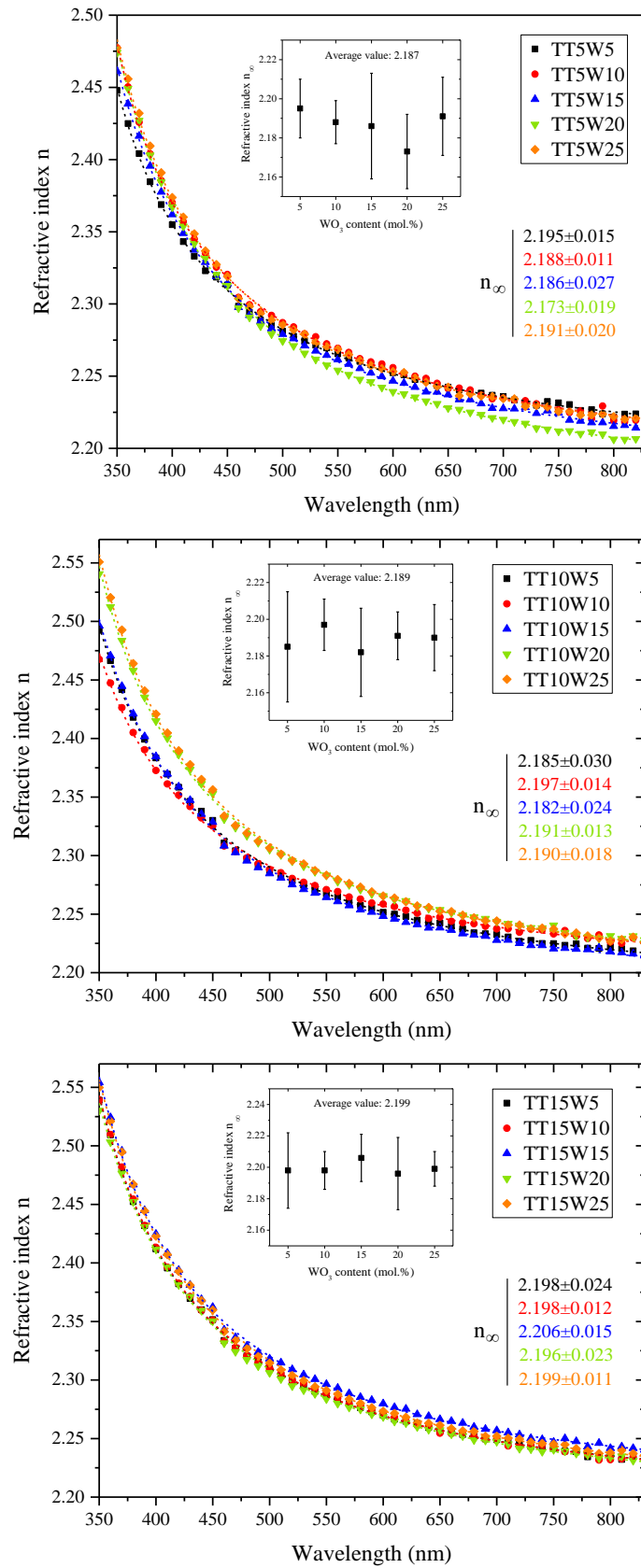
Fig. IV.16. Refractive index dispersion of TTxWy glasses. Each dispersion curve corresponds to the average of three measured from different spots on the same glass sample. Insets: compositional dependence of the refractive index n_∞.

Kim *et al.* [157] have measured the wavelength-dispersion of the refractive index of pure TeO$_2$ glass from 486.1 nm to 1000 nm using spectroscopic ellipsometry. Using the reported data (*cf.* Table I. in [157]), we estimated the n$_\infty$ value using Sellmeier's equation (Fig. IV.17) for the sake of consistency when comparing the linear optical response from TeO$_2$ glass to that of the studied glasses in this work. The obtained n$_\infty$ value of 2.113 is slightly smaller (by ~4%) than the average n$_\infty$ of 2.19 from TTxWy glasses.

The refractive index of pure SiO$_2$ glass was also reported by Kim *et al.*; it has a value of 1.439 (at λ = 1900 nm). Thus, the average n$_\infty$ for TTxWy glasses (2.19) is ~52.4% higher than that of SiO$_2$ glass.
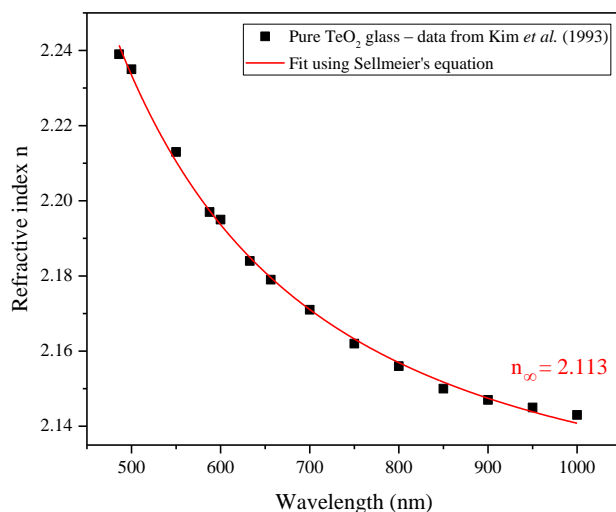
Fig. IV.17. Refractive index dispersion of pure TeO$_2$ glass (data extracted from [157] and fitted using Sellmeier's equation).

It is very important to stress that the n$_\infty$ values reported here are quite high in comparison to other binary or ternary systems (*e.g.,* less than 2.100[1] in TeO$_2$-TiO$_2$-ZnO glasses [98]) where the structural depolymerization occurs upon modifying the TeO$_2$-based glass network. Moreover, the refractive index of TeO$_2$-based glasses tends to decrease upon this transformation (*e.g.,* in alkali-modified systems as shown in Table IV.7) which is clearly not the case here for TTxWy glasses upon adding TiO$_2$ and WO$_3$.

---

[1] Also obtained by spectroscopic ellipsometry at λ = 1450 nm.

Authors	(100-x)TeO$_2$-xM$_y$O system	x (mol.%)	Refractive index n
Honma *et al.* **[218]**	(100-x)TeO$_2$-xLi$_2$O	15.0	2.079
		20.0	2.039
		25.0	1.996
		30.0	1.951
	(100-x)TeO$_2$-xNa$_2$O	10.0	2.092
		12.5	2.068
		15.0	2.042
		20.0	1.988
Dimitrov and Komatsu **[219]**	(100-x)TeO$_2$-xK$_2$O	4.9	2.110
		9.4	2.050
		12.9	2.005
		15.6	1.964
		17.3	1.925
	(100-x)TeO$_2$-xZnO	10.1	2.130
		20.0	2.080
		30.0	2.030
		40.0	1.982
		45.0	1.954

Table IV.7. Evolution of the refractive index in TeO$_2$-based glasses where the transformation of TeO$_4$ units into TeO$_3$ ones takes place.

From optical transmission and ellipsometric measurements, the refractive index remains practically constant upon adding TiO$_2$ and WO$_3$. This behavior is coherent with the results of the structural analysis (*cf. section IV.4)* that incorporating TiO$_2$ or WO$_3$ in the TeO$_2$-rich network does not markedly alter the inherent structural features of Te–O–Te bridges.

IV.5.1.3. Bond network nature from the dispersion energy and electronic polarizability

By applying the single-effective-oscillator model of Wemple and DiDomenico [179] to the refractive index dispersion data (*cf. section III.3.5.1.3*), we extracted optical constants that are closely connected with the bond network nature.

By plotting $1/(n^2-1)$ as a function of $(hv)^2$ and fitting a straight line (Fig. IV.18(a)), oscillator parameters E$_d$ (dispersion energy) and E$_0$ (single oscillator energy) can be determined. In fact, E$_d$ was found to obey the following empirical relationship in more than 100 ionic and covalent crystals [178]: E$_d$ = β N$_c$ Z$_a$ N$_e$. Where β parameter approaches 0.26 ± 0.04 eV and 0.37 ± 0.05 eV in ionic and covalent crystals respectively, N$_c$ is the coordination number of the cation, Z$_a$ the absolute charge number of the anion and N$_e$ the total number of valence electrons per anion.

Since the overall glass network structure (especially that of TeO_2-rich network) is only slightly altered upon adding TiO_2 or WO_3 (*section IV.4*), we consider the short-range N_c parameter in TTxWy glasses to be slightly increasing upon substituting TeO_2 with TiO_2 or WO_3 since globally, Te^{4+} cations are four-fold coordinated while Ti^{4+} and W^{6+} cations are six-fold coordinated.

The E_d and E_0 values lie in the range 26.11–30.37 eV and 6.93–7.99 eV respectively (Table IV.8). The evolutions of the two parameters E_d and E_0 with increasing WO_3 and TiO_2 contents are plotted in Fig. IV.18(b) and Fig. IV.19 for TT5Wy and TTxW5 glasses.

Sample	E_d (eV)	E_0 (eV)	α_{O2-} (E_g-based) ($\mathring{A}^3$)
TT5W5	30.371 ± 1.116	7.992 ± 0.126	1.593 ± 0.048
TT5W10	28.523 ± 1.355	7.556 ± 0.169	1.653 ± 0.053
TT5W15	28.792 ± 3.164	7.667 ± 0.233	1.727 ± 0.047
TT5W20	27.230 ± 2.289	7.360 ± 0.156	1.807 ± 0.052
TT5W25	28.669 ± 2.066	7.599 ± 0.174	1.810 ± 0.055
TT10W5	27.583 ± 2.798	7.354 ± 0.190	1.564 ± 0.047
TT10W10	29.545 ± 1.137	7.763 ± 0.132	1.682 ± 0.060
TT10W15	27.333 ± 2.545	7.317 ± 0.189	1.731 ± 0.055
TT10W20	26.519 ± 0.851	7.022 ± 0.095	1.777 ± 0.066
TT10W25	26.106 ± 1.138	6.927 ± 0.090	1.823 ± 0.046
TT15W5	26.851 ± 1.673	7.067 ± 0.119	1.669 ± 0.045
TT15W10	26.659 ± 1.169	7.025 ± 0.115	1.717 ± 0.040
TT15W15	27.027 ± 0.834	7.048 ± 0.081	1.750 ± 0.046
TT15W20	27.132 ± 2.321	7.143 ± 0.162	1.797 ± 0.035
TT15W25	26.604 ± 0.809	6.987 ± 0.080	1.813 ± 0.032

Table IV.8. Optical constants of TTxWy glasses.
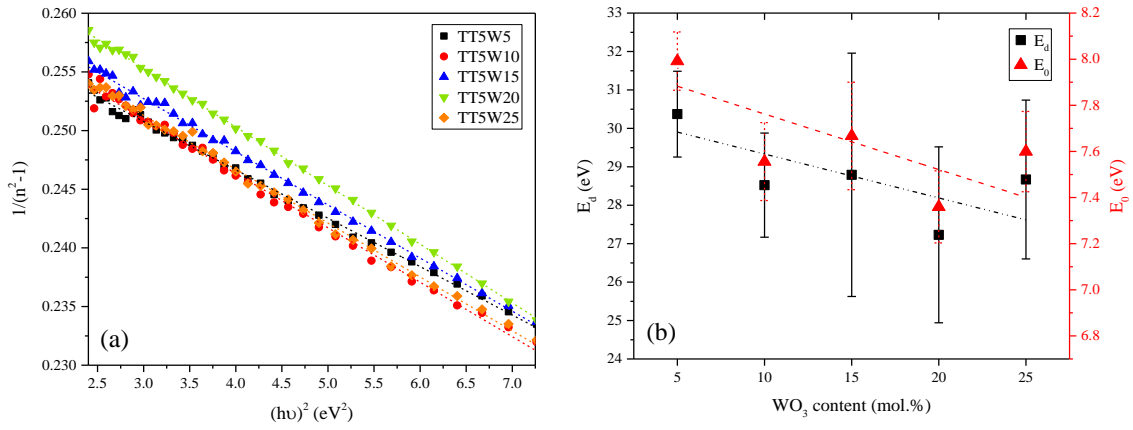
Fig. IV.18. (a) Evolution of $1/(n^2-1)$ as a function of $(h\upsilon)^2$; (b) evolution of oscillator parameters E_d and E_0 upon adding WO_3 in TT5Wy glasses.
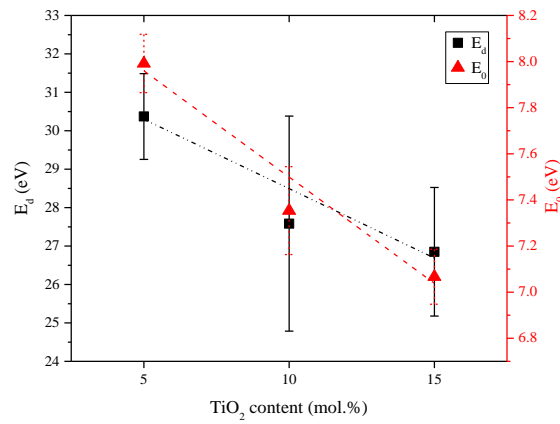
Fig. IV.19. Evolution of oscillator parameters E_d and E_0 upon adding TiO_2 in TTxW5.

Both E_d and E_0 are found to show an overall decrease with increasing TiO_2 and WO_3 contents. From the above equation, it is rational to assign this trend to a decreasing β parameter. Hence, we suggest that this evolution is associated with an ionic character amplification of the glass network, which can simply be supported by the expected ionicity increase upon substituting Te with Ti and W transition metals.

Following the polarizability approach developed by Dimitrov and Komatsu [183] described in *section III.3.5.1.4*, we calculated α_{O2-} for TTxWy glasses (Table IV.8). The values are comprised between $\alpha_{O2-(min)} = 1.56$ Å^3 and $\alpha_{O2-(max)} = 1.82$ Å^3. It is found that upon adding WO_3 from 5 to 25 mol.%, α_{O2-} slightly increases from ~1.6 to ~1.8 Å^3 (*cf.* Fig. IV.20) while remaining practically constant with addition of TiO_2. This slight increase of α_{O2-} values might indicate that the overall glass network becomes slightly more "polarized", and a little more ionic in nature.
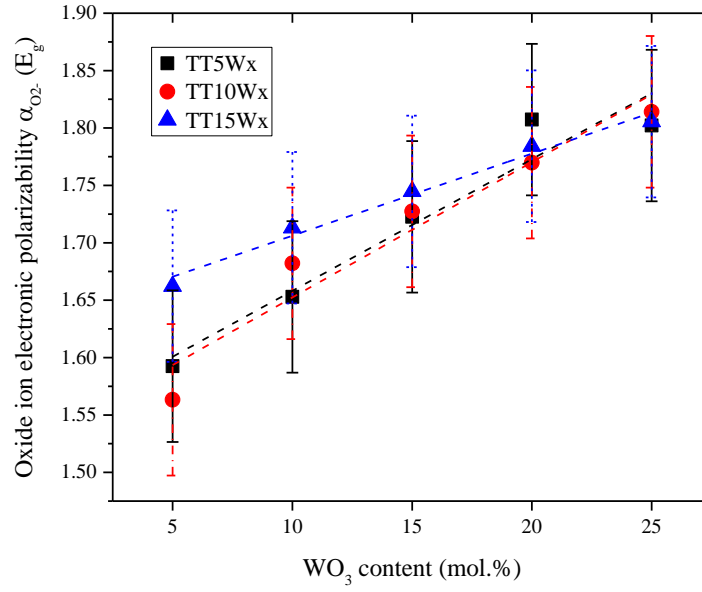
Fig. IV.20. Compositional dependence of the E_g-based $\alpha_{O^{2-}}$ polarizability.

IV.5.2. Nonlinear optical properties of TeO$_2$-TiO$_2$-WO$_3$ glasses

As described in *section III.3.5.3*, the third-order nonlinear optical susceptibilities $\chi^{(3)}$ have been derived from the measured transmittance curves by the Z-scan technique and using equations that involve several parameters such as those related to the laser source, samples' dimension, reference sample data, *etc*. The extracted $\chi^{(3)}$ values for TTxWy glasses (listed in Table IV.9) were normalized to the figure of merit of the reference sample that is silica SiO$_2$ glass which is the most commonly considered model. We consider the $\chi^{(3)}_{SiO2}$ value of $1.5 *10^{-14}$ esu reported by Milam [191] as explained in further detail in *section III.3.5.3*.

First of all, it is important to stress that the extracted $\chi^{(3)}$ values for TTxWy glasses are very high ($\chi^{(3)}_{min} = 5.81 *10^{-13}$ esu and $\chi^{(3)}_{max} = 7.97 *10^{-13}$ esu) with an average of $7.03 *10^{-13}$ esu which is ~46.9 times higher than the reported $\chi^{(3)}$ for SiO$_2$ glass and only 1.07 times lower than that of TeO$_2$ glass ($7.54 *10^{-13}$ esu, adjusted from the reported $14.1 *10^{-13}$ esu by Kim *et al.* [157]).

Sample	Normalized Re($\chi^{(3)}$) (esu)
TT5W5	$6.35 \pm 1.45 *10^{-13}$
TT5W10	$6.63 \pm 1.84 *10^{-13}$
TT5W15	$5.81 \pm 1.33 *10^{-13}$
TT5W20	$6.28 \pm 1.39 *10^{-13}$
TT5W25	$7.01 \pm 1.95 *10^{-13}$
TT10W5	$6.51 \pm 1.61 *10^{-13}$
TT10W10	$7.14 \pm 1.83 *10^{-13}$
TT10W15	$7.09 \pm 1.77 *10^{-13}$
TT10W20	$7.10 \pm 1.83 *10^{-13}$
TT10W25	$7.66 \pm 2.17 *10^{-13}$
TT15W5	$6.74 \pm 1.62 *10^{-13}$
TT15W10	$7.92 \pm 1.88 *10^{-13}$
TT15W15	$7.46 \pm 1.95 *10^{-13}$
TT15W20	$7.97 \pm 2.12 *10^{-13}$
TT15W25	$7.77 \pm 2.00 *10^{-13}$

Table IV.9. Normalized $\chi^{(3)}$ values of TTxWy glasses.

The evolutions of $\chi^{(3)}$ values with addition of WO_3 and TiO_2 are plotted in Fig. IV.21. With such significant error bars of ~25% in average, it seems that $\chi^{(3)}$ remains practically constant in all compositions. This is particularly the case when analyzing the sets of data with increasing WO_3 content (Fig. IV.21(a)). On the other hand, it appears that there is a slight upward trend upon increasing TiO_2 content (Fig. IV.21(b)).
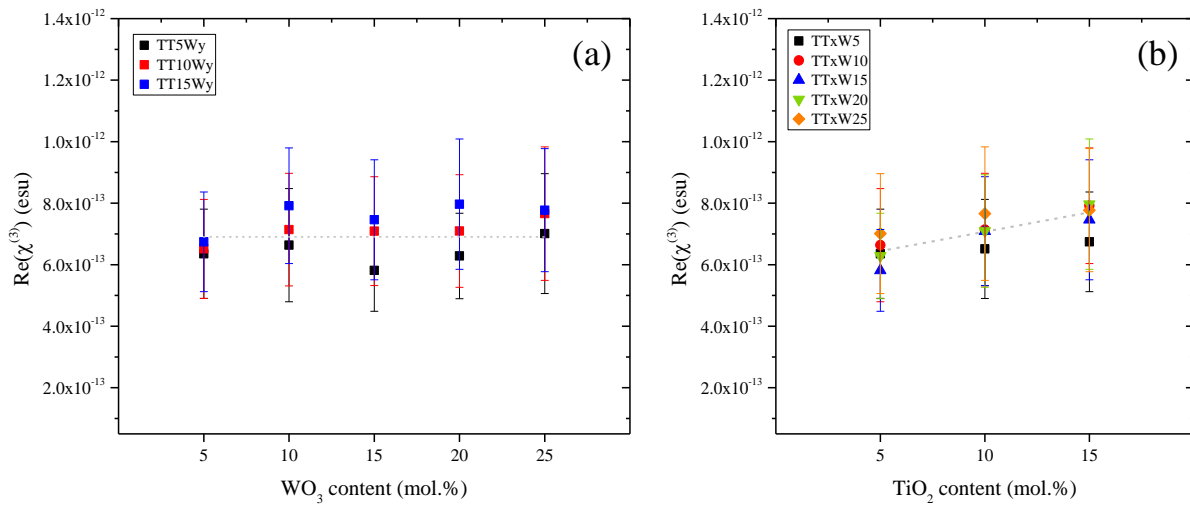

Fig. IV.21. Compositional dependence of normalized $\chi^{(3)}$ values as a function of (a) WO_3 and (b) TiO_2 contents.

To assess the evolution of $\chi^{(3)}$ as a function of TiO_2 and WO_3 contents, we have calculated the average values for each set of TTxWy glasses with either TiO_2 or WO_3 constant. These values are listed below in Table IV.10.

Set of samples	Normalized Re($\chi^{(3)}$) (esu)
TT5Wy	$6.42 \pm 1.59 *10^{-13}$
TT10Wy	$7.10 \pm 1.84 *10^{-13}$
TT15Wy	$7.57 \pm 1.91 *10^{-13}$
TTxW5	$6.44 \pm 1.56 *10^{-13}$
TTxW10	$7.23 \pm 1.85 *10^{-13}$
TTxW15	$6.79 \pm 1.68 *10^{-13}$
TTxW20	$7.12 \pm 1.78 *10^{-13}$
TTxW25	$7.48 \pm 2.04 *10^{-13}$

Table IV.10. Calculated average $\chi^{(3)}$ values of TTxWy glasses.

As mentioned earlier, adding TiO_2 seems to contribute positively on the nonlinear response of TTxWy glasses. In fact, the average value of $\chi^{(3)}$ increases by ~18% from $6.42 \pm 1.59 *10^{-13}$ esu in TT5Wy to $7.57 \pm 1.91 *10^{-13}$ esu in TT15Wy. It is worthwhile to mention that in binary $(100-x)TeO_2-xTiO_2$ glasses, the $\chi^{(3)}$ value increased by ~17% from x = 5 mol.% ($7.59*10^{-13}$ esu) to 15 mol.% ($8.88*10^{-13}$ esu) [41].

The average $\chi^{(3)}$ values also suggest that adding WO_3 results in an increase of the nonlinear response by ~15% from $6.44 \pm 1.56 *10^{-13}$ esu in TTxW5 to $7.48 \pm 2.04 *10^{-13}$ esu in TTxW25. Again, this is in agreement with the evolution in binary $(100-x)TeO_2-xWO_3$ glasses where an increase by 12% was recorded from x = 10 mol.% ($7.59 *10^{-13}$ esu) to 30 mol.% ($8.50 *10^{-13}$ esu) [41].

We assign the positive contributions to the nonlinear susceptibility $\chi^{(3)}$ upon adding TiO_2 and WO_3 (illustrated in Fig. IV.22) to *(i)* the possible influence of empty *d* orbitals of Ti^{4+} and W^{6+} cations through virtual electronic transitions from the filled valence band to the empty *d*- band as reported by Lines [43], and *(ii)* to the slight structural modifications induced by adding either TiO_2 or WO_3 to the TeO_2-rich network (*cf. section IV.4.*) and thus conserving the original Te–O–Te bridges contributing to the high nonlinear optical performance.

Our suggested structural effect of TiO_2 within the glass network, *i.e.,* phase separation into amorphous TeO_2-rich and amorphous TiO_2-rich regions (of few nanometers) is also in

agreement with the evolution of the nonlinear response of TTxWy glasses upon adding TiO_2. In other words, the presence of such networks of Ti–O–Ti bridges and unaltered Te–O–Te ones could successfully explain these observations. In fact, using the degenerate three-wave mixing technique, Adair *et al.* [220] reported the linear and nonlinear refractive indices of a large set of compounds including some transition-metal oxides such as TiO_2. The latter was found to exhibit the highest nonlinear refractive index n_2 with a value of $55.8 *10^{-13}$ esu which is over 49 times greater than that of SiO_2 (quartz) and two times higher than that of ZnO crystal (*cf.* Table IV in [220]).
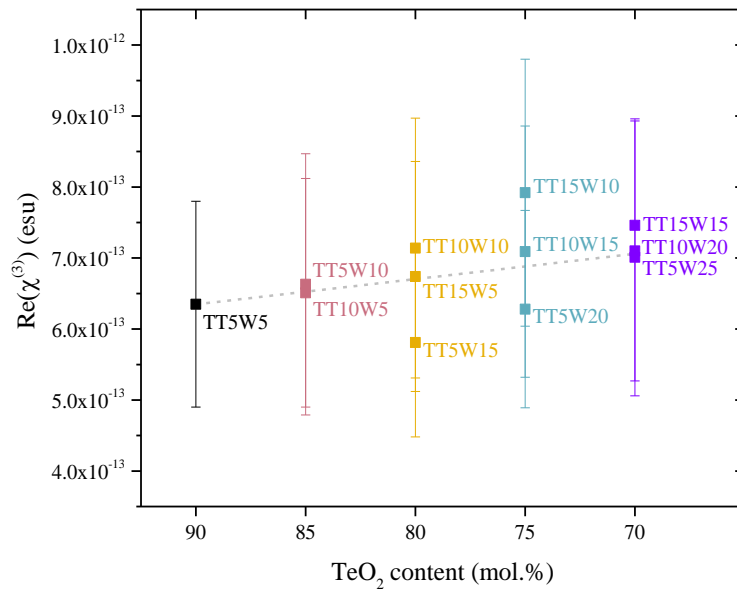
Fig. IV.22. Evolution of normalized $\chi^{(3)}$ in TTxWy glasses as a function of TeO_2 content.

In general, compared to other ternary TeO_2-based glass systems such as the recently studied TeO_2-TiO_2-ZnO glasses by Ghribi *et al.* [53,98], our TTxWy glasses exhibit higher third-order nonlinear susceptibilities $\chi^{(3)}$, namely ~1.7 higher in average. Moreover, no matter the chosen $\chi^{(3)}_{SiO2}$ reference value to obtain $\chi^{(3)}$ for TTxWy glasses Table IV.9, the latter exhibit values that are at least 3.3 times higher than those of TeO_2-MO-R_2O (M = Zn, Mg and R = Li, Na, K) glasses reported by Castro-Beltrán *et al.* [221], and where the fitting of transmittance curves was used to obtain the nonlinear refractive index instead of normalizing using a reference sample.

Globally, the nonlinear optical performance of TTxWy glasses is in quite good agreement with the structural interpretation established in *section IV.4* which suggests only slight modifications

of the glass network upon substituting TeO_2 with either TiO_2 or WO_3. Besides, the slight increase of $\chi^{(3)}$ upon adding TiO_2 agrees with the central role of TiO_2 in maintaining the original TeO_2-based framework in TeO_2-based glasses as previously reported by many others.

IV.6. Discussion and concluding remarks

New TeO_2-based glasses have been prepared and investigated within the ternary (100-x-y)TeO_2-xTiO_2-yWO_3 system. Density, thermal, structural and optical properties of the prepared glasses have been measured and analyzed as a function of TiO_2 and WO_3 contents. The glass-forming domain in this system incorporates fifteen compositions and extends from x = 5 to 15 mol.% in TiO_2 and from y = 5 to 25 mol.% in WO_3. The prepared TTxWy glasses exhibit moderate thermal stabilities ($\Delta T_{(min)} = 31\,°C$ and $\Delta T_{(max)} = 57\,°C$) and glass transition temperatures that increase with addition of either TiO_2 or WO_3 ($T_{g(min)} = 328\,°C$ and $T_{g(max)} = 426\,°C$).

Interestingly, coherent correlations have been established between the structural features of TTxWy glasses and their measured optical (linear and nonlinear) properties.

The structural properties of TTxWy glasses were examined using Raman spectroscopy to highlight the structural roles and effects of adding TiO_2 and WO_3 on the short- to medium-range structure. We report the following structural trends:

- Globally, only minor structural modifications are taking place upon adding TiO_2 or WO_3, *(i)* indicating that TTxWy glasses collectively share common features of the pure TeO_2 glass network and *(ii)* suggesting the absence of Te–O–Te bond network depolymerization (*i.e.*, the absence of induced transformation of TeO_4 into TeO_3 units).

- Upon adding TiO_2, we argue that a phase separation occurs between amorphous TeO_2-network and amorphous "rutile-like" TiO_2-rich regions (assumed to be of a nanometric size) in binary TTx and ternary TTxWy glasses, thus explaining the limited glass-forming domain to only 15 mol.%. Therefore, it seems unlikely that hybrid Te–O–Ti bridges build the bond network in these glasses. This idea of phase separation is also supported by the application of Dietzel's cationic field strength on the binary TeO_2-TiO_2 system.

- Upon adding WO_3, we argue that *(i)* only a minor change affects the crosslinked network of Te–O–Te bridges; *(ii)* at low WO_3 contents, uniformly dispersed WO_6

octahedra exist in the glass network; and *(iii)* at higher WO_3 contents, amorphous WO_3-like regions continuously grow before the crystallization of γ-WO_3 at 30 mol.% of WO_3. Let us recall that Sekiya *et al.* [103] have suggested the same scenario for TeO_2-WO_3 glasses.

These glasses possess high linear refractive indices with an average of ~2.19 ($n_{\infty(min)}$ = 2.17 and $n_{\infty(max)}$ = 2.21) that remain practically constant upon adding TiO_2 or WO_3. The evolution of the dispersion energy suggests a slight increase of the network's ionicity upon substituting TeO_2 with TiO_2 and WO_3, which is in agreement with the observed slight increase of the electronic oxide ion polarizability.

The third-order nonlinear susceptibilities $\chi^{(3)}$ of TTxWy glasses were measured using the Z-scan technique. The extracted $\chi^{(3)}$ responses are remarkably high, *i.e.*, with an average of $7.03 \ast 10^{-13}$ esu that is ~46.9 times stronger than the reported $\chi^{(3)}$ for conventional SiO_2 glass. The obtained results show that continuous addition of TiO_2 and WO_3 might contribute positively to the nonlinear response with an increase of $\chi^{(3)}$ by ~18% from TT5Wy ($6.42 \pm 1.59 \ast 10^{-13}$ esu) to TT15Wy ($7.57 \pm 1.91 \ast 10^{-13}$ esu), and by ~15% from TTxW5 ($6.44 \pm 1.56 \ast 10^{-13}$ esu) to TTxW25 ($7.48 \pm 2.04 \ast 10^{-13}$ esu). Generally, the extracted $\chi^{(3)}$ values are higher than those reported for other TeO_2-based systems especially the ones where the structural depolymerization takes place (*e.g.*, ZnO- or alkali-containing glasses).

As a perspective, we would suggest to *(i)* examine the evolving bond network nature of the investigated glasses by deriving the splitting of the longitudinal optical and transverse optical (LO-TO) modes by means of infrared reflectance spectroscopy, *(ii)* probe the existence of the phase-separated "rutile-like" TiO_2-rich regions using cryogenic transmission electron microscopy and *(iii)* examine the origins of the positive contribution of TiO_2 to the nonlinear susceptibility $\chi^{(3)}$ in the framework of the structural model proposed in this work. In other words, it would be interesting to reveal to which extent the presence of nanosized amorphous TiO_2-rich regions in the glass network improves the nonlinear response of TiO_2-containing TeO_2-based glasses.

In the next chapter, we approach, in the same spirit, the glass-forming domain exploration and study of the structural and optical properties of the ternary TeO_2-$NbO_{2.5}$-WO_3 glasses accommodating $NbO_{2.5}$ instead of TiO_2.

Chapter V. Synthesis, thermal, structural and optical properties of new glasses within the TeO$_2$-NbO$_{2.5}$-WO$_3$ system

V.1. Introduction

Following the same investigation approach of glasses reported in the previous chapter, we examine a second ternary TeO$_2$-based system containing NbO$_{2.5}$ and WO$_3$ oxides. Aside from a handful of structural and optical investigations on specific glass compositions [109,128,129], there is, to the best of our knowledge, no reported systematic study on the TeO$_2$-NbO$_{2.5}$-WO$_3$ glassy system (*cf. section I.5.4.2* for more details on the previous works).

In this chapter, we report the obtained glass-forming domain within the TeO$_2$-NbO$_{2.5}$-WO$_3$ system and the measured properties from the prepared glasses, namely, their densities, thermal characteristics, structural and optical (linear and nonlinear) properties.

V.2. Glass-forming domain determination

We have examined the glass-forming domain within the (100-x-y)TeO$_2$-xNbO$_{2.5}$-yWO$_3$ system (TNxWy) under the experimental conditions outlined in *section III.2.3*. The amorphous nature of TNxWy samples was analyzed using XRD to elucidate the glass-forming domain given in Fig. V.1(a). The longest compositional lines extend from x = 5 to 25 mol.% in NbO$_{2.5}$ and y = 5 to 25 mol.% in WO$_3$. In total, seventeen melt compositions have yielded transparent yellowish glasses that shifted to honey-brown with increasing WO$_3$ molar content and remained practically unchanged upon adding NbO$_{2.5}$ (*cf.* Fig. V.1(b)).

Using X-ray powder diffraction, we detected the presence of WO$_{2.83}$ (or W$_6$O$_{17}$) crystals [222,223] in partially crystallized TNxW30 samples (Fig. V.2). This compound has been detected previously from TT15W15 upon heating (*cf. section IV.3.2*). At relatively high NbO$_{2.5}$ content, crystals of Nb$_6$TeO$_{17}$ [119] (*cf. section I.5.3.1*) are detected in TN15W25, TN20W15, TN25W10 and TN30W5 samples.
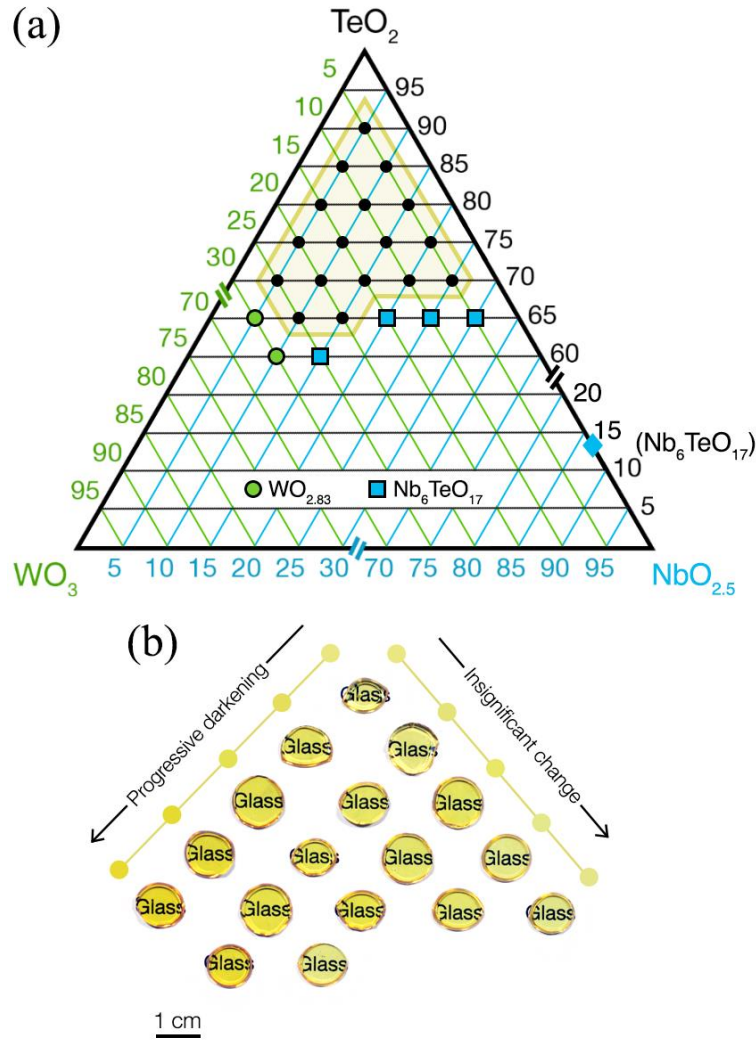
Fig. V.1. Glass-forming domain obtained in the $(100-x-y)TeO_2-xNbO_{2.5}-yWO_3$ system (labeled TNxWy) surrounded by the yellow frame. Blue and green colored squares and spots correspond to partially crystallized samples in $WO_{2.83}$ and Nb_6TeO_{17} respectively. (b) Photograph of the obtained glass pellets in their polished state.

The prepared samples were systematically analyzed by EDS in order to check their chemical compositions. This technique provides only an approximate quantitative analysis. The results (*cf.* Table V.1) show that the experimental glass compositions are generally in good agreement with the theoretical ones with the exception of some sample compositions such as TN5W5, TN5W25 and TN10W25 where relatively strong differences can be noticed.
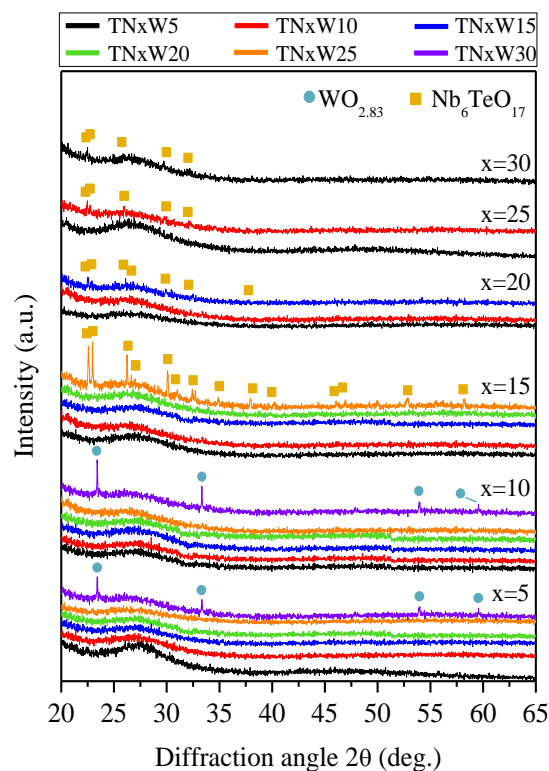
Fig. V.2. X-ray diffraction patterns of the prepared TNxWy samples.

Sample	Theoretical composition (mol.%)			Measured composition (mol.%) ± 2 mol.%		
	TeO$_2$	NbO$_{2.5}$	WO$_3$	TeO$_2$	NbO$_{2.5}$	WO$_3$
TN5W5	90	5	5	87	3	10
TN10W5	85	10	5	86	6	8
TN15W5	80	15	5	82	10	8
TN20W5	75	20	5	78	14	8
TN25W5	70	25	5	74	18	8
TN5W10	85	5	10	85	3	12
TN10W10	80	10	10	79	7	14
TN15W10	75	15	10	77	11	12
TN20W10	70	20	10	73	13	14
TN5W15	80	5	15	78	3	19
TN10W15	75	10	15	75	7	18
TN15W15	70	15	15	71	10	19
TN5W20	75	5	20	73	3	24
TN10W20	70	10	20	70	6	24
TN15W20	65	15	20	66	9	25
TN5W25	70	5	25	65	2	33
TN10W25	65	10	25	62	6	32

Table V.1. Comparison between the expected and measured TNxWy glass compositions.

V.3. Physical properties of TeO$_2$-NbO$_{2.5}$-WO$_3$ glasses

V.3.1. Density and molar volume

Using helium pycnometry, we have measured the densities of TNxWy glasses and extracted molar volumes for each composition by considering their theoretical molar masses. The obtained values are jointly listed in Table V.2.

Sample	Density (g.cm^{-3})	Molar volume (cm^3.mol^{-1})
TN5W5	4.667 ± 0.007	34.68 ± 0.06
TN10W5	4.870 ± 0.003	32.97 ± 0.06
TN15W5	4.815 ± 0.004	33.06 ± 0.06
TN20W5	4.723 ± 0.005	33.42 ± 0.06
TN25W5	4.508 ± 0.014	34.72 ± 0.10
TN5W10	4.777 ± 0.004	34.64 ± 0.06
TN10W10	4.928 ± 0.006	33.31 ± 0.06
TN15W10	4.871 ± 0.007	33.43 ± 0.06
TN20W10	4.837 ± 0.006	33.38 ± 0.06
TN5W15	4.993 ± 0.004	33.87 ± 0.06
TN10W15	5.010 ± 0.014	33.49 ± 0.12
TN15W15	4.962 ± 0.005	33.54 ± 0.06
TN5W20	5.052 ± 0.002	34.19 ± 0.06
TN10W20	5.061 ± 0.007	33.86 ± 0.06
TN15W20	4.928 ± 0.002	34.50 ± 0.06
TN5W25	5.153 ± 0.006	34.22 ± 0.06
TN10W25	5.056 ± 0.006	34.61 ± 0.06

Table V.2. Densities and molar volumes of TNxWy glasses.

In general, the measured densities and molar volumes increase with WO$_3$ and slightly decrease with NbO$_{2.5}$. The density increase extent upon adding WO$_3$ at constant NbO$_{2.5}$ content varies from one series of samples to the other. For instance, an increase by ~10% is recorded from TN5W5 (4.67 g.cm^{-3}) to TN5W25 (5.15 g.cm^{-3}) and by ~4% from TN10W5 (4.87 g.cm^{-3}) to TN10W25 (5.06 g.cm^{-3}). On the other hand, the density's compositional dependence upon adding NbO$_{2.5}$ shows a peculiar behavior in TeO$_2$-rich compositions as it first increases for instance by ~4% from TN5W5 (4.67 g.cm^{-1}) to TN10W5 (4.87 g.cm^{-3}) before decreasing by ~7% to TN25W5 (4.51 g.cm^{-3}) as emphasized in Fig. V.3. This unexpected behavior in the TeO$_2$-richest compositions could be explained by their positions at the boundary of the glass-forming domain.
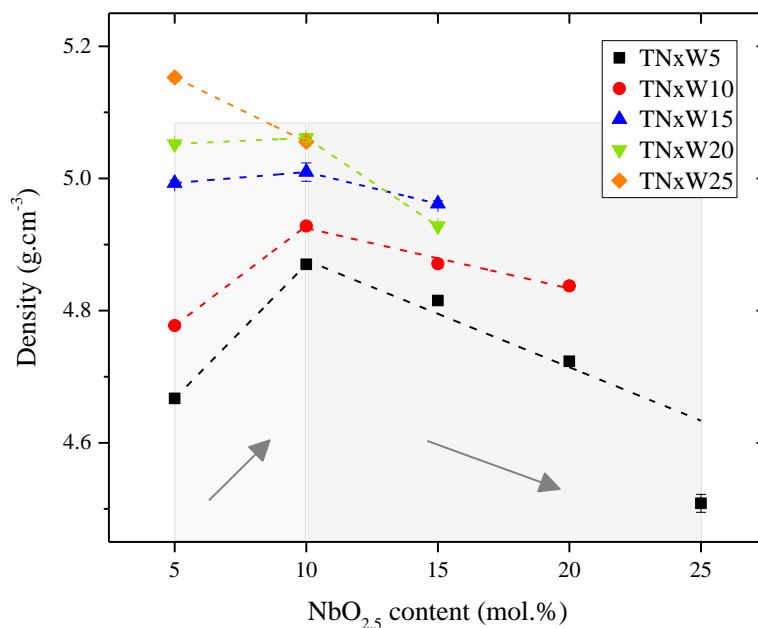
Fig. V.3. Density evolution of TNxWy glasses as a function NbO$_{2.5}$ content.

It can be argued that the compositional dependence of density follows the *additive density rule*: densities of raw oxides NbO$_{2.5}$, TeO$_2$ and WO$_3$ are respectively 4.55, 6.13 and 7.16 g.cm^{-3}. Thus, we assign the glass density increase upon adding WO$_3$ to the higher molar mass of WO$_3$ (231.8 g.mol^{-1}) compared to that of TeO$_2$ (159.6 g.mol^{-1}); and the decrease upon adding NbO$_{2.5}$ from 10 to 25 mol.% to its lower molar mass of 132.9 g.mol^{-1}.

V.3.2. Thermal characteristics

The thermal properties of TNxWy glasses were measured by DSC in order to evaluate the compositional dependence of their glass transition temperatures T$_g$ and thermal stabilities ΔT. The analyzed glass samples were in powdered form and weighing ~20 mg.

As shown in Table V.3 and Fig. V.4, T$_g$ increases linearly upon adding either NbO$_{2.5}$ or WO$_3$ (T$_{g(min)}$ = 333 °C and T$_{g(max)}$ = 403 °C). It increases by ~21% from TN5W5 (333 °C) to TN25W5 (403 °C) and by ~15% from TN5W5 to TN5W25 (381 °C). We assign the T$_g$ increase to the fact that W–O and Nb–O bonds have higher dissociation energies compared to Te–O bonds, namely, 720, 726.5 and 377 kJ.mol^{-1} respectively [194].

Sample	T_g (°C) ± 1	T_O (°C) ± 1	ΔT (°C) ± 1
TN5W5	333	393	60
TN10W5	348	397	49
TN15W5	366	432	66
TN20W5	382	452	70
TN25W5	403	448	45
TN5W10	346	407	61
TN10W10	362	414	52
TN15W10	378	445	67
TN20W10	397	456	59
TN5W15	360	429	69
TN10W15	374	428	54
TN15W15	387	447	60
TN5W20	370	426	56
TN10W20	386	451	65
TN15W20	389	445	56
TN5W25	381	436	55
TN10W25	393	462	69

Table V.3. Thermal characteristics of TNxWy glasses measured by DSC.

The thermal stabilities ΔT of TNxWy glasses (Table V.3) are relatively low with $\Delta T_{min} = 45$ °C and $\Delta T_{max} = 70$ °C. It appears that adding $NbO_{2.5}$ or WO_3 does not significantly improve ΔT from one TNxWy composition to another. Having an average ΔT of ~60 °C, these glasses are more stable against devitrification compared to TTxWy glasses (*section IV.3.2*) which have an average ΔT of 44 °C.

By comparison, the thermal stabilities of TNxW5 samples are relatively lower than those reported for binary TeO_2-$NbO_{2.5}$ glasses with values ranging between ~43 and ~98 °C according to Blanchandin *et al.* [114]. However, by ignoring the weak first exothermic events after T_g on the DSC curves of TN5W5, TN15W5 and TN20W5 samples (*cf.* Fig. V.4), one could rather assign higher thermal stabilities exceeding 100 °C to these compositions. This also applies to other compositions such as TN5W10 and TN15W10.
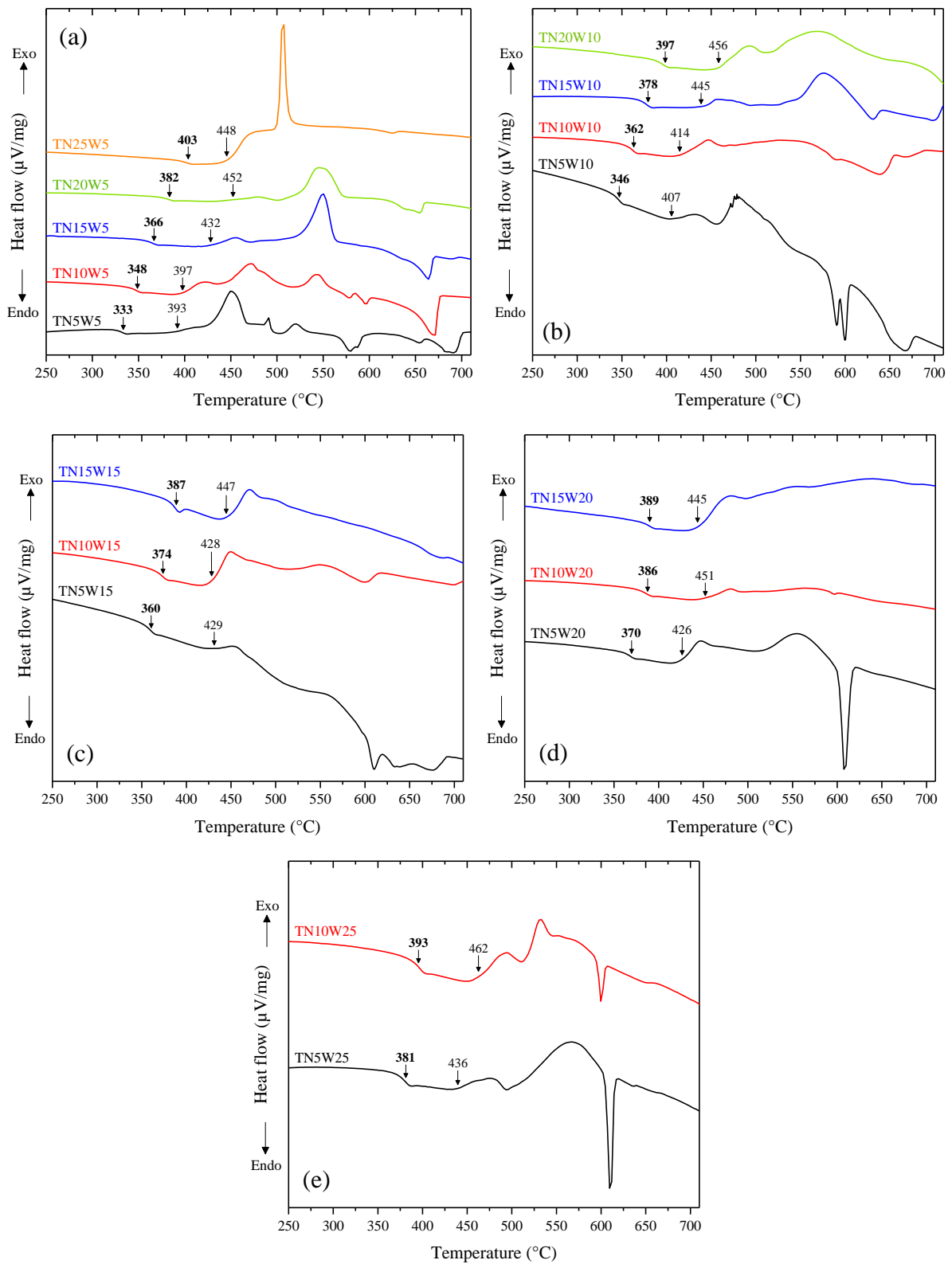
Fig. V.4. DSC curves of TNxWy glasses with the glass transition and onset crystallization temperatures given in bold and non-bold typefaces respectively.

As previously outlined in *section I.5.3*, Blanchandin *et al.* [114] investigated the equilibrium and non-equilibrium phase diagram of the binary (100-x)TeO_2-x$NbO_{2.5}$ system. Using high-temperature X-ray diffraction, they identified the crystallizing phases from the binary glasses with x = 2.5, 5, 7.5, 10, 12.5, 15, 20 and 25 mol.%. The recorded sequence of exothermic peaks from their DSC curves (*cf.* Fig. 3 in [114]) is in relatively good agreement with our ternary TNxW5 glasses (Fig. V.4(a)); whereas, the exothermic peaks of the latter are broader probably due to a more disordered glass network, manifested by the presence of additional W–O coordination polyhedra. Therefore, the crystallizing phases in TNxW5 glasses can be safely assigned in agreement with those crystallizing from binary (100-x)TeO_2-x$NbO_{2.5}$ glasses, *i.e.,* δ-, γ- and α-TeO_2 and then $Nb_2Te_4O_{13}$ depending on the $NbO_{2.5}$ content. For example, the δ-TeO_2 phase which is the first to appear upon heating TeO_2-rich compositions is likely to crystallize from TN5W5 and TN10W5 samples explaining thus the large number of exothermic events (compared to TNxW5 with x = 15, 20 and 25).

Identifying the crystallization temperature and nature of tungsten oxide(s) (*e.g.,* γ-WO_3 and/or $WO_{2.83}$) solely from the DSC curves is a challenging task due to notable peak overlapping of the recorded exothermic events; however, such pieces of information can be obtained by performing high-temperature X-ray diffraction measurements on the glass samples.

V.4. Structural properties of TeO₂-NbO₂.₅-WO₃ glasses

V.4.1. Background and state-of-the-art

It is accepted among the previous investigators that adding $NbO_{2.5}$ leads to the **structural depolymerization** (transformation of TeO_4 disphenoids into TeO_3 trigonal pyramids via the formation of intermediate TeO_{3+1} units) [108,121,125]. According to Berthereau *et al.* [121], the predominant units in binary (100-x)TeO_2-x$NbO_{2.5}$ (x = 9.5, 18.2, 26.1, 33.4 mol.% [1]) glasses are TeO_4 and TeO_{3+1} and the proportion of the latter increases upon adding $NbO_{2.5}$ as revealed by their extended X-ray absorption fine structure (EXAFS) measurements.

Hoppe *et al.* [120] investigated the structure of (100-x)TeO_2-x$NbO_{2.5}$ (x = 11.4, 18.2 and 30.5 mol.%) glasses by neutron and X-ray diffraction techniques. By determining the local environments around Te and Nb atoms via the fitting of the first-neighbor peaks, the authors argued that a structural transition from **network-modifying** (for x ≤ 18.2 mol.%) to **network-**

---

[1] Converted from original molar concentrations in Nb_2O_5 to enable comparison with TNxWy glasses.

forming behavior (for x > 18.2 mol.%) takes place upon adding $NbO_{2.5}$ with the formation of Nb–O–Nb bridges.

By investigating the structure of (100-x)TeO_2-x$NbO_{2.5}$ (x = 9.5, 18.2, 26.1, 33.4 and 40 mol.%) glasses using Raman spectroscopy, Soulis *et al.* [94] argued that the amorphous networks contain three types of linkages, namely Te–O–Te, Te–O–Nb and Nb–O–Nb bridges.

Finally, two more recent studies by Lin *et al.* [125] and Kaur *et al.* [108] agree with the previously described role of $NbO_{2.5}$ in reducing the connectivity of Te–O–Te bond network by transforming the TeO_4 units into TeO_3 ones.

V.4.2. Structural effect of adding $NbO_{2.5}$

In the following, we closely examine the Raman spectra to interpret the structural trends in TNxWy glasses as a function of $NbO_{2.5}$ content (at constant WO_3 content). To do so, we analyze the evolution of the parameters of each band based on the spectral decomposition results (*cf. section III.3.4.3.* for details on the decomposition process).

The recorded spectra from TNxWy glasses are jointly presented in Fig. V.5. Since the same structural evolutions are observed from TNxW5, TNxW10, TNxW15, TNxW20 and TNxW25 samples, we suggest to focus on the set of TNxW5 for the sake of simplicity (Fig. V.6). At first glance, one can notice the important change in the ~535-725 cm^{-1} range with a noticeable intensity increase of the bands G and H from TN5W5 to TN25W5. Slight increasing of Raman intensity is observed within ~200-400 cm^{-1} and ~850-950 cm^{-1} regions. On the other hand, in the low-wavenumber region (< 100 cm^{-1}), an intensity decrease of the boson peak is recorded along with an insignificant red-shift of ~6 cm^{-1} from TN5W5 to TN25W5.

We assign in Table V.4 the observed Raman bands to their corresponding vibrational modes. The assignment origin of the bands associated with vibrations of Te–O and W–O bonds is the same as in *section IV.4.3*; that of the bands associated with bonds involving Nb–O bonds, namely, Te–O–Nb (band E), Te–O– – –Nb (bands G–H), Nb–O–Nb (bands G–H) and shortest Nb–O (band M) linkages is based on the vibrational properties of $Nb_2Te_4O_{13}$, $Nb_2Te_3O_{11}$ and H-Nb_2O_5 crystalline phases (*cf. section I.5.3.1* for their Raman spectra analysis).
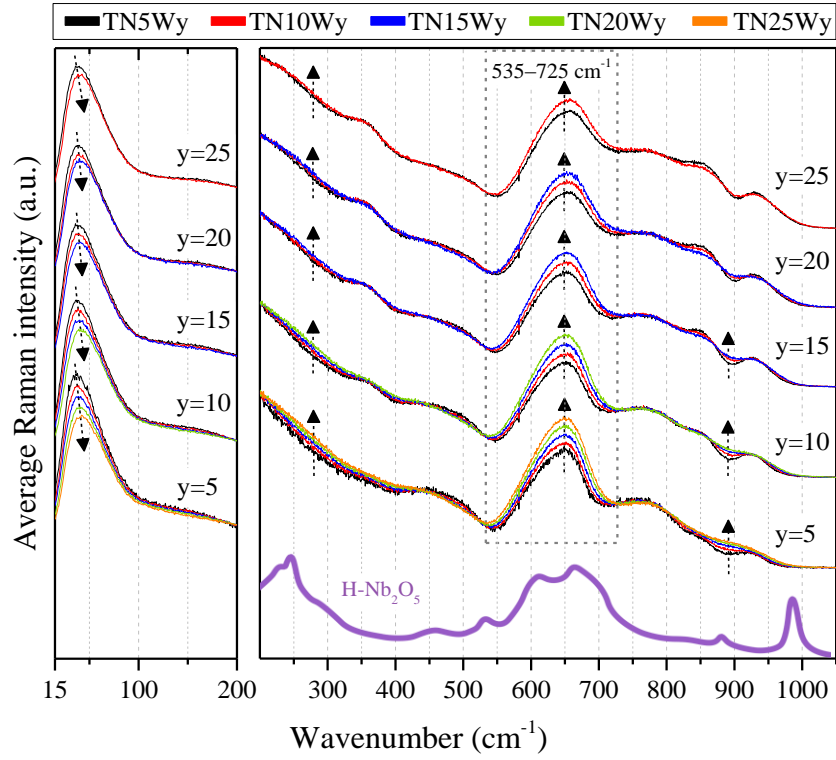
Fig. V.5. Evolution of total-area averaged VH-polarized Raman spectra of TNxWy glasses as a function of NbO$_{2.5}$ content. The Raman spectrum of H-Nb$_2$O$_5$ is reproduced from Fig. 34 in [94].
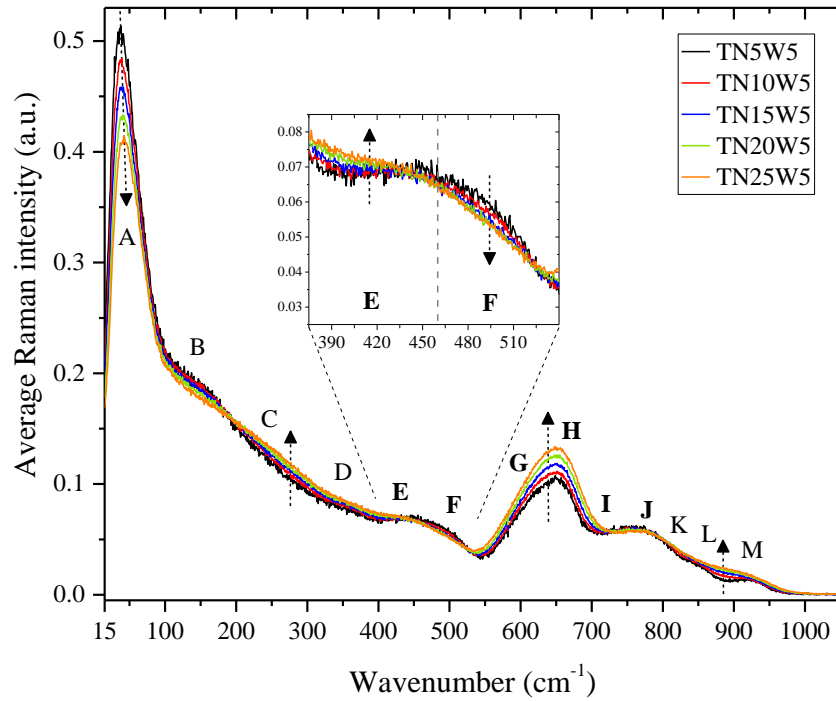

Fig. V.6. Total-area averaged VH-polarized Raman spectra of TNxW5 glasses. The labels A–M correspond to the inserted bands for spectral decomposition. Inset: zoom of the region 375-540 cm^{-1}.

Inserted band	Wavenumber (cm^{-1})	Raman band assignments
A	36.0 – 39.8	• The boson peak, ascribed to an excess density of vibrational states [168].
B	146.9 *(fixed)*	• Intra-chain vibrations of Te–Te bonds (as in amorphous t-Te) [169].
C	243.6 *(fixed)*	• Bending vibrations of WO$_6$ octahedra (as in γ-WO$_3$) [101].
D	351 *(fixed)*	• Bending vibrations of distorted WO$_6$ octahedra [101].
E	**425 *(fixed)***	• **Symmetric stretching vibrations in nearly symmetric Te–O–Te bridges (as in γ-TeO$_2$)** [63,64]. • Symmetric stretching vibrations of Te–O–Nb bridges (as in Nb$_2$Te$_4$O$_{13}$ and Nb$_2$Te$_3$O$_{11}$ [94]).
F	**497.3 – 522**	• **Symmetric stretching vibrations in Te–O–Te bridges** [63,64].
G	**607 *(fixed)***	• **Asymmetric stretching vibrations in nearly symmetric Te–O–Te bridges (as in γ-TeO$_2$)** [63,64]. • Stretching vibrations of highly asymmetric and almost terminal Te–O– – –Nb linkages [94]. • Stretching vibrations of Nb–O in Nb–O–Nb bridges (as in H-Nb$_2$O$_5$ [94]).
H	**658.8 – 661.1**	• **Asymmetric stretching vibrations in asymmetric Te–O–Te bridges** [63,64]. • Stretching vibrations of highly asymmetric and almost terminal Te–O– – –Nb linkages [94]. • Stretching vibrations of Nb–O in Nb–O–Nb bridges (as in H-Nb$_2$O$_5$ [94]).
I	**715 *(fixed)***	• **Asymmetric stretching vibrations in asymmetric Te–O–Te bridges** [63,64]. • Symmetric stretching vibrations in W–O–W bridges (as in γ-WO$_3$) [101].
J	**772 *(fixed)***	• **Asymmetric stretching of essentially covalent Te–$_{eq}$O bonds** [63,64].
K	820 *(fixed)*	• Asymmetric stretching vibrations in W–O–W bridges (as in γ-WO$_3$) [101].
L	852.3 – 845.9	• Stretching vibrations of W–O bonds in W–O–W bridges.
M	920.4 – 898.5	• Asymmetric stretching vibrations of W–O bonds [101]. • Stretching vibrations of the shortest Nb–O bonds [94].

Table V.4. Wavenumbers and vibrational assignments of the inserted bands. Raman bands arising from TeO$_2$ network and their assignments are highlighted in bold typeface. In the spectral decomposition process, the wavenumbers of A, F, H, L and M bands were unconstrained and are given herein as wavenumber ranges from the set of TNxW5 glasses with increasing x.

The obtained decomposition results, namely, the wavenumber, width and intensity of each inserted band, were used to calculate the bands' areas for each decomposed Raman spectrum. Then, the normalized intensity of each band is calculated by dividing the band area by the molar concentration(s) of the oxide(s) of which the constituent ionic species are responsible for that vibration (*cf.* Table V.4 for the assignments). We have calculated the normalized intensities of

bands E, G and H by dividing their areas by the sum of TeO_2 and $NbO_{2.5}$ molar contents; those of bands F, I and J by dividing their areas by TeO_2 content. The compositional dependence of the normalized intensities in TNxW5 glasses is plotted in Fig. V.7. Similar band evolutions are observed in other sets of TNxWy samples at constant WO_3 content and increasing $NbO_{2.5}$ content.
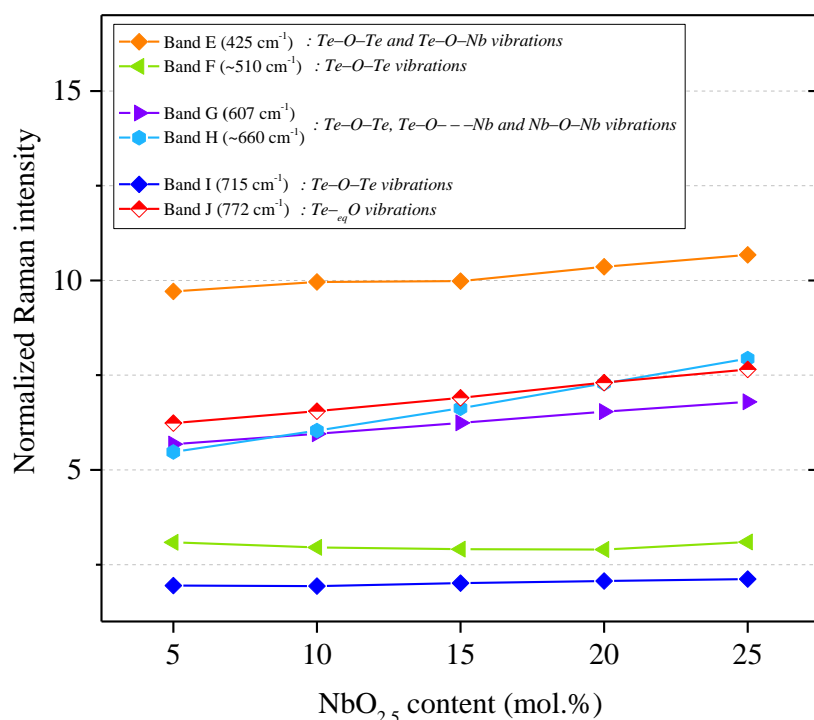
Fig. V.7. Compositional dependence of the normalized intensities of inserted bands for spectral decomposition of TNxW5 glasses (at constant WO_3 content).

Let us now focus on the decomposition results as a function of $NbO_{2.5}$ content from the mid- to high-wavenumber range 400-1000 cm^{-1}.

- ***In the 400-550 cm^{-1} region:***

As can be seen in the inset of Fig. V.6, the intensities of the two bands E and F seem to evolve in opposite directions. It can be seen from Fig. V.7 that while the normalized intensity of band E slightly increases by ~10%, the band F remains practically constant. The same steady evolution of band F which, unlike band E, is solely due to Te–O–Te bridges was observed in TTxWy glasses upon adding WO_3 from 5 to 25 mol.% (*cf.* Fig. IV.11). Taking into account the compositional evolutions of the two bands E and F, we argue that continuous adding of $NbO_{2.5}$

results in an **increase of the number of Te–O–Nb and/or nearly symmetric Te–O–Te bridges (as in γ-TeO₂)**.

- *In the 550-800 cm⁻¹ region:*

The normalized intensities of bands G and H increase by ~20% and ~45% respectively upon adding NbO$_{2.5}$ (Fig. V.7). To appropriately interpret the structural trend based on the evolution of these two bands, it is important to consider the shape of the corresponding Raman band (within the range of 535-725 cm⁻¹, *cf.* Fig. V.5). A simple visual analysis indicates that its intensity increases upon adding NbO$_{2.5}$ with no apparent band shift. From the viewpoint of the TeO₂-rich network in TNxW5 glasses, the fact that this large band does not red-shift might renounce any significant structural depolymerization. In the opposite case, *i.e.,* when a weak modifier cation such as Tl⁺ is incorporated within the TeO₂-rich network, a significant red-shift of this band is observed due to the simultaneous intensity *decrease* of the Raman band assigned to Te–O bond vibrations in TeO₄ units and *increase* of the one assigned to Te–O bond vibrations in TeO₃ units (*cf.* Fig. I.5). It is important to note that the stretching vibrations of Nb–O–Nb bridges are also observed in the 535-725 cm⁻¹ range (*cf.* Raman spectrum of H-Nb₂O₅ in Fig. V.5). Regarding the evolutions of bands I and J, their normalized intensities show marginal and stronger upward (increase by ~23%) trends respectively (Fig. V.7). Therefore, we argue that the evolution of bands G–J probably suggests **both a slight structural depolymerization of the Te–O–Te bond network and increasing number of Te–O–Nb and/or Nb–O–Nb bridges**.

It is relevant to assess the evolution of Raman band ratios corresponding to the two ultimate TeO₄ and TeO₃ structural units. In this spirit, Ghribi *et al.* [98] suggested to gauge the depolymerization extent (ratio of TeO₃/TeO₄) as a function of ZnO content in TeO₂-TiO₂-ZnO glasses by calculating the following ratio of normalized intensities: $(I_H + I_I)/(I_G + I_H + I_J)$ where the numerator holds the sum of intensity relative to bands due to stretching vibrations of Te–O in TeO₃ units, and denominator to those in TeO₄ units. We have calculated this ratio in TNxW5 glasses and the obtained results are illustrated in Fig. V.8. It is important to stress that the ratio values do not quantitatively reflect the ratio of TeO₃/TeO₄ but rather a qualitative evolution. This can be explained by the following reasons:

- The Raman intensity is proportional to both the number of vibrating entities and the extent of the polarizability change.

- It is complicated to sharply distinguish TeO_3 from TeO_{3+1} and TeO_4 units as there are no clear-cut boundaries due to a large panel of slightly distinct intermediate units demonstrating broad distributions of Te–O bond lengths.
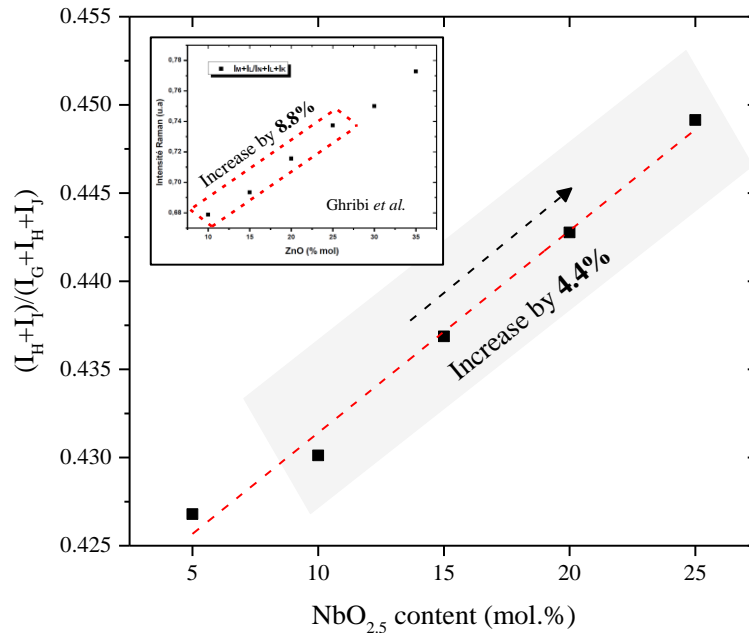
Fig. V.8. Evolution of the ratio $(I_H + I_I)/(I_G + I_H + I_J)$ in TNxW5 glasses. Inset: evolution of the same ratio in (95-y)TeO_2-5TiO_2-yZnO glasses as a function of ZnO content as reported by Ghribi *et al.* [98].

The observed increase of the ratio $(I_H + I_I)/(I_G + I_H + I_J)$ in TNxW5 glasses might indicate a slight transformation of TeO_4 into TeO_3 structural units. It is important to emphasize that this ratio increase in our TNxW5 glasses (by 4.4% from 10 to 25 mol.% $NbO_{2.5}$) is twice weaker than in (95-y)TeO_2-5TiO_2-yZnO glasses upon adding ZnO from 10 to 25 mol.% (*cf.* inset in Fig. V.8). This suggests that the structural effect of $NbO_{2.5}$ in depolymerizing the Te–O–Te bond network of TNxW5 glasses is weaker than that of ZnO; and very likely much weaker than the influence of alkali or alkaline-earth oxides which strongly induce the structural depolymerization of TeO_4 units into TeO_3 ones. Therefore, it can be argued that **$NbO_{2.5}$ has only a weak depolymerizing effect on the TeO_2-rich network by transforming TeO_4 into TeO_{3+1} and TeO_3 units.**

From the evolution of the Nb–O–Nb bond network, it seems that $NbO_{2.5}$ demonstrates a relatively close structural behavior as WO_3 in a way that increasing its content from 5 to 25 mol.% results in an increase of the number of $NbO_{2.5}$-rich regions until the crystallization of Nb_6TeO_{17} at 30 mol.% of $NbO_{2.5}$. As expressed in *section I.5.3.1*, the structure of this compound

has not been resolved yet; however, given the high $NbO_{2.5}$:TeO_2 ratio (6:1), one can predict the predominant contribution of Nb–O–Nb bridges in its crystal lattice. This shifting behavior of $NbO_{2.5}$ from a network modifier towards a network former as manifested by the presence of $NbO_{2.5}$-rich regions is in agreement with the obtained results from binary TeO_2-$NbO_{2.5}$ glasses by Hoppe *et al.* [120].

- ***In the 800-1000 cm^{-1} region:***

It should be noted that the intensity of the shoulder centered at ~880 cm^{-1} (*cf.* Fig. V.5) which is due to stretching vibrations of the shortest (terminal) Nb–O bonds increases but very moderately with $NbO_{2.5}$. This means that its expected normalized intensity must rather decrease since adding twice more $NbO_{2.5}$ (*e.g.,* from 5 to 10 mol.%) does not yield twice more intense response in this region. This suggests that **less and less terminal Nb–O bonds exist at the expense of Nb–O–Nb (bands G and H) and Te–O–Nb (band E) bridges**. This is in total agreement with the previously discussed evolution of these two varieties of bridges, *i.e.,* their number increase upon adding $NbO_{2.5}$. We omitted in Fig. V.7 the evolution of the normalized intensity of this shoulder centered at ~880 cm^{-1} for the two following reasons: *(i)* the shoulder is strongly overlapping with the surrounding bands L and M, and *(ii)* due to the influence of the band M (also due to the asymmetric stretching vibrations of W–O bonds) of which the normalized intensity changes as a function of the molar ratio of TeO_2 to WO_3 (*cf. section IV.4*). It is important though to keep in mind that the existence of terminal Nb–O bonds within the glass network demonstrates the weak depolymerizing effect of $NbO_{2.5}$. In other words, not all O^{2-} anions of $NbO_{2.5}$ are being transferred to the Te–O–Te bond network to induce the structural depolymerization, but instead, according to Dietzel's field strength theory (*cf. Chapter II* for more details), the Nb^{5+} cations with a relatively high cationic field strength of 1.263 (compared to 0.990 for Te^{4+}) form strong bonds with O^{2-} ions.

To sum up on the structural effect of $NbO_{2.5}$, it can be suggested that it is simultaneously manifested by *(i)* the weak structural depolymerization of Te–O–Te bond network and *(ii)* the existence of $NbO_{2.5}$-rich regions upon adding $NbO_{2.5}$.

V.4.3. Structural effect of adding WO_3: Comparison between TNW and TTW systems

The recorded Raman spectra of TNxWy glasses with increasing WO_3 content are presented in Fig. V.9. Similar intensity evolutions (upon adding WO_3) are observed at different $NbO_{2.5}$ contents. In comparison with TTxWy glasses, the Raman spectral evolution as a function of

WO₃ content is identical when comparing, for example, the TT5Wy and TN5Wy sets of glasses (*cf.* Fig. V.10); however as expected, there are some differences in terms of Raman intensities especially in the low- to mid-wavenumber region (~15-550 cm⁻¹). These discrepancies are essentially due to distinct structural effects of TiO_2 (in TT5Wy) and $NbO_{2.5}$ (in TN5Wy) on the short- to medium-range structure of the overall glass network.
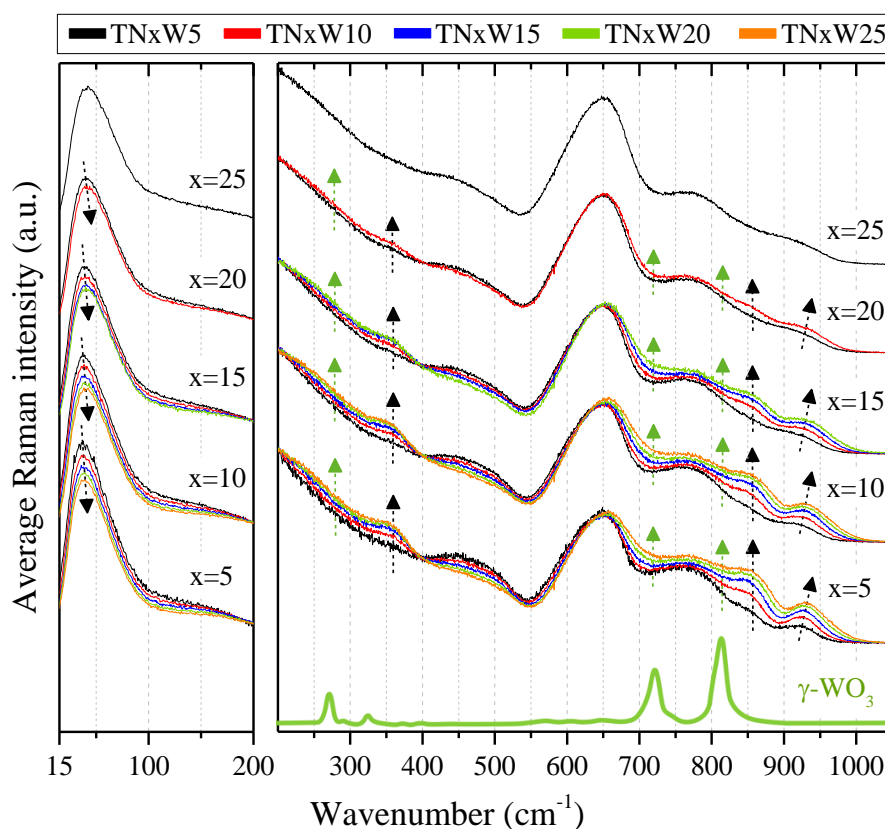
Fig. V.9. Evolution of total-area averaged VH-polarized Raman spectra of TNxWy glasses as a function of WO₃ content. The Raman spectrum of γ-WO₃ is reproduced from Fig. 2 in [101].
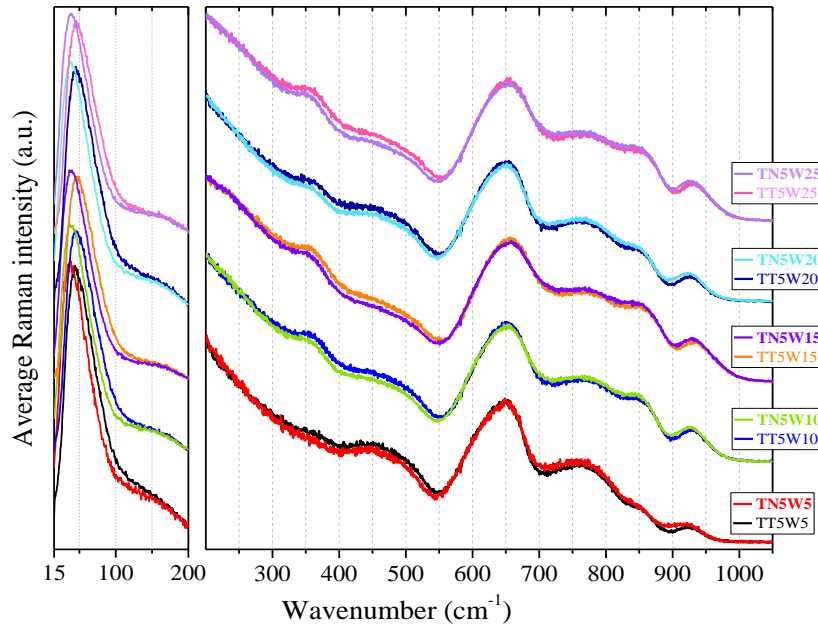
Fig. V.10. Comparison between the spectra of TT5Wy and TN5Wy glasses at different WO₃ contents.

To closely analyze the structural trends as a function of WO₃ content in TNxWy glasses, we have examined the evolution of the decomposed bands' normalized intensities. The obtained results for TN5Wy glasses are given below in Fig. V.11. Close tendencies are observed in other TNxWy sets of glasses (at constant NbO$_{2.5}$) with increasing WO₃ content (*cf.* Table V.5).
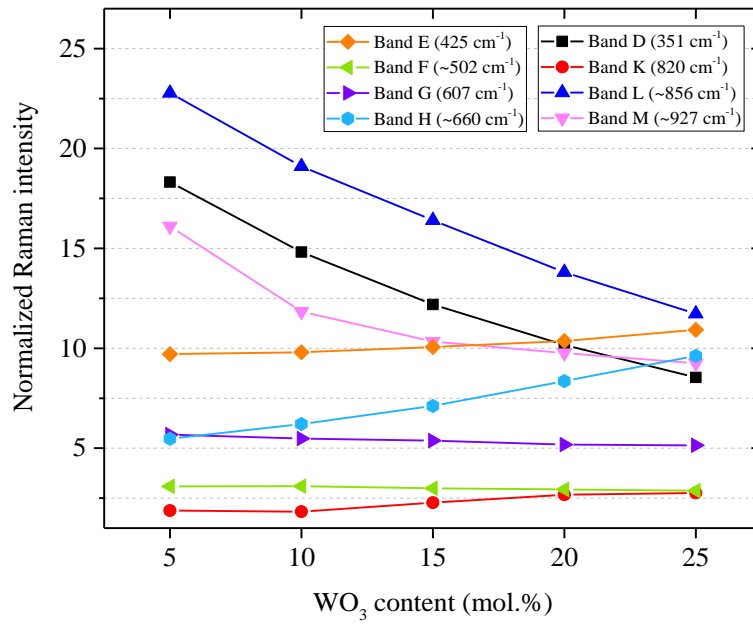
Fig. V.11. Compositional dependence of the normalized intensities of inserted bands for spectral decomposition of TN5Wy glasses.

Set of samples	Samples	Raman band normalized intensity			
		Band E	Band F	Band G	Band H
TN5Wy	TN5W5	9.709	3.088	5.682	5.474
	TN5W10	9.796	3.100	5.483	6.205
	TN5W15	10.066	2.995	5.375	7.114
	TN5W20	10.363	2.933	5.181	8.356
	TN5W25	10.923	2.870	5.139	9.626
Intensity evolution (%)		+12.51	-7.06	-9.56	+75.84
TN10Wy	TN10W5	9.960	2.791	5.951	6.039
	TN10W10	10.127	2.719	5.805	6.866
	TN10W15	10.420	2.712	5.792	7.904
	TN10W20	10.830	2.642	5.781	9.086
	TN10W25	11.270	2.646	5.821	10.438
Intensity evolution (%)		+13.15	-5.21	-2.18	+72.83
TN15Wy	TN15W5	9.981	2.907	6.240	6.626
	TN15W10	10.207	2.873	6.213	7.547
	TN15W15	10.441	2.973	6.268	8.624
	TN15W20	10.570	2.785	6.185	9.721
Intensity evolution (%)		+5.90	-4.19	-0.89	+46.73
TN20Wy	TN20W5	10.359	2.717	6.537	7.282
	TN20W10	10.560	2.739	6.617	8.254
Intensity evolution (%)		+1.94	+0.80	+1.22	+13.36
TN25Wy	TN25W5	10.676	2.708	6.797	7.938

Table V.5. Decomposition results of bands E-H at the Raman spectra of TNxWy glasses.

The evolutions of the normalized intensities of bands E-G suggest a minor structural modification of the bond network of TNxWy glasses (Fig. V.11) which is in agreement with TTxWy glasses (*cf. section IV.4.3*). While the bands F and G remain practically constant upon adding WO_3, the band E shows a slight increase of its normalized intensity that might be associated with a slightly increasing number of nearly symmetric Te–O–Te bridges. As previously highlighted in the *section IV.4.3*, the increasing normalized intensity of the band H (assigned to asymmetric stretching vibrations in asymmetric Te–O–Te bridges) is the result of its broadening due to a number increase of W–O–W bridges in the glass network upon adding WO_3 which complicates the interpretation of this band. The evolutions of the normalized intensities of bands D and K-M are also in accord with those observed for TTxWy glasses suggesting again a progressively reducing number of uniformly dispersed WO_6 octahedra at the expense of WO_3-rich regions with increasing WO_3 content.

V.5. Linear and nonlinear optical properties of TeO$_2$-NbO$_{2.5}$-WO$_3$ glasses

In the following, we report and discuss the linear and nonlinear optical properties recorded from double side polished glass pellets in the TeO$_2$-NbO$_{2.5}$-WO$_3$ system. The set of optical parameters and characterization techniques mentioned here are introduced in *section III.3.5*.

V.5.1. Linear optical properties of TeO$_2$-NbO$_{2.5}$-WO$_3$ glasses

V.5.1.1. Refractive index, optical band gap and Urbach energies by UV-Vis-NIR optical transmission

V.5.1.1.1. Refractive index from the optical transmission spectra

We recorded the optical transmission spectra from TNxWy glass pellets (1.44-1.47 mm in thickness) over a wide wavelength range extending from 300 to 3300 nm (*cf.* Fig. V.12). The optical transmission spectra of 16 out of 17 glass samples show a transparency over 75% in the 800-2600 nm range. The exception is the sample TN5W5 showing a slightly lower transparency of ~73%, which might be due to its peculiar composition (richest in TeO$_2$) at the boundary of the glass-forming domain. As for TTxWy glasses (*cf. section IV.5.1.1*), the absorption band onsetting at 2800 nm corresponds to the stretching mode of bound hydroxyl groups (R-OH), and symmetric and asymmetric stretching modes of water molecules [215].

As shown in the plots of the five sets of glasses (Fig. V.12), there is no specific trend of the optical transmission as a function of NbO$_{2.5}$ content. The transmission percentage is neither enhanced nor reduced upon adding NbO$_{2.5}$ but it rather slightly fluctuates within a relatively narrow range of less than 2%. This is also the case with increasing WO$_3$ content (Fig. V.13).

The linear refractive indices were extracted from the optical transmission data at $\lambda = 1.5$ µm using the following equation: $T = 2n/(n^2+1)$. The refractive indices ($n_{1.5}$) are listed in Table V.6. Generally, the obtained results suggest a practically constant behavior of the refractive index upon adding either NbO$_{2.5}$ or WO$_3$ with high values ranging approximately from 2.06 to 2.12. It should be stressed that because of the Fresnel reflection at the air-glass interface, the above equation slightly underestimates the actual refractive index value, which will then be provided from the ellipsometric measurements.
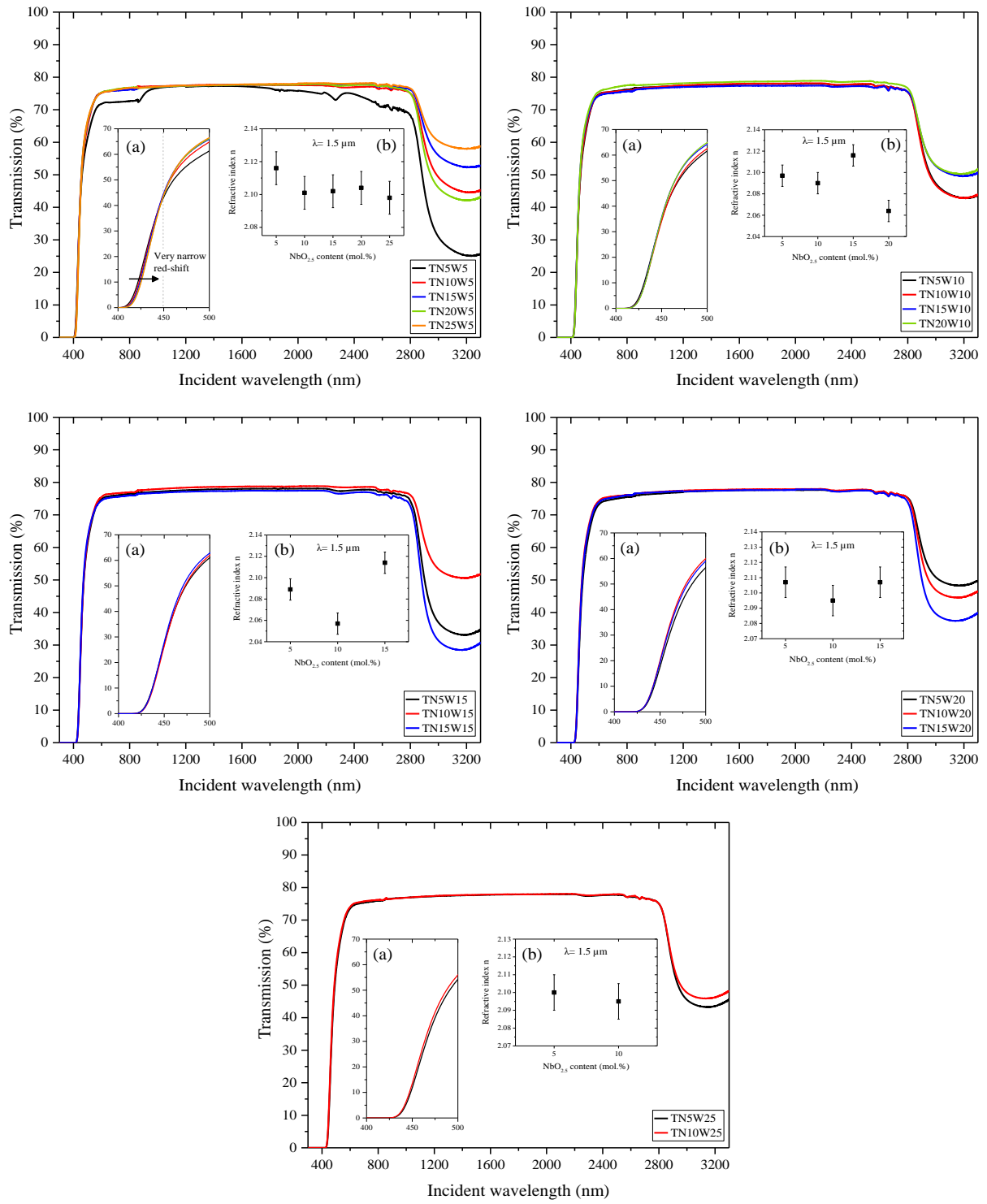
Fig. V.12. UV-Vis-NIR optical transmission spectra of TNxWy glasses. Insets: (a) zoom-in plot of the UV absorption edge; (b) compositional dependence of the refractive index $n_{1.5}$ extracted at 1.5 µm.
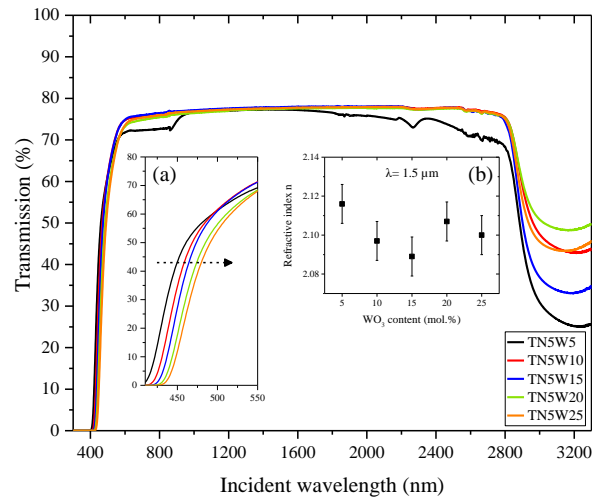
Fig. V.13. UV-Vis-NIR optical transmission spectra of TN5Wy glasses. Insets: (a) zoom-in plot of the UV absorption edge; (b) compositional dependence of the refractive index $n_{1.5}$ extracted at 1.5 µm.

Sample	$n_{1.5}$ ± 0.010	n_∞	E_g (eV) ± 0.020	E_U (eV) ± 0.002
TN5W5	2.116	2.142 ± 0.008	2.920	0.114
TN10W5	2.101	2.125 ± 0.005	2.913	0.110
TN15W5	2.102	2.149 ± 0.022	2.904	0.107
TN20W5	2.104	2.129 ± 0.019	2.897	0.106
TN25W5	2.098	2.145 ± 0.011	2.892	0.105
TN5W10	2.097	2.124 ± 0.006	2.860	0.109
TN10W10	2.090	2.134 ± 0.024	2.855	0.107
TN15W10	2.116	2.127 ± 0.019	2.850	0.104
TN20W10	2.064	2.149 ± 0.008	2.847	0.104
TN5W15	2.089	2.132 ± 0.006	2.832	0.108
TN10W15	2.057	2.140 ± 0.011	2.827	0.107
TN15W15	2.114	2.124 ± 0.008	2.822	0.105
TN5W20	2.107	2.128 ± 0.006	2.802	0.108
TN10W20	2.095	2.116 ± 0.008	2.800	0.106
TN15W20	2.107	2.138 ± 0.012	2.796	0.107
TN5W25	2.100	2.136 ± 0.023	2.777	0.108
TN10W25	2.095	2.145 ± 0.033	2.775	0.106

Table V.6. Refractive indices $n_{1.5}$ and n_∞, optical band gap E_g and Urbach E_U energies of TNxWy glasses.

The UV absorption edge slightly red-shifts from 410-415 nm upon adding NbO$_{2.5}$ in TNxW5 glasses, and across narrower regions in WO$_3$-rich compositions until it starts to marginally blue-

shift in TNxW25 glasses (Fig. V.12) implying a gradual decrease of the optical band gap energy E_g. Upon adding WO_3 (for example in TN5Wy glasses, *cf.* Fig. V.13), a stronger red-shift is observed within a larger wavelength range (400-437 nm). The color evolution of glass samples (described in *section V.2*) is in agreement with the detected red-shifts of the absorption edge.

We have also extracted both the optical band gap E_g and Urbach E_U energies for all TNxWy glasses from their respective UV absorption edges.

V.5.1.1.2. Optical band gap energy E_g

Based on the wavelength-dependence of the approximate absorption coefficient α (Fig. V.14(a)), we plotted $(\alpha h\nu)^{\frac{1}{2}}$ versus the incident photon energy hν (commonly known as Tauc plot) to estimate the E_g (Fig. V.14(b)). The E_g values lie in the range of 2.77–2.92 eV (*cf.* Table V.6).

Adding $NbO_{2.5}$ from 5 to 25 mol.% in TNxW5 glasses results in a steady evolution of E_g from 2.92 eV to 2.89 eV. On the other hand, adding WO_3 induces a slight decrease of 5% from TN5W5 (2.92 eV) to TN5W25 (2.78 eV). These evolutions of E_g upon adding $NbO_{2.5}$ and WO_3 are in agreement with the literature on the TeO_2-Nb_2O_5, TeO_2-ZrO_2-WO_3 and TeO_2-BaO-Nb_2O_5 systems [123,216,217]. Similar to the effect of TiO_2 in TTxWy glasses, E_g seems to remain fairly constant in WO_3-rich ones (2.78 eV in TN5W25 and TN10W25).

V.5.1.1.3. Urbach energy E_U

The extracted values of Urbach energy E_U remained fairly stable (0.109 eV in TN5Wy glasses) with increasing WO_3 content (Table V.6). However, a slight decrease (from 0.114 to 0.105 eV) is observed upon adding $NbO_{2.5}$ from TN5W5 to TN25W5 (Fig. V.15(f)). E_U is characteristic of the width of the band-tails thus estimating the density of localized states [175] (*cf. section III.3.5.1.2*). A highly disordered glass network is characterized by a higher density of localized states and thus having a high E_U value.
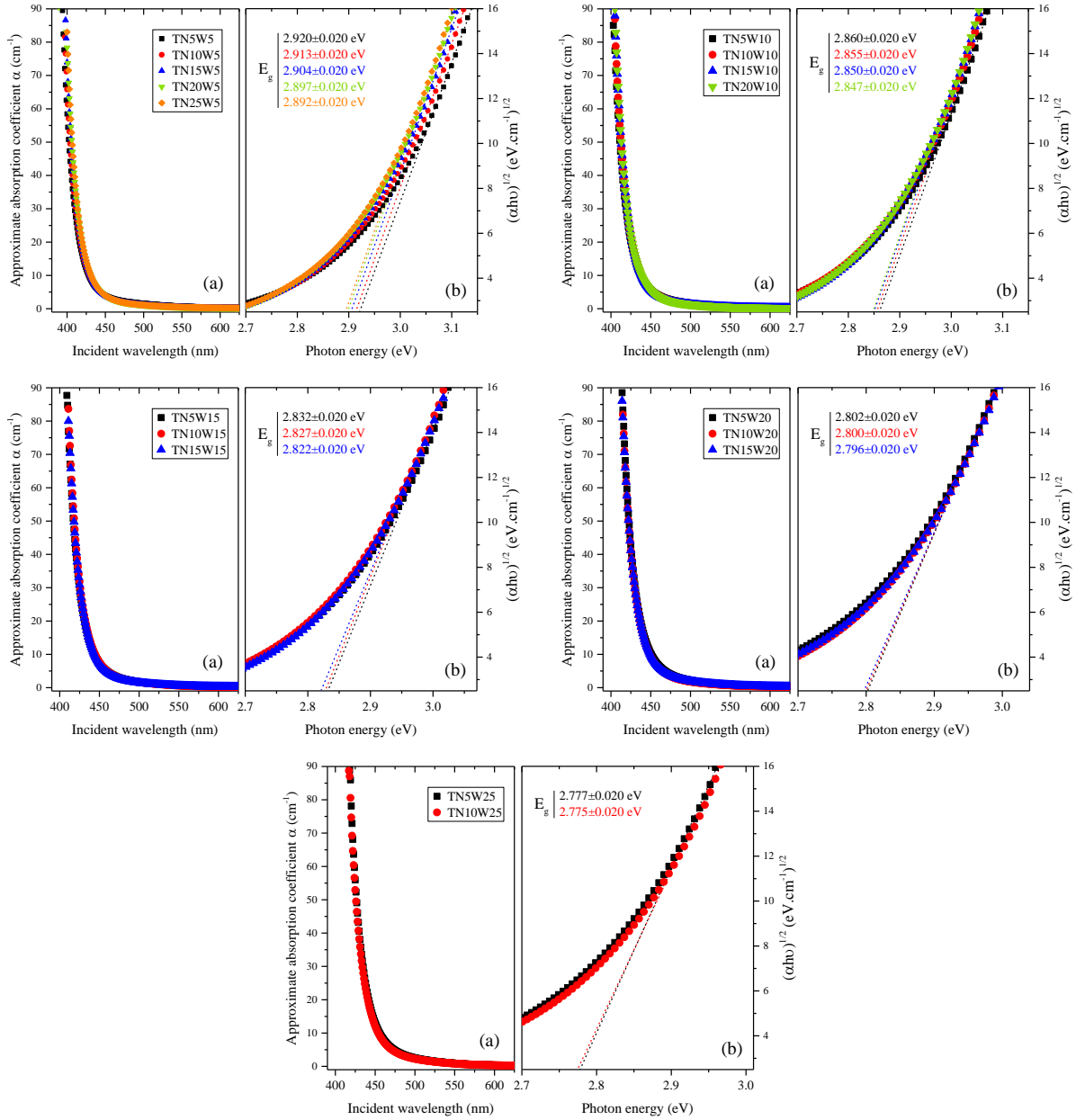
Fig. V.14. (a) Evolution of the approximate absorption coefficient α as a function of the incident wavelength in TNxWy glasses; (b) Tauc's plot for the optical band gap derived from the absorption coefficient.

It is worth mentioning that the estimated E_U values of TNxWy are slightly higher than those extracted for TTxWy glasses (ranging between 0.104 and 0.114 eV *vs.* 0.096 and 0.108 eV respectively). These values are very close to those reported in literature for $NbO_{2.5}$- and WO_3-containing TeO_2-based glasses (ranging between 0.096 and 0.114 eV, see *e.g.,* [109]). Therefore, it can be argued that adding $NbO_{2.5}$, same as TiO_2 in TTxWy glasses, might slightly lessen the overall structural disorder of the glass network. However, this effect seems slightly

stronger with TiO$_2$ (inducing a decrease of E$_U$ by ~9% from TT5W5 to TT15W5) than with NbO$_{2.5}$ (decrease by ~6% from TN5W5 to TN15W5).
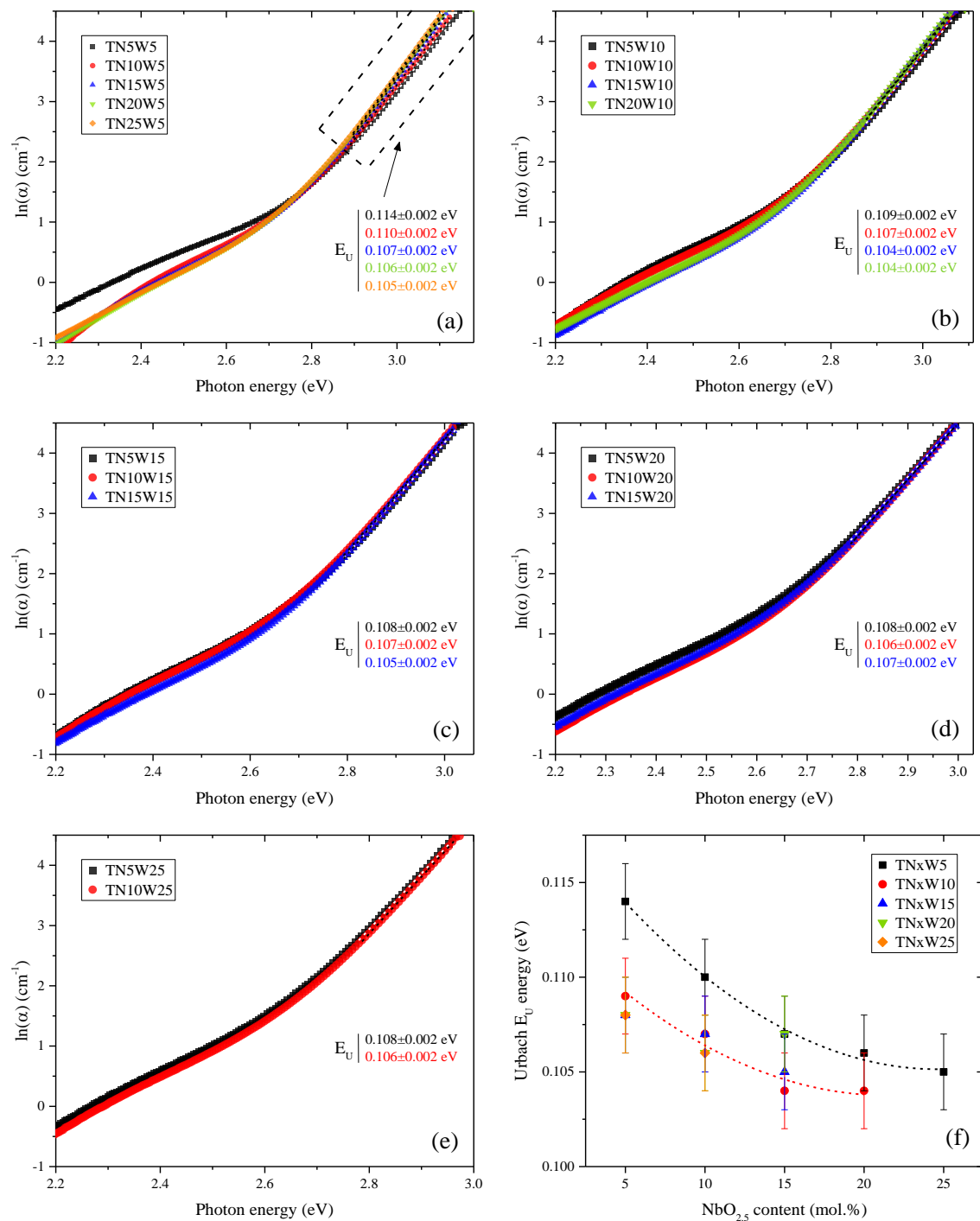
Fig. V.15. (a-e) Plots of ln(α) versus hν for Urbach energy E$_U$ determination of TNxWy glasses; (f) evolution of E$_U$ as a function of NbO$_{2.5}$ content.

V.5.1.2. Refractive index dispersion by spectroscopic ellipsometry

We have measured the wavelength-dispersion of the linear refractive index from TNxWy glass pellets (Fig. V.16) in the range of 350-830 nm, and derived the refractive indices n_∞ (*cf.* Table V.6) extrapolated to infinite wavelength using Sellmeier's dispersion formula as described in *section III.3.5.2.2*.

Similar to the observed trend in TTxWy glasses, the dependence of n_∞ index on WO_3 content suggests a rather constant behavior (average value of 2.14 in TNxW5 and TNxW25). Moreover, it seems that the refractive index remains practically constant upon adding $NbO_{2.5}$ from an average of 2.13 in TN5Wy glasses to 2.15 in TN25Wy (corresponding to the unique TN25W5 sample). A similar steady evolution of the refractive index in binary TeO_2-$NbO_{2.5}$ [129] is observed with values of 2.214-2.216 upon adding $NbO_{2.5}$ from 10 to 30 mol.%. With $n_{\infty(average)}$ of 2.134, these extracted n_∞ for TNxWy glasses are lower than those of TTxWy glasses ($n_{\infty(average)}$ of 2.19), and ~3% lower than those reported for the binary glasses. It is very important to stress that the n_∞ values reported here are higher in comparison to other binary or ternary systems (*e.g.,* less than 2.100 in TeO_2-TiO_2-ZnO glasses [98]) where a more consequential structural depolymerization occurs upon modifying the TeO_2-based glass network.

Fig. V.16. Refractive index dispersion of TNxWy glasses. Each dispersion curve corresponds to the average of three measured curves from different spots on the same glass sample. Insets: compositional dependence of the refractive index.

V.5.1.3. Bond network nature from the dispersion energy and electronic polarizability

Using two models available in the literature, we have gathered more optical constants such as the dispersion energy E_d and oxide ion polarizability α_{O2-} (Table V.7). It is interesting to

evaluate how these optical constants evolve as a function of the glass composition to get further insights into the short- to medium-range structure upon adding $NbO_{2.5}$ and WO_3.

Sample	E_d (eV)	E_0 (eV)	α_{O2^-} (E_g-based) (Å^3)
TN5W5	28.221 ± 0.744	7.910 ± 0.105	2.002 ± 0.100
TN10W5	25.588 ± 0.320	7.332 ± 0.065	1.878 ± 0.090
TN15W5	25.911 ± 1.743	7.213 ± 0.131	1.895 ± 0.080
TN20W5	24.938 ± 1.212	7.097 ± 0.114	1.932 ± 0.085
TN25W5	25.716 ± 0.677	7.188 ± 0.076	2.023 ± 0.090
TN5W10	26.121 ± 0.304	7.477 ± 0.058	1.985 ± 0.065
TN10W10	25.666 ± 1.975	7.269 ± 0.174	1.989 ± 0.080
TN15W10	26.196 ± 1.232	7.485 ± 0.126	2.014 ± 0.070
TN20W10	25.824 ± 0.321	7.179 ± 0.064	2.023 ± 0.100
TN5W15	24.658 ± 0.331	7.004 ± 0.050	2.046 ± 0.060
TN10W15	25.739 ± 0.989	7.235 ± 0.116	2.031 ± 0.060
TN15W15	23.905 ± 0.642	6.858 ± 0.093	2.050 ± 0.065
TN5W20	24.927 ± 0.268	7.113 ± 0.049	2.101 ± 0.060
TN10W20	25.882 ± 0.539	7.488 ± 0.094	2.086 ± 0.055
TN15W20	25.706 ± 1.031	7.244 ± 0.109	2.147 ± 0.055
TN5W25	25.599 ± 1.613	7.234 ± 0.133	2.125 ± 0.060
TN10W25	27.089 ± 2.853	7.565 ± 0.231	2.165 ± 0.055

Table V.7. Optical constants of TNxWy glasses.

The oscillator parameters E_d and E_0 are obtained from the plots of $1/(n^2-1)$ as a function of $(h\nu)^2$ (Fig. V.17(a)) using the single-effective-oscillator model of Wemple and DiDomenico [179] as explained in more details in *section III.3.5.1.3*. As previously stated, E_d was found to obey the following relationship in ionic and covalent crystals [178]: $E_d = \beta N_c Z_a N_e$. Where β parameter approaches 0.26 ± 0.04 eV and 0.37 ± 0.05 eV in ionic and covalent crystals respectively, N_c is the coordination number of the cation, Z_a the absolute charge number of the anion and N_e the total number of valence electrons per anion.
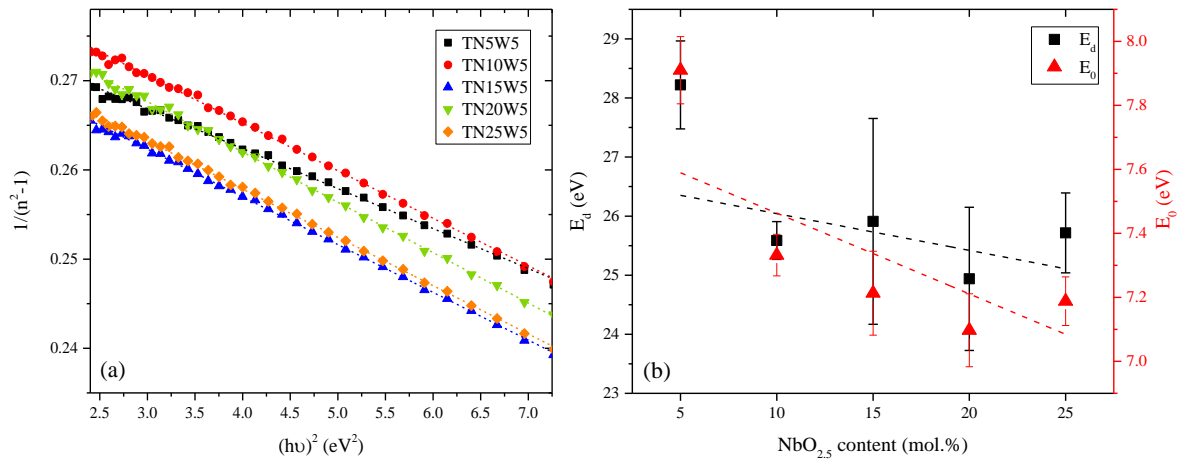
Fig. V.17. (a) Evolution of $1/(n^2-1)$ as a function of $(h\upsilon)^2$. (b) Evolution of oscillator parameters E_d and E_0 upon adding WO_3 in TNxW5 glasses.

The estimated E_d and E_0 values lie in the range 23.91–28.22 eV and 6.86–7.91 eV respectively. It appears that E_d slightly decreases in TNxW5 glasses (*cf.* Fig. V.17(b)) which might be related to the following: *(i)* A slight decrease of the coordination number of Te^{4+} cation upon adding $NbO_{2.5}$ as a result of the transformation of TeO_4 into TeO_{3+1} and TeO_3 units. This would be connected to a slightly decreasing the coordination number N_c; however, at the same time, adding $NbO_{2.5}$ would also contribute in increasing this parameter since Nb^{5+} cations are six-fold coordinated (versus four- or three-fold coordinated Te^{4+} cations). *(ii)* Increase of the bond network's ionicity when substituting TeO_2 with $NbO_{2.5}$ associated with a decreasing β parameter.

Based on the polarizability approach developed by Dimitrov and Komatsu [183], we calculated the oxide ion polarizabilities α_{O2^-} (*cf. section III.3.5.1.4*). We found α_{O2^-} to increase upon adding WO_3 by ~6% from 2.002 to 2.125 Å^3 (Table V.7); adding $NbO_{2.5}$ is found to increase α_{O2^-} by ~8% from 1.878 Å^3 in TN10W5 to 2.023 Å^3 in TN25W5 (*cf.* Fig. V.18). The extracted value for TN5W5 sample is higher than expected given that α_{O2^-} progressively increases with $NbO_{2.5}$ from TN10W5 to TN25W5. This might be connected with the briefly discussed discrepancy in *section V.5.1.1.1.*
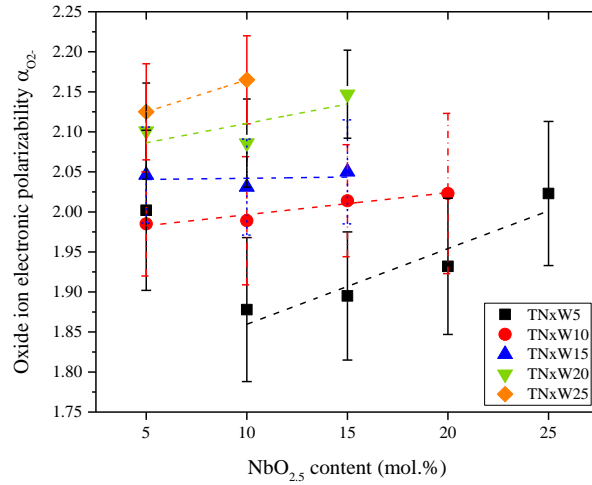
Fig. V.18. Evolution of $\alpha_{O^{2-}}$ as a function of $NbO_{2.5}$ content.

V.5.2. Nonlinear optical properties of TeO$_2$-NbO$_{2.5}$-WO$_3$ glasses

Using the Z-scan technique under the experimental conditions described in *section III.3.5.3*, we have derived the third-order nonlinear susceptibilities $\chi^{(3)}$ for the ternary TNxWy glasses (Table V.8)) using Milam's $\chi^{(3)}_{SiO2}$ value of 1.5 *10^{-14} esu [191] as a reference. The TNxWy glasses exhibit $\chi^{(3)}$ values of 5.48 *10^{-13} esu in average (~29% lower than those in TTxWy glasses of 7.03 *10^{-13} esu in average). Nevertheless, it is important to note that the extracted $\chi^{(3)}$ values are very high ($\chi^{(3)}_{min}$ = 4.75 *10^{-13} esu and $\chi^{(3)}_{max}$ = 6.38 *10^{-13} esu) with an average of 5.48 *10^{-13} esu which is ~37 times higher than the $\chi^{(3)}$ value of SiO$_2$ glass (1.5 *10^{-14} esu [191]) and only ~1.4 times lower than that of TeO$_2$ glass (7.54 *10^{-13} esu [157]).

The compositional dependence of $\chi^{(3)}$ values as a function of $NbO_{2.5}$ and WO$_3$ is given in Fig. V.19. Their evolution upon adding $NbO_{2.5}$ suggests a fairly constant behavior from 5.05 ± 1.00 *10^{-13} esu in TN5W5 to 5.05 ± 1.61 *10^{-13} esu in TN25W5. Likewise, adding WO$_3$ seems to maintain the $\chi^{(3)}$ values practically stable. This constant behavior with increasing WO$_3$ content was observed in TTxWy glasses as well (*section IV.5.2*).

Sample	Normalized Re($\chi^{(3)}$) (esu)
TN5W5	$5.05 \pm 1.00 *10^{-13}$
TN10W5	$4.99 \pm 0.94 *10^{-13}$
TN15W5	$5.66 \pm 1.33 *10^{-13}$
TN20W5	$6.24 \pm 1.23 *10^{-13}$
TN25W5	$5.05 \pm 1.61 *10^{-13}$
TN5W10	$5.33 \pm 1.17 *10^{-13}$
TN10W10	$5.42 \pm 1.16 *10^{-13}$
TN15W10	$5.03 \pm 1.05 *10^{-13}$
TN20W10	$6.38 \pm 2.11 *10^{-13}$
TN5W15	$5.62 \pm 1.39 *10^{-13}$
TN10W15	$4.82 \pm 1.11 *10^{-13}$
TN15W15	$6.05 \pm 1.44 *10^{-13}$
TN5W20	$4.75 \pm 0.95 *10^{-13}$
TN10W20	$5.27 \pm 1.00 *10^{-13}$
TN15W20	$5.40 \pm 1.22 *10^{-13}$
TN5W25	$5.36 \pm 1.23 *10^{-13}$
TN10W25	$5.82 \pm 1.05 *10^{-13}$

Table V.8. Normalized $\chi^{(3)}$ values of TNxWy glasses.

To evaluate the $\chi^{(3)}$ dependence on the $NbO_{2.5}$ and WO_3 contents, we calculated the average $\chi^{(3)}$ values for each set of TNxWy glasses with either $NbO_{2.5}$ or WO_3 constant (*cf.* Table V.9).

Set of samples	Normalized Re($\chi^{(3)}$) (esu)
TN5Wy	$5.22 \pm 1.15 *10^{-13}$
TN10Wy	$5.26 \pm 1.05 *10^{-13}$
TN15Wy	$5.54 \pm 1.26 *10^{-13}$
TN20Wy	$6.31 \pm 1.67 *10^{-13}$
TN25Wy	$5.05 \pm 1.61 *10^{-13}$
TNxW5	$5.40 \pm 1.22 *10^{-13}$
TNxW10	$5.54 \pm 1.37 *10^{-13}$
TNxW15	$5.50 \pm 1.31 *10^{-13}$
TNxW20	$5.14 \pm 1.06 *10^{-13}$
TNxW25	$5.59 \pm 1.14 *10^{-13}$

Table V.9. Calculated average $\chi^{(3)}$ values of TNxWy glasses.
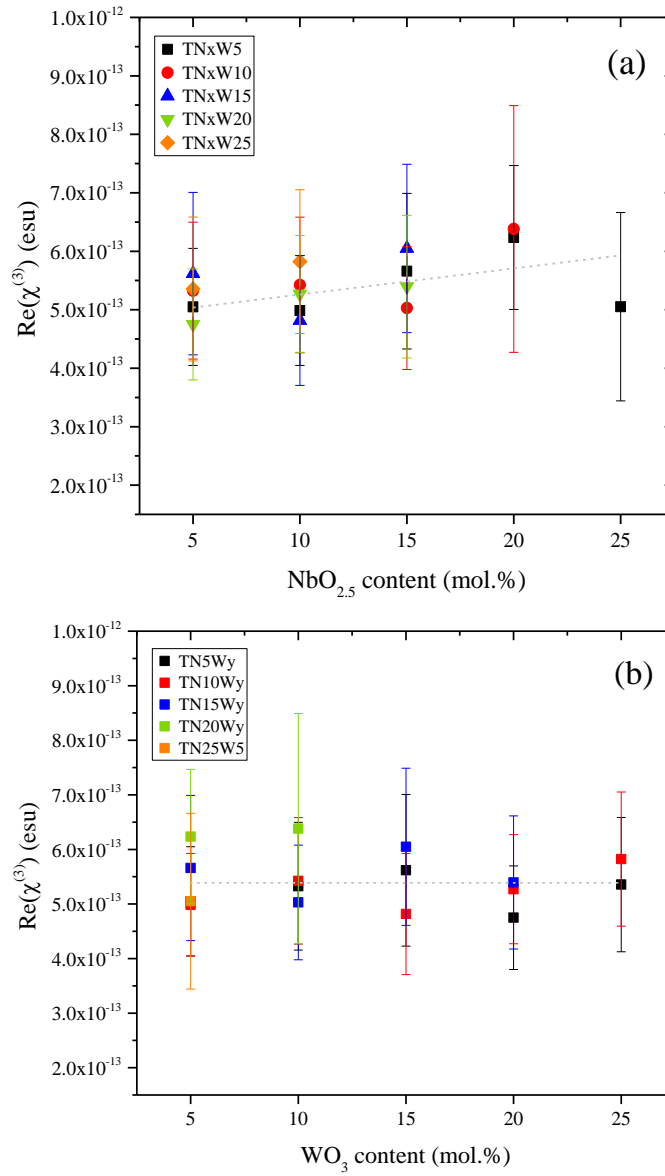
Fig. V.19. Evolution of normalized $\chi^{(3)}$ values as a function of (a) $NbO_{2.5}$ and (b) WO_3 contents.

It appears that adding $NbO_{2.5}$ positively contributes to the $\chi^{(3)}$ in TNxWy glasses. In fact, the average value of $\chi^{(3)}$ seems to increase by ~21% from $5.22 \pm 1.15 *10^{-13}$ esu in TN5Wy to $6.31 \pm 1.67 *10^{-13}$ esu in TN20Wy (*cf.* Table V.9). Such a positive contribution might be due to an increase of Te–O–Nb and Nb–O–Nb bridges upon adding $NbO_{2.5}$ as highlighted in *section V.4.2*. The lower $\chi^{(3)}$ value of $5.05 \pm 1.61 *10^{-13}$ esu measured from TN25W5 sample might be explained by its composition situated at the glass-forming boundary. It is worthwhile to mention that the binary $(100-x)TeO_2$-$xNbO_{2.5}$ glasses exhibit higher $\chi^{(3)}$ values ranging from $7.540 *10^{-13}$ esu (x = 10 mol.%) to $9.037 *10^{-13}$ esu (x = 30 mol.%) [41]. Moreover, a slight increase of $\chi^{(3)}$ by ~4% is suggested upon adding WO_3 from $5.40 \pm 1.22 *10^{-13}$ esu in TNxW5 to $5.59 \pm 1.14 *10^{-13}$ esu in TNxW25 (Table V.9). This is in agreement with the evolution in both

TTxWy (from $6.44 \pm 1.56 \times 10^{-13}$ in TTxW5 to $7.48 \pm 2.04 \times 10^{-13}$ in TTxW25) and binary $(100-x)TeO_2-xWO_3$ glasses (from 7.59×10^{-13} esu at x = 10 mol.% to 8.50×10^{-13} esu at x = 30 mol.% [41]).

The overall evolution of the nonlinear response of TNxWy glasses upon substituting TeO_2 with either $NbO_{2.5}$ or WO_3 is shown in Fig. V.20. This positive contribution to the nonlinear susceptibility $\chi^{(3)}$ could be explained by *(i)* the possible influence of empty *d* orbitals of each of Nb^{5+} and W^{6+} cations via virtual electronic transitions to *d*-orbitals and to the conduction band *sp*-orbitals as reported by Lines [43], and *(ii)* the slight structural modifications induced by adding $NbO_{2.5}$ and WO_3 to the TeO_2-rich network. Nevertheless, it is very important to keep in mind that these derived values are only approximate $\chi^{(3)}$ responses with significant error bars of ~25% in average; thus, those discussed evolutions can also be considered as practically steady.
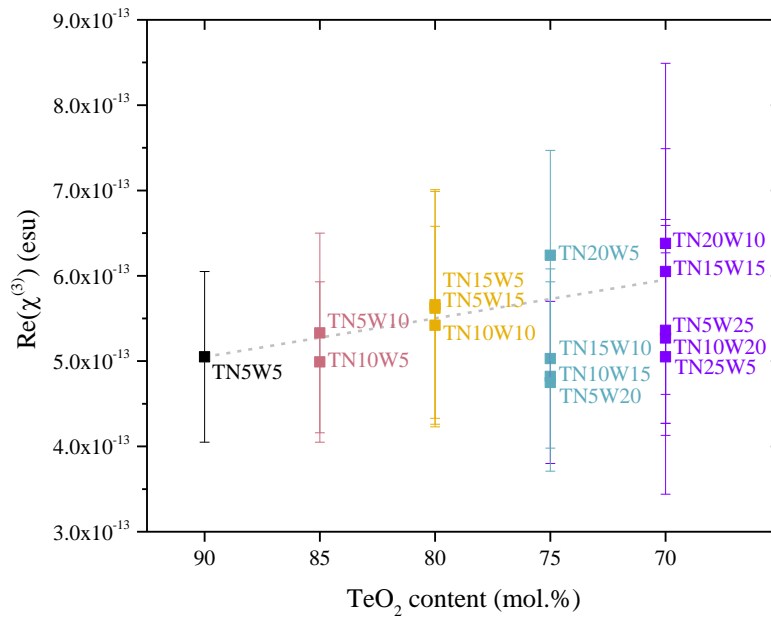
Fig. V.20. Evolution of normalized $\chi^{(3)}$ values as a function of TeO_2 content.

Generally, the evolution of the nonlinear optical performance of TNxWy glasses is consistent with the structural interpretations established in *section V.4* suggesting that only relatively slight modifications occur throughout the glass network with addition of either $NbO_{2.5}$ or WO_3. As previously established, adding $NbO_{2.5}$ induces only a slight network depolymerization towards the TeO_{3+1} and TeO_3 units. Finally, the steady evolution of $\chi^{(3)}$ values upon adding $NbO_{2.5}$ or

WO$_3$ highly suggests the absence of any striking structural depolymerization of the Te–O–Te bond network.

V.6. Discussion and concluding remarks

The glass-forming domain, density, thermal, structural and optical properties of (100-x-y)TeO$_2$-xNbO$_{2.5}$-yWO$_3$ glasses have been investigated and analyzed as a function of NbO$_{2.5}$ and WO$_3$ contents. The explored glass-forming domain holds seventeen compositions and extends from x = 5 to 25 mol.% in NbO$_{2.5}$ and y = 5 to 25 mol.% in WO$_3$. The prepared TNxWy glasses exhibit moderate thermal stabilities ($\Delta T_{(min)} = 45$ °C and $\Delta T_{(max)} = 70$ °C) and glass transition temperatures that increase with addition of either NbO$_{2.5}$ or WO$_3$ ($T_{g(min)} = 333$ °C and $T_{g(max)} = 403$ °C).

The average ΔT stabilities of TNxWy glasses are ~40% higher than those of TTxWy (*cf. section IV.3.2*). This improved thermal stability in the presence of NbO$_{2.5}$ could be explained by the active participation of NbO$_6$ octahedra in the Te–O–Te bond network (versus phase separation of amorphous TiO$_2$-rich regions in TTxWy glasses) as established from the Raman spectral decomposition results reported in *section V.4.2*.

We report the following structural trends:

- The structural effect of incorporating NbO$_{2.5}$ is demonstrated in both *(i)* a weak structural depolymerization of the Te–O–Te bond network accompanied by an increasing number of Te–O–Nb and/or Nb–O–Nb bridges and *(ii)* existence of NbO$_{2.5}$-rich regions upon continuous addition of NbO$_{2.5}$ until the crystallization of Nb$_6$TeO$_{17}$ compound which corresponds to a high NbO$_{2.5}$:TeO$_2$ ratio of 6:1.

- Adding WO$_3$ results, at low WO$_3$ contents, in uniformly dispersed WO$_6$ octahedra throughout the glass network, and at higher WO$_3$ contents, in amorphous "WO$_3$-rich" regions that continuously grow prior to the crystallization of WO$_{2.83}$ in TNxW30 samples. These trends are similar to those elucidated from TTxWy glasses. This idea is in agreement with the one proposed by Sekiya *et al.* [103] and recently highlighted in the TeO$_2$-TiO$_2$-WO$_3$ glassy system [192].

The revealed structural properties are consistently correlated to the measured optical (linear and nonlinear) properties. The studied TNxWy glasses exhibit high linear refractive indices ($n_{\infty(min)} = 2.12$ and $n_{\infty(max)} = 2.15$) with an average n_∞ of 2.13 which is ~1.5 times higher than the

refractive index of SiO_2 glass and practically equal to that of TeO_2 glass. It is found that the measured n_∞ values remain practically constant upon adding either $NbO_{2.5}$ or WO_3. The observed slight decrease of the dispersion energy upon adding $NbO_{2.5}$ might be connected with *(i)* the slight decrease of the coordination number of Te^{4+} cation as a result of the weak structural depolymerization (transformation of TeO_4 units into TeO_{3+1} and TeO_3 ones), and *(ii)* an increasing ionicity of the glass network upon substituting TeO_2 with transition-metal oxide $NbO_{2.5}$ (also suggested to be the case in TTxWy glasses upon substituting TeO_2 with TiO_2 and WO_3).

The third-order nonlinear susceptibilities $\chi^{(3)}$ of TNxWy glasses were measured by means of the Z-scan setup. The extracted $\chi^{(3)}$ values are very high ($\chi^{(3)}_{min} = 4.75 *10^{-13}$ esu and $\chi^{(3)}_{max} = 6.38 *10^{-13}$ esu) with an average of $5.48 *10^{-13}$ esu that is ~37 times stronger than the reported $\chi^{(3)}$ value for SiO_2 glass and only ~1.4 times lower than that of TeO_2 glass. Moreover, they are found to remain practically steady with addition of $NbO_{2.5}$ and WO_3: from TN5Wy ($5.22 \pm 1.15 *10^{-13}$ esu) to TN25Wy ($5.05 \pm 1.61 *10^{-13}$ esu), and from TNxW5 ($5.40 \pm 1.22 *10^{-13}$ esu) to TNxW25 ($5.59 \pm 1.14 *10^{-13}$ esu) respectively. Even though these $\chi^{(3)}$ values are lower than those recorded from TTxWy glasses (average of $7.02 *10^{-13}$ esu), they remain higher than those reported for other TeO_2-based systems particularly those where a significant structural depolymerization takes place (*e.g.,* ZnO- or alkali-containing glasses).

General conclusion

The present work represents a contribution to the structural description of TeO_2-based glasses via the Raman spectroscopic approach. The primary focus is laid on revealing the structural and optical properties of new ternary glasses within the TeO_2-TiO_2-WO_3 and TeO_2-$NbO_{2.5}$-WO_3 systems. We embarked upon investigating these systems for the following reasons. In the literature, it is established that binary TeO_2-TiO_2 glasses maintain the original structural organization of pure TeO_2 glass and positively contribute to the linear and nonlinear optical properties. Moreover, addition of WO_3 and/or $NbO_{2.5}$ results in an improvement of thermal and optical properties of TeO_2-based glasses.

In the perspective of providing fresh insights into the structural features of TeO_2-based glasses, we applied the cationic field strength theory, one of the classical theories on glass formation, to predict the structural behaviors in binary TeO_2-based glasses based on the criterion of the field strength difference ΔFS between the two constituent types of cations. A number of 111 binary TeO_2-MO_x crystals and 31 binary TeO_2-based glasses have been considered in the framework of this study. Globally, these behaviors are found in good agreement with the experimental works reported in the literature. One of the noteworthy results obtained using this theoretical approach is the predicted phase separation in binary TeO_2-TiO_2 glasses into two pure phases: TeO_2-rich and TiO_2-rich networks.

We have prepared and examined new glasses in the form of pellets within the two ternary TeO_2-TiO_2-WO_3 (TTxWy glasses with a total of fifteen compositions) and TeO_2-$NbO_{2.5}$-WO_3 (TNxWy glasses with a total of seventeen compositions) systems. A special focus was dedicated to the compositional-dependence of their structural and optical (linear and nonlinear) properties. Interestingly, consistent correlations between the measured structural and optical properties are established. The obtained insights are organized in the following illustration for both systems.
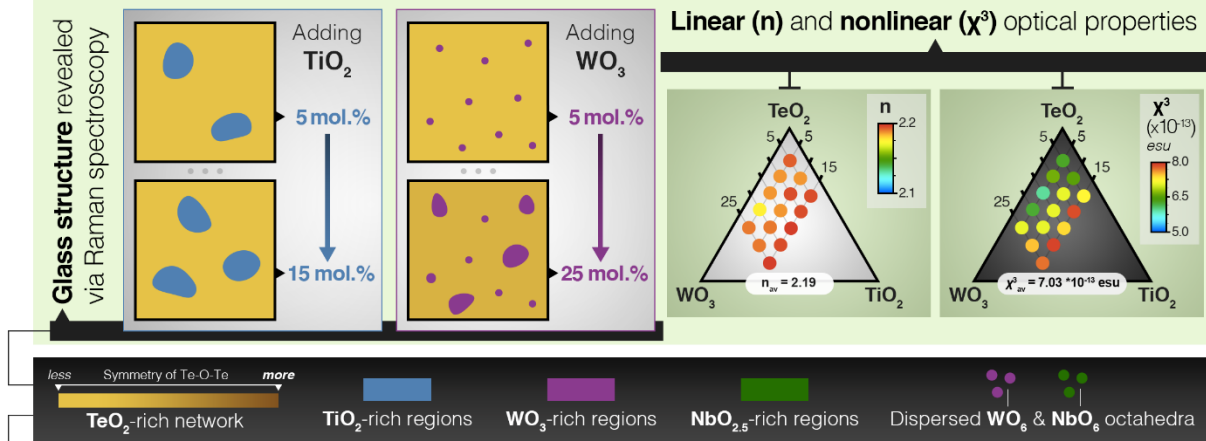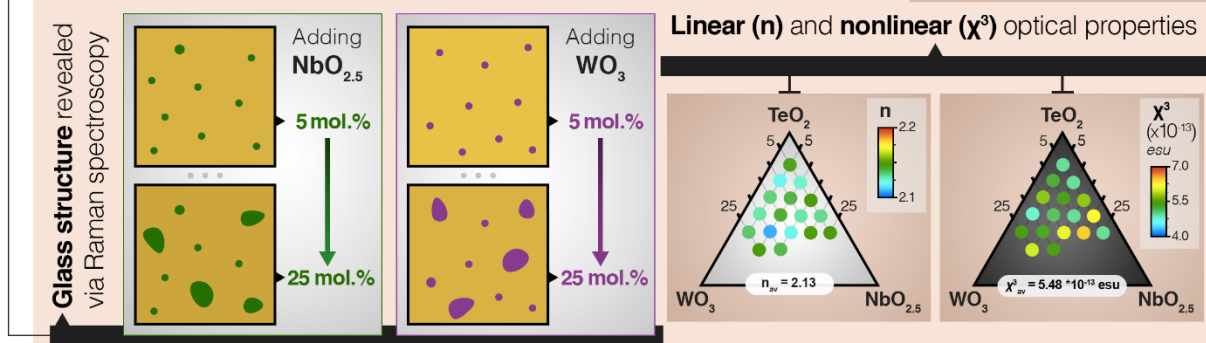
Using a Raman spectroscopic approach based on the full-scale spectral decomposition, we elucidated the structural effects of adding TiO_2 and WO_3 on the short- to medium-range structure in TTxWy glasses. The obtained results suggest the following structural trends:

- Globally, only minor structural modifications occur with addition of TiO_2 or WO_3. This indicates that *(i)* these glasses commonly share features of the original TeO_2 glass network and suggests *(ii)* the absence of any significant structural depolymerization of the Te–O–Te bond network.

- Adding TiO_2 results essentially in a phase separation between amorphous TeO_2-network and amorphous "rutile-like" TiO_2-rich regions (assumed to be of a nanometric size), thus explaining the limited glass-forming domain to only 15 mol.%. Hence, it appears unlikely that hybrid Te–O–Ti bridges construct the bond network in these glasses. This idea of phase separation is also supported by the application of Dietzel's cationic field strength on the binary TeO_2-TiO_2 system. In a future work, we would like to confirm the existence of such TiO_2-rich regions using cryogenic transmission electron microscopy.

- Upon adding WO_3, we argue that only a minor change affects the Te–O–Te bond network. At low WO_3 content, uniformly dispersed WO_6 octahedra are expected to exist in the glass network, and at a higher WO_3 content, amorphous WO_3-rich regions continuously grow before the crystallization of γ-WO_3 at 30 mol.% in WO_3.

The investigated TTxWy glasses exhibit high linear refractive indices with an average of ~2.19 ($n_{\infty(min)}$ = 2.17 and $n_{\infty(max)}$ = 2.21) that remain fairly constant with addition of TiO_2 or WO_3. The estimated evolution of the dispersion energy supports a slight increase of the glass network's ionicity upon the substitution of TeO_2 with TiO_2 and WO_3, which is in agreement with the moderate increase of the electronic oxide ion polarizability. The measured nonlinear susceptibilities $\chi^{(3)}$ of TTxWy glasses are remarkably high, namely, with an average of 7.03 *10^{-13} esu that is ~46.9 times higher than the reported $\chi^{(3)}$ value for SiO_2 glass (1.5 *10^{-14} esu [191]). Furthermore, it seems that upon adding TiO_2 and WO_3, $\chi^{(3)}$ is slightly enhanced with an increase by ~18% from TT5Wy (6.42 ± 1.59 *10^{-13} esu) to TT15Wy (7.57 ± 1.91 *10^{-13} esu) and by ~15% from TTxW5 (6.44 ± 1.56 *10^{-13} esu) to TTxW25 (7.48 ± 2.04 *10^{-13} esu).

Along the same lines, we revealed the structural effects of adding $NbO_{2.5}$ and WO_3 on the short- to medium-range structural network in TNxWy glasses. The gained insights can be summarized as follows:

- We argue that the influence of incorporating $NbO_{2.5}$ is manifested in both *(i)* a weak induced structural depolymerization of the Te–O–Te bond network and *(ii)* occurrence of $NbO_{2.5}$-rich regions with continuous addition of $NbO_{2.5}$ until the crystallization of Nb_6TeO_{17} compound which corresponds to a high $NbO_{2.5}$:TeO_2 ratio of 6:1.

- Adding WO_3 leads to *(i)* uniformly dispersed WO_6 octahedra throughout the glass network (at low WO_3 contents), and *(ii)* amorphous "WO_3-rich" regions (at higher WO_3 contents). Such regions continuously grow until the crystallization of $WO_{2.83}$ in partially crystallized TNxW30 samples. These structural trends are similar to those revealed from TTxWy glasses.

The prepared TNxWy glasses also possess high linear refractive indices with an average of ~2.13 ($n_{\infty(min)}$ = 2.12 and $n_{\infty(max)}$ = 2.15) that remain essentially constant upon adding $NbO_{2.5}$ or WO_3. The estimated slight decrease of the dispersion energy with addition of $NbO_{2.5}$ might be the result of *(i)* a slight decrease of the coordination number of Te^{4+} cation due to the transformation of TeO_4 into TeO_{3+1} and TeO_3 units, and *(ii)* an increase of the bond network's ionicity when substituting TeO_2 with the transition-metal oxide $NbO_{2.5}$. Likewise, high

nonlinear susceptibilities $\chi^{(3)}$ were recorded from TNxWy glasses with an average of 5.48 $*10^{-13}$ esu (slightly lower than TTxWy glasses) that is ~36.5 times stronger than the reported $\chi^{(3)}$ value for SiO_2 glass. These $\chi^{(3)}$ values are found to remain practically steady with addition of $NbO_{2.5}$ and WO_3: from TN5Wy (5.22 ± 1.15 $*10^{-13}$ esu) to TN25Wy (5.05 ± 1.61 $*10^{-13}$ esu), and from TNxW5 (5.40 ± 1.22 $*10^{-13}$ esu) to TNxW25 (5.59 ± 1.14 $*10^{-13}$ esu) respectively.

Generally, the compositional-dependence of the linear and nonlinear optical properties of TTxWy and TNxWy glasses exhibits a practically steady behavior which agrees with the established structural descriptions using Raman spectroscopy. Moreover, the extracted $\chi^{(3)}$ values are higher than those reported for other TeO_2-based systems especially the ones where a strong structural depolymerization takes place (*e.g.,* ZnO- or alkali-containing glasses).

References

[1] G. Lifante, Integrated photonics: fundamentals, J. Wiley, Hoboken, NJ, 2003.

[2] V.A.G. Rivera, D. Manzani, eds., Technological advances in tellurite glasses, Springer International Publishing, Cham, 2017. doi:10.1007/978-3-319-53038-3.

[3] R.A.H. El-Mallawany, Tellurite glasses handbook: physical properties and data, 2nd ed, Taylor & Francis, Boca Raton, FL, 2011.

[4] E. Fargin, A. Berthereau, T. Cardinal, G. Le Flem, L. Ducasse, L. Canioni, P. Segonds, L. Sarger, A. Ducasse, Optical non-linearity in oxide glasses, J. Non-Cryst. Solids. 203 (1996) 96–101. doi:10.1016/0022-3093(96)00338-9.

[5] B. Jeansannetas, S. Blanchandin, P. Thomas, P. Marchet, J.C. Champarnaud-Mesjard, T. Merle-Méjean, B. Frit, V. Nazabal, E. Fargin, G. Le Flem, M.O. Martin, B. Bousquet, L. Canioni, S. Le Boiteux, P. Segonds, L. Sarger, Glass structure and optical nonlinearities in thallium(I) tellurium(IV) oxide glasses, J. Solid State Chem. 146 (1999) 329–335. doi:10.1006/jssc.1999.8355.

[6] S. Suehara, P. Thomas, A. Mirgorodsky, T. Merle-Méjean, J.C. Champarnaud-Mesjard, T. Aizawa, S. Hishita, S. Todoroki, T. Konishi, S. Inoue, Non-linear optical properties of TeO_2-based glasses: ab initio static finite-field and time-dependent calculations, J. Non-Cryst. Solids. 345–346 (2004) 730–733. doi:10.1016/j.jnoncrysol.2004.08.191.

[7] S. Suehara, P. Thomas, A.P. Mirgorodsky, T. Merle-Méjean, J.C. Champarnaud-Mesjard, T. Aizawa, S. Hishita, S. Todoroki, T. Konishi, S. Inoue, Localized hyperpolarizability approach to the origin of nonlinear optical properties in TeO_2-based materials, Phys. Rev. B. 70 (2004). doi:10.1103/PhysRevB.70.205121.

[8] E.M. Roginskii, V.G. Kuznetsov, M.B. Smirnov, O. Noguera, J.-R. Duclère, M. Colas, O. Masson, P. Thomas, Comparative Analysis of the Electronic Structure and Nonlinear Optical Susceptibility of α-TeO_2 and β-TeO_3 Crystals, J. Phys. Chem. C. 121 (2017) 12365–12374. doi:10.1021/acs.jpcc.7b01819.

[9] A.P. Mirgorodsky, M. Soulis, P. Thomas, T. Merle-Méjean, M. Smirnov, Ab initio study of the nonlinear optical susceptibility of TeO_2-based glasses, Phys. Rev. B. 73 (2006) 134206. doi:10.1103/PhysRevB.73.134206.

[10] M. Soulis, T. Merle-Méjean, A.P. Mirgorodsky, O. Masson, E. Orhan, P. Thomas, M.B. Smirnov, Local molecular orbitals and hyper-susceptibility of TeO_2 glass, J. Non-Cryst. Solids. 354 (2008) 199–202. doi:10.1016/j.jnoncrysol.2007.07.036.

[11] M. Smirnov, A. Mirgorodsky, O. Masson, P. Thomas, Quantum mechanical study of pre-dissociation enhancement of linear and nonlinear polarizabilities of $(TeO_2)_n$ oligomers as a key to understanding the remarkable dielectric properties of TeO_2 glasses, J. Phys. Chem. A. 116 (2012) 9361–9369. doi:10.1021/jp303014k.

[12] M. Tite, A. Shortland, S. Paynter, The beginnings of vitreous materials in the near east and Egypt, Acc. Chem. Res. 35 (2002) 585–593. doi:10.1021/ar000204k.

[13] E.D. Zanotto, J.C. Mauro, The glassy state of matter: Its definition and ultimate fate, J. Non-Cryst. Solids. 471 (2017) 490–495. doi:10.1016/j.jnoncrysol.2017.05.019.

[14] W.H. Zachariasen, The atomic arrangement in glass, J. Am. Chem. Soc. 54 (1932) 3841–3851. doi:10.1021/ja01349a006.

[15] A.J. Leadbetter, A.C. Wright, Diffraction studies of glass structure, J. Non-Cryst. Solids. 7 (1972) 23–36. doi:10.1016/0022-3093(72)90015-4.

[16] C.A. Angell, The old problems of glass and the glass transition, and the many new twists, Proc Natl Acad Sci U A. 92 (1995) 6675–6682.

[17] A.K. Varshneya, Fundamentals of inorganic glasses, Academic Press, Boston, 1994.

[18] P.G. Debenedetti, F.H. Stillinger, Supercooled liquids and the glass transition, Nature. 410 (2001) 259–267. doi:10.1038/35065704.

[19] W. Vogel, The development of the classical structure theories, Struct. Cryst. Glas. (1971) 14–20. doi:10.1016/B978-0-08-006998-2.50005-0.

[20] A. H. Dietzel, Die kationenfeldstärken und ihre beziehungen zu entglasungsvorgängen, zur verbindungsbildung und zu den schmelzpunkten von silikaten, Z Electrochem. 48 (1942) 9–23.

[21] H. Scholze, Glass. Nature, Structure, and Properties, Springer New York, New York, NY, 1991. doi:10.1007/978-1-4613-9069-5.

[22] W. Vogel, Glass chemistry, 2nd ed., Springer Berlin Heidelberg, 1994.

[23] A.K. Yadav, P. Singh, A review of the structures of oxide glasses by Raman spectroscopy, RSC Adv. 5 (2015) 67583–67609. doi:10.1039/C5RA13043C.

[24] J.E. Stanworth, Tellurite glasses, Nature. 169 (1952) 581–582. doi:10.1038/169581b0.

[25] J. J. Berzelius, Ann. Phys. Chem. 32 (1834) 577.

[26] V. Lenher, E. Wolesensky, A study of the metallic tellurites, J. Am. Chem. Soc. 35 (1913) 718–733. doi:10.1021/ja02195a007.

[27] J.P. Poley, Dielectric properties of tellurite glasses, Nature. 174 (1954) 268–268. doi:10.1038/174268a0.

[28] P.L. Baynton, Colour of tellurite glasses, Nature. 176 (1955) 691–692. doi:10.1038/176691b0.

[29] G.W. Brady, X-Ray study of tellurium oxide glass, J. Chem. Phys. 24 (1956) 477–477. doi:10.1063/1.1742510.

[30] G.W. Brady, Structure of tellurium oxide glass, J. Chem. Phys. 27 (1957) 300–303. doi:10.1063/1.1743690.

[31] T. Ito and H. Sawada, The crystal structure of tellurite (TeO_2), Zeitschrift fur Kristallographie. 102 (1939) 13–25.

[32] Y.S. Bobovich, A.K. Yakhkind, Raman spectra of some tellurite glasses and corresponding crystals, Zh. Struki. Khim. 4 (1963) 924–927.

[33] Y.S. Bobovich, A.K. Yakhkind, Raman spectra of certain tellurite glasses and crystals, J. Struct. Chem. 4 (1964) 851–853. doi:10.1007/BF00747731.

[34] A.K. Yakhkind, Tellurite glasses, J. Am. Ceram. Soc. 49 (1966) 670–675. doi:10.1111/j.1151-2916.1966.tb13197.x.

[35] T.P. Tulub, Y.S. Bobovich, Opt. -Mekh. Prom. 9 (1961) 40.

[36] E.F. Lambson, G.A. Saunders, B. Bridge, R.A. El-Mallawany, The elastic behaviour of TeO_2 glass under uniaxial and hydrostatic pressure, J. Non-Cryst. Solids. 69 (1984) 117–133. doi:10.1016/0022-3093(84)90128-5.

[37] Imaoka M., Yamazaki T., Studies of the glass-formation range of tellurite systems, J. Ceram. Assoc. Jpn. 76 (1968) 160–172. doi:10.2109/jcersj1950.76.873_160.

[38] E.V. Zorin, M.F. Churbanov, G.E. Snopatin, I.A. Grishin, T.A. Petrova, V.G. Plotnichenko, Microinhomogeneities in tellurite glasses, Inorg. Mater. 41 (2005) 775–778. doi:10.1007/s10789-005-0208-8.

[39] J.S. Wang, E.M. Vogel, E. Snitzer, Tellurite glass: a new candidate for fiber devices, Opt. Mater. 3 (1994) 187–203. doi:10.1016/0925-3467(94)90004-3.

[40] R. Stegeman, L. Jankovic, H. Kim, C. Rivero, G. Stegeman, K. Richardson, P. Delfyett, Y. Guo, A. Schulte, T. Cardinal, Tellurite glasses with peak absolute Raman gain coefficients up to 30 times that of fused silica, Opt. Lett. 28 (2003) 1126. doi:10.1364/OL.28.001126.

[41] S.-H. Kim, T. Yoko, Nonlinear optical properties of TeO_2-based glasses: MO_x-TeO_2 (M= Sc, Ti, V, Nb, Mo, Ta, and W) binary glasses, J. Am. Ceram. Soc. 78 (1995) 1061–1065. doi:10.1111/j.1151-2916.1995.tb08437.x.

[42] R. Stegeman, C. Rivero, K. Richardson, G. Stegeman, P. Delfyett, Jr., Y. Guo, A. Pope, A. Schulte, T. Cardinal, P. Thomas, J.-C. Champarnaud-Mesjard, Raman gain measurements of thallium-tellurium oxide glasses, Opt. Express. 13 (2005) 1144. doi:10.1364/OPEX.13.001144.

[43] M.E. Lines, Influence of d orbitals on the nonlinear optical response of transparent transition-metal oxides, Phys. Rev. B. 43 (1991) 11978–11990. doi:10.1103/PhysRevB.43.11978.

[44] S. Manning, H. Ebendorff-Heidepriem, T.M. Monro, Ternary tellurite glasses for the fabrication of nonlinear optical fibres, Opt. Mater. Express. 2 (2012) 140–152. doi:10.1364/OME.2.000140.

[45] N. Berkaïne, J. Cornette, D. Hamani, P. Thomas, O. Masson, A. Mirgorodsky, M. Colas, J. Duclère, T. Merle-Mejéan, J.-C. Champarnaud-Mesjard, M. Smirnov, Structure and dielectric properties of tellurium oxide-based materials, Adv. Electroceramic Mater. II. (2010) 63–74. doi:10.1002/9780470930915.ch7.

[46] A. Gulenko, O. Masson, A. Berghout, D. Hamani, P. Thomas, Atomistic simulations of TeO_2-based glasses: interatomic potentials and molecular dynamics, Phys. Chem. Chem. Phys. 16 (2014) 14150. doi:10.1039/c4cp01273a.

[47] J.C. McLaughlin, S.L. Tagg, J.W. Zwanziger, The structure of alkali tellurite glasses, J. Phys. Chem. B. 105 (2001) 67–75. doi:10.1021/jp0025779.

[48] C.R. Becker, S.L. Tagg, J.C. Huffman, J.W. Zwanziger, Crystal structures of potassium tetratellurite, $K_2Te_4O_9$, and potassium ditellurite, $K_2Te_2O_5$, and structural trends in solid alkali tellurites, Inorg. Chem. 36 (1997) 5559–5564. doi:10.1021/ic970497m.

[49] M. Koçak, C. Platte, M. Trömel, Bariumhexaoxoditellurat(IV,VI): Sauerstoffkoordinationszahl fünf am vierwertigen Tellur, Acta Crystallogr. B. 35 (1979) 1439–1441. doi:10.1107/S0567740879006646.

[50] B.O. Loopstra, K. Goubitz, The structures of four caesium tellurates, Acta Crystallogr. C. 42 (1986) 520–523. doi:10.1107/S0108270186095537.

[51] Y. Himei, A. Osaka, T. Nanba, Y. Miura, Coordination change of Te atoms in binary tellurite glasses, J. Non-Cryst. Solids. 177 (1994) 164–169. doi:10.1016/0022-3093(94)90526-6.

[52] T. Sekiya, N. Mochida, A. Ohtsuka, Raman spectra of MO-TeO_2 (M= Mg, Sr, Ba and Zn) glasses, J. Non-Cryst. Solids. 168 (1994) 106–114. doi:10.1016/0022-3093(94)90125-2.

[53] N. Ghribi, M. Dutreilh-Colas, J.-R. Duclère, T. Hayakawa, J. Carreaud, R. Karray, A. Kabadou, P. Thomas, Thermal, optical and structural properties of glasses within the TeO_2-TiO_2-ZnO system, J. Alloys Compd. 622 (2015) 333–340. doi:10.1016/j.jallcom.2014.10.063.

[54] T. Sekiya, N. Mochida, A. Soejima, Raman spectra of binary tellurite glasses containing tri- or tetra-valent cations, J. Non-Cryst. Solids. 191 (1995) 115–123. doi:10.1016/0022-3093(95)00290-1.

[55] D. Linda, M. Dutreilh-Colas, D. Hamani, P. Thomas, A. Mirgorodsky, J.-R. Duclère, O. Masson, M. Loukil, A. Kabadou, New glasses within the Tl_2O-Ag_2O-TeO_2 system: Thermal characteristics, Raman spectra and structural properties, Mater. Res. Bull. 45 (2010) 1816–1824. doi:10.1016/j.materresbull.2010.09.024.

[56] M.A.. Silva, Y. Messaddeq, S.J.. Ribeiro, M. Poulain, F. Villain, V. Briois, Structural studies on TeO_2-PbO glasses, J. Phys. Chem. Solids. 62 (2001) 1055–1060. doi:10.1016/S0022-3697(00)00278-X.

[57] M. Udovic, P. Thomas, A. Mirgorodsky, O. Durand, M. Soulis, O. Masson, T. Merle-Méjean, J.C. Champarnaud-Mesjard, Thermal characteristics, Raman spectra and structural properties of new tellurite glasses within the Bi_2O_3–TiO_2–TeO_2 system, J. Solid State Chem. 179 (2006) 3252–3259. doi:10.1016/j.jssc.2006.06.016.

[58] O. Noguera, T. Merle-Méjean, A.P. Mirgorodsky, P. Thomas, J.-C. Champarnaud-Mesjard, Dynamics and crystal chemistry of tellurites. II. Composition- and temperature-dependence of the Raman spectra of $x(Tl_2O)+(1−x)TeO_2$ glasses: evidence for a phase separation?, J. Phys. Chem. Solids. 65 (2004) 981–993. doi:10.1016/j.jpcs.2003.11.020.

[59] I. P. Kondratyuk, L. A. Murdoyan, Y. V. Pisarevskij, V. I. Simonov, Precision X-ray structural investigation of acoustooptical α-TeO_2 single crystals, Kristallografiya. 32 (1987) 609–607.

[60] P.A. Thomas, The crystal structure and absolute optical chirality of paratellurite α-TeO_2, J. Phys. C Solid State Phys. 21 (1988) 4611–4627. doi:10.1088/0022-3719/21/25/009.

[61] V. H. Beyer, Verfeinerung der kristallstruktur von tellurit, dem rhombischen TeO_2, 124 (1967) 228–237.

[62] S. Blanchandin, P. Marchet, P. Thomas, J.C. Champarnaud-Mesjard, B. Frit, A. Chagraoui, New investigations within the TeO_2-WO_3 system: phase equilibrium diagram and glass crystallization, J. Mater. Sci. 34 (1999) 4285–4292. doi:10.1023/A:1004667223028.

[63] J.C. Champarnaud-Mesjard, S. Blanchandin, P. Thomas, A. Mirgorodsky, T. Merle-Méjean, B. Frit, Crystal structure, Raman spectrum and lattice dynamics of a new metastable form of tellurium dioxide: γ-TeO_2, J. Phys. Chem. Solids. 61 (2000) 1499–1507. doi:10.1016/S0022-3697(00)00012-3.

[64] A.P. Mirgorodsky, T. Merle-Méjean, J.-C. Champarnaud, P. Thomas, B. Frit, Dynamics and structure of TeO_2 polymorphs: model treatment of paratellurite and tellurite; Raman scattering evidence for new γ- and δ-phases, J. Phys. Chem. Solids. 61 (2000) 501–509. doi:10.1016/S0022-3697(99)00263-2.

[65] M. Durand, B. Ayrault, Y. Marqueton, E.A. Decamps, Lattice dynamics of paratellurite, Phys. Status Solidi B. 78 (1976) 767–777. doi:10.1002/pssb.2220780238.

[66] V. Lemos, F. Cerdeira, M. Cardona, Atomic motions corresponding to zone center phonons in paratellurite, Phys. Status Solidi B. 88 (1978) 199–206. doi:10.1002/pssb.2220880123.

[67] H. Uwe, H. Tokumoto, Pressure-induced ferroelastic transition and internal displacement in TeO_2, Phys. Rev. B. 19 (1979) 3700–3707. doi:10.1103/PhysRevB.19.3700.

[68] A.S. Pine, G. Dresselhaus, Raman scattering in paratellurite, TeO_2, Phys. Rev. B. 5 (1972) 4087–4093. doi:10.1103/PhysRevB.5.4087.

[69] D.M. Korn, A.S. Pine, G. Dresselhaus, T.B. Reed, Infrared reflectivity of paratellurite, TeO_2, Phys. Rev. B. 8 (1973) 768–772. doi:10.1103/PhysRevB.8.768.

[70] P.S. Peercy, I.J. Fritz, G.A. Samara, Temperature and pressure dependences of the properties and phase transition in paratellurite (TeO_2: Ultrasonic, dielectric and Raman and Brillouin scattering results, J. Phys. Chem. Solids. 36 (1975) 1105–1122. doi:10.1016/0022-3697(75)90053-0.

[71] O. Noguera, Propriétés structurales, vibrationnelles et diélectriques de matériaux à base d'oxyde de tellure, PhD thesis, Université de Limoges, 2003.

[72] M. Ceriotti, F. Pietrucci, M. Bernasconi, *Ab initio* study of the vibrational properties of crystalline TeO_2: The α, β, and γ phases, Phys. Rev. B. 73 (2006) 1–17. doi:10.1103/PhysRevB.73.104304.

[73] D.W. Muenow, J.W. Hastle, R. Hauge, R. Bautista, J.L. Margrave, Vaporization, thermodynamics and structures of species in the tellurium + oxygen system, Trans. Faraday Soc. 65 (1969) 3210. doi:10.1039/tf9696503210.

[74] D.S. Yakovlev, A.P. Mirgorodskii, A.V. Tulub, B.F. Shchegolev, Nonempirical calculation of linear and nonlinear polarizability of TeO_2-based molecular clusters and piezoelectric properties of crystalline tellurium oxide, Opt. Spectrosc. 92 (2002) 449–454. doi:10.1134/1.1465473.

[75] V. Rodriguez, M. Couzi, F. Adamietz, M. Dussauze, G. Guery, T. Cardinal, P. Veber, K. Richardson, P. Thomas, Hyper-Raman and Raman scattering in paratellurite TeO_2: Hyper-Raman and Raman scattering in paratellurite TeO_2, J. Raman Spectrosc. 44 (2013) 739–745. doi:10.1002/jrs.4251.

[76] M. Weil, Redetermination of the γ-form of tellurium dioxide, IUCrData. 2 (2017). doi:10.1107/S2414314617017576.

[77] D. Hamani, Cristallochimie de matériaux à base de dioxyde de tellure : vers un modèle structural pour l'étude des composés vitreux, PhD thesis, Université de Limoges, 2010.

[78] S. Yamanaka, M. Miyake, Study of the ternary Ti-Te-O system, J. Common Met. 159 (1990) 179–189. doi:10.1016/0022-5088(90)90146-B.

[79] G. Meunier, J. Galy, Sur une déformation inédite du reseau de type fluorine. Structure cristalline des phases MTe_3O_8 (M = Ti, Sn, Hf, Zr), Acta Crystallogr. B. 27 (1971) 602–608. doi:10.1107/S0567740871002620.

[80] M. Udovic, M. Valant, D. Suvorov, Dielectric characterisation of ceramics from the TiO_2–TeO_2 system, J. Eur. Ceram. Soc. 21 (2001) 1735–1738. doi:10.1016/S0955-2219(01)00105-4.

[81] T.B. Ghosh, S. Dhabal, A.K. Datta, On crystallite size dependence of phase stability of nanocrystalline TiO_2, J. Appl. Phys. 94 (2003) 4577–4582. doi:10.1063/1.1604966.

[82] D.A.H. Hanaor, C.C. Sorrell, Review of the anatase to rutile phase transformation, J. Mater. Sci. 46 (2011) 855–874. doi:10.1007/s10853-010-5113-0.

[83] C.M.B. Henderson, K.S. Neuhoff, A.R. Lennie, Temperature Dependence of Rutile (TiO_2) and Geikielite ($MgTiO_3$) Structures Determined Using Neutron Powder Diffraction, The Open Mineralogy Journal. 3 (2009) 1–11.

[84] Z. Cheng, T. Liu, C. Yang, H. Gan, F. Zhang, J. Chen, Study on the electronic structures of the reduced anatase TiO_2 by the first-principle calculation, J. Phys. Chem. Solids. 73 (2012) 302–307. doi:10.1016/j.jpcs.2011.10.020.

[85] J.K. Burdett, T. Hughbanks, G.J. Miller, J.W. Richardson, J.V. Smith, Structural-electronic relationships in inorganic solids: powder neutron diffraction studies of the rutile and anatase polymorphs of titanium dioxide at 15 and 295 K, J. Am. Chem. Soc. 109 (1987) 3639–3646. doi:10.1021/ja00246a021.

[86] C.C. Evans, Nonlinear optics in titanium dioxide: from bulk to integrated optical devices, PhD thesis, Harvard University, 2013.

[87] L. Martinu, D. Poitras, Plasma deposition of optical films and coatings: A review, J. Vac. Sci. Technol. Vac. Surf. Films. 18 (2000) 2619–2645. doi:10.1116/1.1314395.

[88] M. Batzill, E.H. Morales, U. Diebold, Influence of Nitrogen Doping on the Defect Formation and Surface Properties of TiO_2 Rutile and Anatase, Phys. Rev. Lett. 96 (2006). doi:10.1103/PhysRevLett.96.026103.

[89] C.A. Chen, Y.S. Huang, W.H. Chung, D.S. Tsai, K.K. Tiong, Raman spectroscopy study of the phase transformation on nanocrystalline titania films prepared via metal organic vapour deposition, J. Mater. Sci. Mater. Electron. 20 (2009) 303–306. doi:10.1007/s10854-008-9595-3.

[90] A. Várez, M.L. Sanjuán, M.A. Laguna, J.I. Peña, J. Sanz, G.F. de la Fuente, Microstructural development of the $La_{0.5}Li_{0.5}TiO_3$ lithium ion conductor processed by the laser floating zone (LFZ) method, J. Mater. Chem. 11 (2001) 125–130. doi:10.1039/b003305g.

[91] O. Frank, M. Zukalova, B. Laskova, J. Kürti, J. Koltai, L. Kavan, Raman spectra of titanium dioxide (anatase, rutile) with identified oxygen isotopes (16, 17, 18), Phys. Chem. Chem. Phys. 14 (2012) 14567. doi:10.1039/c2cp42763j.

[92] L. Bindi, C. Cipriani, The crystal structure of winstanleyite, $TiTe_3O_8$, from the Grand Central mine, Tombstone, Arizona, Can. Mineral. 41 (2003) 1469–1473. doi:10.2113/gscanmin.41.6.1469.

[93] W.L. Roberts, T.J. Campbell, G.R. Rapp, Encyclopedia of minerals, 2nd ed, Van Nostrand Reinhold, New York, 1990.

[94] M. Soulis, Structure et propriétés optiques non linéaires des verres à base d'oxyde de tellure : approche cristallochimique et calculs ab-initio, PhD thesis, Université de Limoges, 2007.

[95] J.-C. Sabadel, PhD, Université de Montpellier II, 1997.

[96] J.C. Sabadel, P. Armand, D. Cachau-Herreillat, P. Baldeck, O. Doclot, A. Ibanez, E. Philippot, Structural and nonlinear optical characterizations of tellurium oxide-based glasses: TeO_2–BaO–TiO_2, J. Solid State Chem. 132 (1997) 411–419. doi:10.1006/jssc.1997.7499.

[97] M.A. Villegas, J.M.F. Navarro, Physical and structural properties of glasses in the TeO_2–TiO_2–Nb_2O_5 system, J. Eur. Ceram. Soc. 27 (2007) 2715–2723. doi:10.1016/j.jeurceramsoc.2006.12.003.

[98] N. Ghribi, Synthèse, caractérisations structurale et élastique de nouveaux matériaux tellurites pour des applications en optique non linéaire, PhD thesis, Université de Limoges, 2015.

[99] M. Udovic, P. Thomas, A. Mirgorodsky, O. Masson, T. Merle-Mejean, C. Lasbrugnas, J.C. Champarnaud-Mesjard, T. Hayakawa, Formation domain and characterization of new glasses within the Tl_2O–TiO_2–TeO_2 system, Mater. Res. Bull. 44 (2009) 248–253. doi:10.1016/j.materresbull.2008.10.001.

[100] S. Tanisaki, Crystal structure of monoclinic tungsten trioxide at room temperature, J. Phys. Soc. Jpn. 15 (1960) 573–581. doi:10.1143/JPSJ.15.573.

[101] M.F. Daniel, B. Desbat, J.C. Lassegues, B. Gerand, M. Figlarz, Infrared and Raman study of WO_3 tungsten trioxides and WO_3, xH_2O tungsten trioxide hydrates, J. Solid State Chem. 67 (1987) 235–247. doi:10.1016/0022-4596(87)90359-8.

[102] E. Salje, Lattice dynamics of WO_3, Acta Crystallogr. Sect. A. 31 (1975) 360–363. doi:10.1107/S0567739475000757.

[103] T. Sekiya, N. Mochida, S. Ogawa, Structural study of WO_3-TeO_2 glasses, J. Non-Cryst. Solids. 176 (1994) 105–115. doi:10.1016/0022-3093(94)90067-1.

[104] I. Shaltout, Y. Tang, R. Braunstein, A.M. Abu-Elazm, Structural studies of tungstate-tellurite glasses by Raman spectroscopy and differential scanning calorimetry, J. Phys. Chem. Solids. 56 (1995) 141–150. doi:10.1016/0022-3697(94)00150-2.

[105] P. Charton, L. Gengembre, P. Armand, TeO_2-WO_3 glasses: Infrared, XPS and XANES structural characterizations, J. Solid State Chem. 168 (2002) 175–183. doi:10.1006/jssc.2002.9707.

[106] P. Charton, Matériaux vitreux des systèmes TeO_2-Ga_2O_3-WO_3 et TeO_2-Sb_2O_4-WO_3 pour l'optique non linéaire : synthèse, caractérisations structurales et mesures physiques, PhD thesis, Université de Montpellier II, 2002.

[107] G. Upender, S. Bharadwaj, A.M. Awasthi, V. Chandra Mouli, Glass transition temperature-structural studies of tungstate tellurite glasses, Mater. Chem. Phys. 118 (2009) 298–302. doi:10.1016/j.matchemphys.2009.07.058.

[108] A. Kaur, A. Khanna, V.G. Sathe, F. Gonzalez, B. Ortiz, Optical, thermal, and structural properties of Nb_2O_5–TeO_2 and WO_3–TeO_2 glasses, Phase Transit. 86 (2013) 598–619. doi:10.1080/01411594.2012.727998.

[109] D.M. Munoz-Martín, TeO_2-based film glasses for photonic applications: structural and optical properties., PhD, Universidad Complutense de Madrid, 2010.

[110]   S.K.J. Al-Ani, C.A. Hogarth, R.A. El-Malawany, A study of optical absorption in tellurite and tungsten-tellurite glasses, J. Mater. Sci. 20 (1985) 661–667. doi:10.1007/BF01026540.

[111]   J. Galy, O. Lindqvist, The crystal structure of $Te_3Nb_2O_{11}$, J. Solid State Chem. 27 (1979) 279–286. doi:10.1016/0022-4596(79)90168-3.

[112]   F. Garbassi, J.C.J. Bart, G. Petrini, XPS study of tellurium—niobium and tellurium—tantalum oxide systems, J. Electron Spectrosc. Relat. Phenom. 22 (1981) 95–107. doi:10.1016/0368-2048(81)80019-9.

[113]   O. Yamaguchi, T. Shirai, Y. Mukaida, K. Shimizu, Formation and transformation of $3TeO_2 \cdot Nb_2O_5$, J Chem Soc Dalton Trans. (1988) 2087–2090. doi:10.1039/DT9880002087.

[114]   S. Blanchandin, P. Thomas, P. Marchet, J.C. Champarnaud-Mesjard, B. Frit, Equilibrium and non-equilibrium phase diagram within the TeO_2-rich part of the TeO_2-Nb_2O_5 system, J. Mater. Chem. 9 (1999) 1785–1788. doi:10.1039/a900788a.

[115]   H. Schäfer, R. Gruehn, F. Schulte, Die modifikationen des niobpentoxids, Angew. Chem. 78 (1966) 28–41. doi:10.1002/ange.19660780104.

[116]   K. Kato, Structure refinement of h-Nb_2O_5, Acta Crystallogr. B. 32 (1976) 764–767. doi:10.1107/S0567740876003944.

[117]   A. Le Viet, R. Jose, M.V. Reddy, B.V.R. Chowdari, S. Ramakrishna, Nb_2O_5 photoelectrodes for dye-sensitized solar cells: Choice of the polymorph, J. Phys. Chem. C. 114 (2010) 21795–21800. doi:10.1021/jp106515k.

[118]   S. Blanchandin, J.C. Champarnaud-Mesjard, P. Thomas, B. Frit, Crystal structure of $Nb_2Te_4O_{13}$, J. Alloys Compd. 306 (2000) 175–185. doi:10.1016/S0925-8388(00)00783-0.

[119]   I.A. Khodyakova, V.A. Dolgikh, B.A. Popovkin, A.V. Novoselova, Russ. J. Inorg. Chem. 27 (1982) 1235–1241.

[120]   U. Hoppe, E. Yousef, C. Rüssel, J. Neuefeind, A.C. Hannon, Structure of zinc and niobium tellurite glasses by neutron and x-ray diffraction, J. Phys. Condens. Matter. 16 (2004) 1645–1663. doi:10.1088/0953-8984/16/9/013.

[121]   A. Berthereau, E. Fargin, A. Villezusanne, R. Olazcuaga, G. Le Flem, L. Ducasse, Determination of local geometries around tellurium in TeO_2–Nb_2O_5 and TeO_2–Al_2O_3 oxide glasses by XANES and EXAFS: Investigation of electronic properties of evidenced oxygen clusters by ab initio calculations, J. Solid State Chem. 126 (1996) 143–151. doi:10.1006/jssc.1996.0322.

[122]   Y.B. Saddeek, E.R. Shaaban, F.M. Abdel-Rahim, K.H. Mahmoud, Thermal analysis and infrared study of Nb_2O_5–TeO_2 glasses, Philos. Mag. 88 (2008) 3059–3073. doi:10.1080/14786430802499012.

[123]   A. Berthereau, Y. Le Luyer, R. Olazcuaga, G. Le Flem, M. Couzi, L. Canioni, P. Segonds, L. Sarger, A. Ducasse, Nonlinear optical properties of some tellurium (IV) oxide glasses, Mater. Res. Bull. 29 (1994) 933–941. doi:10.1016/0025-5408(94)90053-1.

[124]   T. Hayakawa, M. Hayakawa, M. Nogami, P. Thomas, Nonlinear optical properties and glass structure for MO–Nb_2O_5–TeO_2 (M=Zn, Mg, Ca, Sr, Ba) glasses, Opt. Mater. 32 (2010) 448–455. doi:10.1016/j.optmat.2009.10.006.

[125]   J. Lin, W. Huang, L. Ma, Q. Bian, S. Qin, H. Wei, J. Chen, Crystallization of TeO_2−Nb_2O_5 glasses and their network structural evolution, Materials Science-Poland. 27 (2009).

[126]   V.V. Safonov, Interactions in the TeO_2-TiO_2-WO_3 System, Russ. J. Inorg. Chem. 53 (2008) 460–461. doi:10.1134/S0036023608030224.

[127]   H. Fares, I. Jlassi, H. Elhouichet, M. Férid, Investigations of thermal, structural and optical properties of tellurite glass with WO_3 adding, J. Non-Cryst. Solids. 396–397 (2014) 1–7. doi:10.1016/j.jnoncrysol.2014.04.012.

[128] J. Carreaud, A. Labruyère, H. Dardar, F. Moisy, J.-R. Duclère, V. Couderc, A. Bertrand, M. Dutreilh-Colas, G. Delaizir, T. Hayakawa, A. Crunteanu, P. Thomas, Lasing effects in new Nd^{3+}-doped TeO_2–Nb_2O_5–WO_3 bulk glasses, Opt. Mater. 47 (2015) 99–107. doi:10.1016/j.optmat.2015.06.055.

[129] G. Dai, F. Tassone, A. LiBassi, V. Russo, C.E. Bottani, F. D'Amore, TeO_2-based glasses containing Nb_2O_5, TiO_2, and WO_3 for discrete Raman fiber amplification, IEEE Photonics Technol. Lett. 16 (2004) 1011–1013. doi:10.1109/LPT.2004.824963.

[130] S. Dai, J. Wu, J. Zhang, G. Wang, Z. Jiang, The spectroscopic properties of Er^{3+}-doped TeO_2–Nb_2O_5 glasses with high mechanical strength performance, Spectrochim. Acta. A. Mol. Biomol. Spectrosc. 62 (2005) 431–437. doi:10.1016/j.saa.2005.01.011.

[131] G. Tammann, Kristallisieren und Schmelzen: ein Beitrag zur Lehre der Änderungen des Aggregatzustandes, Leipzig, 1903.

[132] V.M. Goldschmidt, Geochemische verteilungsgesetze der elemente, Oslo : In Kommisjon Hos Jacob Dybwad, 1926.

[133] B.E. Warren, X-ray determination of the structure of glass, J. Am. Ceram. Soc. 17 (1934) 249–254. doi:10.1111/j.1151-2916.1934.tb19316.x.

[134] K.-H. Sun, Fundamental condition of glass formation, J. Am. Ceram. Soc. 30 (1947) 277–281. doi:10.1111/j.1151-2916.1947.tb19654.x.

[135] K. Meyer, H. Hobert, A. Barz, D. Stachel, Infrared spectra and structure of various crystalline ultraphosphates and their glasses, Vib. Spectrosc. 6 (1994) 323–332. doi:10.1016/0924-2031(93)E0055-7.

[136] A.E. Lapshin, N.V. Borisova, V.M. Ushakov, Y.F. Shepelev, Disordering in the structure of cesium silicate $Cs_6Si_{10}O_{23}$, Glass Phys. Chem. 33 (2007) 250–253. doi:10.1134/S1087659607030108.

[137] A.H. Dietzel, Emaillierung, Springer Berlin Heidelberg, Berlin, Heidelberg, 1981. doi:10.1007/978-3-642-50978-0.

[138] J.S. Berkes, R. Roy, Use of ion properties for the prediction of the phase relations in a binary system, Z. Für Krist. 131 (1970) 60–72. doi:10.1524/zkri.1970.131.1-6.60.

[139] A.P. Mirgorodsky, T. Merle-Méjean, P. Thomas, J.-C. Champarnaud-Mesjard, B. Frit, Dynamics and crystal chemistry of tellurites. I. Raman spectra of thallium tellurites: Tl_2TeO_3, $Tl_2Te_2O_5$ and $Tl_2Te_3O_7$, J. Phys. Chem. Solids. 63 (2002) 545–554. doi:10.1016/S0022-3697(01)00192-5.

[140] M. Soulis, A.P. Mirgorodsky, T. Merle-Méjean, O. Masson, P. Thomas, M. Udovic, The role of modifier's cation valence in structural properties of TeO_2-based glasses, J. Non-Cryst. Solids. 354 (2008) 143–149. doi:10.1016/j.jnoncrysol.2007.07.032.

[141] R.D. Shannon, Revised effective ionic radii and systematic studies of interatomic distances in halides and chalcogenides, Acta Crystallogr. Sect. A. 32 (1976) 751–767. doi:10.1107/S0567739476001551.

[142] N. Mochida, K. Takahashi, K. Nakata, S. Shibusawa, Properties and structure of the binary tellurite glasses containing mono- and di-valent cations, Yogyo-Kyokai-Shi. 86 (1978) 316–326. doi:10.2109/jcersj1950.86.995_316.

[143] V. Kozhukharov, M. Marinov, G. Grigorova, Glass-formation range in binary tellurite systems containing transition metal oxides, J. Non-Cryst. Solids. 28 (1978) 429–430. doi:10.1016/0022-3093(78)90092-3.

[144] T. Sekiya, N. Mochida, A. Ohtsuka, M. Tonokawa, Raman spectra of $MO_{1/2}$-TeO_2 (M = Li, Na, K, Rb, Cs and Tl) glasses, J. Non-Cryst. Solids. 144 (1992) 128–144. doi:10.1016/S0022-3093(05)80393-X.

[145]   M. Dutreilh-Colas, P. Charton, P. Thomas, P. Armand, P. Marchet, J.C. Champarnaud-Mesjard, The TeO$_2$-rich part of the TeO$_2$–Ga$_2$O$_3$ system: equilibrium and non-equilibrium phase diagram, J Mater Chem. 12 (2002) 2803–2806. doi:10.1039/B202467P.

[146]   N.A. Zarifah, M.K. Halimah, M. Hashim, Z. Azmi, W.M. Daud, Magnetic behaviour of (Fe$_2$O$_3$)$_x$ (TeO$_2$)$_{1-x}$ glass system due to Iron oxide, Chalcogenide Letters. 7 (2010) 565–571.

[147]   A. Chagraoui, I. Yakine, A. Tairi, A. Moussaoui, M. Talbi, M. Naji, Glasses formation, characterization, and crystal-structure determination in the Bi$_2$O$_3$–Sb$_2$O$_3$–TeO$_2$ system prepared in an air, J. Mater. Sci. 46 (2011) 5439–5446. doi:10.1007/s10853-011-5485-9.

[148]   Y. Kawamoto, K. Clemens, M. Tomozawa, Effects of MoO$_3$, on phase separation of Na$_2$O-B$_2$O$_3$-SiO$_2$ glasses, J. Am. Ceram. Soc. 64 (1981) 292–296. doi:10.1111/j.1151-2916.1981.tb09605.x.

[149]   Y. Taki, K. Shinozaki, T. Honma, T. Komatsu, L. Aleksandrov, R. Iordanova, Coexistence of nano-scale phase separation and micro-scale surface crystallization in Gd$_2$O$_3$–WO$_3$–B$_2$O$_3$ glasses, J. Non-Cryst. Solids. 381 (2013) 17–22. doi:10.1016/j.jnoncrysol.2013.09.014.

[150]   I. Yakine, A. Chagraoui, A. Moussaoui, A. Tairi, Synthesis and characterization of new amorphous and crystalline phases in Bi$_2$O$_3$-Ta$_2$O$_5$-TeO$_2$ system, J. Mater. Environ. Sci. 3 (2012) 776–785.

[151]   T. Sekiya, N. Mochida, S. Ogawa, Structural study of MoO$_3$-TeO$_2$ glasses, J. Non-Cryst. Solids. 185 (1995) 135–144. doi:10.1016/0022-3093(94)00667-9.

[152]   V.G. Plotnichenko, V.O. Sokolov, V.V. Koltashev, E.M. Dianov, I.A. Grishin, M.F. Churbanov, Raman band intensities of tellurite glasses, Opt. Lett. 30 (2005) 1156. doi:10.1364/OL.30.001156.

[153]   O. Lindqvist, W. Mark, J. Moret, The crystal structure of Te$_4$O$_9$, Acta Crystallogr. B. 31 (1975) 1255–1259. doi:10.1107/S0567740875005018.

[154]   O. Lindqvist, J. Moret, The crystal structure of ditellurium pentoxide Te$_2$O$_5$, Acta Crystallogr. B. 29 (1973) 643–650. doi:10.1107/S0567740873003092.

[155]   D. Hamani, A. Plat, M. Colas, J. Cornette, O. Masson, A.P. Mirgorodsky, P. Thomas, Origin of the strong optical nonlinearity of tellurium oxide–based compounds: The specific case of BaTe$_2$O$_6$, J. Alloys Compd. 661 (2016) 92–99. doi:10.1016/j.jallcom.2015.11.160.

[156]   D. Hamani, A. Mirgorodsky, O. Masson, T. Merle-Méjean, M. Colas, M. Smirnov, P. Thomas, Crystal chemistry peculiarities of Cs$_2$Te$_4$O$_{12}$, J. Solid State Chem. 184 (2011) 637–643. doi:10.1016/j.jssc.2011.01.027.

[157]   S.-H. Kim, T. Yoko, S. Sakka, Linear and nonlinear optical properties of TeO$_2$ glass, J. Am. Ceram. Soc. 76 (1993) 2486–2490. doi:10.1111/j.1151-2916.1993.tb03970.x.

[158]   B.E. Warren, X-ray diffraction, Dover ed, Dover Publications, New York, 1990.

[159]   A. Smekal, Zur Quantentheorie der Dispersion, Naturwissenschaften. 11 (1923) 873–875. doi:10.1007/BF01576902.

[160]   C.V. Raman, K.S. Krishnan, A New Type of Secondary Radiation, Nature. 121 (1928) 501–502. doi:10.1038/121501c0.

[161]   J.M. Hollas, Modern spectroscopy, 4th ed, J. Wiley, Chichester ; Hoboken, NJ, 2004.

[162]   D.A. Long, The Raman Effect, John Wiley & Sons, Ltd, Chichester, UK, 2002. doi:10.1002/0470845767.

[163]   R.J. Hemley, Pressure dependence of Raman spectra of SiO$_2$ polymorphs: α-quartz, coesite, and stishovite, in: M.H. Manghnani, Y. Syono (Eds.), Geophys. Monogr. Ser., American Geophysical Union, Washington, D. C., 1987: pp. 347–359. doi:10.1029/GM039p0347.

[164]   V.O. Sokolov, V.G. Plotnichenko, E.M. Dianov, Structure of WO$_3$-TeO$_2$ glasses, Inorg. Mater. 43 (2007) 194–213. doi:10.1134/S0020168507020173.

[165]   A. Mirgorodsky, M. Colas, M. Smirnov, T. Merle-Méjean, R. El-Mallawany, P. Thomas, Structural peculiarities and Raman spectra of TeO$_2$-WO$_3$-based glasses: A fresh look at the problem, J. Solid State Chem. 190 (2012) 45–51. doi:10.1016/j.jssc.2012.02.011.

[166]   O. Yamaguchi, D. Tomihisa, K. Shimizu, A new modification of TiTe$_3$O$_8$, J. Chem. Soc. Dalton Trans. (1988) 2083. doi:10.1039/dt9880002083.

[167]   F.C. MacKintosh, J.X. Zhu, D.J. Pine, D.A. Weitz, Polarization memory of multiply scattered light, Phys. Rev. B. 40 (1989) 9342–9345. doi:10.1103/PhysRevB.40.9342.

[168]   A.P. Sokolov, A. Kisliuk, M. Soltwisch, D. Quitmann, Medium-range order in glasses: Comparison of Raman and diffraction measurements, Phys. Rev. Lett. 69 (1992) 1540–1543. doi:10.1103/PhysRevLett.69.1540.

[169]   T. Vasileiadis, S.N. Yannopoulos, Photo-induced oxidation and amorphization of trigonal tellurium: A means to engineer hybrid nanostructures and explore glass structure under spatial confinement, J. Appl. Phys. 116 (2014) 103510. doi:10.1063/1.4894868.

[170]   A.G. Kalampounias, G. Tsilomelekis, S. Boghosian, Glass-forming ability of TeO$_2$ and temperature induced changes on the structure of the glassy, supercooled, and molten states, J. Chem. Phys. 142 (2015) 154503. doi:10.1063/1.4917536.

[171]   A.G. Kalampounias, G.N. Papatheodorou, S.N. Yannopoulos, A temperature dependence Raman study of the 0.1 Nb$_2$O$_5$-0.9 TeO$_2$ glass-forming system, J. Phys. Chem. Solids. 67 (2006) 725–731. doi:10.1016/j.jpcs.2005.11.001.

[172]   D. De Sousa Meneses, Software utility for the creation of optical function (FOCUS), CEMHTI UPR 3079 CNRS Orléans, France, 2004. http://www.cemhti.cnrs-orleans.fr/pot/software/focus.html.

[173]   J. Singh, ed., Optical properties of condensed matter and applications, John Wiley, Chichester, England ; Hoboken, NJ, 2006.

[174]   N.F. Mott, E.A. Davis, Electronic processes in non-crystalline materials, 2nd ed, Clarendon Press, Oxford, 2012.

[175]   F. Urbach, The long-wavelength edge of photographic sensitivity and of the electronic absorption of solids, Phys. Rev. 92 (1953) 1324–1324. doi:10.1103/PhysRev.92.1324.

[176]   G.D. Cody, T. Tiedje, B. Abeles, B. Brooks, Y. Goldstein, Disorder and the Optical-Absorption Edge of Hydrogenated Amorphous Silicon, Phys. Rev. Lett. 47 (1981) 1480–1483. doi:10.1103/PhysRevLett.47.1480.

[177]   J. Tauc, Optical properties and electronic structure of amorphous Ge and Si, Mater. Res. Bull. 3 (1968) 37–46. doi:10.1016/0025-5408(68)90023-8.

[178]   S.H. Wemple, Refractive-index behavior of amorphous semiconductors and glasses, Phys. Rev. B. 7 (1973) 3767–3777. doi:10.1103/PhysRevB.7.3767.

[179]   S.H. Wemple, M. DiDomenico, Optical dispersion and the structure of solids, Phys. Rev. Lett. 23 (1969) 1156–1160. doi:10.1103/PhysRevLett.23.1156.

[180]   E. Kordes, Physikalisch-chemische untersuchungen über den feinbau von gläsern. I. Mitteilung. Die molrefraktion binärer phosphat-, silikat- und boratgläser, Z. Für Anorg. Allg. Chem. 241 (1939) 1–38. doi:10.1002/zaac.19392410101.

[181]   H.A. Lorentz, Ueber die Beziehung zwischen der Fortpflanzungsgeschwindigkeit des Lichtes und der Körperdichte, Ann. Phys. Chem. 245 (1880) 641–665. doi:10.1002/andp.18802450406.

[182]   L. Lorenz, Über die Refractionsconstante, Wiedem. Ann. 11 (1880) 70.

[183]   V. Dimitrov, T. Komatsu, An interpretation of optical properties of oxides and oxide glasses in terms of the electronic ion polarizability and average single bond strength, Journal of the University of Chemical Technology and Metallurgy. 45 (2010) 219–250.

[184] V. Dimitrov, S. Sakka, Linear and nonlinear optical properties of simple oxides. II, J. Appl. Phys. 79 (1996) 1741–1745. doi:10.1063/1.360963.

[185] R.W. Collins, Ellipsometry in Analysis of Surfaces and Thin Films, in: R.A. Meyers (Ed.), Encycl. Anal. Chem., John Wiley & Sons, Ltd, Chichester, UK, 2000. doi:10.1002/9780470027318.a2507.

[186] Sellmeier, Zur Erklärung der abnormen Farbenfolge im Spectrum einiger Substanzen, Ann. Phys. Chem. 219 (1871) 272–282. doi:10.1002/andp.18712190612.

[187] G. Ghosh, Sellmeier coefficients and dispersion of thermo-optic coefficients for some optical glasses, Appl. Opt. 36 (1997) 1540. doi:10.1364/AO.36.001540.

[188] M. Sheik-Bahae, A.A. Said, T.-H. Wei, D.J. Hagan, E.W. Van Stryland, Sensitive measurement of optical nonlinearities using a single beam, IEEE J. Quantum Electron. 26 (1990) 760–769. doi:10.1109/3.53394.

[189] J.-R. Duclère, T. Hayakawa, E.M. Roginskii, M.B. Smirnov, A. Mirgorodsky, V. Couderc, O. Masson, M. Colas, O. Noguera, V. Rodriguez, P. Thomas, Third order nonlinear optical properties of a paratellurite single crystal, Accepted for publication in J. Appl. Phys., 123 (2018).

[190] D. Linda, J.-R. Duclère, T. Hayakawa, M. Dutreilh-Colas, T. Cardinal, A. Mirgorodsky, A. Kabadou, P. Thomas, Optical properties of tellurite glasses elaborated within the TeO_2-Tl_2O-Ag_2O and TeO_2–ZnO–Ag_2O ternary systems, J. Alloys Compd. 561 (2013) 151–160. doi:10.1016/j.jallcom.2013.01.172.

[191] D. Milam, Review and assessment of measured values of the nonlinear refractive-index coefficient of fused silica, Appl. Opt. 37 (1998) 546. doi:10.1364/AO.37.000546.

[192] M.R. Zaki, D. Hamani, M. Dutreilh-Colas, J.-R. Duclère, O. Masson, P. Thomas, Synthesis, thermal, structural and linear optical properties of new glasses within the TeO_2-TiO_2-WO_3 system, J. Non-Cryst. Solids. 484 (2018) 139–148. doi:10.1016/j.jnoncrysol.2018.01.034.

[193] B.O. Loopstra, H.M. Rietveld, Further refinement of the structure of WO_3, Acta Crystallogr. B. 25 (1969) 1420–1421. doi:10.1107/S0567740869004146.

[194] Y.-R. Luo, Comprehensive handbook of chemical bond energies, CRC Press, Boca Raton, 2007.

[195] G. Upender, C.P. Vardhani, S. Suresh, A.M. Awasthi, V. Chandra Mouli, Structure, physical and thermal properties of WO_3–GeO_2–TeO_2 glasses, Mater. Chem. Phys. 121 (2010) 335–341. doi:10.1016/j.matchemphys.2010.01.050.

[196] V. Dimitrov, M. Arnaudov, Y. Dimitriev, IR-spectral study of the effect of WO_3 on the structure of tellurite glasses, Monatshefte Für Chem. Chem. Mon. 115 (1984) 987–991. doi:10.1007/BF00798766.

[197] B.V.R. Chowdari, P.P. Kumari, Studies on Ag_2O-M_xO_y-TeO_2 (M_xO_y = WO_3, MoO_3, P_2O_5 and B_2O_3) ionic conducting glasses, in: Solid State Ion., Elsevier, 1998: pp. 665–675. doi:10.1016/S0167-2738(98)00393-2.

[198] V. Swamy, B.C. Muddle, Q. Dai, Size-dependent modifications of the Raman spectrum of rutile TiO_2, Appl. Phys. Lett. 89 (2006) 163118. doi:10.1063/1.2364123.

[199] S. Zhou, E. Čižmár, K. Potzger, M. Krause, G. Talut, M. Helm, J. Fassbender, S.A. Zvyagin, J. Wosnitza, H. Schmidt, Origin of magnetic moments in defective TiO_2 single crystals, Phys. Rev. B. 79 (2009). doi:10.1103/PhysRevB.79.113201.

[200] I. Lukačević, S.K. Gupta, P.K. Jha, D. Kirin, Lattice dynamics and Raman spectrum of rutile TiO_2: The role of soft phonon modes in pressure induced phase transition, Mater. Chem. Phys. 137 (2012) 282–289. doi:10.1016/j.matchemphys.2012.09.022.

[201] S.S. Sukhov, V.N. Sigaev, P. Perniche, A. Aronne, E. Fanelli, S. Brovelli, A. Paleari, G.E. Malashkevich, Structure and properties of erbium-titanium-tellurite glass, Glass Ceram. 63 (2006) 399–402. doi:10.1007/s10717-006-0133-6.

[202] N. Gupta, A. Khanna, F. Gonzàlez, R. Iordanova, Thermal characteristics, Raman spectra, optical and structural properties of TiO_2-Bi_2O_3-B_2O_3-TeO_2 glasses, in: 2017: p. 070005. doi:10.1063/1.4980440.

[203] A.S. Koster, F.X.N.M. Kools, G.D. Rieck, The crystal structure of potassium tungstate, K_2WO_4, Acta Crystallogr. B. 25 (1969) 1704–1708. doi:10.1107/S0567740869004602.

[204] H.J. Becher, Ramanspektroskopische untersuchungen zur bildung, phasenbreite und anionenstruktur des kaliumpolywolfram ats $K_2WO_4 \cdot 5$ — $7WO_3$, J. Common Met. 76 (1980) 169–180. doi:10.1016/0022-5088(80)90021-1.

[205] K. Okada, F. Marumo, S. Iwai, The crystal structure of $K_2W_4O_{13}$, Acta Crystallogr. B. 34 (1978) 3193–3195. doi:10.1107/S0567740878014739.

[206] K. Okada, F. Marumo, S. Iwai, The crystal structure of $Rb_{22}W_{32}O_{107}$, Acta Crystallogr. B. 33 (1977) 3345–3349. doi:10.1107/S0567740877010978.

[207] H. Fu, C. Pan, L. Zhang, Y. Zhu, Synthesis, characterization and photocatalytic properties of nanosized Bi_2WO_6, $PbWO_4$ and $ZnWO_4$ catalysts, Mater. Res. Bull. 42 (2007) 696–706. doi:10.1016/j.materresbull.2006.07.017.

[208] B. Manoun, J.M. Igartua, P. Lazor, High temperature Raman spectroscopy studies of the phase transitions in Sr_2NiWO_6 and Sr_2MgWO_6 double perovskite oxides, J. Mol. Struct. 971 (2010) 18–22. doi:10.1016/j.molstruc.2010.02.060.

[209] Y.V. Denisov, A.A. Zubovich, Boson Peak and Medium-Range Order Structure of Alkali Borate Glasses, Glass Phys. Chem. 29 (2003) 345–352. doi:10.1023/A:1025112607893.

[210] E. Stavrou, C. Tsiantos, R.D. Tsopouridou, S. Kripotou, A.G. Kontos, C. Raptis, B. Capoen, M. Bouazaoui, S. Turrell, S. Khatir, Raman scattering boson peak and differential scanning calorimetry studies of the glass transition in tellurium–zinc oxide glasses, J. Phys. Condens. Matter. 22 (2010) 195103. doi:10.1088/0953-8984/22/19/195103.

[211] Y. Ledemi, J.-P. Bérubé, R. Vallée, Y. Messaddeq, Refractive index modification in fluoro-borate glasses containing WO_3 induced by femtosecond laser, J. Non-Cryst. Solids. 385 (2014) 153–159. doi:10.1016/j.jnoncrysol.2013.11.029.

[212] G. Poirier, Y. Messaddeq, S.J.L. Ribeiro, M. Poulain, Structural study of tungstate fluorophosphate glasses by Raman and X-ray absorption spectroscopy, J. Solid State Chem. 178 (2005) 1533–1538. doi:10.1016/j.jssc.2004.10.032.

[213] A.K. Varshneya, Chapter 3 - Glass formation principles, in: Fundam. Inorg. Glas., Academic Press, San Diego, 1994: pp. 27–59.

[214] M. Kunz, I.D. Brown, Out-of-center distortions around octahedrally coordinated d^0 transition metals, J. Solid State Chem. 115 (1995) 395–406. doi:10.1006/jssc.1995.1150.

[215] A.M. Efimov, V.G. Pogareva, A.V. Shashkin, Water-related bands in the IR absorption spectra of silicate glasses, J. Non-Cryst. Solids. 332 (2003) 93–114. doi:10.1016/j.jnoncrysol.2003.09.020.

[216] E.S. Yousef, A. El-Adawy, N. El Koshkhany, E.R. Shaaban, Optical and acoustic properties of TeO_2-WO_3 glasses with small amount of additive ZrO_2, J. Phys. Chem. Solids. 67 (2006) 1649–1655. doi:10.1016/j.jpcs.2006.02.014.

[217] M.M. Umair, A.K. Yahya, M.K. Halimah, H.A.A. Sidek, Effects of increasing tungsten on structural, elastic and optical properties of xWO_3–$(40−x)Ag_2O$–$60TeO_2$ Glass System, J. Mater. Sci. Technol. 31 (2015) 83–90. doi:10.1016/j.jmst.2014.10.002.

[218] T. Honma, N. Ito, T. Komatsu, V. Dimitrov, Thermo-optic properties and electronic polarizability in alkali tellurite glasses, J. Am. Ceram. Soc. 93 (2010) 3223–3229. doi:10.1111/j.1551-2916.2010.03852.x.

[219]   V. Dimitrov, T. Komatsu, Electronic polarizability, optical basicity and non-linear optical properties of oxide glasses, J. Non-Cryst. Solids. 249 (1999) 160–179. doi:10.1016/S0022-3093(99)00317-8.

[220]   R. Adair, L.L. Chase, S.A. Payne, Nonlinear refractive index of optical crystals, Phys. Rev. B. 39 (1989) 3337–3350. doi:10.1103/PhysRevB.39.3337.

[221]   R. Castro-Beltrán, H. Desirena, G. Ramos-Ortiz, E. De la Rosa, G. Lanty, J.S. Lauret, S. Romero-Servin, A. Schülzgen, Third-order nonlinear optical response and photoluminescence characterization of tellurite glasses with different alkali metal oxides as network modifiers, J. Appl. Phys. 110 (2011) 083110. doi:10.1063/1.3654018.

[222]   M. Sundberg, The crystal and defect structures of $W_{25}O_{73}$, a member of the homologous series W_nO_{3n-2}, Acta Crystallogr. B. 32 (1976) 2144–2149. doi:10.1107/S0567740876007280.

[223]   O. Berger, W.-J. Fischer, V. Melev, Tungsten-oxide thin films as novel materials with high sensitivity and selectivity to NO_2, O_3 and H_2S. Part I: Preparation and microstructural characterization of the tungsten-oxide thin films, J. Mater. Sci. Mater. Electron. 15 (2004) 463–482. doi:10.1023/B:JMSE.0000031601.29022.07.

Synthèse, structure et propriétés optiques de nouveaux verres à base d'oxyde de tellure dans les systèmes TeO$_2$-TiO$_2$-WO$_3$ and TeO$_2$-NbO$_{2,5}$-WO$_3$

Ce travail est une contribution à la compréhension de la structure à courte et moyenne distance des verres à base de TeO$_2$ *via* de nouveaux verres au sein des systèmes TeO$_2$-TiO$_2$-WO$_3$ (TTxWy) et TeO$_2$-NbO$_{2.5}$-WO$_3$ (TNxWy). De pertinentes corrélations sont révélées entre leurs propriétés structurales (en utilisant la spectroscopie Raman) et optiques. Globalement, l'ajout de TiO$_2$, WO$_3$ ou NbO$_{2.5}$ n'engendre aucune évolution structurale brutale. L'ajout de TiO$_2$ induit une séparation de phases entre les régions amorphes riches en TiO$_2$ et le réseau riche en TeO$_2$. Cette interprétation est en accord avec le comportement structural prédit par la théorie de Dietzel sur la force de champ cationique. L'ajout de WO$_3$ entraîne l'apparition *(i)* d'octaèdres WO$_6$ uniformément dispersés à travers le réseau des ponts Te–O–Te (pour de faibles teneurs en WO$_3$) et *(ii)* de régions riches en WO$_3$ (pour des teneurs plus importantes en WO$_3$). L'ajout de NbO$_{2.5}$ engendre *(i)* une faible dépolymérisation structurale du réseau Te–O–Te et *(ii)* l'apparition des régions riches en NbO$_{2.5}$. Les verres étudiés sont dotés de forts indices de réfraction linéaires (2.19 dans TTxWy et 2.13 dans TNxWy en moyenne) et de remarquables susceptibilités non linéaires $\chi^{(3)}$ (7.03 *10^{-13} esu dans TTxWy et 5.48 *10^{-13} esu dans TNxWy en moyenne, *i.e.*, ~47 et ~37 fois plus élevées que la valeur de $\chi^{(3)}$ du verre SiO$_2$).

Mots-clés : verres à base de TeO$_2$; structure de verre ; propriétés optiques linéaires et non linéaires ; spectroscopie Raman ; décomposition spectrale Raman ; théorie de force de champ cationique ; transmission optique ; ellipsométrie spectroscopique.

Synthesis, structure and optical properties of new tellurium oxide-based glasses within the TeO$_2$-TiO$_2$-WO$_3$ and TeO$_2$-NbO$_{2.5}$-WO$_3$ systems

In this work, we present a contribution to the understanding of the short- to medium-range structure of TeO$_2$-based glasses *via* new glasses within the TeO$_2$-TiO$_2$-WO$_3$ (TTxWy) and TeO$_2$-NbO$_{2.5}$-WO$_3$ (TNxWy) systems. Consistent correlations are revealed between their structural (using Raman spectroscopy) and optical properties. Globally, no striking structural evolutions take place upon adding TiO$_2$, WO$_3$ or NbO$_{2.5}$. Adding TiO$_2$ results in a phase-separation between amorphous TiO$_2$-rich regions and TeO$_2$-rich network, in harmony with the predicted structural behavior on the basis of Dietzel's cationic field strength theory. Adding WO$_3$ leads to *(i)* uniformly dispersed WO$_6$ octahedra throughout the Te–O–Te network (at low WO$_3$ contents) and *(ii)* amorphous WO$_3$-rich regions (at higher WO$_3$ contents). Adding NbO$_{2.5}$ engenders *(i)* a weak structural depolymerization of the Te–O–Te network and *(ii)* occurrence of NbO$_{2.5}$-rich regions. The investigated glasses exhibit high linear refractive indices (averages of 2.19 in TTxWy and 2.13 in TNxWy) and remarkable nonlinear susceptibilities $\chi^{(3)}$ (averages of 7.03 *10^{-13} esu in TTxWy and 5.48 *10^{-13} esu in TNxWy, *i.e.*, ~47 and ~37 times higher than $\chi^{(3)}$ of SiO$_2$ glass).

Keywords: TeO$_2$-based glasses; glass structure; linear and nonlinear optical properties; Raman spectroscopy; full-scale Raman spectral decomposition; cationic field strength theory; optical transmission; spectroscopic ellipsometry.